



Improvement and tailoring of parts fabricated with Wire and Arc Additive Manufacturing

Tiago Miguel André Rodrigues

Master in Mechanical Engineering

DOCTORATE IN MECHANICAL ENGINEERING

NOVA University Lisbon
September, 2022



Improvement and tailoring of parts fabricated with Wire and Arc Additive Manufacturing

Tiago Miguel André Rodrigues

Master in Mechanical Engineering

Adviser: João Pedro Sousa Oliveira
Assistant Professor, Faculdade de Ciências e Tecnologia, Universidade Nova de Lisboa

Co-advisers: Telmo Jorge Gomes dos Santos
Full Professor, Faculdade de Ciências e Tecnologia, Universidade Nova de Lisboa

Examination Committee:

Chair: António Carlos Bárbara Grilo
Full Professor, Faculdade de Ciências e Tecnologia, Universidade Nova de Lisboa

Rapporteurs: Ana Sofia Figueira Ramos
Assistant Professor, Faculdade de Ciências e Tecnologia, Universidade Coimbra

Carlos Alves da Silva
Assistant Professor, Instituto Superior Técnico

Adviser: João Pedro Sousa Oliveira
Assistant Professor, Faculdade de Ciências e Tecnologia, Universidade Nova de Lisboa

Members: Filipe Samuel Correia Pereira da Silva
Full Professor, Departamento de Engenharia Mecânica da Universidade do Minho

António Carlos Bárbara Grilo
Full Professor, Faculdade de Ciências e Tecnologia, Universidade Nova de Lisboa

Rui Fernando dos Santos Pereira Martins
Associate Professor, NOVA University Lisbon

DOCTORATE IN MECHANICAL ENGINEERING

NOVA University Lisbon
September, 2022

Improvement and tailoring of parts fabricated with Wire and Arc Additive Manufacturing

Copyright © Tiago Miguel André Rodrigues, NOVA School of Science and Technology, NOVA University Lisbon.

The NOVA School of Science and Technology and the NOVA University Lisbon have the right, perpetual and without geographical boundaries, to file and publish this dissertation through printed copies reproduced on paper or on digital form, or by any other means known or that may be invented, and to disseminate through scientific repositories and admit its copying and distribution for non-commercial, educational or research purposes, as long as credit is given to the author and editor.

Acknowledgments

First, I would like to express my sincere thanks to my supervisor, Prof. João Oliveira for his constant guidance, patience, feedback, ability to find resources, and support during the last 3 years.

Second, to my co-supervisor, Prof. Telmo Santos who helped me with his disruptive ideas regarding my experimental work and for his life guidance advises. It is always a pleasure talking to him.

I would like to express my deepest gratitude to Mr. António Guinapo Campos and Mr. Paulo M. G. Magalhães for their everyday assistance and friendship. There isn't any age limitation in true friendship.

I am also grateful to Giovani Gonçalves Ribamar, Julian Avila, and Julián Escobar Atehortúa for their relevant contribution and collaboration in different publications. For their helping useful inputs and comments to my work and by performing Electron Backscatter Diffraction measurements.

My thanks to Amirali Shams and Kaiping Zhang who kindly performed some advanced material characterization at the University of Waterloo.

My deepest thanks to Valdemar Duarte, for his companionship, constant moral support, overwhelming generosity, and altruistic behavior that helped me to go through this journey until its end.

I would like to thank Francisco Werley Cipriano Farias for his friendship and stimulating discussions. Without him sharing his ideas and knowledge this thesis would have been less valuable.

A special thanks to Igor Felice for his goodwill and for helping me with the digital image correlation experiments.

I would always remember my fellow labmates, Francisco Ferreira, Jiajia Shen, Patrick Inácio, Pedro Ferreira, Pedro Fonseca, and Pedro Rendas, with whom I shared unforgettable moments.

I could not have undertaken this journey without Iana, with whom I shared my daily concerns. I'm thankful for her patience, endless support, and advice, for all the good times, and for the sacrifices she has made.

To my parents, Rui and Jacinta, for their constant support, kindness, and love and for their efforts in providing the best education possible.

To Fundação para a Ciência e a Tecnologia (FCT - MCTES) for its financial support via the PhD grant SFRH/BD/144202/2019.

This activity has received funding from the European Institute of Innovation and Technology (EIT) RawMaterials through the project Smart WAAM: Microstructural Engineering and Integrated Non-Destructive Testing. This body of the European Union receives support from the European Union's Horizon 2020 research and innovation program.

Abstract

Wire and arc additive manufacturing (WAAM) is an Additive Manufacturing (AM) process that finds applications in different industrial sectors. It shows to be competitive compared to other AM technologies, mainly due to its low implementation costs, high deposition rates, and the ability to produce medium to large complex parts. Improvement of parts' properties has been the primary goal of the scientific community and was also the main objective of this work, where significant scientific and technological developments were implemented. Different approaches were tested: i) by performing heat treatments; ii) by adding grain refiners to the molten metal; iii) by fabricating Functionally Graded Materials (FGM); iv) by developing a new process variant called Ultra cold Wire and Arc Additive Manufacturing (UC-WAAM).

To fulfill these objectives, laboratory means were developed. Including the development of a multi-wire gas tungsten arc welding (GTAW) torch for creating components with a functional gradient, two prototypes to introduce ceramic particles in the molten pool, and a customized gas metal arc welding (GMAW) torch.

The feasibility of using ceramic particles to refine the grain structure of WAAM parts was experimentally demonstrated on a High Strength Low Alloy (HSLA) steel and Inconel 625. Parts characterization was performed with multi-phenomena techniques: optical and scanning electron microscopy assisted by energy dispersive spectroscopy and electron backscatter diffraction, synchrotron X-ray diffraction, and mechanical testing.

Despite the potential applications of FGM, one of the main limitations is related to significant stresses, chemical incompatibilities, and the possible formation of undesirable intermetallics. In this work, manufacturing of different FGM was successfully produced without defects by applying different building strategies. The results showed that a direct-type interface resulted in superior mechanical properties without intermetallics and smaller residual stresses than a smooth transition build-type.

The development of UC-WAAM lowered the average temperatures experienced by the material and increased the cooling rates during parts fabrication compared to traditional GMAW. An overhang structure was fabricated, highlighting the potential for UC-WAAM to be used for this type of structures.

Keywords

Functionally Graded Material (FGM)

Heat-Treatments

Inoculants

Materials Characterization

Parts' Properties Improvement

Wire and Arc Additive Manufacturing (WAAM)

Resumo

A deposição direta de energia por arco elétrico e fio é um processo de fabrico aditivo que tem encontrando diferentes aplicações em diversos setores industriais. Esta tecnologia tem-se mostrado competitiva em comparação com outras tecnologias de fabrico aditivo, devido aos seus baixos custos de implementação, altas taxas de deposição e capacidade de produzir peças complexas de média/elevada dimensão. A melhoria das propriedades das peças tem sido o principal objetivo da comunidade científica e como tal foi também o principal objetivo deste trabalho, onde foram realizados importantes desenvolvimentos científicos e tecnológicos. Diferentes abordagens foram testadas: i) através de tratamentos térmicos; ii) através da adição de afinadores de grão ao banho de fusão; iii) através do desenvolvimento de materiais com gradiente de funcionalidade (FGM); iv) através do desenvolvimento de uma nova variante de processo denominada Ultra Cold Wire and Arc Additive Manufacturing (UC-WAAM).

De forma a cumprir os objetivos propostos, foram desenvolvidos meios laboratoriais, tais como o desenvolvimento de uma tocha costumizável de alimentação multifio de soldadura com um eletródo não consumível de tungstênio para a criação de componentes com gradiente funcional. Foram ainda desenvolvidos dois protótipos para introduzir partículas cerâmicas no banho de fusão, e uma tocha de soldadura por arco elétrico com gás de proteção.

A viabilidade do uso de partículas cerâmicas para refinar a estrutura de peças produzidas por fabrico aditivo por arco elétrico foi demonstrada experimentalmente num aço de baixa liga alta resistência e no Inconel 625. A caracterização das peças foi realizada com diferentes técnicas, tais como microscópio ótico e eletrónico de varrimento equipado com espectroscopia de energia dispersiva de raios-X, difração de eletrões retrodifundidos, difração de raios X utilizando radiação sincrotrão, e através de diferentes ensaios mecânicos.

Apesar das potenciais aplicações de materiais com gradiente de funcionalidade, uma das suas principais limitações está relacionada com as elevadas tensões residuais, incompatibilidades químicas e a potencial formação de intermetálicos indesejáveis. Neste trabalho, foram produzidos com sucesso e sem defeitos diversos materiais com gradiente funcionalidade através de diferentes estratégias de deposição. Os resultados obtidos demonstraram que uma interface do tipo direta

resultou em propriedades mecânicas superiores, sem compostos intermetálicos e com tensões residuais inferiores do que uma transição gradual entre os materiais utilizados.

O desenvolvimento de uma nova variante de processo permitiu reduzir as temperaturas e as taxas de arrefecimento que se desenvolvem durante a fabricação de peças comparativamente com a soldadura convencional por arco elétrico com gás de proteção. Foi também fabricada uma estrutura sem suporte, destacando o potencial desta nova variante para o fabrico deste tipo de componentes.

Palavras chave

Materiais com gradiente de funcionalidade (MGF)

Tratamentos térmicos

Inoculantes

Caracterização de materiais

Melhoramento de propriedades mecânicas

Deposição directa de energia por arco eléctrico e fio

Contents

ACKNOWLEDGMENTS.....	VII
ABSTRACT	IX
KEYWORDS	XI
RESUMO.....	XIII
PALAVAS CHAVE.....	XV
CONTENTS	XVII
LIST OF FIGURES	XXI
LIST OF TABLES	XXIX
LIST OF ABBREVIATIONS.....	XXXI
LIST OF SYMBOLS.....	XXXV
1. INTRODUCTION	1
1.1 Motivation	1
1.2 Objectives	2
1.3 Major Findings	3
1.4 Document Organization.....	4
1.5 Publications in international indexed journals (ISI/Scopus)	5
2. LITERATURE REVIEW.....	7
2.1 Introduction	7
2.2 Additive manufacturing	7
2.3 Wire and arc additive manufacturing	8
2.4 Solidification and grain formation	9
2.4.1 Nucleation.....	9

2.4.2	Growth	10
2.4.3	Role of solute on grain refinement.....	11
2.4.4	Solidification Map.....	11
2.4.5	Role of inoculants on grain refinement	13
2.5	Common defects in WAAM	15
2.6	Defects mitigation	17
2.7	Summary	20
3.	EXPERIMENTAL SETUP	21
3.1	Introduction	21
3.2	XYZ-motion system equipment	21
3.3	GMAW-based WAAM torch.....	23
3.4	Development of prototypes to introduce refinement particles	24
3.4.1	Prototype 1	25
3.4.2	Prototype 2	25
3.5	Multi-wire feed WAAM torch	28
3.6	Materials and Methods	29
3.6.1	Materials	29
3.6.2	Microstructure Characterization.....	30
3.6.3	Hardness measurements	31
3.6.4	Magnetic Permeability and Electrical conductivity measurements.....	31
3.6.5	Synchrotron X-ray diffraction measurements	32
3.6.6	Residual stress measurements using neutron diffraction	34
3.6.7	Uniaxial Tensile and Compression tests	34
3.6.8	Thermodynamic Calculations	35
3.6.9	Current, Voltage, and Temperature measurements.....	35
3.7	Summary	35
4.	HEAT TREATMENTS ON WIRE AND ARC ADDITIVE MANUFACTURING PARTS.....	37
4.1	Introduction	37
4.1.1	Stainless Steel	37

4.1.2	Inconel 625	38
4.2	Stainless Steel 316L Si Parts	41
4.2.1	Materials and Methods	41
4.2.2	Results and Discussion	42
4.2.3	Conclusions	55
4.3	Inconel 625 parts	56
4.3.1	Materials and Methods	56
4.3.2	Results and Discussion	56
4.3.3	Conclusions	60
4.4	Summary	60
5.	IMPROVEMENT OF PARTS PROPERTIES VIA INSERTION OF REFINEMENT PARTICLES..	61
5.1	Introduction	61
5.1.1	High strength low alloy Steel	61
5.1.2	Inconel 625	62
5.2	Refinement of High strength low alloy Steel WAAM parts	63
5.2.1	Materials and methods	63
5.2.2	Results and Discussion	64
5.2.3	Conclusions	73
5.3	Refinement of Inconel 625 WAAM parts	73
5.3.1	Materials and methods	73
5.3.2	Results and discussion	75
5.3.3	Conclusions	82
5.4	Summary	83
6.	FUNCTIONALLY GRADED MATERIALS ..	85
6.1	Introduction	85
6.1.1	HSLA Steel to Copper alloy	86
6.1.2	Stainless steel 316L to Inconel 625	87
6.2	HSLA Steel to Copper alloy	88
6.2.1	Materials and design	88

6.2.2	Results and discussion	89
6.2.3	Discussion	97
6.2.4	Conclusions	99
6.3	Stainless steel 316L to Inconel 625.....	100
6.3.1	Materials and design	100
6.3.2	Results and discussion	102
6.3.3	Conclusions	119
6.4	Summary	119
7.	DEVELOPMENT OF A NEW WIRE AND ARC ADDITIVE MANUFACTURING VARIANT.....	121
7.1	Introduction	121
7.2	Materials and design	122
7.3	Results and discussion	124
7.3.1	Preliminary UC-WAAM single-beads experiments	124
7.3.2	GMAW-based WAAM and UC-WAAM single walls.....	126
7.3.3	Electrical current measurements	128
7.3.4	UC-WAAM droplet transfer mechanism	129
7.3.5	Thermal analysis comparison between GMAW-based WAAM and UC-WAAM	130
7.3.6	Microstructure analysis of the single walls	133
7.3.7	Mechanical properties of the single walls	134
7.4	Potential applications	135
7.5	Conclusions	136
7.6	Summary	137
8.	CONCLUSIONS AND FUTURE WORKS	139
8.1	Introduction	139
8.2	Major conclusions	139
8.3	Recommendations for future works	142
BIBLIOGRAPHY		145

List of Figures

Figure 1.1 – Schematically representation of the outline and overall objective of this dissertation.....	3
Figure 2.1.....	8
Figure 2.2 - Effect of the temperature gradient, G, and growth rate, R, on the morphology and size of solidification structures [10].	12
Figure 2.3 - Effect of constitutional supercooling on the solidification mode: (a) planar; (b) cellular; (c) columnar dendritic; (d) equiaxed dendritic (S: solid , L: liquid, M: mushy zone) [10].	13
Figure 2.4 - Representation of the three regions ($X_{cs}, X'dl, X_{sd}$) that will determine the grain size. $X_{cs} + X'dl$ is equal X_{nfz} , that is a nucleation-free zone, where nucleation is not possible. The next nucleation event occurs when the ΔTn - S_d curve intersects the bottom of the CS zone (adapted from [14]); T_A : Actual temperature of the melt (°C), T_E : Equilibrium liquidus temperature (°C).....	14
Figure 2.5 - Electron Backscatter Diffraction (EBSD) orientation maps of the Inconel 718 after: a) WAAM (unrolled) , b) WAAM + interlayer rolling (rolled).....	17
Figure 2.6 - Schematic representation of the Hot Forging-WAAM (HF-WAAM) variant, DAC: distance to arc center, F_F : Forging Force [27].	18
Figure 2.7 - a) Representation of thermoelectric cooling setup [34], b) Schematic representation of the inductor heating system [35].....	19
Figure 2.8 - Porosity presence in samples manufacture with: (a) conventional cold metal transfer (CMT); (b) cold metal transfer-pulse advanced (CMT-PADV) (adapted from [40]).....	20
Figure 3.1 - Photograph of the developed XYZ-motion equipment.....	22
Figure 3.2 - Schematic representation of each electrical component and the circuit diagram of the developed XYZ-motion equipment.....	23
Figure 3.3 - 2D view of the GMAW-based WAAM torch: a) Front view; b) Side-view.	24
Figure 3.4 - Customized feeding device used to deposit refinement particles on top of previously deposited layers: a) schematic representation; b) actual device.	25

Figure 3.5 - 2D and 3D view of the particle feeder device attached to the GMAW-based WAAM torch.	26
Figure 3.6 – Illustration of each component in the particle feeder device and the GMAW-based WAAM torch: a) schematic representation; b) actual device; 1) Solution with particle dispenser (syringe), 2) Motor, 3) Power transmission system, 4) Linear rail guide, 5) Connection tubes, 6#1) Bearing support, 6#2) Spring, 6#3) Motor, 7) Shielding gas tube, 8) Conductive part, 9) Torch nozzle, 10) Insulating part and 13) Solution with particles.	27
Figure 3.7 - Section view of the customized feeding device. 5#1) connection tube #1, 5#2) connection tube #2, 9) Torch nozzle, 10) Insulating part, 11) Conductive nozzle, 12) Insulating sleeve, 13) Solution with particles, 14) Welding wire, 15) Welding wire + particles.	28
Figure 3.8 - 3D view of the flux and refinement particles flow into the conductive nozzle. 5#1) connection tube #1, 11) Conductive nozzle, 13) Solution with particles, 14) Welding wire, 15) Welding wire + particles.	28
Figure 3.9 - Multiple-wire feed GTAW-based WAAM torch: a) Solidworks design; b) Experimental Setup and integration in the XYZ-motion equipment.	29
Figure 3.10 - a) Schematic representation of the experimental setup applied to perform the heat treatments in-situ during the transmission of synchrotron X-rays (not at scale); b) Experimental setup.	32
Figure 3.11 - Representation of the setup used for the synchrotron X-ray diffraction measurements.	33
Figure 4.1 - Possible solidification paths in Inconel 625 [91].	40
Figure 4.2 - Schematic representation of the heat treatments applied during in-situ Synchrotron X-ray diffraction measurements. The time-temperature plot also resumes the heating and cooling ramps used.	42
Figure 4.3 - Localization of the specimens taken from the Stainless steel 316 part for microstructure and mechanical characterization.	42
Figure 4.4 - Optical microscope image of the 316 stainless steel: a) and b) As-built, c) After 400 °C 1h, d) After 950 °C 2h, e) After 1050 °C 2h f) After 1200 °C 1h. Inserts b1, c1, d1, e1, and f1 correspond to the high magnification EBSD analysis.	44
Figure 4.5 - Overview of the diffraction patterns of the as-built and heat-treated samples. Inserts illustrate the existence of δ-ferrite after being heat-treated for two hours at 1050 °C.	46
Figure 4.6 - a) and b) Sigma (σ) growth and δ-ferrite dissolution in the isothermal stage at 950 °C after 1 min, 3 min, 15 min, 30 min, and 60 min. Peak intensity normalization of these two spectra regions (where a high density of σ peaks is observed) is conducted based on the maximum intensity of the {411} σ peak. Therefore, green-to-red colors represent the relative kinetics of precipitation of σ , while blue denotes the constant normalized background counts.	48

Figure 4.7 - Intensity evolution of the peaks {110} δ , {211} δ , {331} σ , {411} σ , {420} σ , and {202} σ during the first hour of the isothermal holding at 950 °C. The apparent stabilization of the {110} δ peak after 3 min of isothermal dissolution is explained by the simultaneous precipitation of {202} σ . The initial volumetric expansion is then associated with the dissolution of δ -ferrite, as precipitation of σ results in a modest volumetric contraction.....	48
Figure 4.8 - a) Overall overview of the powder pattern before and after heat treatment for 2 hours at 950 °C; b) Powder diffraction pattern of austenite, δ -ferrite, and σ	49
Figure 4.9 - δ -Ferrite dissolution after isothermal holding at 1050 °C for 1 min, 3 min, 15 min, 30 min, 60 min, and 120 min.....	49
Figure 4.10 - Austenite volume percent evolution during the heat treatments made at 1050 °C 2h and 1200 °C 1h; b) {200} δ reflection before and after solubilization heat treatments.....	50
Figure 4.11 - Lattice parameter evolution of the most prominent FCC peaks during heat treatment at 1200 °C for 1h.....	52
Figure 4.12 - Calculated isopleth for Cr mass percentage. The red crosses mark the composition of ER 316LSi at each heat treatment temperature. The thermodynamic information is taken from the commercial thermodynamic database TCFE11.....	53
Figure 4.13 - a) Hardness measurements across sample's height, b) Boxplot of the hardness measurements displaying the minimum, maximum, median, and quartiles (Q1 and Q3) of each condition.....	54
Figure 4.14 - a) Output signal of Eddy Current Testing (ECT) probe using 1.1 MHz, b) Detailed view of the signal output of ECT delineated with dashed lines, c) Average electrical conductivity measurements with a four-point probe for each condition.....	55
Figure 4.15 - a) Optical microscope observation of the as-built Inconel 625; b) SEM image of the inside of the γ -dendrites; c) Synchrotron X-ray diffraction patterns of the Inconel 625 as-built sample; d) ThermoCalc Scheil-Gulliver calculations.....	57
Figure 4.16 - a) Synchrotron X-ray diffraction patterns of the as-built Inconel 625 sample after 1 hour at 870 °C; b) Detail of the δ precipitation during 1, 5, 15, 30, and 60 minutes at isothermal holding; c) Lattice parameter evolution of γ {200} and γ {220} peaks.....	58
Figure 4.17 - a) Secondary precipitates (δ -phase) formation during heating up to 1150 °C; b) MC-type carbides formation during cooling from 1150 °C down to room temperature.....	59
Figure 4.18 - Synchrotron X-ray diffraction results after Inconel 625 was heat-treated for: a) 4 hours at 750 °C; b) 30 minutes at 1200 °C.....	59
Figure 4.19 - Hardness measurements taken by mapping an area of 5 x 5 mm with a step size of 250 μ m.....	60

Figure 5.1 - Geometry and dimensions of the uniaxial tensile specimens removed from the HSLA steel sample.....	64
Figure 5.2 - Representation of the sample extraction location for each characterization technique.	64
Figure 5.3 - Isometric micrographs of sample: a) HSLA as-built; b) HSLA with 0.66 wt.% SiC.....	65
Figure 5.4 - Scanning electron microscopy image of the HSLA steel sample produced with SiC particles; M-A:martensite-austenite islands.....	65
Figure 5.5 - Scanning electron microscopy images of samples: a) HSLA as-built; b) HSLA with 0.66 wt.% SiC; c) and d), energy dispersive spectra and chemical composition of the SiC-free and SiC-added WAAM parts, respectively. The dashed rectangles in a) and b) show the area used to determine the overall composition of the produced parts.	66
Figure 5.6 - Energy-dispersive X-ray spectroscopy line scan over a SiC particle in a WAAM sample inoculated with 0.66 wt.% of SiC.	67
Figure 5.7 - Electron backscattered diffraction (EBSD) orientation maps of sample: a) HSLA steel as-built; b) HSLA steel with 0.66 wt.% SiC.....	68
Figure 5.8 - Distribution of the misorientation angles of the ferritic grains in the as-built (HSLA steel) and inoculated (HSLA steel + SiC) WAAM parts: a) boundary distribution and b) frequency of low (< 15°) and high angle (> 15° and < 50°, and > 50°) boundaries.	68
Figure 5.9 - Diffractogram of the sample: black) HSLA steel; red) HSLA steel with 0.66 wt.% SiC. γ – Austenite; α -Ferrite.....	69
Figure 5.10 - Tensile curves of SiC and non-SiC WAAM parts tested along the horizontal and vertical directions.	70
Figure 5.11 - Scanning electron microscopy image of a surface fracture of sample: a) HSLA steel; b) HSLA steel with 0.66 wt.% SiC.	71
Figure 5.12 - Hardness values measurements across sample's height: non-inoculated sample (black) and 0.66 wt.% SiC inoculated sample (red).	72
Figure 5.13 - Electrical conductivity measurements with a four-point probe.....	73
Figure 5.14 - SEM images taken from the non-remelted and remelted regions of samples: (a), (b) As-built; (c) (d) Inconel 625 with 0.31 wt.% TiB ₂ ; (e) (f) Inconel 625 with 0.56 wt.% TiB ₂ . Inserts a1, c1, and e1 correspond to higher magnification SEM images.....	76
Figure 5.15 - ThermoCalc Scheil-Gulliver calculations for the Inconel 625 and modified Inconel 625 considering a complete dissolution of TiB ₂ in the matrix.....	77
Figure 5.16 -a) EBSD map of the as-built Inconel 625 sample; b) EBSD map of the Inconel 625 with 0.56 wt.% TiB ₂ ; c) Grain shape parameters obtained from the EBSD maps; d) Low and high grain	

boundaries angle density comparison; Comparison of inverse pole figures of texture for: e) as-built Inconel 625; f) Inconel 625 with 0.56 wt.% TiB ₂	78
Figure 5.17 - Synchrotron X-ray diffraction measurements for the WAAM fabricated parts with and without the introduction of TiB ₂	79
Figure 5.18 - a) Temperature simulated and measured by thermocouples during the deposition of the 1 st layer of the WAAM-fabricated wall; b) Simulation of the maximum temperature of the molten pool at each deposited layer vs the melting temperature of TiB ₂	80
Figure 5.19 - Average hardness measurements taken by mapping an area of 5 x 5 mm with a step size of 250 µm.	81
Figure 5.20 - Summary of yield strength obtained from compression tests taken from the travel and build-up direction.	82
Figure 6.1 - Schematic representation of the functionality graded material of HSLA-steel to Cu-based alloy.	89
Figure 6.2 - a) Cross-section overview of the as-built FGM part; Detail of the region with: b) 100% HSLA steel, c) 100% Cu-Al alloy, d), e), f) and g) interfacial regions.....	90
Figure 6.3 - Synchrotron X-ray diffraction analysis performed in regions comprising only HSLA steel, Cu-Al alloy, and the interface (region E, previously depicted in Figure 6.2 e).	91
Figure 6.4 - Energy-dispersive X-ray spectroscopy (EDS) mapping of the as-built HSLA steel region: a) Fe; B) Mo, c) Ni, d) Electron Backscatter Diffraction (EBSD) inverse pole figure.....	92
Figure 6.5 - Elemental mapping of the as-built copper microstructures obtained by scanning electron microscopy coupled with energy dispersive X-ray spectrometry (SEM-EDS): a) Cu, b) Al, c) Fe; d) Scanning electron microscopy (SEM) image of the secondary phases and precipitates found in the as-built copper alloy; e) EDS line scan across Cu-based alloy secondary phases; f) EBSD orientation maps.	93
Figure 6.6 - EDS mapping of the HSLA-steel to Cu-Al interface region analysis: Scan #1: a) Cu, b) Al, c) Fe; Scan #2: d) Cu, e) Al, f) Fe.	93
Figure 6.7 - a) EBSD phase mapping of the interface region; b) SEM morphologies of δ-ferrite in a Cu FCC matrix; c) SEM morphologies of MA constituents in an α-Fe matrix; d) EDS point analysis at positions marked in b). MA: Martensite-austenite.	94
Figure 6.8 - Hardness measurements taken from the substrate to the last deposited layer of the FGM cross-section.	95
Figure 6.9 - Electric conductivity and electrical impedance measurements taken from the first to the last deposited layer of the FGM cross-section.	96

Figure 6.10 - Representative stress-strain curves of the HSLA-steel and Cu-Al alloy parts and their dissimilar multi-metallic part; SEM image of the fracture surface of b) Functionality graded material; c) As-built HSLA steel; d) As-built Cu-Al alloy.....	97
Figure 6.11 - Cu-Fe Phase diagram with the metastable miscibility gap (dotted curved line) (adapted from [193]), pointing to the composition of the δ -Fe constituent; b) Cu-Al binary phase diagram highlighting the composition in the Cu-FCC constituents in the interface (adapted from [194]).	98
Figure 6.12 - Calculated equilibrium phase diagram considering an alloy with 70 % of the HSLA steel and 30 % of the Cu-Al alloy elements (wt.%) in the molten pool.	99
Figure 6.13 - Build strategies employed to fabricate different FGMS: a) and b) As-built control samples of Inconel 625 and 316L stainless steel, respectively; c) Direct interface from stainless steel to Inconel (FGM 100-100); d) Direct interface from stainless steel to Inconel with post-WAAM heat treatment of 1050 °C for 2 hours (FGM 100-100 HT); e) Smooth transition by varying the percentage of filler material within each layer in concentration steps of 5 wt.% (FGM 5); f) Smooth transition in steps of 5 layers and 20 wt.% (FGM 20) and g) Smooth transition intended to avoid undesirable phases, built-in steps of 5 layers and 5 wt.% (FGM 90-10).....	101
Figure 6.14 –Comparison of the cross-section overview of the samples built with a direct interface with and without heat treatments, respectively, (FGM 100-100 (a), FGM 100-100 HT (j)); Details of the regions with: (b),(c),(f) and (g) 100 wt.% Inconel 625, (d) and (h) interfacial region, and (e) and (i) 100 wt.% 316L Stainless steel.....	103
Figure 6.15 - a) Cross-section overview of the FGM 90-10 built to avoid unwanted concentrations; Detail of the region with: b) 100 wt.% Inconel, c) 90 wt.% Inconel, d) interface region #1, e) interface region #2, f) 10 wt.% Inconel and g) 100 wt.% 316L Stainless steel.	104
Figure 6.16 - Microstructure of the: a) Cross-section of the FGM made in weight percentage steps of 5% (FGM 5); Details of the region with: b) 100 wt.% Inconel, c) 95 wt.% Inconel, d) 85 wt.% Inconel, e) 65 wt.% Inconel, f) 55 wt.% Inconel, g) 45 wt.% Inconel, h) 25 wt.% Inconel, i) 15 wt.% Inconel and j) 100 wt.% 316L Stainless steel.	105
Figure 6.17 - Pseudo-binary FeCrNi diagram (adapted from [203]).....	105
Figure 6.18 - Cracks in sample FGM 20 in the region containing 60 wt.% Inconel and 40 wt.% Stainless steel.	106
Figure 6.19 - Representation of the $\text{Cr}_{\text{eq}}/\text{Ni}_{\text{eq}}$ ratio of the region where the fracture at sample FGM 20 was found.	107
Figure 6.20 - Synchrotron X-ray diffraction analysis performed in samples FGM 100-100 and FGM 100-100 HT in regions comprising: a) Inconel 625, b) Stainless steel 316L, c) Interface.....	108
Figure 6.21 - Synchrotron X-ray measurements taken from the substrate to the last deposited layer in FGM 5.....	109

Figure 6.22 - Scheil-Gulliver calculations for stainless-steel wt.% concentrations of: a) 85 %, b) 70%, and c) 60%; d) Thermodynamic equilibrium calculations considering 50 wt.% of Inconel and stainless steel.....	110
Figure 6.23 - Scanning electron microscopy (SEM) and Energy-dispersive X-ray spectroscopy (EDS) mapping of the interface of: a) to g) FGM 100-100; f) to j) FGM 100-100 HT.....	111
Figure 6.24 - Energy-dispersive X-ray spectroscopy (EDS) line scan across the precipitates in the compositional region with 50 wt.% stainless steel/50 wt.% Inconel.....	112
Figure 6.25 - Residual stresses in the three principal directions (c) of the sample: a) FGM 100-100 (direct interface); b) FGM 5 (smooth transition).	113
Figure 6.26 - Comparison of hardness measurements between samples: a) FGM 90-10 vs FGM 5 (smooth transition); b) FGM 100-100 vs FGM 100-100 HT.	115
Figure 6.27 - Electric conductivity measurements made starting in the first layer and ending on the last deposited one.	116
Figure 6.28 - Average mechanical strength test results after tensile loading three specimens from each condition and respective fracture location.	117
Figure 6.29 - Strain measurements along the X-axis distribution during tensile testing for specimens: FGM 5, FGM 90-10, FGM 100-100, and FGM 100-100 HT.....	118
Figure 6.30 - Scanning electron microscope (SEM) image of the fracture surface of sample: (a) FGM 100-100; (b) FGM 100-100 HT; (c) FGM 5; (d) FGM 90-10; (e) As-built stainless steel 316; (f) As-built Inconel 625.	119
Figure 7.1 - WAAM variants: a) hot-wire GTAW b) arcing wire GTAW, c) Consumable and Non-consumable Indirect Arc Welding Process, d) Compulsively constricted WAAM (adapted from [38,217–219]).	122
Figure 7.2 - Schematic comparison of the electric arc location, electrons flow, and the setup used with a: a) GMAW-based WAAM torch, b) UC-WAAM torch, c) Customized UC-WAAM torch.....	123
Figure 7.3 - Location of the position of the arc start, arc end, and the position of the four thermocouples used to measure the temperatures experienced in the substrate.	124
Figure 7.4 - Ultracold-Wire and Arc Additive Manufacturing: a) Process parameters window with single-beads cross-sections of samples within the feasible process parameters; b) Single-beads appearance of each identified zone.	126
Figure 7.5 - Cross-section images and micrographs of the interlayer region of samples: a) P1, b) P2, c) P3, and d) P4.....	127
Figure 7.6 - Cross-section of the sample built with UC-WAAM using optimal process parameters...	128

Figure 7.7 - Current measurements of the second layer of samples P3 and P4 during: a) 0.5 seconds; b) 0.05 seconds. The average current during fabrication of samples P3 and P4 was 119.8 A and 121.3 A, respectively.....	129
Figure 7.8 - a) High-speed camera image of the arc morphology and molten pool size, b-g) Steps of the droplets transfer mechanism.....	130
Figure 7.9 - Comparison of the temperature measurements obtained from the pairs of thermocouples placed in the substrate during the deposition of each sample.....	131
Figure 7.10 - Thermographic image taken during the deposition of the last layer of: a) P1 (GMAW-based WAAM), b) (UC-WAAM).....	132
Figure 7.11 - Results of the temperature measured in: a) the first layer of samples P1 and P2; b) the fifth layer of samples P1 and P2; c) the first layer of samples P3 and P4; d) the fifth layer of samples P3 and P4.....	133
Figure 7.12 - Cross-section micrographs of samples: a) P1, b) P2, c) P3, and d) P4; (AF: acicular ferrite; PF: Polygonal ferrite).....	134
Figure 7.13 - Hardness values measurements across the sample height: a) P1 and P2; b) P3 and P4.	135
Figure 7.14 - Uniaxial tensile Stress-Elongation curves of the samples built.	135
Figure 7.15 - a) Schematic 3D view of the setup used to build overhang structures; b) UC-WAAM building sequence steps for the overhang structures.....	136

List of Tables

Table 3.1 - Chemical composition of the wire feedstocks used in this work (wt.%).....	30
Table 3.2 - Etchant composition used to reveal the microstructure of each alloy.....	31
Table 4.1 - Phase percentage measurements made with a Python routine of each phase based on three different micrographs of each condition.	45
Table 4.2 - d-spacing values and lattice strain of the main austenite and δ-ferrite peaks before and after stress-relief heat treatment (400 °C for 1 h).....	46
Table 4.3 - Equilibrium calculations using TCFE11 database of Thermo-Calc for the volume percent [%] at the temperatures of interest.	51
Table 4.4 - Comparison of each phase's volume percentage [vol.%] after heat treatment. Measurements were made via the single peak fitting method and via the Rietveld refinement method performed with MAUD.	51
Table 5.1 - Summary of mechanical properties of the SiC-free and SiC-containing HSLA steel parts obtained from uniaxial tensile testing.	70
Table 6.1 - Process parameters used in the experiments.....	88
Table 6.2 - Process parameters used to fabricate the different FGMs.	100
Table 7.1 - Process parameters of single-wall samples built.	124
Table 7.2 - Single walls cross-section characteristics.....	128

List of Abbreviations

Abbreviation	Definition
3D	Three Dimensional
2D	Two Dimensional
AC-GTAW	Arcing Wire-Gas Tungsten Arc Welding
AF	Acicular Ferrite
AISI	American Iron And Steel Institute
AM	Additive Manufacturing
ASTM	American Society For Testing And Materials
AWS	American Welding Society
BCC	Body-Centered Cubic
BJT	Binder Jetting
CAD	Computer-Aided-Design
CC-WAAM	Compulsively Constricted Wire And Arc Additive Manufacturing
CET	Columnar To Equiaxed Transition
CMT	Cold Metal Transfer
CNC-IADW	Consumable And Non-Consumable Indirect Arc Welding Process
CS	Constitutional Supercooling
CTWD	Contact Tip To Work Distance
DC	Direct Current
DED	Directed Energy Deposition
DIC	Digital Image Correlation

DIL	Dilatometer
EBF ³	Electron-Beam Freeform Fabrication
EBSD	Electron Backscatter Diffraction
EC	Eddy Current
ECT	Eddy Current Testing
EDS	Energy-Dispersive X-ray Spectroscopy
ER	Electric Rod
FCC	Face-Centered Cubic
FEM	Finite Element Method
FGM	Functionally Graded Material
FWHM	Full-Width Half Maximum
GMAW	Gas Metal Arc Welding
GTAW	Gas Tungsten Arc Welding
HAGB	High Angle Grain Boundaries
HF-WAAM	Hot-Forging Wire and Arc Additive Manufacturing
HSLA	High Strength Low Alloy
HT	Heat Treatment
HWAAM	Hot Wire Wire and Arc Additive Manufacturing
IACS	International Annealed Copper Standard
Inc625	Inconel 625
LAGB	Low Angle Grain Boundaries
LENS	Laser Engineered Net Shaping
LMD	Laser Metal Deposition
MA	Martensite-Austenite
MEX	Material Extrusion
MIG	Metal Inert Gas
MJT	Material Jetting
NI	National Instruments

PBF	Powder Bed Fusion
PF	Polygonal Ferrite
PTFE	Polytetrafluoroethylene
PWHT	Post WAAM Heat Treatment
RP	Rapid Prototyping
SEM	Scanning Electron Microscope
SHL	Sheet Lamination
SINQ	Swiss Spallation Neutron Source
SLM	Selective Laser Melting
SS 316L	Stainless Steel 316L
TCP	Topologically Close-Packed
TIG	Tungsten Inert Gas
TS	Travel Speed
UC-WAAM	Ultra Cold Wire and Arc Additive Manufacturing
UTS	Ultimate Tensile Strength
WAAM	Wire And Arc Additive Manufacturing
WFS	Wire Feed Speed
XRD	X-ray Diffraction

List of Symbols

C_0 [wt.%]	Solute composition
d [m]	Lattice spacing
D_L (m^2/s)	Chemical diffusivity coefficient of solute in liquid
E [Pa]	Elastic modulus
F_k	Structure factor of the k plane family
F_p	Fraction of phase p
G [$^\circ C/m$]	Temperature gradient
I_{pk}	Intensity of each peak
k	Equilibrium partition coefficient
L [J/kg]	Latent heat
M	Peak multiplicity
m_l [$^\circ C/\text{wt.\%}$]	Slope of the liquidus line in a phase diagram
n_p	Number of peaks of phase p
Q	Growth restriction factor
R [m/s]	Growth rate
T_s [$^\circ C$]	Solidification temperature
V_p [m^3]	Cell volume

X'_{dl} [μm]	Diffusion distance from the S/L interface to the point where the sufficient cs has been generated for nucleation to occur
X_{cs} [μm]	Distance at which a previously nucleated grain must grow to establish sufficient cs ahead of the S/L interface
X_{sd} [μm]	Distance from the end of the diffusion field to the next most potent particle where a new nucleation event can take place
γ_{nm} [J/m^2]	Surface tension between the nucleus and the melt
ΔG_{Nuc} [J]	Free energy barrier for nucleation
ΔT [$^\circ\text{C}$]	Temperature variation
ΔT_n [$^\circ\text{C}$]	Critical undercooling
θ_{wa} [rad]	Wetting angle
θ_{hkl} [rad]	Scattering angle
λ [m]	Wavelength
ν	Poisson ratio
ρ [kg/m^3]	Density

1.

INTRODUCTION

1.1 Motivation

Over the past decades, technological advances have changed the available materials, manufacturing processes, and designs. During the development of new products, these three factors: materials, design, and manufacturing, have to interact with each other. If the designs become more complex, new materials and manufacturing processes may need to be developed to cope with the new limits imposed by novel and constrained design demands. If new materials are developed, manufacturing processes must be adapted, and the designs may need to be modified. Additive Manufacturing (AM) processes have been continuously developed and can push design and materials limits by fabricating complex structures with tailored mechanical properties in short delivery times.

Amongst the technologies used for AM of metallic alloys, especially in the Directed Energy Deposition (DED) category, Wire Arc Additive Manufacturing (WAAM) emerged as a cost-efficient technology to produce medium to large-scale parts. It requires low capital investment, presents high deposition rates, and can overcome issues related to processing industrial-relevant materials such as Nickel and Titanium alloys.

WAAM uses the equipment commonly used in arc welding to deposit the material layer-by-layer. Therefore, the similarities with welding result in several issues that must be addressed to meet certain requirements. These issues include high residual stresses, porosity, solidification cracking, and highly textured microstructures that lead to anisotropic properties. Therefore, new process variants should be developed to unlock the full potential of WAAM in processing different alloys.

Production of Functionally Graded Materials (FGM) has been one hot topic in the scientific community. WAAM has shown to be a good candidate to produce these since multiple materials can be added to the same molten pool at different rates and changed, if needed, within each layer. Still, there is a lack of research in this field, as a limited combination of materials has been tested, and most published studies contain solidification cracks in the transition regions.

1.2 Objectives

This thesis aimed to develop WAAM variants capable of enhancing and tailoring metal parts' properties by reducing the formation of undesirable microstructural features such as coarse grains, undesirable phases, and cracking. Moreover, WAAM features high heat accumulation, so there is also a need to develop variants that prevent excessive heat accumulation while maintaining the high deposition rates associated with this process. Each topic of this work covered significant scientific and technological challenges. For each objective a piece of equipment to deposit the samples with each process variant had to be created from scratch, involving knowledge of prototype creation and manufacturing processes. Then, to further characterize and discuss the results of each section, where different materials were used, it was required theoretical concepts and knowledge of material science fundamentals.

Different heat treatments were tested on stainless steel 316L and Inconel 625 parts to dissolve undesirable phases, promote microstructure homogenization, and reduce residual stresses.

To overcome the issues related to the highly textured microstructure, one of the objectives involved using ceramic particles to provide nucleation sites and refine the grain structure, improving the mechanical properties of HSLA steel and Inconel 625 samples. Two different functional prototypes and ways to introduce the particles to the molten pool were developed and tested.

Moreover, another objective was to fully demonstrate the potential of WAAM to fabricate Functionally Graded Material (FGM). A high strength low alloy (HSLA) steel was joined to a copper alloy and stainless steel 316L was deposited with Inconel 625. Different building strategies were explored to optimize the interface between the materials in terms of mechanical properties and control the phases formed.

Another objective was to test a new AM arc-based welding technique that pushes the electric arc away from the molten pool. It consists of an electric arc established between the tungsten electrode and the filler wire to overcome the heat accumulation issues that increase with the number of layers, which will further create high residual stresses, cause distortions, and eventually initiate cracks.

The research tasks completed in this dissertation are listed in Figure 1.1.

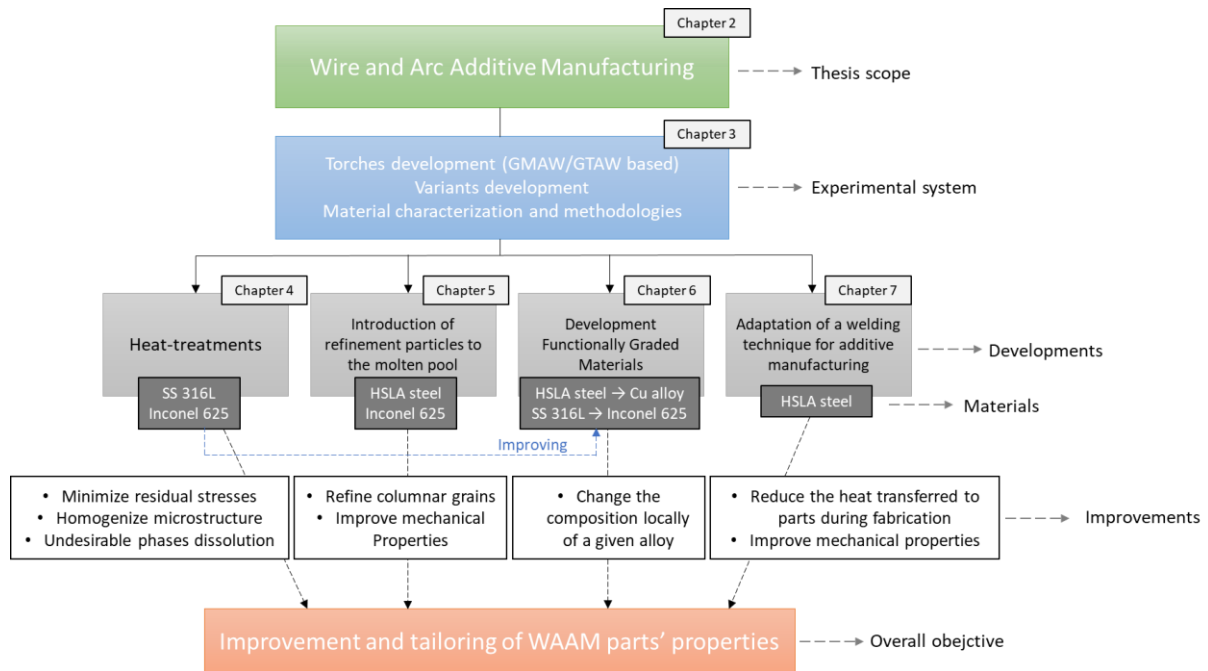


Figure 1.1 – Schematically representation of the outline and overall objective of this dissertation.

1.3 Major Findings

Different heat treatments were performed on stainless steel 316L and Inconel 625 WAAM parts to evaluate the influence of temperature and time on the phases' dissolution, mechanical properties, and grain size. It was found that the desired heat treatment temperature for both alloys is 1050 °C, as it can dissolve the precipitates in the as-built parts without significant losses in mechanical properties and extensive grain growth. This temperature was later used and enhanced the properties of the functionally graded material made with these two materials.

Additions of ceramic particles were made in-situ via two different developed devices and techniques. The first device was used to insert SiC particles mixed with an ethanol gel between the deposition of HSLA steel layers. The second device comprises a new feeding mechanism developed to introduce particles coaxially with the welding wire. This mechanism was used to add TiB₂ particles to the molten pool of Inconel 625. It was found that such particles, regardless of the method used to introduce them, could promote a more homogeneous microstructure with refined equiaxed grains. Characterization techniques, such as optical microscopy, scanning electron microscopy coupled with energy dispersive spectroscopy and electron backscatter diffraction, and synchrotron X-ray diffraction, were used. These have demonstrated the grain refinement effect of the particles but also confirmed a partial dissolution of the ceramic particles, which were responsible for forming phases that were not present in the as-built condition samples.

Functionally graded HSLA steel-Copper and Stainless steel 316L-Inconel 625 parts were produced using the twin-wire and arc additive manufacturing (T-WAAM) technique. The FGMs revealed a well-bonded interface free of defects in both material sets. The results confirmed that a direct material interface can result in strengths and elongations superior to one of the base materials. Even though layers had around 1 mm in height, with a direct interface, the process characteristics resulted in an interface region larger than 12 mm, which was the main reason for the HSLA steel-Copper FGM not to present any defects. The interface combined dendritic-type Fe (BCC) constituents and β (AlCu_3) precipitates in a Cu matrix. A smooth transition from stainless steel 316L to Inconel 625 resulted in the formation of secondary phases that were not present in the as-built materials nor in the FGM's built with a direct interface, such as the δ -phase (Ni_3Nb) and MC carbides. Digital image correlation performed during uniaxial tensile testing revealed that the fracture location in the direct and smooth transition FGM's occurred at the region containing 50 and 70 wt.% of stainless steel 316L, respectively. The specimens underwent a ductile fracture with considerable plastic deformation in all tensile tests. The gradient regions were characterized using different techniques, and the results showed a gradient of properties from one material to another.

1.4 Document Organization

This thesis is structured into eight chapters and is organized as follows.

Chapter §2 provides an overview of the WAAM's state of the art. It starts with localizing the WAAM within the Additive Manufacturing (AM) processes, highlighting its features and advantages (§2.2 and §2.3). Then a brief description of the nucleation and growth mechanisms that occur during the solidification of fusion-based processes is given in §2.4. Section §2.4.5 details the inoculants' role in grain refinement, highlighting critical theories and considerations. The typical defects found in different materials are summarized in §2.5, and the recent findings and breakthroughs recently reported for both in-process and post-process properties improvement are included in §2.6.

Chapter §3 describes the customized positioning system framework (§3.2), the customized GMAW-based torch (§3.3), and the development of two different prototypes used to introduce refinement particles in the molten pool that would be attached to the GMAW-based torch (§3.4). It also describes the GTAW-based torch with a multiple-wire feed system (§3.5). Materials and methodologies used to characterize the samples made in this study are presented in §3.6.

Chapter §4 starts with a brief introduction (§4.1) of the interest and challenges of the materials that will be investigated in this chapter (stainless steel 316L and Inconel 625). Then it is presented the results of different heat treatments performed on these materials (§4.2 and §4.3, respectively) fabricated with GMAW-based WAAM. Each heat treatment was performed in-situ with synchrotron X-ray diffraction to detect phase changes and potential dissolution.

A series of experiments using the prototypes presented in §3.4 are described in Chapter §5. It introduces the theories and findings behind grain refinement by adding micro/nanoparticles with higher melting points than liquid metal. SiC particles are added to an HSLA steel in section §5.2, then TiB₂ particles are used to refine the grains of Inconel 625 parts (§5.3).

Chapter §6 presents the production of FGMs using the multiple wire feed system developed. The motivation to build each pair of FGM is given in section §6.1, highlighting AM's challenges and ongoing developments to perform the materials transitions tested. Section §6.2 details the experimental design and results of the HSLA steel to Copper alloy FGM. Experimental information on the production of the stainless steel 316L-Inconel 625 and characterization results are discussed in §6.3.

Chapter §7 discusses the various welding processes already used in WAAM and the results obtained with the welding variant that will be further adapted for WAAM (§7.1). First, it is searched for the feasible window of parameters with this new process. Then, using the same process parameters, the results with this new variant are compared with a GMAW-based deposition. The droplet transfer mechanism is discussed, highlighting the differences in the thermal behavior between both processes (§7.3). Section §7.4 demonstrates a potential application for this new WAAM variant.

Chapter §8 resumes the main findings of each chapter and gives suggestions to continue the work developed in this thesis.

1.5 Publications in international indexed journals (ISI/Scopus)

The scientific output of this work published in international indexed journals is listed below:

- [1] Tiago A. Rodrigues, V.R. Duarte, D. Tomás, Julian A. Avila, J.D. Escobar, Emma Rossinyol, N. Schell, Telmo G. Santos, J.P. Oliveira, *In-situ strengthening of a high strength low alloy steel during Wire and Arc Additive Manufacturing (WAAM)*, Additive Manufacturing, Volume 34, 2020, 101200, ISSN 2214-8604, <https://doi.org/10.1016/j.addma.2020.101200>.
- [2] Tiago A. Rodrigues, Valdemar R. Duarte, R.M. Miranda, Telmo G. Santos, J.P. Oliveira, *Ultracold-Wire and arc additive manufacturing (UC-WAAM)*, Journal of Materials Processing Technology, Volume 296, 2021, 117196, ISSN 0924-0136, <https://doi.org/10.1016/j.jmatprotec.2021.117196>.
- [3] Tiago A. Rodrigues, J.D. Escobar, Jiajia Shen, Valdemar R. Duarte, G.G. Ribamar, Julian A. Avila, Emad Maawad, Norbert Schell, Telmo G. Santos, J.P. Oliveira, *Effect of heat treatments on 316 stainless steel parts fabricated by wire and arc additive manufacturing: Microstructure and synchrotron X-ray diffraction analysis*, Additive Manufacturing, Volume 48, Part B, 2021, 102428, ISSN 2214-8604, <https://doi.org/10.1016/j.addma.2021.102428>.

[4] Tiago A. Rodrigues, N. Bairrão, Francisco Werley Cipriano Farias, A. Shamsolhodaei, Jiajia Shen, N. Zhou, Emad Maawad, Norbert Schell, Telmo G. Santos, J.P. Oliveira, *Steel-copper functionally graded material produced by twin-wire and arc additive manufacturing (T-WAAM)*, Materials & Design, Volume 213, 2022, 110270, ISSN 0264-1275, <https://doi.org/10.1016/j.matdes.2021.110270>.

[5] Tiago A.Rodrigues, Francisco Werley Cipriano Farias, Kaiping Zhang, A. Shamsolhodaei, Jiajia Shen, N. Zhou, Norbert Schell, Jan Capek, E. Polatidis, Telmo G. Santos, J. P. Oliveira, *Wire and Arc Additive Manufacturing of Stainless Steel 316L/Inconel 625 Functionally Graded Material: Development and Characterization*, Journal of Materials Research and Technology, 2022, ISSN 2238-7854, <https://doi.org/10.1016/j.jmrt.2022.08.169>

Ongoing journal paper under revision process:

[6] Tiago A.Rodrigues, Francisco Werley Cipriano Farias, Julian A. Avila, Emad Maawad, Norbert Schell, Telmo G. Santos, J. P. Oliveira, *Effect of heat treatments on Inconel 625 fabricated by Wire and Arc Additive Manufacturing (WAAM): an in-situ synchrotron X-ray diffraction analysis*

Ongoing journal papers under preparation are presented below:

[7] Tiago A.Rodrigues, A. Malfeito, Francisco Werley Cipriano Farias, V. Duarte, João Lopes, Julian A. Avila, N. Schell, Telmo G. Santos, J. P. Oliveira, *Inconel 625-TiB₂ parts fabricated by Wire and Arc Additive Manufacturing (WAAM)*

The submission of this last work is still pending since the technological developments involved are being considered for a provisional patent application.

2.

LITERATURE REVIEW

2.1 Introduction

This chapter presents a literature review of the most significant features of WAAM. Since WAAM is based on arc welding techniques, particular attention is given to the fundamentals of arc welding. The state of the art of other process developments is presented, such as variants to control the microstructure, minimize residual stresses, and avoid defects in the as-built parts. The main research fields surrounding the topics of each chapter in this thesis are later extended at the beginning of each chapter. The knowledge acquired from the literature review was the source of inspiration for the work developed in this thesis.

2.2 Additive manufacturing

In recent decades, AM has been developed for the rapid prototyping (RP) industry. However, it is also becoming a widely accepted manufacturing option for a wide range of products, designs, and materials. According to the ISO/ASTM 52900:2021 standard, AM is defined as a “process of joining materials to make parts from 3D model data, usually layer upon layer, as opposed to subtractive manufacturing and formative manufacturing methodologies” [1]. Building 3D objects using data from a computer-aided design (CAD) model is the breakthrough of additive manufacturing technologies. It allows to build complex and customized parts in one stage, reducing many conventional processing steps. AM processes can produce components with customizable complex shapes that are difficult or impossible to fabricate by traditional means such as forging, machining, and die casting. The use of these conventional manufacturing processes is inadequate for the flexibility of modern designs due to the costs associated with producing a die or machining. The transition to making parts by AM also decreases the waste of material, tools, and the overall cost.

The ISO/ASTM 52900:2021 standard divides AM processes into seven classes. These are binder jetting (BJT), directed energy deposition (DED), material extrusion (MEX), material jetting (MJT), powder bed fusion (PBF), sheet lamination (SHL), and vat photopolymerization (VPP). DED refers to

processes in which focused thermal energy (using a laser, electron beam, or arc) is used to fuse materials as they are being deposited. WAAM is a promising manufacturing process that competes with other AM processes. Its advantages with respect to powder bed fusion, DED-laser powder, and DED-Laser wire are illustrated in Figure 2.1. WAAM outperforms other AM technologies in several aspects, such as part size, platform flexibility, post-treatment necessity, mechanical properties, material usage efficiency, and cost savings [2]. However several improvements still need to be made to increase the design's complexity and reduce the need for a surface finish. Some of these topics will be discussed in the next section.

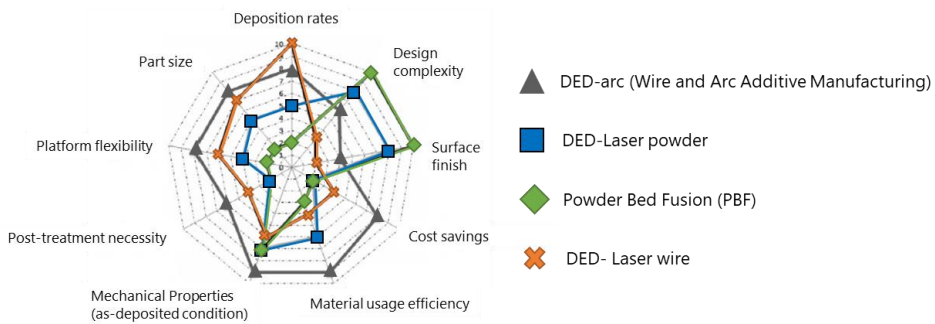


Figure 2.1 - Advantages of WAAM over other AM processes (adapted from [2]).

This thesis will focus on processes inserted in the category DED-arc, which combines an electric arc as the heat source and a wire as feedstock. DED-arc is commonly referred to as WAAM. Since this terminology is well established in the scientific community and is typically used, this thesis will refer to the process as WAAM for a better understanding.

2.3 Wire and arc additive manufacturing

WAAM is a variant within the metal AM group based on the fundamentals of arc welding, where a wire feedstock material is melted by an electric arc and deposited in a layer-by-layer fashion. The critical feature of WAAM is the high deposition rates, typically within the range of 1-10 kg/h [3], making this process more suitable for fabricating large parts. Another crucial characteristic relates to the low implementation costs, as the elements used for WAAM are the same consumables, power sources, and positioning equipment already used for several years in welding. Moreover, zero material waste is obtained if the final part is not subsequently machined, offering high-efficiency material usage and a significant reduction in costs compared to conventional machining from a solid block [4]. These factors make WAAM more interesting for building large components for industrial applications, such as oil and gas, nuclear sectors, and processing alloys where subtractive technologies, such as titanium and nickel alloys, are very costly.

Depending on the nature of the heat source, WAAM relies either on the welding principles of gas metal arc welding (GMAW) or gas tungsten arc welding (GTAW). GMAW is a fusion-based arc welding process where the arc is established between the tip of a consumable wire and the workpiece

under an inert or active shielding gas that protects the weld pool and adjacent material. With deposition rates up to 10 kg/h, GMAW-based is the process preferentially used in WAAM. However, GMAW-based WAAM is less stable and generates more weld fumes and spatter since the electric current flows through the feedstock. In GTAW, the electric arc is established between a non-consumable tungsten electrode and the workpiece or with previously deposited layers. The material in the form of wire is added laterally to the molten pool. GTAW was one of the first arc welding processes that became widespread. However, the deposition rates are significantly lower (1-2 kg/h) than GMAW-based WAAM, which is why most research uses the former process.

2.4 Solidification and grain formation

2.4.1 Nucleation

For solidification to begin, a liquid must be cooled below its equilibrium melting temperature to nucleate a solid phase within the liquid. However, depending on the pureness of the liquid, the level of undercooling, ΔT , can vary. For example, the difference between the liquid temperature and the melting temperature of a pure liquid nickel can be up to 250 °C before any transformation occurs. This type of undercooling is very rare, as typically, nucleation of a solid phase occurs at undercooling of only 1 °C. Nucleation can either occur homogeneously or heterogeneously. Homogeneous nucleation refers to when some of the atoms in the liquid cluster form a small sphere of solid. Heterogeneous nucleation occurs in the presence of solid particles in the liquid. They can be either external particles such as oxides, nitrides, or sulfides or an existing solid substrate that will facilitate nucleation by initiating crystal growth from them. In both nucleation types, the formation of a nucleus will depend on the competition between the driving force for the phase change and the energy required to form a new interface [5]. The free energy barrier for nucleation, ΔG_{Nuc} [J], on a heterogeneous substrate is given by equation (1), where γ_{nm} [J/m²] is the specific surface energy, or the surface tension between the nucleus and the melt, T_s [°C] is the solidification temperature, ΔT [°C] the undercooling, L [J/kg] is the latent heat, and ρ [kg/m³] the density. The parameter $f(\theta_{wa})$ can be calculated following equation (2) and is purely dependent on the wetting angle or contact angle θ_{wa} [rad] between the liquid and the heterogeneous nucleation substrate. In the case of homogeneous nucleation, equation (1) is still valid, but the wetting angle would be zero, and $f(\theta_{wa})$ would be equal to its maximum value of 1. Accordingly to equation (1), the thermodynamic barrier to nucleation decreases when the substrate presents a low wetting angle with the liquid melt. Also, nucleation probability will increase with higher levels of undercooling [6].

$$\Delta G_{Nuc} = \left(\frac{16\pi}{3} \right) \left(\frac{\gamma_{nm}^3 T_s^2}{L^2 \rho^2 \Delta T^2} \right) f(\theta_{wa}) \quad (1)$$

$$f(\theta_{wa}) = \frac{(2 + \cos \theta_{wa})(1 - \cos \theta_{wa})^2}{4} \leq 1 \quad (2)$$

In the case of welding and AM, heterogeneous and homogeneous nucleation can happen concurrently. However, heterogeneous nucleation will dominate the solidification process since the interfacial energy between the new solid phase and the old liquid phase is significantly lower due to the existence of a substrate.

2.4.2 Growth

During solidification, growth is the phenomenon that follows nucleation. After the material cools below the liquidus temperature on pre-existing solid grains, the grain grows by epitaxy from the substrate or previously deposited layers in the first stage. However, since the material being deposited in AM has the same chemical composition as the previous layer, grain growth occurs spontaneously with no activation energy barrier from the previous layer. The second stage of solidification is growth-controlled. The number of grains within a layer remains constant as solidification proceeds via lengthening the dendrites and dendrite arm thickening. In the case of cubic crystals, these grains grow rapidly and preferentially along the <001> crystallographic directions [6].

Once a nucleus is formed, it will continue to grow, as such growth is limited by the kinetics of atoms attached to the interface, capillarity, and diffusion of heat and mass. When the liquid solidifies, the solute atoms in the liquid will be redistributed, and such atoms' dispersal will depend on several factors, such as thermodynamics, kinetics, diffusion, and undercooling. However, during the solidification of an alloy, the solute will pile up ahead of the S/L interface due to the smaller solubility of the solid when the distribution coefficient is less than unity ($k<1$), resulting in a non-equilibrium solidification condition. After cooling, this can become a problem as solidification cracking can be promoted by excessive solute segregation. The solute distribution during solidification also influences the phase transformation regardless of the cooling rate. For example, in nickel superalloys, as the concentration of Nb and C rises in the remaining liquid, there is an increased tendency for eutectic reactions to occur near the final stages of solidification, resulting in the formation of undesirable precipitates such as NbC and Laves phase. Moreover, depleting the matrix from Nb will decrease the solid solution strengthened effect [7].

Given that WAAM uses the heat source equipment of traditional welding processes, the final structures will be similar to those found in welding. Solidification presents a major material processing challenge since parts fabricated by WAAM usually comprise large columnar grains formed by epitaxial growth from the substrate aligned along the buildup direction normal to the solid/liquid (S/L) interface. The grain growth progresses without interruption due to minimal grain nucleation events during solidification, resulting in the infiltration of columnar grains through numerous layers [8]. Although these structures can be beneficial for applications requiring high temperature creep resistance [9], homogeneous equiaxed grains are more desirable, as they provide higher strength, toughness, and corrosion resistance, and enhance fatigue life [10].

2.4.3 Role of solute on grain refinement

During non-equilibrium solidification, solute segregation is unavoidable in metallic alloys. The amount of each element in the solute will directly influence the solute segregation at the front of the S/L interface, which further restricts the growth of grains and the development of a constitutional supercooling (CS) region. CS provides the driving force to activate further nucleation events in the constitutional supercooled region, and those newly formed grains can also restrict the growth of the previously developed grains. The parameter that has been used to quantify the effect of solute on the grain size is the growth restriction factor, Q , which is equal to the sum of the contribution of each element in the solute. The value of Q is calculated according to equation (3), where m_l [$^{\circ}\text{C}/\text{wt.\%}$] is the slope of the liquidus line in a phase diagram, k is the equilibrium solute partition coefficient, and C_0 [wt.%] is the solute composition.

$$Q = \sum m_l C_0 (k - 1) \quad (3)$$

2.4.4 Solidification Map

Besides its composition, the key parameters that determine the final grain morphology of a given alloy are the temperature gradient, G [$^{\circ}\text{C}/\text{cm}$], growth rate, R [cm/s], and the degree of undercooling. The ratio between G/R determines the morphology of the solidification structure, while the product $G \times R$ controls the size of the solidification microstructure. Figure 2.2 presents the relationship that G and R have on the size and morphology of the final structure. As it can be seen, depending on the temperature gradient and growth rate, the solidification mode of an alloy can either be planar, cellular, columnar dendritic, or equiaxed dendritic. The columnar-to-equiaxed transition (CET) is also governed by the control of the G and R parameters, and control of these parameters is one approach to avoid the formation of columnar grains. The CET occurs when nucleation of sufficiently numerous equiaxed dendrites takes place in the constitutionally undercooled liquid in front of the S/L interface.

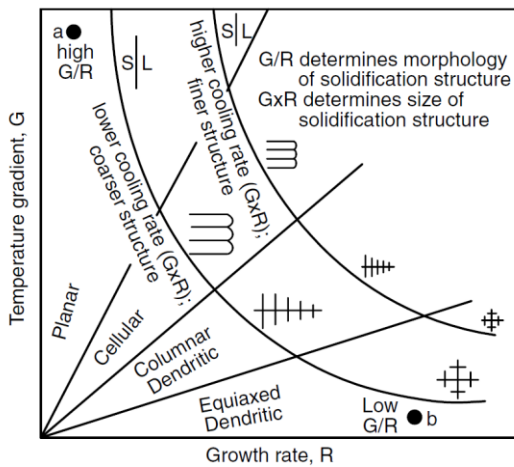


Figure 2.2 - Effect of the temperature gradient, G, and growth rate, R, on the morphology and size of solidification structures [11].

The thickness of the S/L interface in a steady state is given by D_L/R , with R being the growth rate and D_L being the chemical diffusivity coefficient of solute in liquid (m^2/s). Moreover, the slope of the line tangent to the temperature profile at the S/L interface (G) is equal to $\Delta T / (D_L/R)$. Therefore, to ensure a planar growth of the S/L interface, the criterion expressed in equation (4) must be met. According to this equation and the representation in Figure 2.3, as the degree of CS increases, the solidification mode will change from planar to cellular, to columnar dendritic, and finally to equiaxed dendritic. The shaded area under the liquidus temperature distribution indicates the region of constitutional supercooling where the actual liquid temperature is below the liquidus temperature. The part where dendrites and the liquid phase coexist is called the mushy zone and is referred to as M in Figure 2.3. Typically, undercooling is the sum of different contributions associated with solute diffusion, thermal diffusion, attachment kinetics, and solid-liquid interface curvature, respectively. However, solute diffusion predominates for most metallic alloys. It is now understood that CET is favored when the growth rate and constitutional supercooling increase and when the temperature gradient decrease.

$$\frac{G}{R} \geq \frac{\Delta T}{D_L} \quad (4)$$

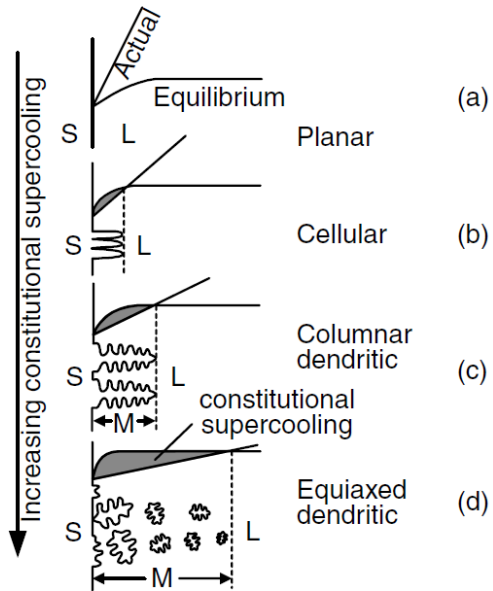


Figure 2.3 - Effect of constitutional supercooling on the solidification mode: (a) planar; (b) cellular; (c) columnar dendritic; (d) equiaxed dendritic (S: solid, L: liquid, M: mushy zone) [11].

The lack of nucleation events ahead of the solid/liquid (S/L) interface to generate new refined equiaxed grains is an issue in materials that do not undergo solid-state phase transformations, such as austenitic stainless steel and nickel alloys. Since post-WAAM heat treatments cannot be used to refine the grains in these materials, the use of process add-ons that can control the temperatures in-situ and the use of refinement particles is essential. During parts fabrication, the deposited material undergoes various heating and cooling cycles and experiences a decrease in the cooling rates with an increase in parts' height as the heat accumulates from the previous layers. Eventually, these process characteristics will result in inhomogeneous properties and structures at different levels of parts' height [12,13].

2.4.5 Role of inoculants on grain refinement

McCartney [14] defined grain refinement as the deliberate suppression of growth of columnar or twinned columnar grains in ingots and castings and the formation of an equiaxed solidification structure. In principle, the mechanisms of grain refinement are straightforward: numerous potent particles provide nucleating sites to provide nucleation sites and solutes with high growth restriction factors. Moreover, the growth of the nucleated grains must not be too fast. Otherwise, those which form first will quickly grow and consume nucleation sites that could have been available for other grains to nucleate.

The Interdependence Theory was developed by StJohn et al. [15], which shows the interdependence between grain growth and nucleant selection. The theory can predict the final grain size by determining three terms. The first, X_{cs} [μm], is the distance at which a previously nucleated grain must

grow to establish sufficient CS ahead of the S/L interface to trigger nucleation on the nearest most potent particle. The second term, X'_{dl} [μm], is the diffusion distance from the S/L interface to the point where sufficient CS has been generated for nucleation. The third term, X_{sd} [μm], relates to the distance from the end of the diffusion field to the next most potent particle where a new nucleation event can occur. The grain size determination can be determined using equation (5), and Figure 2.4 illustrates the distances mentioned above.

$$d_{gs} = X_{cs} + X'_{dl} + X_{sd} \quad (5)$$

The sum of the first (X_{cs}) and second (X'_{dl}) terms of equation (5) represent a nucleation-free zone (X_{nfz} [μm]) where nucleation is completely suppressed as the amount of CS (ΔT [$^{\circ}\text{C}$]) is insufficient for triggering new nucleation events on potent particles. X_{cs} can be replaced with $\frac{D \cdot \Delta T_n}{R \cdot Q}$, and X'_{dl} with $\frac{4.6D}{R} \left(\frac{C_l^* - C_0}{C_l^*(1-k)} \right)$, where D [m^2/s] is the diffusion rate in the liquid, ΔT_n [$^{\circ}\text{C}$] is the critical undercooling necessary for a nucleation event to occur on the most potent nucleant particles, R [m/s], is the growth rate, Q the growth restriction factor, C_l^* , the composition of the liquid at the S/L interface, and C_0 , the alloy composition.

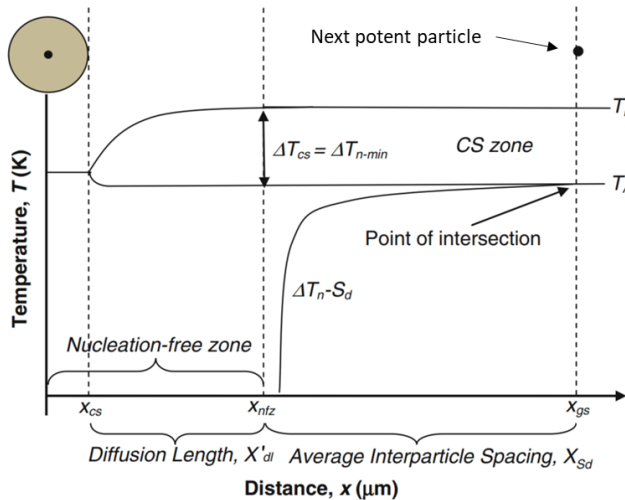


Figure 2.4 - Representation of the three regions (X_{cs} , X'_{dl} , X_{sd}) that will determine the grain size. $X_{cs} + X'_{dl}$ is equal X_{nfz} , that is a nucleation-free zone, where nucleation is not possible. The next nucleation event occurs when the ΔT_n - S_d curve intersects the bottom of the CS zone (adapted from [15]); T_A : Actual temperature of the melt ($^{\circ}\text{C}$), T_E : Equilibrium liquidus temperature ($^{\circ}\text{C}$).

Equation (5) can also be simplified to equation (6) by performing some simplifications as described in StJohn et al. work [16]. From equations (5) and (6), the first terms of equation (6) are then equal to the nucleation free zone, X_{nfz} , and are given by $\frac{5.6D\Delta T_n}{RQ}$. Equation (6) highlights that no new nucleation will occur as the amount of CS is not at its maximum value within this zone. Therefore, in order to reduce

the size of the nucleation-free zone, the grain size D and ΔT_n need to decrease, and Q and R values must increase. However, reducing the value of ΔT_n (i.e., increasing the particle potency) means using larger particles, which could harm the mechanical properties of the fabricated parts. Therefore, modifying R by changing the welding parameters and Q by changing the alloy chemistry would be more effective.

$$d_{gs} = \frac{5.6D\Delta T_n}{RQ} + X_{sd} \quad (6)$$

Each nucleation event sets off another growth sequence, creating another nucleation-free zone until nucleation on the next available particle is triggered when sufficient CS is re-established. The creation of a nucleation-free zone and the fact that nucleation of particles occurs when the CS region first intersects the particle distribution $\Delta T_n - S_d$ curve implies that only a very small proportion of particles become active nucleants. $\Delta T_n - S_d$ refers to the relationship between the average particle spacing, S_d , and nucleation undercooling, ΔT_n . The inverse relationship between ΔT_n and S_d means that it is more likely to find an effective nucleant particle farther from the previously nucleated grain than closer [15]. Thus, according to this theory, forming a nucleation-free zone is the main reason for low particle usage efficiency as 1-2 % of added particles act as heterogeneous nucleation sites [17]. Therefore, promoting nucleation and grain refinement is of utmost importance, minimizing the nucleation-free zone by controlling alloy chemistry and growth rate.

2.5 Common defects in WAAM

Research and developments have allowed WAAM to be successfully used, mainly because there is considerable knowledge accumulated from welding processes and metallurgy. Due to the similarities to arc-based welding, the same type of defects will occur in WAAM, such as cracking, porosity, and delamination [18]. With that said, some issues still need to be addressed for critical applications before achieving mass industrialization. WAAM can only be industry-established when the challenges related to high heat input levels are well handled and controlled, as they will lead to high-level residual stresses and distortions. Considering that WAAM features a diverse amount of process parameters, namely wire material, wire diameter, substrate material, preheating substrate, welding equipment, shielding gas, voltage, current, contact tip to work distance (CTWD), wire-feed speed (WFS), travel speed (TS), path programming strategy, interpass temperature and so on, defects can occur for multiple reasons.

Avoiding significant residual stresses is one of the top priorities that must be addressed. These occur due to repetitive heating and cooling, which induce cyclical expansion and contraction of the material. Residual stresses are stationary stresses at equilibrium in a material portion after all external forces are removed. Therefore, after unclamping the substrate, these stresses, which can be as high as the yield strength of the material [19,20], will cause the part to bend to balance the internal stresses. If

these residual stresses exceed the local yield stress of the material, plastic deformation occurs, but if it exceeds the ultimate tensile strength, a fracture is expected. Residual stresses will negatively affect the mechanical properties and lead to distortions, compromising the design and functionality of the final build.

Porosity is a common defect, and especially prevalent when processing Aluminium alloys, but it can also occur in other materials. Pores will negatively affect the final mechanical properties, particularly fatigue strength, and elongation. These types of defects are generally classified as either raw material or process-induced. As seen in the literature, the wire quality, in terms of microcracks, surface contamination, such as moisture, grease, and the presence of hydrocarbon compounds, is one of the causes of pores formation [21,22]. Also, the shielding gas flow rate should be adequate to protect the molten pool from atmospheric gas and avoid turbulence flow, as the shielding gas could mix with the surrounding air, resulting in poor shielding conditions and promoting contamination of the molten pool. Therefore, researchers have developed a device that ensures a laminar shielding gas flow. Overall, this device decreased atmospheric contamination by three orders of magnitude [23]. Moreover, poor path planning and inadequate selection of process parameters can also originate pores.

Solidification cracking is frequently observed in fusion welding and occurs during the terminal stages when the solidifying weld metal tends to contract due to solidification shrinkage and thermal contraction. The metallurgical factors that affect the solidification cracking susceptibility include the solidification temperature range, the amount and distribution of liquid at the terminal stage of solidification, the primary solidification phase, the surface tension of the grain boundary liquid, and the grain structure promoted by excessive solute segregation [7].

DuPont [20] confirmed that an alloy with a wider solidification temperature range will have increased solidification cracking susceptibility. The increase in the solidification temperature range can be attributed to increased P and S impurities, which tend to migrate to grain boundaries forming low-melting compounds, leading to solidification cracking in low-alloy carbon steel, nickel-base alloys, and ferritic stainless steel. In nickel-based superalloys, it was confirmed that eutectic reactions can promote the extension of the solidification temperature range at the final stage of solidification [24].

The cracking susceptibility in austenitic stainless steel will be higher if the primary solidification phase is austenite rather than δ -ferrite. Therefore the ratio of the Cr/Ni equivalent should be carefully controlled so that the primary phase to solidify is δ -ferrite. Moreover, the boundary area between δ -ferrite and austenite will be a sink for S and P, reducing solidification cracking susceptibility. Regarding carbon steels, an increase in the carbon content will form austenite first expanding the solidification temperature range and will promote martensite formation, increasing the potential for solidification cracking [7].

2.6 Defects mitigation

As seen, some issues still need further research. Therefore, some groups have developed new ways and adopted standard welding practices to mitigate some of the problems mentioned above.

At Cranfield University, high-pressure interlayer rolling has been developed. It consists of imposing a load of up to 100 kN onto a roller traveling over the already deposited layers. High-pressure rolling is a versatile technique for reducing residual stresses, distortions, and porosity and improving the mechanical properties. This technique is applied between consecutive layers, deforming the underlying material and recrystallizing the grains. Martina et al. [25] showed that high-pressure interlayer rolling of Ti-6Al-4V induces prior β grain refinement, promotes thickness reduction of the α -phase lamellae, and an overall modification of the microstructure from columnar to equiaxed. Xu et al. [26] applied the interlayer rolling process to Inconel 718 deposited with plasma. They confirmed that after rolling and standard heat treatment, the strength and elongation of the parts exceeded the wrought standards of Inconel 718. However, the grains were not uniform throughout the height of the samples, as the microstructure consisted of alternating bands of finely equiaxed grains and small columnar grains, as shown in Figure 2.5.

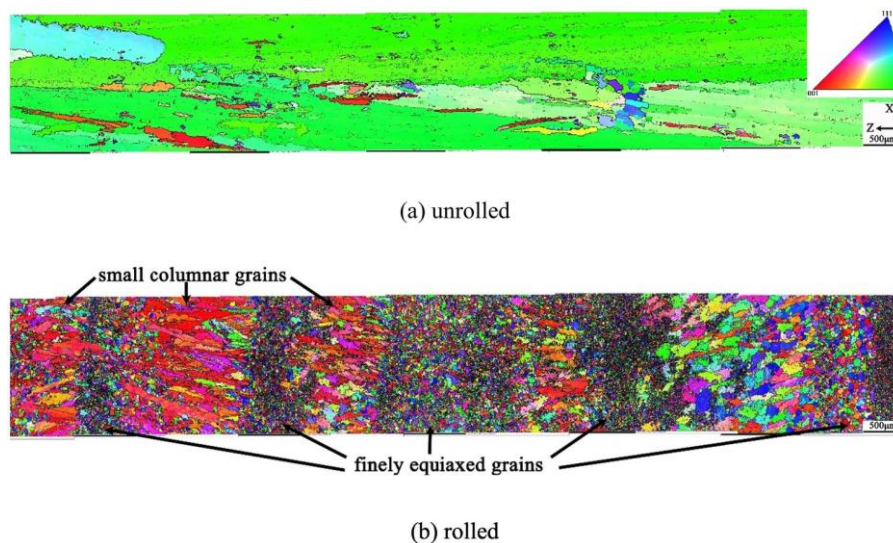


Figure 2.5 - Electron Backscatter Diffraction (EBSD) orientation maps of the Inconel 718 after: a) WAAM (unrolled), b) WAAM + interlayer rolling (rolled).

More recently, Duarte et al. [27,28] developed another variant, Hot Forging-WAAM (HF-WAAM), which consisted of locally forging the deposited layer through a pneumatic hammer. The deformation can be made through a hammer placed inside the gas nozzle or via a modified gas nozzle adapted to deform the hot material, as schematically represented in Figure 2.6. The deformation occurs at high temperatures, allowing the use of low forces compared to interlayer rolling (up to 55 N). This variant has different process parameters that will influence the final result, including forging force, F_F [N],

forging frequency, F_f [Hz], distance to arc center, DAC [mm], and hammer geometry, as the radius of the gas nozzle, defines the DAC. This variant promoted grain refinement and was seen to reduce material anisotropy and porosities in stainless steel 316L and in a Copper-based alloy. This technique can be applied as the material is deposited without compromising lead times, as occurs with interlayer rolling.

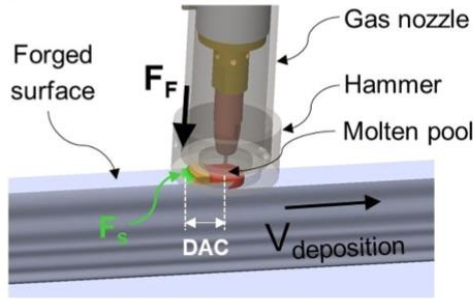


Figure 2.6 - Schematic representation of the Hot Forging-WAAM (HF-WAAM) variant, DAC: distance to arc center, F_f : Forging Force [28].

Significant improvements in material properties and reduction of the residual stresses can also be achieved with machine hammer peening and laser shock peening [18,29]. Hönnige et al. [30] used machine hammer peening and showed its effectiveness on Ti-6Al-4V parts by refining the β -grain size from several cm to less than 0.5 mm. Although the deformation depth was only 0.5 mm, the next layer depth had a penetration of 0.7 mm, suggesting that refined grains would be eliminated with every new layer. However, this was not the case as the new recrystallized β -grain orientations were able to grow significantly further below the peened surface (up to 2.4 mm). This result was possible due to the relatively low plastic strain required to promote deformation on the β -grains. Laser shock peening was performed laterally on Aluminium 2319 parts, and it was found that the modified layers that underwent plastic deformation had a significant grain refinement effect (decrease of average grain size by 22 %) and increased dislocation density. Modified parts had increased hardness and yield strength. However, this method only had noticeable effects within the first millimeter of the wall, as the induced plastic deformation was not enough to refine the complete cross-section [29].

Besides being reduced with in-situ deformation variants, residual stresses can also be decreased by controlling the thermal cycle during fabrication. Other strategies can be applied to minimize heat accumulation during WAAM, including controlling the time between each layer or the interpass temperature [31–33]. This parameter is one of the most important as it determines the conditions of heat dissipation by conduction through the part, directly affecting the cooling rate and, consequently, the microstructure and mechanical properties. Moreover, the interpass temperature is directly related to the wettability of the subsequent layers and will influence the part's waviness and wall appearance. However, the heat accumulation will increase as the number of layers increases. This type of strategy on its own becomes inadequate, as longer times will be necessary to wait for a specific interpass

temperature to be reached. Therefore the use of process add-ons is essential to perform interlayer cooling or heating as needed. These methods include using compressed CO₂ gas to impose a forced cooling between layers, which benefits include: better surface finishing with less oxidation, refined microstructure, improved mechanical properties, and enhanced manufacturing efficiency of Ti-6Al-4V parts [34]. Another strategy is placing heat sinks alongside the WAAM walls to help dissipate the heat [35] and coils mounted on the sidewalls that transfer heat to the part to perform pre-heating and post-heat treatment [36]. Heat sinks decreased the surface waviness by about 60%, and the total fabrication time can decrease by nearly 60% since a continuous heat dissipation condition is achieved without needing to adjust process parameters. The coils mounted on the sidewalls reduced the residual stresses and distortion of as-built parts and could overcome the interpass temperature issue, opening the possibility of maintaining a constant interpass temperature throughout the full deposition.

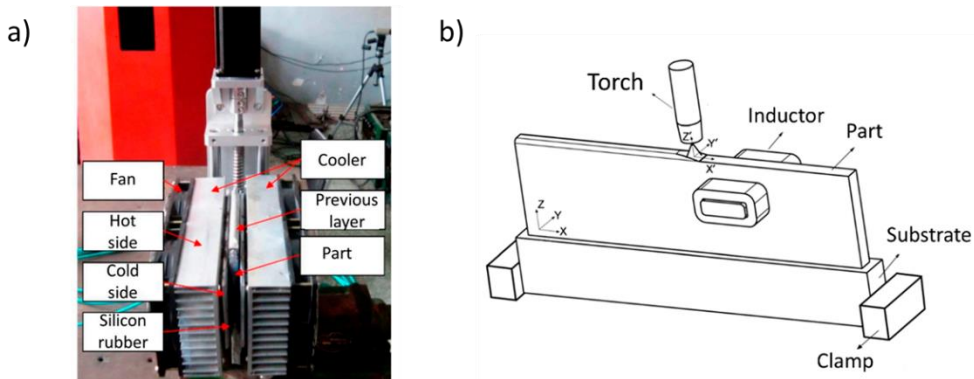


Figure 2.7 - a) Representation of thermoelectric cooling setup [35], b) Schematic representation of the inductor heating system [36].

Pre-heating the substrate is one of the most efficient methods to mitigate residual stresses and cracking since it reduces thermal gradients and homogenizes temperature distribution [37]. Alberti et al. [38] compared depositions performed with and without pre-heating at 300 °C and concluded that pre-heating could also increase each layer's wettability and enhance the regularity of wall thickness, decreasing surface waviness.

Other welding techniques that reduce the heat input involve using a process variant that will be discussed later, named hot-wire arc additive manufacturing (HWAAM). This variant uses another power source, which assists in melting the filler material and reduces the amount of arc heat input in a GTAW-like application. The secondary power source has the positive pole connected to the filler wire while the negative one is connected to the substrate. Besides a visible change in the wall geometry, due to different heat inputs, the size of Ti-6Al-4V columnar β-grains decreased in the sample built with HWAAM, resulting in a mixture of short columnar grains and equiaxed ones. This mixture promoted elongations of 12.6 and 12.8% in the longitudinal and transversal directions, respectively, in opposition to the 23.0 and 9.2% obtained with conventional WAAM, thus, confirming the appropriateness of this method to produce near-isotropic parts [39].

The deposition strategy is also critical in fusion-based additive manufacturing processes to avoid pores and lack of fusion and control the temperatures in the as-built part. The influence of three different deposition building strategies (oscillation, parallel, and weaving) was studied on maraging steels' surface waviness and porosity [40]. Due to the massive local heat accumulation, the oscillation strategy resulted in small shrinkage holes. Both parallel and weaving strategies avoided pores and reduced heat accumulation. However, weaving was a better strategy to improve the bead shape and surface finish and reduce the contact angle, favoring defect-free overlapping of adjacent beads.

Moreover, a variant of GMAW, known as cold metal transfer (CMT), can be used to reduce the process heat input. CMT is an advanced material transfer process incorporating a control system that detects when the electrode wire tip contacts the molten pool. By activating a servomotor, the wire is retracted to control the droplet transfer. CMT in a pulse advanced transfer mode was found to eliminate pores in WAAM of aluminum alloys that were present with conventional CMT [41]. Figure 2.8 a) and b) depict the macrostructure of aluminum processed with conventional cold metal transfer and with CMT in a pulse advanced mode (CMT-PADV), respectively, where the non-existence of pores with CMT-PADV is visible.

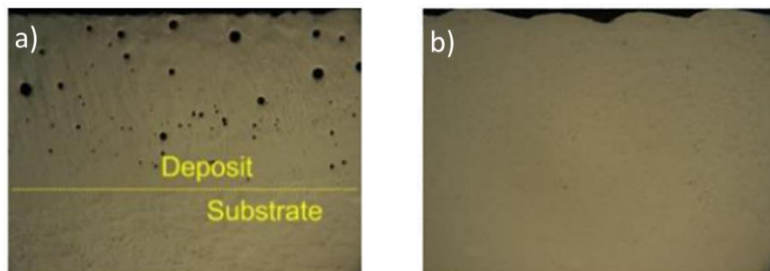


Figure 2.8 - Porosity presence in samples manufacture with: (a) conventional cold metal transfer (CMT); (b) cold metal transfer-pulse advanced (CMT-PADV) (adapted from [41]).

In addition, porosities can also be avoided by controlling the quality of the raw materials (gas and wire), cleaning the substrate before deposition, and performing interpass rolling or forging.

2.7 Summary

A review of the literature related to the research performed in this work has been conducted, focusing on the Wire and arc additive manufacturing process, the common issues encountered during the metal deposition process, and the variants and methods developed to mitigate some of the problems mentioned. The findings in the literature helped shape the focus of this research.

3. □

EXPERIMENTAL SETUP

3.1 Introduction

The thesis involved the development of each piece of equipment to perform each experiment made in this work. It began with the development of the 3-axis movement system as described in section 3.2, which will carry in its moving head the customized welding torches and prototypes presented in the following sections. A GMAW-based and GTAW-based WAAM torches are respectively presented in sections 3.3 and 3.5, respectively.

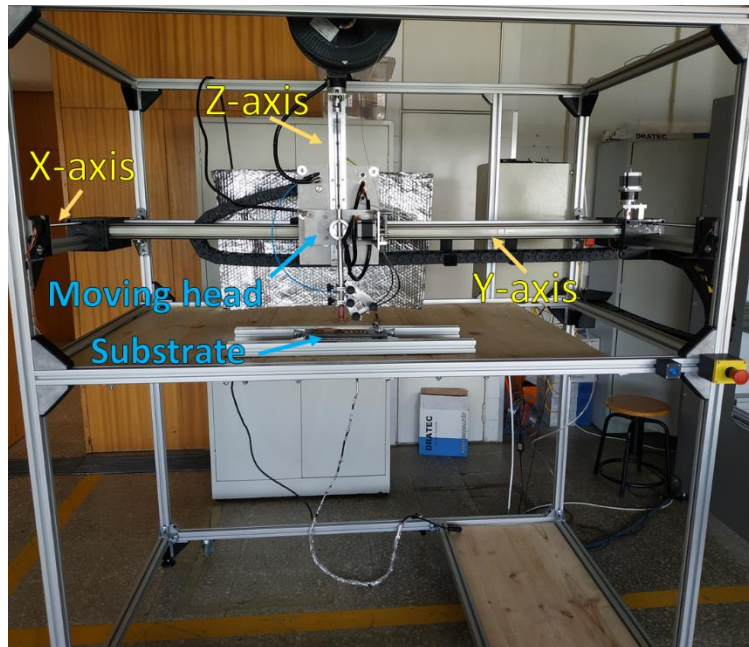
3.2 XYZ-motion system equipment

11 The first task of this work involved the design, production, and assembly of both mechanical and
12 electrical systems of the 3-axis movement system depicted in Figure 3.1. This medium-sized 3-axis
13 motion system would allow performing every experiment in this work, as different customized WAAM
14 torches could be coupled into the system. The equipment was designed to fulfill the following
15 requirements:

- Human-size scale equipment with easy access to the moving head to perform maintenance operations;
 - Capability for additional instrumentation to be coupled on the working platform;
 - Control of the shielding gas, welding machine power source, wire feed motors, and positioning system independently of each other;
 - Travel speeds up to 700 mm/min.

22 The design of the equipment was made using SolidWorks. The frame is made of 40 x 40 mm Bosch
23 Rexroth's profile, offering excellent stiffness and versatility for other machine components to assemble
24 to the mainframe quickly. M10 leadscrews ensured the motion XYZ motion system on the X-axis, and
25 a *drylin* ® ZLW-1040 Standart-02 provided the motion of the Y-axis. The Z-axis was guided by a linear
26 guide rail. The motion system comprised four 57STH56 NEMA-23 Bipolar stepper motors (2 for the X-

1 axis, 1 for the Y-axis, and 1 for the Z-axis), all controlled by *TB6600* stepper drivers, which can sub-
2 divide motor steps into further increments up to 32 times to achieve higher resolution.
3



4
5 Figure 3.1 - Photograph of the developed XYZ-motion equipment
6

7 The control board was an *Arduino Mega 2560* connected to the *Ramps 1.5* shield. *Arduino* was
8 flashed with an adaptation of the open-source firmware named *Marlin*, which drives most of the
9 world's 3D printers. The user-friendly *Repetier Host* software was used to operate the moving head in
10 the three orthogonal axes. The software also allowed to:

- 11 • Control the torch travel speed;
12 • Control the wire feed speed of each XYZ-axis motor independently and each motor that
13 will be later used in the multi-wire welding torch;
14 • Activate and deactivate the welding source and shielding gas via a relay connected to an
15 analogical port in *Ramps 1.5*;
16 • Communicate with the end-stoppers.

17 A welding machine from *KEMPY*, model *Pro MIG 3200* (power source), was used to deposit the
18 material in the GMAW-based WAAM detailed in sections 4, 5, and 7. The fabrication of functionality
19 graded materials (chapter 6) was made using a *Great Tool Spitfire TIG DC 1700 HF* welding machine.
20 This power source possesses a high-frequency start, enabling the arc to start without needing to
21 contact the tungsten with the substrate. A schematic diagram of the components used in the motion
22 system is presented in Figure 3.2.
23

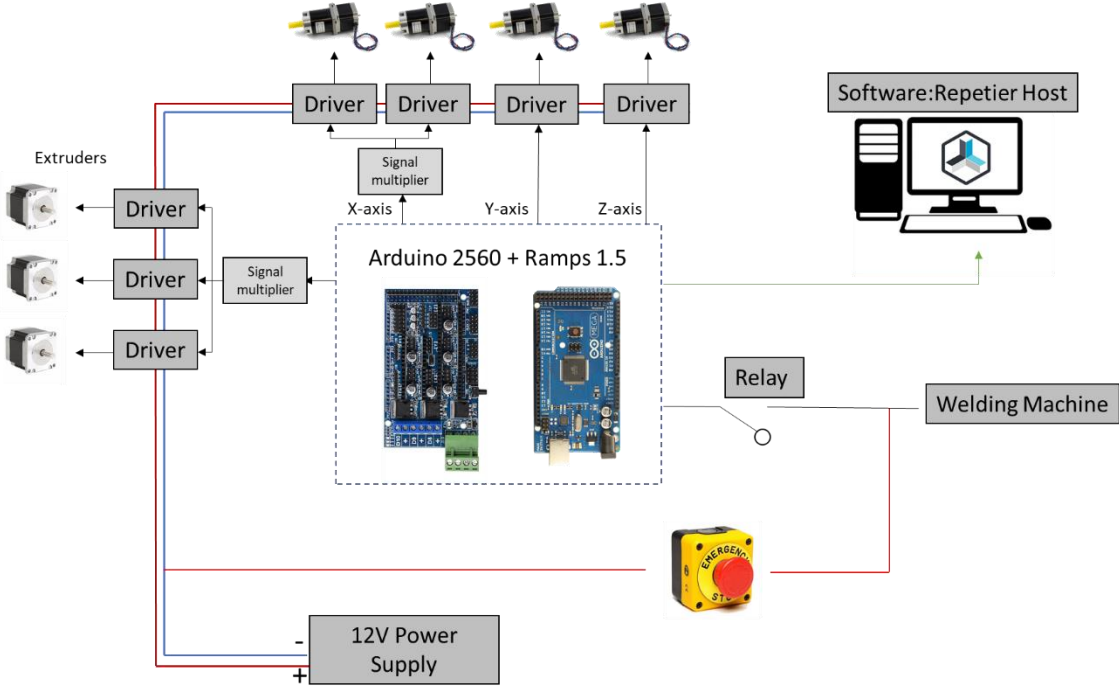


Figure 3.2 - Schematic representation of each electrical component and the circuit diagram of the developed XYZ-motion equipment.

Since commercially available welding torches are not versatile enough to work along with the new process variants presented in this work, two different welding torches: i) GMAW-based WAAM, and ii) GTAW-based WAAM, were designed and produced. Each torch could be coupled with different add-ons or be used in its standard configuration.

3.3 GMAW-based WAAM torch

The GMAW-based WAAM torch, presented in Figure 3.3, consisted of a wire-feed system in which the guided wire is fed coaxially with the shielding gas and introduced perpendicularly to the molten pool. The customized GMAW welding torch decouples every input, which can be independently controlled. These are the electrical power (intensity and voltage), the welding feed speed, and the shielding gas. Such permits the use of different combinations of process parameters and change the parameters even during processing. The customized welding torch comprises the wire feeder system, shielding gas inlet tube, a conductive element where the current passes through, and a torch nozzle. To avoid an electric arc being established between the torch nozzle and the part being fabricated, an insulating PTFE part electrically isolates the torch nozzle from the electric arc circuit.

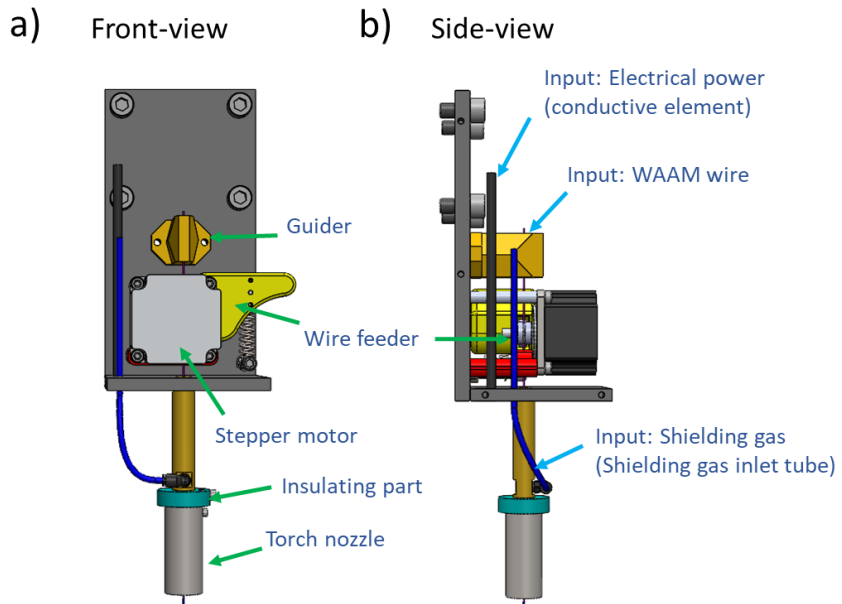


Figure 3.3 - 2D view of the GMAW-based WAAM torch: a) Front view; b) Side-view.

The following innovations comprise controlled system mechanisms for tailoring WAAM parts during fabrication by adding refinement particles.

3.4 Development of prototypes to introduce refinement particles

In welding, grain refinement of the fusion zone can be achieved by adding fine particles. Over the years, the most common technique has been coating the substrate or the grooves with particles before welding. In AM powder-based processes, adding reinforcement particles can be easily made by adding them to the feedstock powder [42]. However, such solution cannot regulate the weight of refinement particles per feedstock weight, and neither allows for a change in the concentration of particles during parts fabrication. Moreover, this solution cannot be used to mix particles with different volumes, as it would be difficult to homogenize the solution in terms of spatial distribution.

Wei et al. [43] presented a solution with a vibration-assisted system to mix and dispense mixtures of SiC and stainless powder feedstock through a needle that can be used in Selective Laser Melting (SLM) or a Laser metal deposition (LMD) application. This technique could change concentrations during parts fabrication. However, no integration of this system with a power source to melt the powder was developed to date.

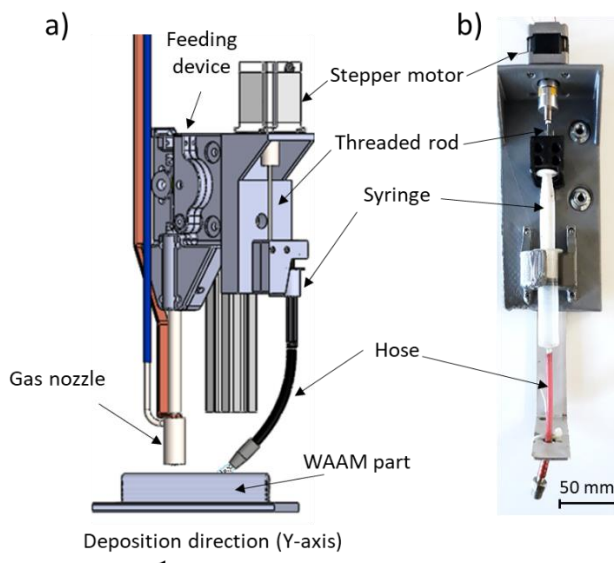
In WAAM, the techniques to insert refinement particles in the molten pool also comprise spraying the substrate or the last deposited layer with the particles dispersed in an alcohol gel solution [44,45]. In

1 all these cases, the welding process used was gas tungsten arc welding (GTAW), which can only be
2 automated when used on a 6-axis robot to build complex features, as the wire feedstock has to be fed
3 collinearly with the deposition direction. WAAM is increasingly being studied by different research
4 groups and is starting to be incorporated into the industry. Therefore, the solutions presented in this
5 chapter were applied to the GMAW process and can be of use and interest in the upcoming years.

6 **3.4.1 Prototype 1**

7 The first solution comprises an automatic device in which the refinement particles are previously
8 mixed with alcohol gel. A motor actuates on a syringe that contains the solution inside and extrudes it
9 in a controlled way onto the substrate and the previously deposited layers. The mechanism was
10 activated after the deposition of each layer, and only after the arc was extinguished. This customized
11 device was connected to the torch previously depicted in Figure 3.3, and the setup is illustrated in
12 Figure 3.4.

13



14

15 Figure 3.4 - Customized feeding device used to deposit refinement particles on top of previously deposited layers:
16 a) schematic representation; b) actual device.

17

18 The alcohol gel evaporates when in contact with the (still hot) already deposited layer, promoting
19 particle adhesion to the deposited material. Then, particles are incorporated into the molten pool as
20 the next layer is added. This solution was used to perform the experiments in section 5.2.

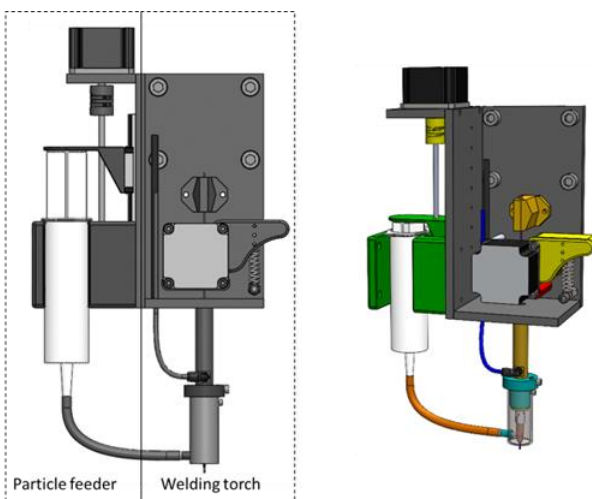
21 **3.4.2 Prototype 2**

22 The previous solution was limited to parts whose path planning was made only in one direction, and it
23 was necessary to wait for the previously deposited layer to cool down to a temperature of 200-300 °C
24 to extrude the particles in the alcohol solution, leading to delays in the production times. Therefore, a

1 new, improved solution was developed, introducing the particles coaxially with the wire, allowing the
2 deposition of complex geometric features to be printed with WAAM.

3 This second prototype was developed accordingly to the following requirements: i) modularity of the
4 welding torch and the system that feeds the particles, ii) introducing the particles coaxially with the
5 wire to allow complex geometric features to be printed with wire and arc additive manufacturing
6 without adding complexity to the path planning, iii) Control the weight percentage of particles in each
7 layer segment, independently of the wire feed speed. The customized particle feeder device
8 (prototype 2) was attached to the previously presented GMAW-based WAAM torch and is
9 schematically presented in Figure 3.5.

10



11

12 Figure 3.5 - 2D and 3D view of the particle feeder device attached to the GMAW-based WAAM torch.
13

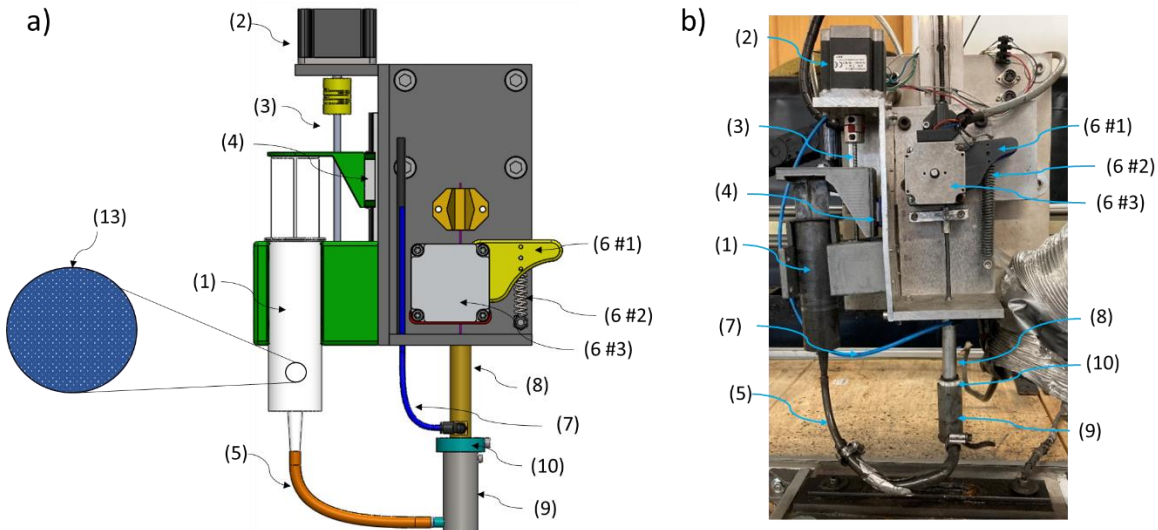
14 For this solution to work, the key element in the particle feeder module is a flux SW21 acquired from
15 NEVEX, which is mixed with the refinement particles and then added to the welding pool. The flux
16 creates an emulsion where the refinement particles are suspended but do not sediment due to their
17 high viscosity. The flux has a low boiling point and evaporates when in contact with a hot surface,
18 leaving the particles to adhere to the welding wire or flow together with the shielding gas.

19 The mixed solution is placed inside a dispenser, like a syringe or other similar (1). A stepper motor (2)
20 or another actuator provides the driving force transmitted to the dispenser containing the particles
21 suspended in this flux to control particle flow rate. A power transmission system (3) of a flexible shaft
22 coupling, lead screw, and a linear rail guide (4) allows fine control of the particles' amount. The
23 actuation mechanism can start and stop the flow of the solution and change the weight percentage of
24 particles locally in the part. After leaving the dispenser (1), the particles flow inside the connection
25 tubes (5), which are connected to the nozzle in the welding torch module, as illustrated in Figure 3.6.

26 The customized welding torch is composed of the wire feeder components (6#1: bearing support, 6#2:
27 spring, and 6#3: motor), a shielding gas inlet tube (7), and a conductive element where the current

1 passes through (8), and a torch nozzle (9). To avoid an electric arc being established between the
2 torch nozzle and the part being fabricated, an insulating part (10) electrically isolates the torch nozzle
3 from the electric arc circuit.

4



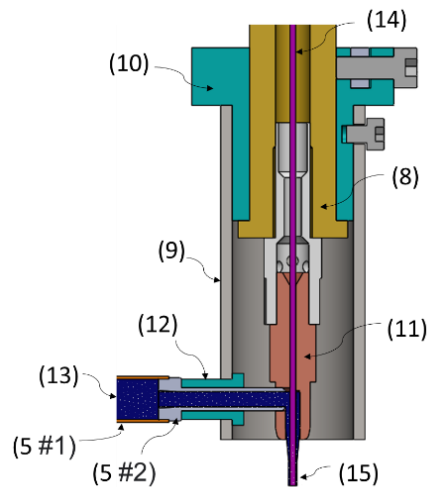
5

6 Figure 3.6 – Illustration of each component in the particle feeder device and the GMAW-based WAAM torch: a)
7 schematic representation; b) actual device; 1) Solution with particle dispenser (syringe), 2) Motor, 3) Power
8 transmission system, 4) Linear rail guide, 5) Connection tubes, 6#1) Bearing support, 6#2) Spring, 6#3) Motor, 7)
9 Shielding gas tube, 8) Conductive part, 9) Torch nozzle, 10) Insulating part and 13) Solution with particles.

10

11 The connection tubes (5) are connected to a modified conductive nozzle (11), as shown in Figure 3.7
12 and Figure 3.8. The connection tube (5) enters via a hole made in the torch nozzle (9) and is
13 electrically isolated with a non-conductive sleeve (12). As the solution (paste + particles (13)) reaches
14 the conductive nozzle (11), it is heated up, and the flux evaporates after reaching a specific
15 temperature leaving the particles to be fed into the molten pool. The inoculation procedure can occur
16 in two ways: by adhering to the welding wire (14,15) or by flowing with the shielding gas to the molten
17 pool. This solution was employed in the experiments made in Chapter 5.3.

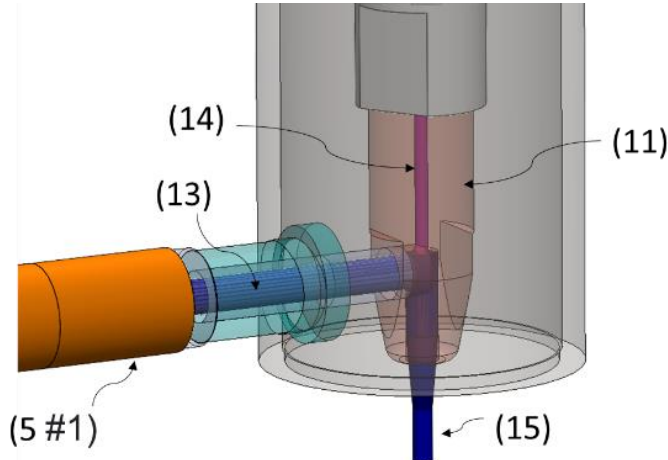
18



1

2 Figure 3.7 - Section view of the customized feeding device. 5#1) connection tube #1, 5#2) connection tube #2, 9)
 3 Torch nozzle, 10) Insulating part, 11) Conductive nozzle, 12) Insulating sleeve, 13) Solution with particles, 14)
 4 Welding wire, 15) Welding wire + particles.

5



6

7 Figure 3.8 - 3D view of the flux and refinement particles flow into the conductive nozzle. 5#1) connection tube #1,
 8 11) Conductive nozzle, 13) Solution with particles, 14) Welding wire, 15) Welding wire + particles.

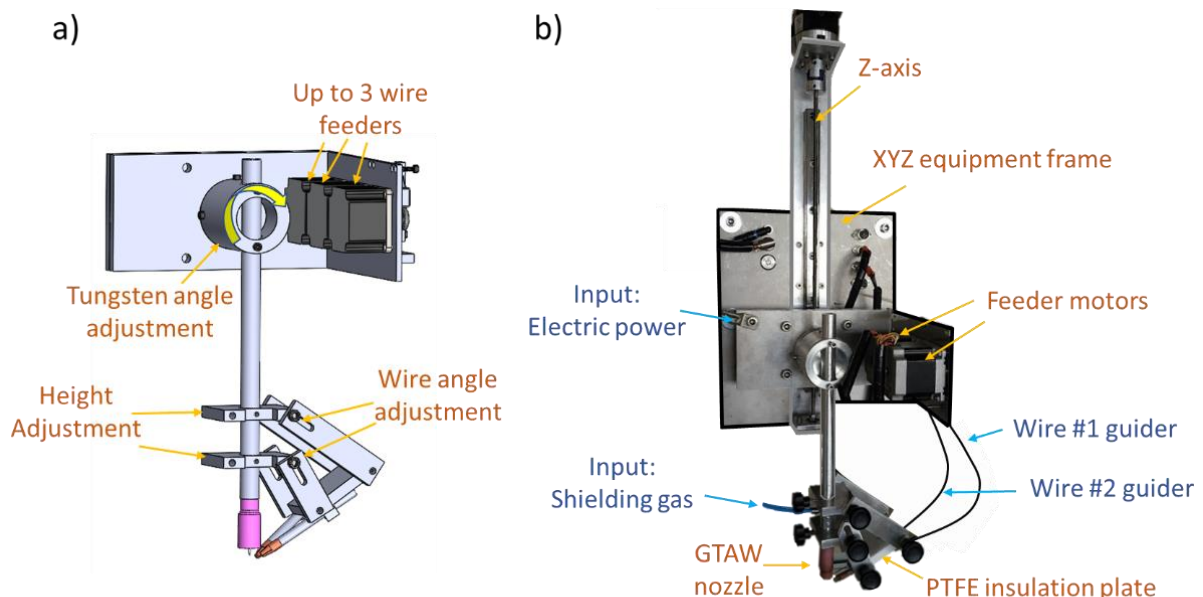
9

10 3.5 Multi-wire feed WAAM torch

11 A multi-wire feed GTAW-based WAAM torch was developed to be integrated into the XYZ motion
 12 equipment and be able to produce the FGMs. In this prototype, each input should be independently
 13 controlled, such as electrical power, shielding gas flow rate, torch angle, wire feed angle, and the wire
 14 feed speed of each motor. The system consisted of a triple-independent wire-feed system that guides
 15 each wire laterally to the tip of the tungsten electrode. Each wire guider is supported by a PTFE part
 16 which grants adjustments of the angle at which the wires are fed to the molten pool. Moreover, this
 17 PTFE insulation plate ensures that the wires do not have the same electrical potential as the tungsten

1 or the substrate, as the electrical arc should only be established between these former two. Three
2 bipolar stepper motors (SCA5618X2804-B) were used and were also connected to the 1.5 Ramps by
3 TB6600 stepper drivers. Both SolidWorks design and experimental integration in the XYZ-motion
4 equipment are presented in Figure 3.9. To control each motor independently from the other and the
5 amount of each wire in the molten pool, a script was added in the Repetier Host software using the G-
6 code commands: M163 and M164. The angle between the wire and the substrate was set to 30°. The
7 distance between the tip of the tungsten electrode and the substrate (or the previously deposited
8 layers) was set to 5 mm. The non-consumable electrode used was a Ceriated tungsten electrode
9 (AWS classification EWCe-2) with a diameter of 2.4 mm. The torch allows 4 degrees of freedom to
10 adjust the GTAW nozzle's position, to test and identify the best relative position between the molten
11 pool, tungsten electrode, and wire nozzles.

12



13

14 Figure 3.9 - Multiple-wire feed GTAW-based WAAM torch: a) Solidworks design; b) Experimental Setup and
15 integration in the XYZ-motion equipment.
16

17 3.6 Materials and Methods

18 3.6.1 Materials

19 Five different feedstock wires with 1 mm in diameter were used throughout this thesis. The respective
20 chemical composition and supplier are detailed in Table 3.1. In every experiment, the substrate used
21 was mild steel with an average hardness of 170 HV.
22

1

Table 3.1 - Chemical composition of the wire feedstocks used in this work (wt.%).

Alloy (AWS classification) [Wire supplier]	C	Mn	Si	Nb	Ti	Al	V	Ni	Cr	Mo	Cu	Fe
Stainless steel 316 (ER 316LSi) [Lincoln Eletirc in §4.2 and SuperOn in §6.3]	0.03	1.60	0.65	-	-	-	-	11	18.5	2.50	0.75	Bal.
Inconel 625 (ER NiCrMo-3) [Dratec]	0.1	0.5	0.5	3.5	0.4	0.4	-	Bal.	21.5	9	0.5	5
HSLA steel_1 (ER110S-G) [Dratec]	0.08	-	1.7	-	-	-	0.08	0.44	1.35	0.23	0.25	Bal.
HSLA steel (ER120S-G) [Lincoln Eletirc]	0.1	1.8	0.7	-	-	-	-	1.9	0.3	0.5	-	Bal.
Copper-aluminum (ERCuAl-A2) [Dratec]	-	0.5	-	-	-	8.5	-	0.5	-	-	-	0.8

2

- 3 **3.6.2 Microstructure Characterization**
- 4 **3.6.2.1 Optical and Scanning electron microscopy**
- 5 All samples were analyzed using different characterization techniques. Before microscopic
6 observations and hardness measurements, samples were polished using abrasive papers with grits
7 from P80 to P2000 and polished using a 3 µm diamond suspension. A Leica DMI 5000 M optical
8 microscope, a SU3800 Hitachi scanning electron microscope (SEM), a Zeiss FESEM 1530 SEM, and
9 an FEI Quanta FEG – Inspect-F5 SEM equipped with an electron backscatter diffraction (EBSD)
10 camera were used. EBSD measurements were performed using an acceleration voltage of 20 kV and
11 a step size of 150 nm. The chemical composition and composition of each etchant used to reveal the
12 microstructure of the different processed materials are presented in Table 3.2.
- 13 The geometric appearance of the as-deposited WAAM walls cross-sections detailed in chapter 7 was
14 evaluated via optical microscopy using *ImageJ* software, as described in the literature [46].
- 15

1

Table 3.2 - Etchant composition used to reveal the microstructure of each alloy.

Alloy (AWS classification)	Reagent	Composition		Immersion time
Stainless steel 316 (ER 316LSi)	Vilella's	Ethanol	100 ml	
		Hydrochloric acid	5 ml	60-120 s
		Picric Acid	1 g	
HSLA steel (ER110S-G and ER120S-G)	Nital	Ethanol	90 ml	2-5 s
		Nitric acid	10 ml	
Inconel 625 (ER NiCrMo-3)	-	Distilled water	100 mL	15-20 s
		Chromium trioxide	10 g	Electro etching (5V DC)
Copper-aluminum (ER-CuAl-A2)	-	Ethanol	71 ml	
		Hydrochloric acid	24 ml	1-5 s
		Iron(II) chloride	5 g	

2

3.6.3 Hardness measurements

3 Hardness measurements were performed using a Mitutoyo HM-112 Hardness Testing Machine, under
 4 a load of 1 kgf, for 10 s across the sample's total height. Some results were obtained by performing
 5 measurements starting on the substrate to the last deposited layers in steps of 250 µm. In other
 6 cases, when the average and standard deviation hardness values are plotted, those results were
 7 acquired by averaging a matrix of 5 x 5 mm with a step size of 250 µm.

8 3.6.4 Magnetic Permeability and Electrical conductivity 9 measurements

10 Magnetic permeability measurements were performed using an absolute helicoidally shielded eddy
 11 current (EC) probe with a 3 mm diameter from *Olympus*, operating in bridge mode. Calibration tests
 12 were made accordingly to previous work by Santos et al. [47]. The calibration involved using different
 13 magnetic permeability standards (ferrite samples) to distinguish between different materials with
 14 unknown magnetic permeabilities. The calibration was performed so that only the imaginary part of the
 15 electrical impedance of the probe conferred changes in the magnetic permeability of each sample. A
 16 four-point potential drop technique previously described in Sorger et al. [48] was used to measure the
 17 changes in electrical conductivity between samples. Measurements were made across the full height,
 18 starting in the substrate. The probe has a needle spacing of 635 µm, and a current of 80 mA was
 19 imposed between the external needles.

3.6.5 Synchrotron X-ray diffraction measurements

Synchrotron X-ray diffraction measurements were performed in-situ at the High Energy Materials Science beamline at PETRA III, DESY (Hamburg, Germany) with a beam energy of 87.1 keV (0.14235 Å) and also with a beam energy of 100 keV (0.1234 Å). The highest energy was used in the in-situ heat treatment experiments (chapter 4), as the lowest energy was used to capture the diffraction patterns of samples made in chapters 5 and 6. A total of 4 synchrotron X-ray diffraction campaigns were carried out during this thesis.

A 2D Perkin Elmer detector with a pixel size of 200 µm was used to capture the Debye-Scherrer diffraction rings. These were then integrated along the whole azimuthal angle (ϕ) using freely available Fit2D software [49] to obtain conventional (Intensity vs d-spacing or Intensity vs $2\theta_{hkl}$) diffraction patterns. The beam spot was set to 1 x 1 mm, and the sample-to-detector distance varied from 1220 to 1517 mm depending on the beamline. LaB₆ calibrant powder was used to estimate the instrumental peak broadening associated with the beamline, and the exposure time was set to 5 seconds. At each measurement, dark images were also acquired and subtracted to reduce the noise of the detector images.

The setup used during in-situ synchrotron X-ray diffraction measurements is depicted in Figure 3.10. The induction coils allowed the X-ray beam to pass through the sample without hitting any other material inside the equipment. Material expansion/shrinkage during heating and cooling was measured using a modified Bähr DIL-805 dilatometer in a chamber filled with Argon to avoid oxidation during each heat treatment.

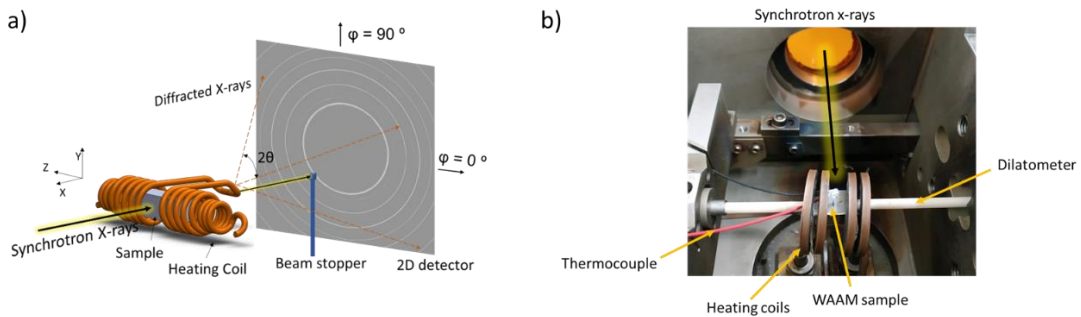


Figure 3.10 - a) Schematic representation of the experimental setup applied to perform the heat treatments in-situ during the transmission of synchrotron X-rays (not at scale); b) Experimental setup.

The remaining experiments were performed by making line scans with a distance between consecutive spots of 1 mm. The analysis started on the substrate and continued through each layer until the last deposited layer, as schematically illustrated in Figure 3.11.

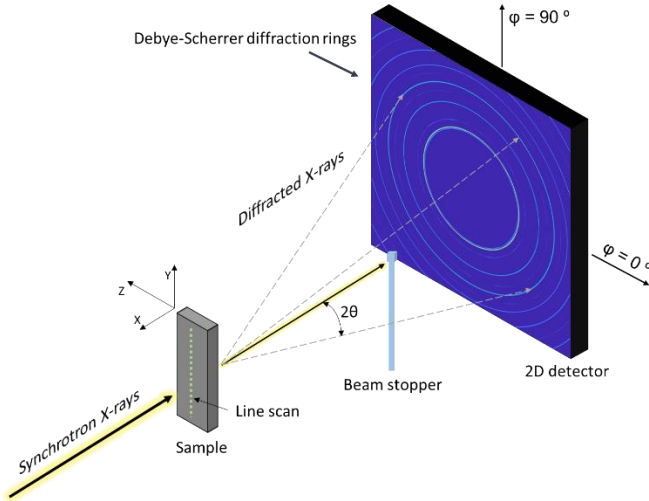


Figure 3.11 - Representation of the setup used for the synchrotron X-ray diffraction measurements.

An in-house python-based routine was used to fit the diffraction peaks. The python routine used a Python package named *xrdfit* [50], which implemented a *Pseudo-Voigt* profile function to fit peaks and extract the analyzed data in this study, i.e., the peak position, full width half maximum (FWHM), and area under the fitted peaks. This information was then used to quantify the current phases at any given point during the heat treatments, following the methodology detailed in Escobar et al.'s work [51]. The austenite and ferrite volume fractions were measured using equations (7) and (8). F_p is the fraction of austenite/ferrite, n_p is the number of peaks of austenite/ferrite considered, k represents each $\{hkl\}$ family/peak, I_{pk} is the intensity of each peak, and R_{pk} is a scalar containing the effect of the remaining parameters: theoretical cell volume (V_p), the multiplicity of the peak (M), and the structure factor (F_k) of the $\{hkl\}$ plane family. The R_{pk} was calculated for all presented phases of austenite and ferrite. The final volume fraction of austenite was calculated by the following equation (9). This method to quantify the volume fraction of each phase was compared with actual Rietveld refinements measurements using MAUD software [52]. The lattice strain for certain $(h k l)$ peaks was calculated accordingly equation (10), where d is the interplanar spacing and d_0 is the corresponding stress-free counterpart. Phase identification of the X-ray diffraction patterns was made using HighScore Plus.

$$F_p = \frac{\frac{1}{n_p} \sum_K^{n_{pk}} \frac{I_{pk}}{R_{pk}}}{\sum_p \frac{1}{n_p} \sum_K^{n_{pk}} \frac{I_{pk}}{R_{pk}}} \quad (7)$$

$$R_{pk} = \frac{F_k^2 \times M}{V_p^2} \quad (8)$$

$$F_{p_austenite} = \frac{F_{p_austenite}}{F_{p_austenite} + F_{p_ferrite}} \quad (9)$$

$$\text{Lattice strain } \varepsilon_{hkl} = \left(\frac{d - d_0}{d_0} \times 10^6 \right)_{hkl} \quad (10)$$

3.6.6 Residual stress measurements using neutron diffraction

Residual stresses were measured in FGM 100-100 and FGM 5 samples using neutron diffraction, as detailed in section 6.3. These measurements were made on the POLDI instrument at the Swiss Spallation Neutron Source, SINQ, at the Paul Scherrer Institute, Switzerland. A cubic gauge volume of $3.8 \times 3.8 \times 3.8 \text{ mm}^3$ was defined by a pair of diaphragms in the incident beam and a radial collimator on the diffracted beam. The data were fitted using a Gaussian function and the Pawley fit method implemented in Mantid [53]. Strains were measured in the samples' longitudinal, normal, and transverse directions. The d-spacings of each plane were calculated using Bragg's law equation (11). Where $\lambda [\text{m}]$ is the neutron wavelength, $d [\text{m}]$ is the lattice spacing or the distance between sets of parallel crystallographic planes characterized by the Miller indices hkl , and $\theta_{hkl} [\text{rad}]$ is the scattering angle.

$$d_{hkl} = \frac{\lambda}{2 \sin \theta_{hkl}} \quad (11)$$

Since every change in the lattice spacing of the material indicates changes in the material strains, equation (12) was used to measure the principal strains (ε), where i denotes each direction (x, y, z), and d and d_0 , correspond to the strained and unstrained conditions, respectively.

$$\varepsilon_{ii} = \frac{d_i - d_{0,i}}{d_{0,i}} \quad (12)$$

Finally, the principal stresses were calculated using the triaxial form of Hooke's Law equation (13), where $E [\text{Pa}]$ is the elastic modulus, and $v [-]$ is the Poisson's ratio.

$$\sigma_{ii} = \frac{E}{(1 + v)(1 - 2v)} [(1 - v)\varepsilon_{ii} + v(\varepsilon_{jj} + \varepsilon_{kk})] \quad (13)$$

3.6.7 Uniaxial Tensile and Compression tests

Uniaxial tensile tests were performed on an MTS servo-hydraulic press with a capacity of 100 kN and the compression tests were on an Autograph Shimadzu AG500Kng equipped with a Shimadzu load cell SFL-50kN AG. The displacement rate was always set at 1 mm/min, and Digital Image Correlation (DIC) was performed using Ncorr 2D digital image correlation MATLAB package [54] on the samples fabricated in chapter 6.3. It used a subset radius of 15 pixels and a subset spacing of 3 pixels. The yield strength, both in tensile and compression tests, was determined by getting the X-coordinate of

1 the point where the stress-strain curve deviates from a straight line, indicating that the material has
2 started to plastic deform.

3 **3.6.8 Thermodynamic Calculations**

4 ThermoCalc was used with the TCNI8 and TCFE11 databases to assess the phases that would form
5 during solidification. The Scheil-Gulliver model was used, which assumes equilibrium at the solid/liquid
6 interface, complete diffusion in the liquid, negligible diffusion in the solid, fast diffusion of carbon and
7 nitrogen (interstitial elements), and negligible dendrite tip undercooling [55].

8 **3.6.9 Current, Voltage, and Temperature measurements**

9 A LabVIEW program was designed to measure both current and voltage during depositions. An open-
10 loop LEM HTA 1000-S current transducer was used for the current measurements. The voltage was
11 measured directly by a DAQ National Instruments (NI) 6008 through a voltage divider, and the
12 measured points were the substrate and the conductive nozzle support.

13 Type-K thermocouples were mounted on the substrate to evaluate the temperature during parts
14 fabrication. A Fluke TI400 thermographic infrared camera placed 500 mm away from the WAAM
15 torches was also used to assess the temperatures during the depositions. An emissivity of 0.84 was
16 used to measure the steel temperatures between 500-800 °C. This emissivity was based on a
17 previous work result [12] where the value was calibrated with thermocouples reference values.

18 **3.7 Summary**

19 Chapter 3 discusses the customized XYZ-motion system, the torches developed, and the
20 characterization techniques used throughout the work. The first described torch was based on the
21 welding principles of GMAW and was used to perform the experiments made in chapters 4, 5, and 7.
22 In chapter 5, this torch was used with two different add-ons designed and developed to feed particles
23 to the molten pool of WAAM. Also, a multi-wire torch based on the principles of GTAW was created,
24 where the material is fed laterally to an electric arc established between tungsten and the workpiece.
25 This multi-wire torch was used in the experiments made in chapter 6 to build functionally graded
26 materials by simultaneously feeding two wires to the same electric arc. This torch was also employed
27 in the experiments made in chapter 7 to establish the electric arc between the tungsten and the
28 lateral-fed wire.

29

4.

HEAT TREATMENTS ON WIRE AND ARC ADDITIVE MANUFACTURING PARTS

4.1 Introduction

4.1.1 Stainless Steel

Austenitic stainless steels are widely used in several industrial applications where exceptional corrosion resistance and excellent mechanical properties at elevated temperatures are required, including nuclear energy [56,57], petrochemical, and chemical industries [58]. For example, parts from a reactor core in nuclear applications that required high strength and corrosion resistance at operating temperatures between 280-550 °C [59,60]. The mechanical strength of austenitic stainless steel is reduced considerably above 500 °C [61], and the fatigue crack propagation accelerates under operational temperatures above 150 °C [62]. Austenitic stainless steels are also an economical structural material used for marine and biomedical applications [63,64]. Stainless steels are relatively expensive to machine from a billet, making complex parts more feasible and cheaper to fabricate with additive manufacturing technologies. Regarding additively manufactured austenitic stainless steel samples, Lou et al. [65] highlight the necessity of producing an equiaxed microstructure through annealing, which increases the corrosion fatigue resistance.

Austenitic stainless steels manufactured by WAAM typically exhibit δ -ferrite dendrites within an austenitic (γ) matrix [27]. Some authors found that δ -ferrite can prevent hot cracking by accommodating large amounts of pure S and P in the interdendritic areas [66–69] while acting as a strengthener. The multiple heating/cooling cycles experienced, combined with the long soaking times at high temperatures, affect the microstructure evolution in WAAM fabricated parts and can result in the formation of undesired secondary phases [12]. When austenitic stainless steels experience low cooling rates and long exposure times between 550–900 °C, Cr-rich carbides ($M_{23}C_6$ and M_7C_3) [70] will form, as well as the potential for precipitating intermetallic deleterious phases increases, such as sigma (σ) [71], chi (χ) [72–74], and Laves phase [70]. Especially in WAAM, it has been reported that

1 the as-fabricated microstructures of austenitic stainless steels, as a result of microsegregation of Cr
2 during solidification, can contain σ depending on the process parameters and location within the
3 sample [75,76]. The σ -phase leads to hardening and embrittlement and therefore has received
4 particular attention [77,78]. In addition, σ consumes chromium and molybdenum from the austenite
5 matrix, deteriorating its corrosion resistance ability [79].

6 The solidification conditions and multiple heating/cooling cycles during fusion-based additive
7 manufacturing can render different microstructure features compared to conventionally used
8 processes such as casting. The commonly used heat treatments for welding and wrought material
9 may also need to be adapted when producing WAAM parts. Some authors [80] have suggested that at
10 950 °C, δ -ferrite could dissolve without the precipitation of secondary phases after post-weld heat
11 treatment. However, this work will show that the same heat treatment condition will render different
12 microstructure features when applied to the WAAM 316L stainless steel parts.

13 It has also been discussed that δ -ferrite can serve as nucleation sites for the precipitation of $M_{23}C_6$
14 and σ upon annealing cycles around 720 °C. However, proper annealing cycles around 1050 °C can
15 completely dissolve δ -ferrite, avoiding the formation of secondary precipitates [81]. The presence of
16 compositional segregation and δ -ferrite are mostly unavoidable. Therefore, understanding the
17 microstructural evolution of WAAMed stainless steels after heat treatment is a topic of great interest to
18 the additive manufacturing community. In-situ synchrotron X-ray diffraction measurements are
19 especially useful in this case to understand the kinetics of phase transformations.

20 Section 4.2 will investigate the phase transformations during heat treatments performed on stainless
21 steel 316L using synchrotron X-ray diffraction. The kinetics of δ -ferrite dissolution was studied during
22 post-WAAM heat treatment at 400, 950, 1050, and 1200 °C. These heat treatments were selected
23 based on the literature [75,82–84]. Complementary EBSD analysis was performed to confirm the
24 morphology, size, and distribution of δ -ferrite and σ before and after heat treatment. At the same time,
25 hardness and electrical conductivity measurements were used to demonstrate the differences that
26 each phase can have on the final properties of the processed materials. The observations made in this
27 work provide a new understanding of the effects of time and temperature on the microstructural
28 evolution of stainless steel after WAAM. It also provided a valuable guide to designing or optimizing
29 heat treatment routes relevant to additively manufactured parts.

30 **4.1.2 Inconel 625**

31 Nickel-based superalloys are the second most popular material studied by the additive manufacturing
32 (AM) community after titanium alloys, which is mainly due to their high fabrication cost using traditional
33 methods and outstanding performance at high temperatures. Inconel 625 is a solid solution
34 strengthened Ni-based alloy initially developed as a replacement for stainless steel 316 in steam
35 power plants. However, it is commonly used in marine, nuclear, and chemical processing applications

1 where moderate strength and creep resistance are required at elevated temperatures (up to 800 °C)
2 [85].

3 The microstructure of Inconel 625 after welding or fusion-based additive manufacturing cannot be
4 directly compared with its wrought counterparts, as the enrichment of Nb in the interdendritic region
5 during solidification favors the formation of MC (M: Nb, Ti) carbides and Laves phase (A_2B , A: Ni, Cr,
6 and Fe; B: Nb, Mo, Ti; D_{024} ; hexagonal; $P6_3/mmc$) by eutectic reactions [51,52]. Precipitation of blocky
7 M_6C (M: Si, Ni, Cr) and $M_{23}C_6$ (M: Cr) carbides can also occur in the 760–980 °C temperature range.
8 Segregation and precipitation of Laves phase, which possesses a low melting point, increases the
9 solidification range temperature, reducing the alloy weldability or printability (due to hot cracking –
10 liquation, and solidification) [86]. This alloy is solid solution strengthened. However, the precipitation of
11 intermetallic phases, such as γ' (Ni_3Al , Ti; L_{12} ; cubic, $Pm\bar{3}m$) and metastable γ'' (Ni_3Nb ; D_{022} ;
12 tetragonal; $I4/mmm$) can occur during thermal cycling induced by heat treatments and/or AM
13 processes. Moreover, the precipitation of undesirable δ -phase (Ni_3Nb ; D_{0a} ; orthorhombic; $Pmmn$) can
14 reduce the material ductility and toughness. This phase can directly precipitate from γ at aging
15 temperatures below 750 °C or replace the γ'' phase when exposed to higher temperatures (750 < T <
16 950 °C) [87,88]. Even though the δ -phase is thermodynamically more stable than γ'' , the slow
17 precipitation kinetics of the δ -phase allows the γ'' phase to precipitate first [89].

18 Cr, Mo, and Nb are the main alloying elements responsible for the solid-solution strengthening of the
19 austenite matrix. Cr is fundamental in providing corrosion resistance by forming a stable chromium
20 oxide (Cr_2O_3) surface layer. As shown in Figure 4.1, forming Nb-rich Laves phase and carbides during
21 solidification largely depends on the composition. Depending on the C/Nb ratio, three different paths
22 can be followed. In path 1, when the C/Nb ratio is high, there is the formation of $\gamma + NbC$. Path 2
23 represents an intermediate C/Nb ratio which leads first to the formation of $\gamma + NbC$, followed by Laves
24 phase formation. At low C/Nb ratios, only Laves phase forms. Only when the carbon content is less
25 than 0.005 wt.% does the formation of Laves phase occur without carbide products [90]. Besides Nb
26 and C, Fe and Si can still affect the formation of Laves phase, as it was observed that low contents of
27 Fe and Si are beneficial to lowering the amount of Laves phase [91]. Topologically close-packed
28 (TCP) phases such as Laves phase will reduce the alloy's mechanical properties as they consume
29 their principal elements, depleting the matrix from solute elements, thus reducing the solid solution
30 strengthening effect. Moreover, the formation of Laves phase in the last stage of solidification will
31 widen the solidification temperature range, increasing the susceptibility to solidification cracking [91].

32

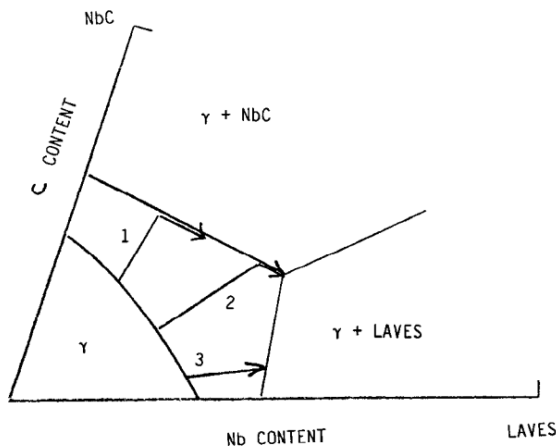


Figure 4.1 - Possible solidification paths in Inconel 625 [92].

Post-process heat treatments performed in solid-solution strengthened alloys are conducted for several reasons, including dissolving undesirable secondary phases, homogenizing, and relieving residual stresses. Since the effect of the heat treatments largely depends on the initial condition of the superalloy microstructure, the already commonly studied heat treatments for Inconel 625 processed by traditional means (ex: casting) may have a different effect on Inconel 625 parts fabricated by AM technologies. Recommended stress-relief heat treatments for Inconel 625 are done in the 700-900 °C temperature range [24]. However, in AM parts, at a temperature of 800 °C, the δ-phase precipitates in just 4 hours, and when the aging temperature is raised to 870 °C, the kinetics of δ-phase precipitation is increased, as 1 hour is enough to form a significant volume fraction (between 5 to 10 %) [93]. An 8 hour heat treatment at different temperatures was performed by Cortial et al. [94] on welded Inconel 625. In the temperature range of 650-750 °C, the improved mechanical strength, and decreased ductility were linked to the precipitation of the γ" phase. Between 750-950 °C, the γ" phase dissolved, and the orthorhombic intermetallic δ-phase formed deteriorating the hardness, yield strength, ultimate tensile strength, ductility, and impact strength. Above 850 °C, M₆C carbides formed along the grain boundaries. At 1000 °C, the ductility and impact strength are partially restored due to the dissolution of the δ-phase, and the amount of M₆C grain boundary carbides increased slightly. At 1000 °C, the welds were essentially fully homogenized.

Xu et al. [95] studied the effect of heat treatments on Inconel 625 parts fabricated by Wire and Arc Additive Manufacturing (WAAM) and found that heat treatment of 980 °C for 1 hour dissolved a large amount of Laves phase and led to the precipitation of the δ-phase. The heat treatment at 1080 °C for 1 hour resulted in the complete dissolution of Laves phase, and the mechanical properties were severely diminished due to the excessive grain growth. Grain growth occurs due to the dissolution of the δ-phase, which will no longer pin the grain boundaries during the heat treatment.

Typically, the properties of as-built WAAMed Inconel 625 are better than those after heat treatment. However, post-process heat treatments can still provide improved corrosion resistance and reduce

1 residual stresses. Finding appropriate heat treatments to prevent embrittlement of Inconel 625 parts is
2 of interest given the relevance of this material in multiple key industries. Section 4.3 will assess by in-
3 situ X-ray diffraction measurements the effect of different heat treatments on the microstructure
4 evolution of Inconel 625.

5 **4.2 Stainless Steel 316L Si Parts**

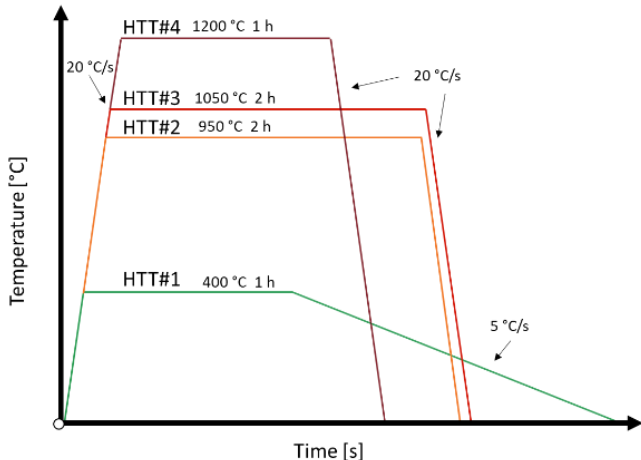
6 **4.2.1 Materials and Methods**

7 A GMAW-based WAAM wall with 180 x 110 x 8 mm was built with a wire feed speed of 4 m/min, a
8 travel speed of 300 mm/min, a voltage of 19.5 V, and a current of 88 A. These parameters were
9 chosen based on the window of parameters recommendations from the welding wire supplier. A zig-
10 zag deposition strategy with 90 seconds of idle time between each torch stop/start was selected to
11 build the 75-layer WAAM part. This deposition strategy was used to check if different regions through
12 the part's height would have different properties since the holding times at specific temperatures would
13 be different.

14 A python-based routine was used to calculate the percentage of each phase based on at least three
15 optical microscopy images on the microstructure images. From this routine, the average and
16 associated standard deviations were determined.

17 Four post-WAAM heat treatments (PWHT) were performed in-situ during synchrotron X-ray diffraction
18 measurements with a beam energy of 100 keV. The four different heat treatments were performed as
19 follows: HT#1 consisted of a stress relief heat treatment at 400 °C for 1 hour, followed by air cooling;
20 HT#2 aimed at promoting σ precipitation and was performed at 950 °C for 2 hours, followed by forced
21 gas (Ar) cooling; HT#3 was performed at 1050 °C for 2 hours, followed by forced gas (Ar) cooling;
22 while HT#4 was performed at 1200 °C for 1 hour, also followed by forced gas (Ar) cooling. It should be
23 noticed that the selection of imposing forced gas cooling aims to avoid the precipitation of
24 intermetallics after the termination of the high-temperature plateau. All conditions were heated to the
25 target treatment temperature at a rate of 20 °C/s. As for the cooling conditions, HT#1 had a cooling
26 rate of 5 °C/s, while the remaining heat treatments had a cooling rate of 20 °C/s. A schematic
27 representation of the heat treatments performed is depicted in Figure 4.2. The final volume fraction of
28 austenite was calculated following equations (7), (8), and (9). For that purpose the peaks: $\delta\{220\}$,
29 $\gamma\{222\}$, $\gamma\{311\}$, $\delta\{211\}$, $\gamma\{220\}$, $\delta\{200\}$, $\gamma\{200\}$, $\delta\{110\}$, $\gamma\{111\}$ were tracked. This method to quantify
30 the volume fraction of each phase was compared with actual Rietveld refinements measurements
31 using MAUD software [52]. The lattice strain for certain (h k l) peaks was calculated as detailed in
32 section 3.6.4. The d-spacing of the as-built sample was considered as d_0 when calculating the lattice
33 strain in the sample heat-treated at 400 °C for 1 hour, following equation (10). Figure 4.3 details the
34 position within a given WAAM wall where specimens were taken for microstructure and mechanical
35 characterization.

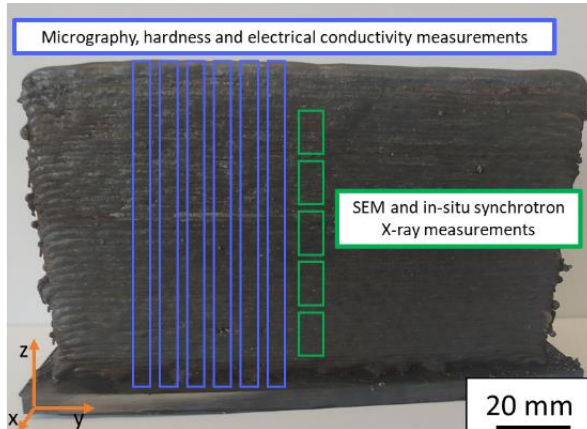
1



2

3 Figure 4.2 - Schematic representation of the heat treatments applied during in-situ Synchrotron X-ray diffraction
4 measurements. The time-temperature plot also resumes the heating and cooling ramps used.

5



6

7 Figure 4.3 - Localization of the specimens taken from the Stainless steel 316 part for microstructure and
8 mechanical characterization.

9

10 4.2.2 Results and Discussion

11 4.2.2.1 Macroscopic Characterization

12 Figure 4.4 a) shows a micrograph of the as-built sample with primary dendrites composed of δ-ferrite
13 aligned with the solidification direction (Z-axis). The produced samples' micrographs are depicted in
14 Figure 4.4 b) to f). The as-built condition (Figure 4.4 b) is characterized by δ-ferrite dendrites oriented
15 perpendicular to the deposition direction in an austenitic (y) matrix. After the stress relief heat
16 treatment, the microstructure maintained similar characteristics to the as-built condition (Figure 4.4 c).
17 With the increase in the heat treatment temperature to 1050 °C, the columnar features became more
18 unnoticeable with the dissolution of δ-ferrite dendrites arms (Figure 4.4 e). Finally, when the heat
19 treatment was set to 1200 °C, almost no evidence of the original microstructure of the as-built material

1 existed. Only some tiny islands of residual δ -ferrite dispersed in the matrix are depicted (refer to
2 Figure 4.4 f).

3 Figure 4.4 a) depicts a variation in the morphology of δ -ferrite in the as-built sample. Typically, layers
4 comprise skeletal-type ferrite in the non-remelted area and lathy-ferrite in the remelted area between
5 layers [75,96], which is explained by the higher cooling rates in the remelted zone since it is the first
6 portion of volume to solidify [97].

7 Stainless steels solidify in one of four possible ways: mode A - single-phase austenite (Liquid \rightarrow
8 Liquid + $\gamma \rightarrow \gamma$); mode AF - austenite with secondary ferrite (Liquid \rightarrow Liquid + $\gamma \rightarrow$ Liquid + $\gamma + \delta \rightarrow \gamma + \delta$);
9 mode FA - primary ferrite with secondary austenite (Liquid \rightarrow Liquid + $\delta \rightarrow$ Liquid + $\delta + \gamma \rightarrow \delta + \gamma$); and mode F - single-phase Ferrite (Liquid \rightarrow Liquid + $\delta \rightarrow \delta$) [97]. The determination of the
10 solidification mode can be based on the chromium to equivalent nickel ratio Cr_{eq}/Ni_{eq} . For the material
11 used in this work, the Cr_{eq}/Ni_{eq} ratio is 1.69. Considering Schaeffler's diagram, it corresponds to a
12 ferritic-austenitic (FA) solidification mode in which δ -ferrite is the leading phase, and austenite (γ) is
13 the second phase. The austenite begins to form between the liquid and δ -ferrite dendrites in a
14 peritectic reaction [98]. Austenite will continue to solidify from the rest of the melt afterward. The
15 diffusion-controlled δ -ferrite to austenite transformation will continue during cooling and stop when the
16 diffusion is no longer possible, resulting in a skeletal and lathy ferrite type [99].

18 4.2.2.1 Electron backscatter diffraction analysis

19 Figure 4.4 inserts depict each condition's electron backscatter diffraction (EBSD) phase maps. As-built
20 and stress-released (400 °C for 1h) samples contain skeletal-type δ -ferrite dispersed in the austenite
21 matrix. The sample heat-treated at 950°C exhibits σ both in a skeletal-type structure and along the
22 grain boundaries. The increase in the temperature to 1050 °C revealed a lower fraction and size of
23 δ -ferrite, as only small islands are present. In the 1200 °C condition, δ -ferrite practically disappeared,
24 as some retained amount can still be noticed in the micrographs.

25 Sigma (σ) can take up to thousands of hours to precipitate directly from austenite [24]. Padilha et al.
26 [101] found in a creep test performed at 600 °C that σ precipitation in austenite only occurred after
27 5481 h (228 days). The following reasons explain the low kinetics of σ precipitation from austenite: i)
28 low solubility of C and N within the σ , which causes carbides and nitrides to form instead of promoting
29 the σ transformation; ii) very slow diffusion of substitutional elements in austenite; and iii) different
30 crystal structures between σ and austenite, which hinders nucleation of the former. This lack of lattice
31 coherence, as well as the high interfacial energy between both phases, is the reason that leads to an
32 increased interface cracking susceptibility when σ is present in these materials [78]. Contrarily, the σ
33 precipitated very quickly from residual δ -ferrite [13] as it prefers high Cr-concentrated regions, as
34 present in higher quantities in δ -ferrite [102].

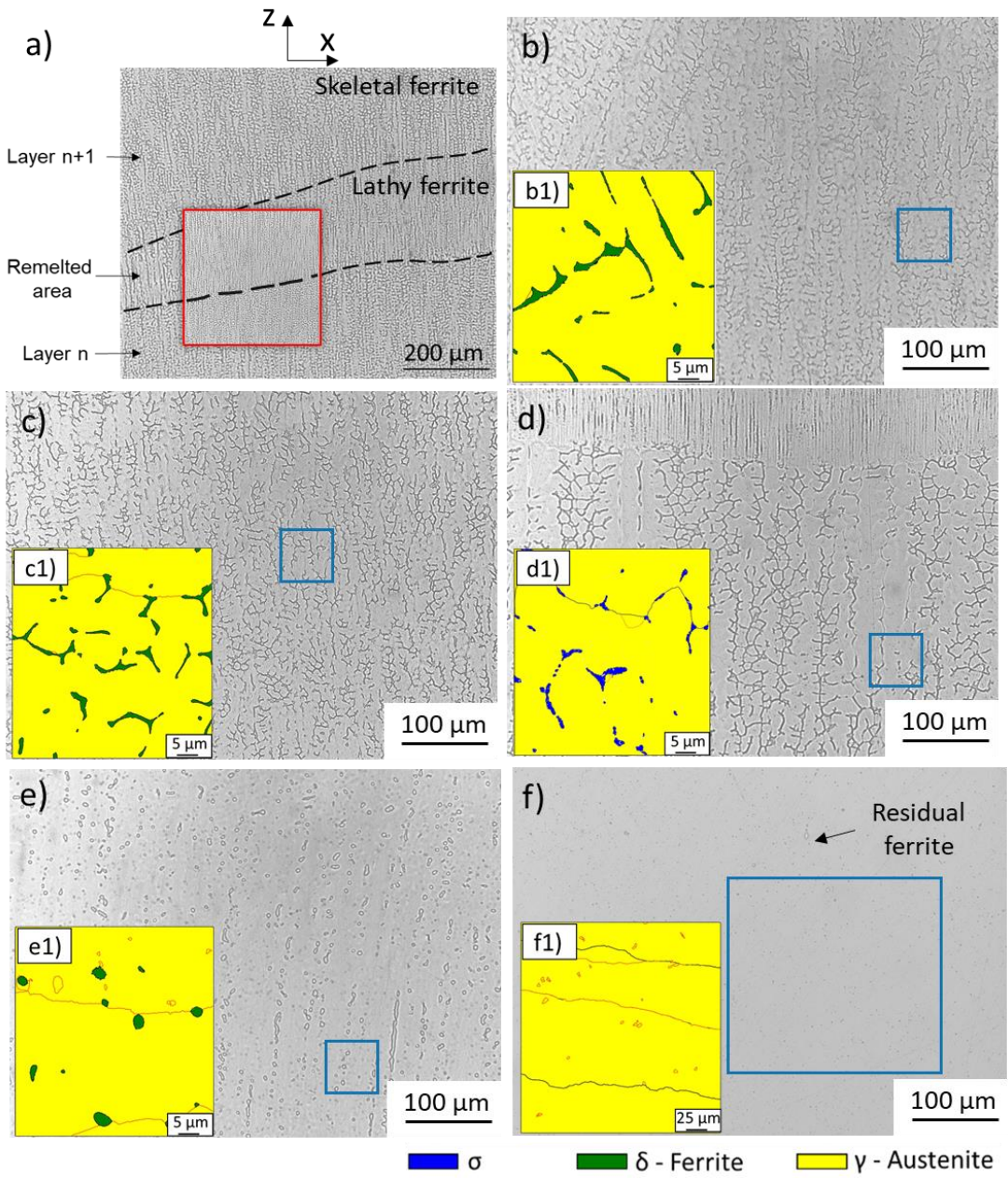


Figure 4.4 - Optical microscope image of the 316 stainless steel: a) and b) As-built, c) After 400 °C 1h, d) After 950 °C 2h, e) After 1050 °C 2h f) After 1200 °C 1h. Inserts b1, c1, d1, e1, and f1 correspond to the high magnification EBSD analysis.

Perron et al. [71] proposed three mechanisms for the precipitation of σ : i) it involves nucleation at the γ/δ interface, which is a high interface energy site place beneficial for heterogeneous nucleation, and also a high Cr-region; ii) direct precipitation in the corners or triple points in the δ -ferrite, resulting from the Cr, Mo, and Ni concentration profiles; iii) eutectoid decomposition of δ -ferrite onto σ and austenite ($\delta \rightarrow \sigma + \gamma$).

1 Due to the preservation of the skeletal type ferrite shown in the micrographs and the EBSD maps
2 (refer to Figure 4.4 d), it can be perceived that the appearance of σ results from direct precipitation on
3 the δ -ferrite islands. By precipitating within δ -ferrite, σ consumes the Cr content and ultimately
4 occupies the entire δ -ferrite islands.

5 The percentage of δ -ferrite and σ content was calculated from the optical microscope images
6 previously depicted in Figure 4.4 with a Python routine, and the results are presented in Table 4.1.
7 The percentage of δ -ferrite in the as-built sample, heat-treated at 400 °C, and heat-treated at 1050 °C
8 sample, is respectively 16.9, 17, and 2.8 %. The percentage of σ in the sample heat-treated at 950 °C
9 is around 16.8 %. Regarding the undissolved δ -ferrite in the sample heat-treated at 1200 °C, its
10 content is below 0.5 %.

11

12 Table 4.1 - Phase percentage measurements made with a Python routine of each phase based on three different
13 micrographs of each condition.

Condition	Austenite (γ)	δ -Ferrite	σ -phase
As-built	83.1	16.9	-
400 °C 1h	83	17	-
950 °C 2h	83.2	-	16.8
1050 °C 2h	97.2	2.8	-
1200 °C 1h	99.5	0.5	-

14 **4.2.2.2 Synchrotron X-ray diffraction analysis**

15 **Ex-situ microstructural characterization**

16 Figure 4.5 depicts the diffraction patterns of the as-built sample and those after completion of the
17 selected heat treatments. The as-built sample identifies diffraction peaks corresponding to the
18 austenite and δ -ferrite phases. Even though WAAM parts are kept at high temperatures for long
19 periods during fabrication, no carbides or other undesirable phases than δ -ferrite were detected in the
20 as-built sample. Precipitation of σ was confirmed after two hours at 950 °C. Multiple diffraction peaks
21 corresponding to σ are evidenced in the orange spectra of Figure 4.5. An apparent reduction in the
22 intensity of the δ -ferrite peaks is observed after the heat treatment at 1050 and 1200 °C. However, as
23 seen in the insert of Figure 4.5, δ -ferrite is still present after being heat-treated at 1050 °C for 2 hours.

24

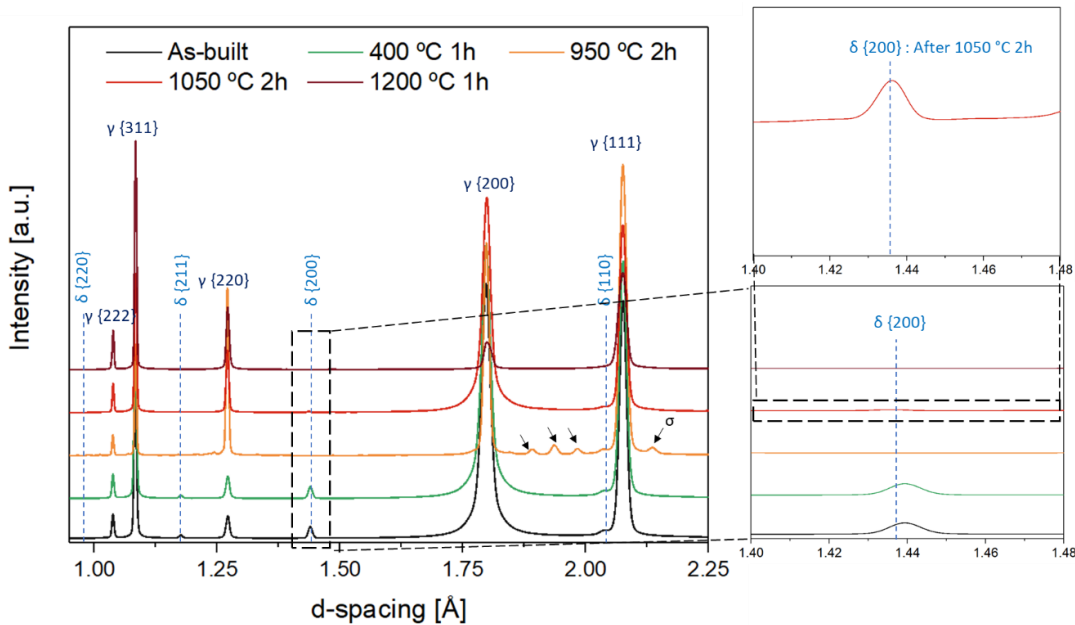


Figure 4.5 - Overview of the diffraction patterns of the as-built and heat-treated samples. Inserts illustrate the existence of δ -ferrite after being heat-treated for two hours at 1050 °C.

Table 4.2 shows the evolution of the d-spacing for several diffraction peaks of both austenite and ferrite after the stress-relief heat treatment. It is interesting to note the shift of both ferrite and austenite peaks to higher d-spacing values (or correspondingly to lower scattering angles), indicating a change in the microstrain state, as typically seen in post-processing stress relief heat treatments [103].

Table 4.2 - d-spacing values and lattice strain of the main austenite and δ -ferrite peaks before and after stress-relief heat treatment (400 °C for 1 h).

Peak	d-spacing [Å]	d-spacing [Å]	Lattice strain
	As-built	Stress-relief	[$\times 10^{-6}$]
$\gamma\{311\}$	1.0835	1.0845	922
$\delta\{211\}$	1.1742	1.1758	1362
$\gamma\{220\}$	1.2709	1.2714	393
$\delta\{200\}$	1.4362	1.4397	2437
$\gamma\{200\}$	1.7967	1.7983	891
$\delta\{110\}$	2.0413	2.0435	1078
$\gamma\{111\}$	2.0742	2.0810	3278

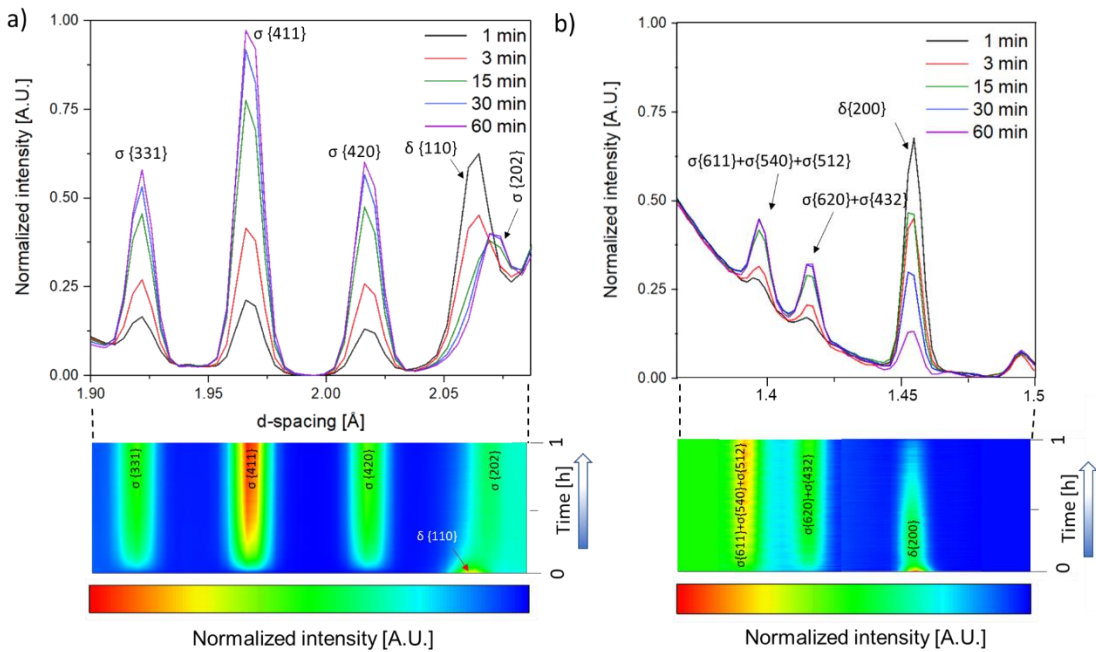
1 **In-situ phase transformations**

- 2 • Precipitation of σ from δ -ferrite at 950 °C

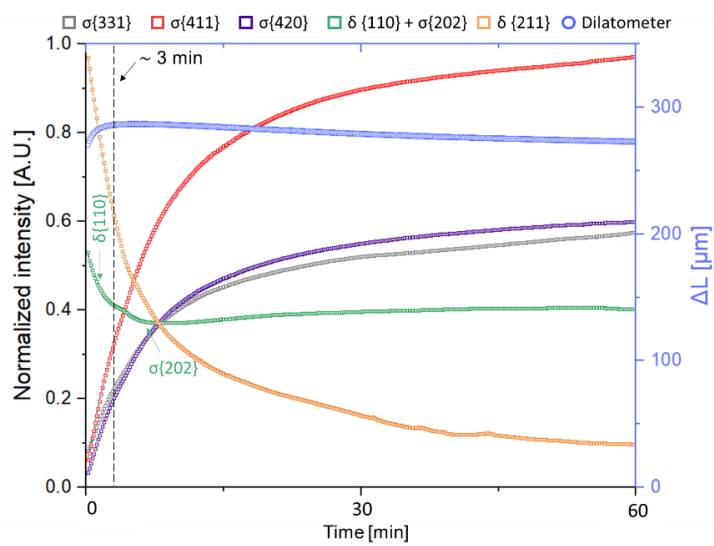
3 Figure 4.6 a) details the evolution of several diffracted σ planes ($\{202\}_{\sigma}$, $\{420\}_{\sigma}$, $\{411\}_{\sigma}$, and $\{311\}_{\sigma}$)
4 during the first hour of isothermal holding at 950 °C. These results were retrieved after isolating
5 portions of the spectra containing a large density of σ peaks. To obtain a kinetic observation of the σ
6 precipitation, the intensity was normalized based on the last observed $\{411\}_{\sigma}$ peak intensity at the end
7 of the isothermal stage. Notice that the intensity of σ peaks is too small to obtain reliable sequential
8 fitting. Therefore, a semiquantitative approach to σ precipitation kinetics and dissolution of δ -ferrite can
9 be obtained by this method. This experiment observed that the σ started to precipitate during the first
10 minute at isothermal holding. Qualitatively it was observed in Figure 4.6 a) that after 15 minutes of
11 heat treatment at 950 °C, the $\{110\}_{\delta}$ peak disappeared, and the $\{202\}_{\sigma}$ overlapped. However, due to
12 the peak broadening of the σ reflection, which decreases over time, and due to the existence of $\{200\}_{\delta}$
13 peak after 60 minutes (refer to Figure 4.6 b), it is evidenced that the partial transformation of δ ferrite
14 to σ was not finished after 15 minutes.

15 The dilatometry results of the first hour of the heat treatment performed at 950 °C are depicted in
16 Figure 4.7. The peak intensity evolution is based on the normalized intensity plot shown in Figure 4.6
17 a). The observed behavior illustrates a slight contraction in the sample during the first hour of
18 isothermal holding. Rivolta et al. [104] showed that σ precipitation from δ -ferrite leads to a slight
19 contraction in the dilatometric curve. The increase in σ peak intensity and the continuous dissolution of
20 δ -ferrite indicate a constant transformation of δ to σ during the isothermal stage of the heat treatment.
21 The fast kinetics of δ to σ transformation indicates that σ -growth is likely to be controlled by a small-
22 scale atomic rearrangement of body-centered cubic (BCC) into the tetragonal crystal structure. Instead
23 of long-range diffusion of substitutional alloying elements [105].

24



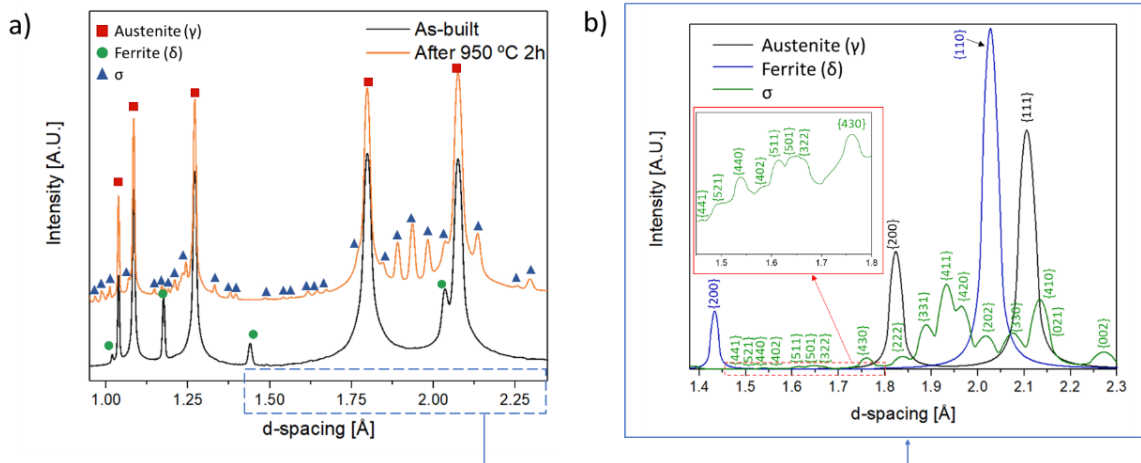
1 Figure 4.6 - a) and b) Sigma (σ) growth and δ -ferrite dissolution in the isothermal stage at 950 °C after 1 min,
2 3 min, 15 min, 30 min, and 60 min. Peak intensity normalization of these two spectra regions (where a high
3 density of σ peaks is observed) is conducted based on the maximum intensity of the {411} σ peak. Therefore,
4 green-to-red colors represent the relative kinetics of precipitation of σ , while blue denotes the constant normalized
5 background counts.
6



8 Figure 4.7 - Intensity evolution of the peaks {110} δ , {211} δ , {331} σ , {411} σ , {420} σ , and {202} σ during the first
9 hour of the isothermal holding at 950 °C. The apparent stabilization of the {110} δ peak after 3 min of isothermal
10 dissolution is explained by the simultaneous precipitation of {202} σ . The initial volumetric expansion is then
11 associated with the dissolution of δ -ferrite, as precipitation of σ results in a modest volumetric contraction.
12
13

1 After the two hours of heat treatment at 950 °C, no δ -ferrite peaks were found, as detailed in Figure
 2 4.8 a). The large density of σ -phase peaks and the convolution of $\{110\}_{\delta}$ and $\{202\}_{\sigma}$ peaks are shown
 3 in a simulated XRD spectrum in Figure 4.8 b).

4

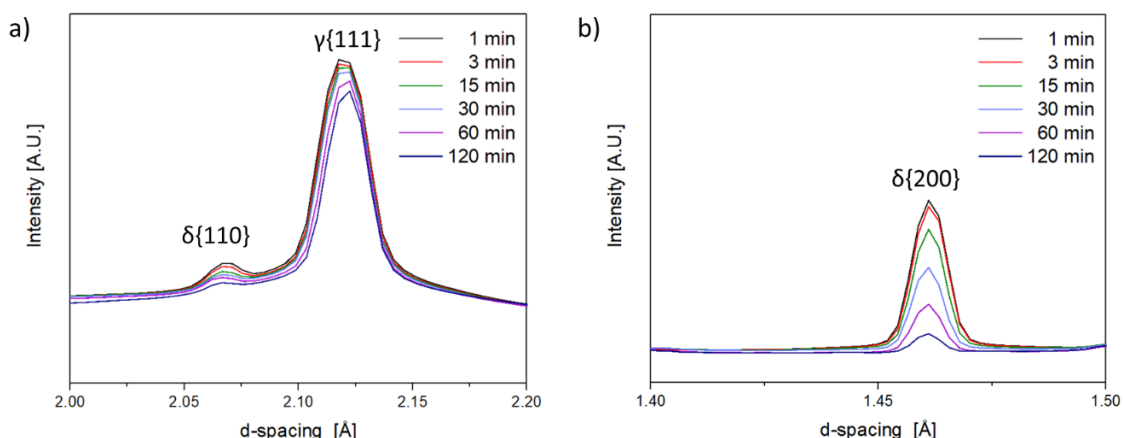


5
 6 Figure 4.8 - a) Overall overview of the powder pattern before and after heat treatment for 2 hours at 950 °C; b)
 7 Powder diffraction pattern of austenite, δ -ferrite, and σ .

8

9 Figure 4.9 depicts the evolution of the $\{111\}_{\gamma}$, $\{110\}_{\delta}$, and $\{200\}_{\delta}$ peaks during isothermal holding at
 10 1050 °C for 120 minutes. The reduction in the scattered intensity of ferrite is accompanied by a
 11 decrease in the austenite reflection intensity. A texture change can explain this since no other
 12 compounds were formed during this heat treatment. Solubilization heat treatments did not reveal any
 13 σ precipitation.

14



15
 16 Figure 4.9 - δ -Ferrite dissolution after isothermal holding at 1050 °C for 1 min, 3 min, 15 min, 30 min, 60 min, and
 17 120 min.

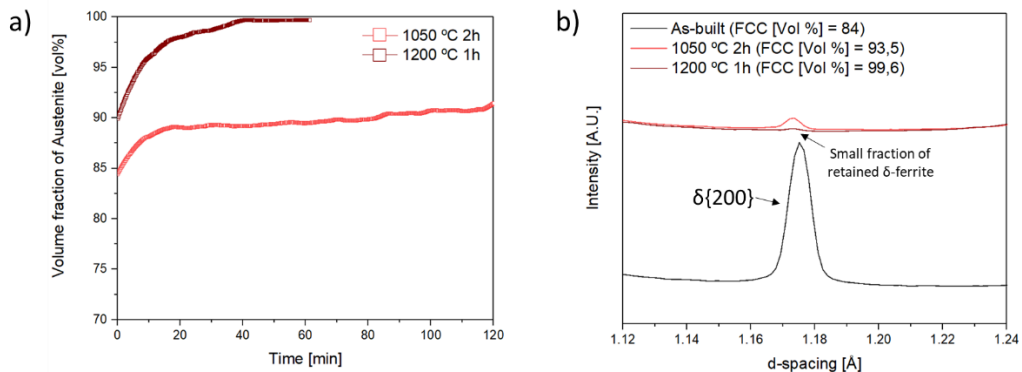
18

19 To monitor the dissolution of the δ -ferrite during the PWHT, the scattered intensity, full width at half
 20 maximum (FWHM), and area of the fitted peaks of the face-centered cubic (FCC) reflections ($\{111\}_{\gamma}$,

1 {200} γ , {220} γ , {311} γ and BCC reflections ({110} δ , {200} δ , {211} δ) were calculated to measure the
 2 volume percent of austenite during heat treatment, resorting the equations (7), (8), and (9). It was
 3 determined that in the as-built condition, the amount of δ -ferrite embedded in the austenite matrix
 4 ranged between 84 and 89 % (refer to the starting point in Figure 4.10 a). These differences in the
 5 ferrite content can be explained by the recursive alternation between skeletal and lathy ferrite in the
 6 samples before heat treatment, which may vary ferrite content. So, if the beam is analyzing a slightly
 7 different region of the material, minor changes in the δ -ferrite amount can occur.

8 The volume percent of undissolved δ -ferrite was higher in the PWHT performed at 1050 °C than in the
 9 PWHT at 1200 °C (Figure 4.10 b). The undissolved amount of δ -ferrite was approximately 6.5 % and
 10 0.4 %, respectively. The continuous increase in the volume percent of austenite during isothermal
 11 holding at 1050 °C suggests that two hours were insufficient to reach an equilibrium state. Since
 12 thermodynamic equilibrium calculations (refer to Table 4.3) predict a complete dissolution of the ferrite
 13 phase at 1050 °C and a residual amount of 2.6 % at 1200 °C. Two potential concurrent effects can
 14 explain this: i) the heat treatment time was insufficient to reach an equilibrium condition; ii) the
 15 segregation of alloying elements during WAAM can locally change the material's chemistry, delaying
 16 the dissolution kinetics [106].

17



18

19 Figure 4.10 - Austenite volume percent evolution during the heat treatments made at 1050 °C 2h and 1200 °C 1h;
 20 b) {200} δ reflection before and after solubilization heat treatments.

21

22 After the heat treatment, the final fraction of δ -ferrite decreases with an increase in the solubilization
 23 temperature. The complete dissolution of δ -ferrite in austenitic stainless steels can be hard to achieve
 24 since long heat treatment schedules are required [71,107].

25

26

27

28

1 Table 4.3 - Equilibrium calculations using TCFE11 database of Thermo-Calc for the volume percent [%] at the
 2 temperatures of interest.

T [°C]	Austenite [vol.%]	δ-Ferrite [vol.%]	σ [vol.%]	Laves [vol.%]	M ₂₃ C ₆ [vol.%]
400 °C	72	23	-	5	-
950 °C	99.95	-	-	-	0.05
1050 °C	100	-	-	-	-
1200 °C	97.4	2.6	-	-	-

3 Table 4.4 compares the volume fraction measurements made using the single peak fitting method vs
 4 the Rietveld refinement method. A maximum deviation of 0.62 % was measured, proving that the
 5 method used to measure the volume fraction when only two phases are presented is valid. Moreover,
 6 with MAUD, it was possible to calculate 15.7 % as the final volume fraction of σ in the sample heat-
 7 treated at 950 °C. The fact that the final volume fraction of σ (15.74 %) is practically the same as the
 8 initial δ-ferrite volume fraction measured for the as-built condition (15.75 %), supports that σ grows
 9 from the δ-ferrite. A fundamental reason why the σ preferentially grows into the δ-ferrite is that the
 10 ferrite is thermodynamically metastable at temperatures where the σ precipitates [105]. The
 11 precipitation of σ was restricted to the δ-ferrite segregation zones, and no δ-ferrite dissolution to the
 12 austenite matrix occurred. These results are also in agreement with the ones already presented in
 13 Table 4.1, which measured phase percentage based on the micrographs characteristics.

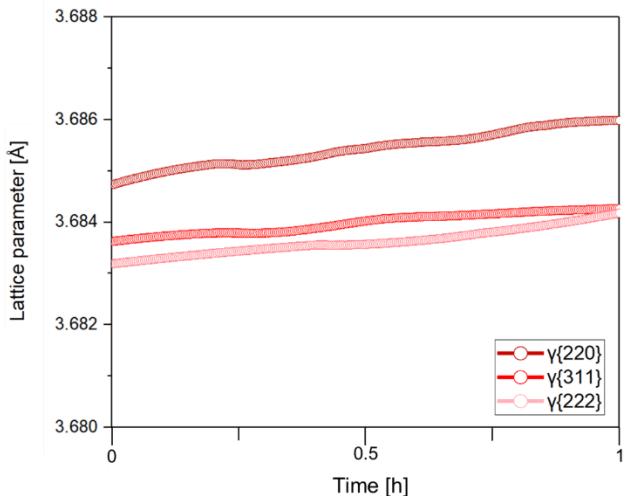
14
 15 Table 4.4 - Comparison of each phase's volume percentage [vol.%] after heat treatment. Measurements were
 16 made via the single peak fitting method and via the Rietveld refinement method performed with MAUD.

Condition	Phase	Austenite [vol.%]		δ-Ferrite [vol.%]		σ [vol.%]	
		Method	Single peak fitting	MAUD	Single peak fitting	MAUD	Single peak fitting
	As-built		83.75	84.25	16.25	15.75	n.a.
	After 400 °C 1h		83.90	83.6	16.1	16.40	n.a.
	After 950 °C 2h	Not measured		84.26	n.a.	n.a.	Not measured
	After 1050 °C 2h		93.5	94.12	6.5	5.88	n.a.
	After 1200 °C 1h		99.7	99.54	0.3	0.46	n.a.

17 The lattice parameters calculated from the lattice spacing (d-spacing) for different {hkl} planes are
 18 given for the higher intensity peaks of austenite ({220},{331},{222}) in Figure 4.11. During isothermal

1 holding at 1200 °C, the lattice parameter expands, which is attributed to the dissolution of ferrite that
2 changes the austenite composition [108,109].

3



4

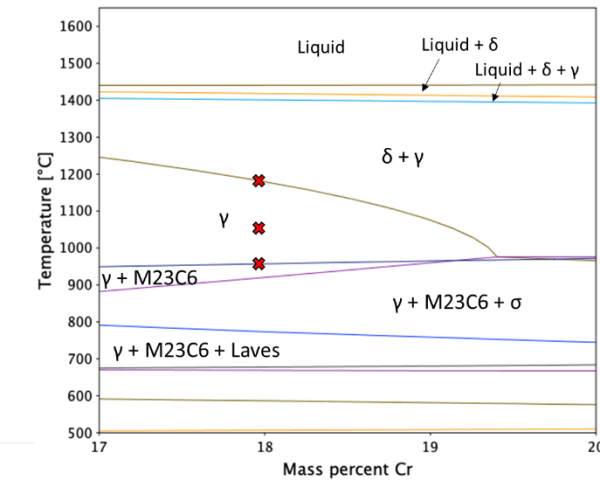
5 Figure 4.11 - Lattice parameter evolution of the most prominent FCC peaks during heat treatment at 1200 °C for
6 1h.

7

8 Thermodynamic equilibrium calculations based on the TCFE11 database of Thermo-Calc (Table 4.3)
9 were used to predict the equilibrium phases of the stainless steel using the nominal composition given
10 in Table 3.1. Figure 4.12 depicts the equilibrium phase diagram with isopleths for each equilibrium
11 phase as a function of temperature and the Cr mass percentage. Red crosses mark the ER 316LSi
12 composition for each heat treatment temperature. It should be noticed that some discrepancies
13 between the X-ray diffraction results, and the equilibrium CalPhaD-based calculations exist. At 400 °C,
14 a 5 % volume fraction of Laves was expected, not found either by high-energy X-ray diffraction or
15 microscopic analysis. Since the effect of each heat treatment largely depends on the initial
16 microstructure, the thermodynamic calculations do not consider the as-built microstructure, which
17 consists of large δ-ferrite dendrites, but rather the material's nominal composition. Laves phase
18 precipitation is sluggish and may occur over extended heat treatment times at 400 °C. Padilha et al.
19 [101] showed that Laves only precipitate at 550 °C after 10 000 hours.

20 Additionally, δ-ferrite is not expected to exist in equilibrium at 950, 1050, or 1200 °C. The
21 experimentally observed residual δ-ferrite is not related to an equilibrium phase (formed above 1200
22 °C) but to insufficient decomposition. This can be explained since the selected heat treatment
23 conditions are not equilibrium conditions: i. e. the chosen time for the post-WAAM heat treatment is
24 not enough to reach an equilibrium condition.

25



1
2 Figure 4.12 - Calculated isopleth for Cr mass percentage. The red crosses mark the composition of ER 316LSi at
3 each heat treatment temperature. The thermodynamic information is taken from the commercial thermodynamic
4 database TCFE11.
5

6 4.2.2.3 Hardness measurements

7 Vickers hardness plots as a function of the distance from the substrate are presented in Figure 4.13.
8 As it can be seen, the higher hardness corresponds to the as-built and stress-relieved sample
9 conditions, ranging from 170 to 200 HV. Higher temperatures resulted in a more significant dissolution
10 of δ -ferrite and, therefore, in lower hardness values. A maximum of 174 HV was observed in the
11 sample heat-treated at 1050 °C, while a maximum of 163 HV was found in the sample heat-treated at
12 1200 °C. Even though there is no δ -ferrite on the sample heat-treated at 950 °C, the slight difference
13 between the average values with the as-built condition is explained by the similar hardness between
14 the σ and δ -ferrite that exists in similar amounts.

15 The stress-relieved sample (400°C 1h) had similar hardness values to the non-stress-relieved one and
16 can be explained by the multiple thermal cycles developed during fabrication. After one layer is built, it
17 is subjected to considerable periods at temperatures between 300-500 °C, thus experiencing an in-situ
18 (at least partial) stress-relieving mechanism during production. The more predominant variable that
19 affects the hardness is the amount of δ -ferrite, as the hardness values obtained for the two different
20 solubilization temperatures are lower than for the other heat treatment conditions.
21

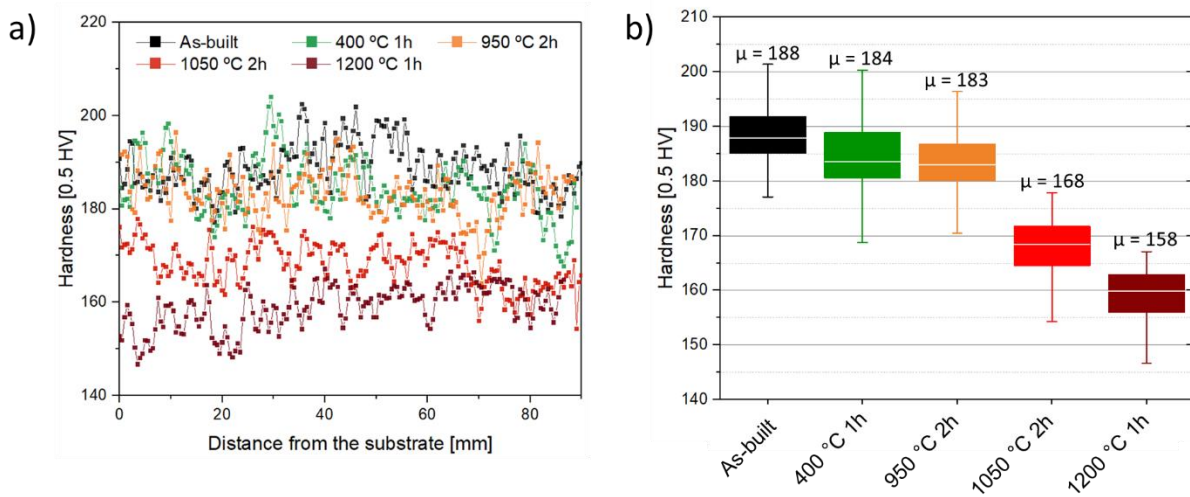


Figure 4.13 - a) Hardness measurements across sample's height, b) Boxplot of the hardness measurements displaying the minimum, maximum, median, and quartiles (Q1 and Q3) of each condition.

4.2.2.4 Electrical conductivity and magnetic permeability measurements

Eddy current testing (ECT) and the four-point probe technique were used to evaluate magnetic permeability and electrical conductivity changes, respectively. The results are depicted in Figure 4.14. An inverse relation between the amount of δ -ferrite and the magnetic permeability was verified with ECT. The signal output decreased with the gradual decrease of δ -ferrite after PWHT at 1050 and 1200 °C. δ -ferrite is responsible for increasing the material's magnetic permeability, but sigma is not because it is not ferromagnetic. If there were no X-ray diffraction measurements, δ -ferrite and σ -phase could be identified using ECT since the microstructure images (detailed in Figure 4.4 b and d) do not permit identifying which constituents are present. The results show that the magnetic permeability of the samples containing δ -ferrite (as-built and heat-treated at 400 °C for 1h) is three times higher than the sample that contains the σ (heat-treated at 950 °C 2h). The technique is susceptible to variations of magnetic permeability. Thus, variations in the δ -ferrite amount could be identified, as shown in Figure 4.14 b).

The average measurements of the electrical conductivity of these samples are between 2.17 and 2.21 %IACS. The high standard deviation does not let any relationship between the amount of ferrite and the grain size to be established.

21

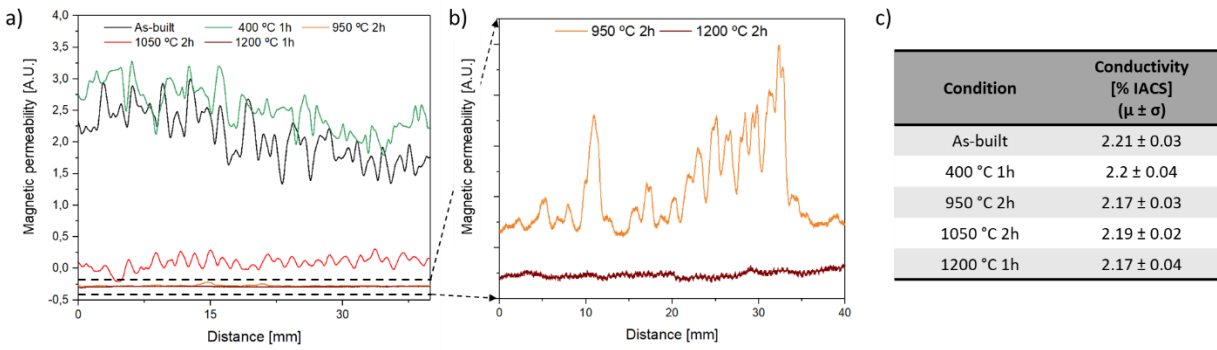


Figure 4.14 - a) Output signal of Eddy Current Testing (ECT) probe using 1.1 MHz, b) Detailed view of the signal output of ECT delineated with dashed lines, c) Average electrical conductivity measurements with a four-point probe for each condition.

4.2.3 Conclusions

A comprehensive study on the effect of post-WAAM heat treatments applied on 316L stainless steel was performed. By combining advanced microstructure characterization and in-situ X-ray diffraction measurements, the following are the significant findings of this work:

- The as-built WAAM samples presented an austenitic matrix with skeletal-type δ -ferrite and lathy-ferrite aligned with the solidification direction (Z-axis). No other secondary phases were discernible;
- After the stress relief at 400°C, the microstructure retained similar characteristics to that of the as-built condition. Synchrotron X-ray diffraction showed that both the δ -ferrite and austenite peaks shifted to lower scattering angles, evidencing a change in microstrain. This heat treatment decreased the sample hardness by an average of 4 HV;
- There is no clear morphological difference between the as-built sample and the sample heat-treated at 950 °C for two hours. However, electron backscatter diffraction confirmed that δ -ferrite acted as a nucleation site for the precipitation of undesirable σ -phase. The precipitation of the σ -phase was geometrically restricted to the δ -ferrite segregation zones;
- In-situ observations showed that σ precipitation started within the first minutes of isothermal holding at 950 °C, and two hours was enough to transform $\delta \rightarrow \sigma$ entirely. A hardness decrease of 5 HV was achieved after this heat treatment;
- A temperature of 1050 °C was enough to promote δ -ferrite dissolution, avoiding the precipitation of the metastable σ -phase. Efficient dissolution of δ -ferrite dendrites can be achieved with higher solubilization temperature, as heat treatments performed at 1050 and 1200 °C resulted in an δ -ferrite retained amount of approximately 6.5 % and 0.4, respectively;
- Eddy's current testing distinguished σ from δ -ferrite in the stainless steel WAAM parts. These results are promising for in-situ inspections of significant components that cannot be easily segmented or transported.

1 **4.3 Inconel 625 parts**

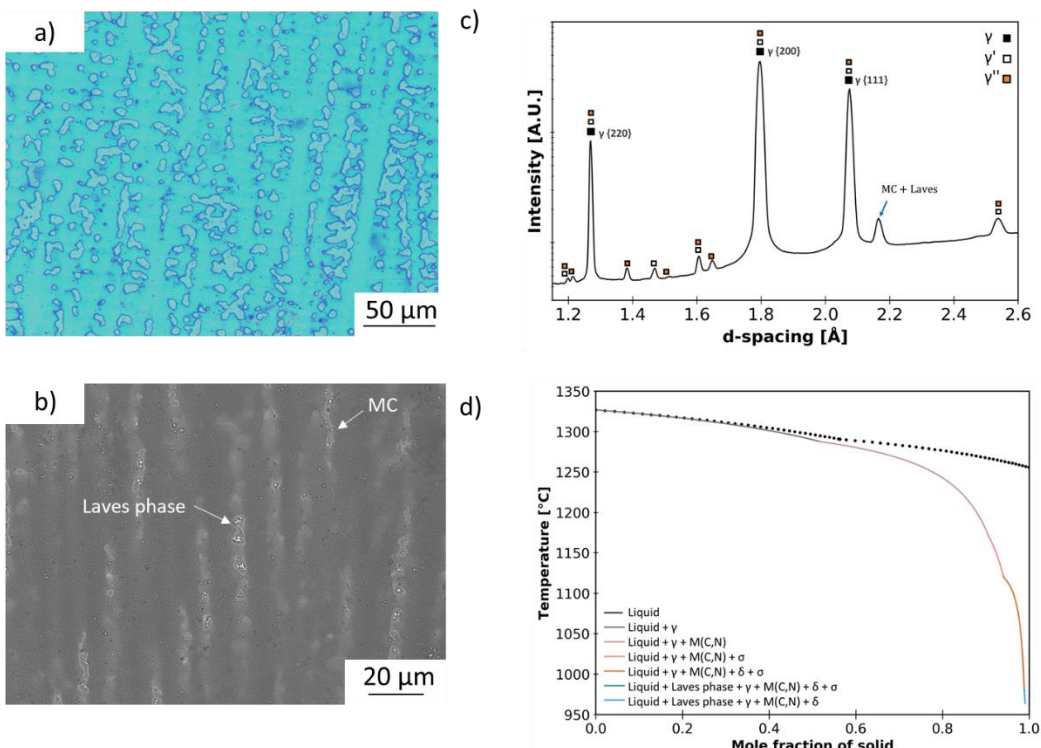
2 **4.3.1 Materials and Methods**

3 In this work, a 55-layer WAAM single-wall 110 mm length using the GMAW-based WAAM torch was
4 fabricated. A wire feed speed of 4 m/min, a travel speed of 250 mm/min, a voltage of 19 V, and a
5 current of 73 A were used. These parameters were chosen based on the window of parameters
6 recommendations from the welding wire supplier. A zig-zag deposition strategy with 90 seconds of idle
7 time between each torch stop/start was used. This deposition strategy was used to check if different
8 regions through the part's height would have different properties since the holding times at specific
9 temperatures would be different. Four different post-WAAM heat treatments were conducted in-situ
10 during high-energy synchrotron X-ray diffraction measurements with a beam energy of 100 keV
11 (0.1234 Å): i) 750 °C for 4 hours, followed by forced gas cooling (Ar); ii) 870 °C during 1 hour followed
12 by another 1 hour at 1050 °C, followed by forced gas cooling (Ar); iii) 870 °C for 1 hour plus another 1
13 hour at 1150 °C, followed by forced gas cooling (Ar); and finally iv) 1200 °C for 30 minutes, followed
14 by forced gas cooling (Ar). Each heating and cooling rate was set to 10 °C/s.

15 **4.3.2 Results and Discussion**

16 The microstructure of the as-built sample is depicted in Figure 4.15 a) and presents columnar
17 dendrites aligned with the build-up direction. Figure 4.15 b) depicts an SEM micrograph of the as-built
18 microstructure in which precipitates are visible inside the γ-dendrites resembling the Laves phase
19 morphology and MC-type carbides. These carbides can play a role in pinning the migration of grain
20 boundaries, increasing the alloy strength [110]. A representative synchrotron X-ray diffraction pattern
21 of the as-built sample is detailed in Figure 4.15 c). It is shown that the material is mainly composed of
22 an γ-matrix with γ', γ'', Laves phase, and MC-type carbides. A strong growth texture due to preferred
23 solidification along the <100> crystallographic direction resulted in a high {200}γ peak intensity. Based
24 on the Scheil-Gulliver calculations (refer to Figure 4.15 d), this superalloy solidification sequence starts
25 with the Liquid → γ reaction, followed by MC precipitation via eutectic reaction (Liquid → γ + MC). The
26 rejection of alloying elements, such as Nb and Mo, to the interdendritic regions, favors the precipitation
27 of eutectic products. Besides Laves, the Scheil-Gulliver calculations predicted precipitation of σ and δ,
28 which were not observed in the synchrotron X-ray diffraction patterns

29



1
2 Figure 4.15 - a) Optical microscope observation of the as-built Inconel 625; b) SEM image of the inside of the γ -
3 dendrites; c) Synchrotron X-ray diffraction patterns of the Inconel 625 as-built sample; d) ThermoCalc Scheil-
4 Gulliver calculations.
5

6 The first annealing temperature of 870 °C was intended to relieve the stresses formed during WAAM,
7 which can be up to 525 MPa [111]. This temperature is the industry-recommended stress relief
8 temperature for Inconel 625 parts. However, 1 hour at 870 °C was responsible for the precipitation of
9 the undesired δ -phase during isothermal holding (refer to Figure 4.16 a). Xing et al. [112] studied the
10 transformation of γ'' to δ , concluding that δ forms in the stacking faults of the close-packed plane of
11 the γ'' phase by shear mode, which resembles the bainite transformation in steels.

12 As the time-resolved X-ray diffraction patterns results show (refer to Figure 4.16 b), the δ -phase
13 rapidly starts to form, within less than 5 minutes of heat treatment, and 1 hour was not sufficient to
14 fully dissolve the γ'' phase. Since the presence of δ is detrimental to the material's mechanical
15 properties, a second-stage heat treatment is necessary to dissolve it. The lattice parameter evolution
16 of the γ {200} and γ {220} peaks is presented in Figure 4.16 c). As δ forms, it removes Nb from the
17 matrix, thus resulting in a decrease of the lattice parameter in the γ -phase.
18

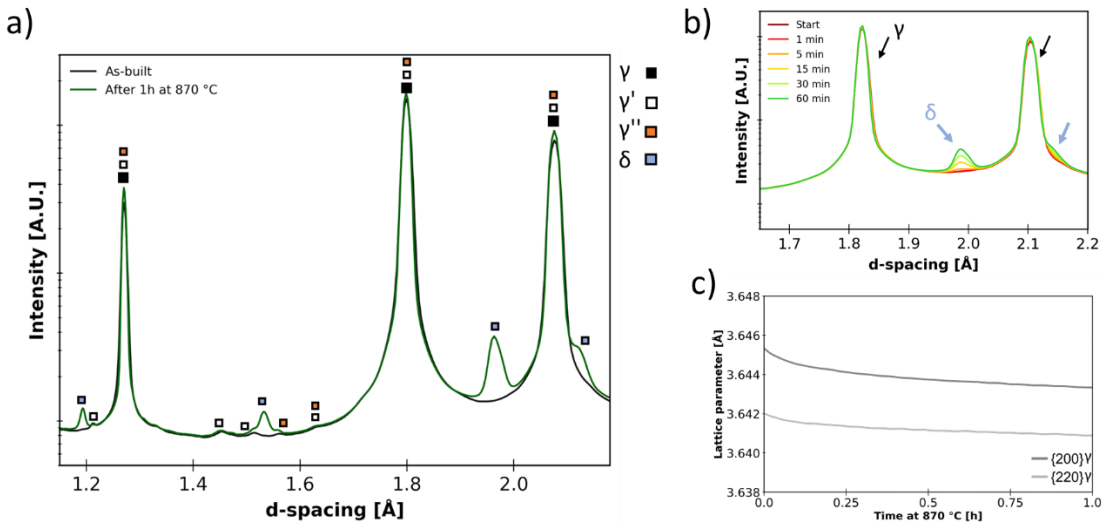


Figure 4.16 - a) Synchrotron X-ray diffraction patterns of the as-built Inconel 625 sample after 1 hour at 870 °C; b) Detail of the δ precipitation during 1, 5, 15, 30, and 60 minutes at isothermal holding; c) Lattice parameter evolution of γ {200} and γ {220} peaks.

The homogenization heat treatments at 1050 and 1150 °C were designed to dissolve other segregation-induced phases in the as-built samples into the matrix while minimizing grain growth. The second step of both heat treatments (1050 and 1150 °C) was responsible for the dissolution of the previously formed δ -phase. During heating (refer to Figure 4.17 a), the δ -phase diffraction peaks become already untraceable at approximately 1000 °C. Moreover, during cooling from 1150 °C, MC-type carbides are formed and stabilized at room temperature (Figure 4.17 b). In the literature, some authors have suggested that the δ -phase can be formed at temperatures as high as 1050 °C [113], which was not verified in the present work, as the heat-treatment performed at 1050 °C fully dissolved the δ -phase. This can be related to composition changes induced by the non-equilibrium solidification conditions typical of WAAM.

The presented results do not follow those previously presented in the literature, which showed that M_6C precipitates form during stress relief heat treatment (870 °C for 1 hour) and that the homogenization heat treatment (1150 °C for 1 hour) promoted Laves phase precipitation and grain growth without dissolving the M_6C carbides [114]. Again, the existence of a highly segregated microstructure (compared to wrought parts) can justify this mismatch, as also observed in 316L stainless steel fabricated by WAAM [115].

The heat treatment performed at 750 °C for 4 hours showed that the γ'' (Ni_3Nb) phase has precipitated and becomes noticeable a peak broadening of the main γ peaks, as seen in Figure 4.18 a). The X-ray diffraction patterns of the sample heat-treated at 1200 °C for 30 min confirmed that the carbides, γ' and γ'' phases that formed during fabrication remain unchanged (Figure 4.18 b).

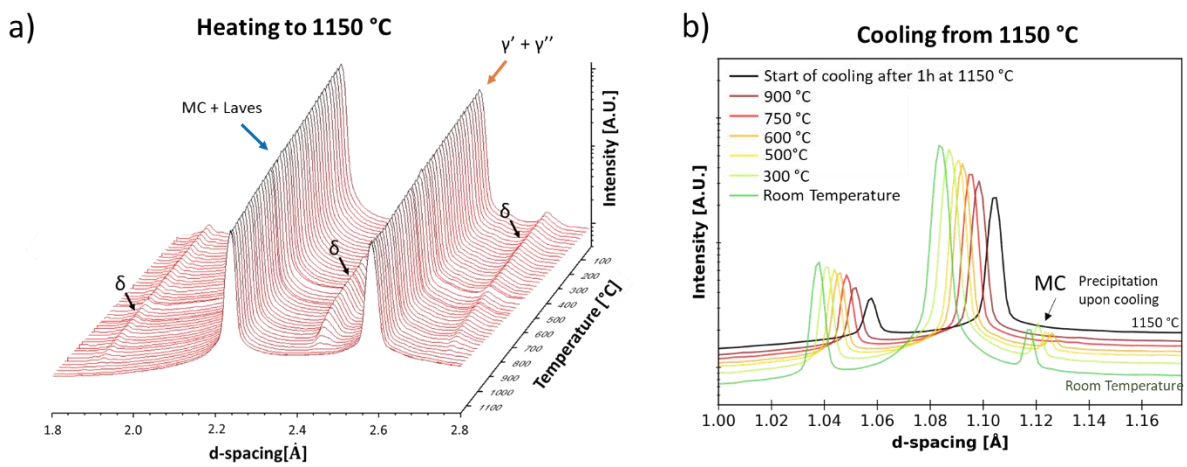


Figure 4.17 - a) Secondary precipitates (δ -phase) formation during heating up to 1150 °C; b) MC-type carbides formation during cooling from 1150 °C down to room temperature.

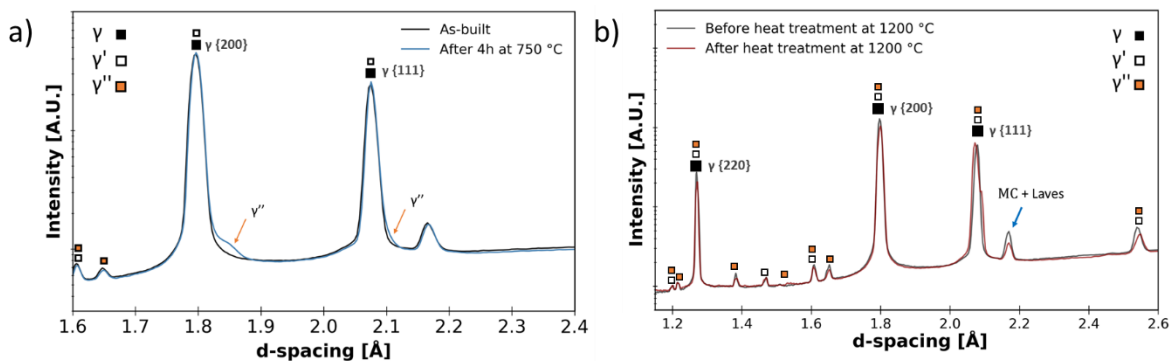


Figure 4.18 - Synchrotron X-ray diffraction results after Inconel 625 was heat-treated for: a) 4 hours at 750 °C; b) 30 minutes at 1200 °C.

Hardness measurements (Figure 4.19) showed that the selected heat treatments on Inconel 625 WAAM parts can have a significant impact on the final material's hardness. The as-built sample had an average hardness of 225 HV. With the heat treatment at 750 °C, the γ'' precipitation increased hardness by 11 HV (an increase of $\approx 5\%$). Between the heat treatments that started with the stress relief heat treatment (870 °C for 1h) followed by annealing, the sample annealed at 1150 °C resulted in a decrease of the hardness of 21 HV (a decrease of $\approx 10\%$), while the one performed at 1050 °C experienced only a marginal decrease of 2 HV. This difference is related to extensive grain growth experienced by the sample heat-treated at 1150 °C. In conclusion, regarding the mechanical properties, there was no significant difference between the second step heat treatment performed at 1150 °C at 1h, with the heat treatment performed at 1200 °C for 30 minutes

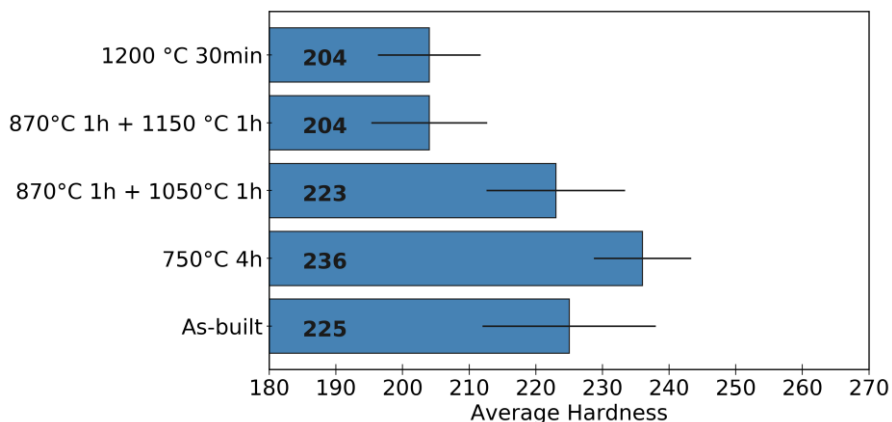


Figure 4.19 - Hardness measurements taken by mapping an area of 5 x 5 mm with a step size of 250 µm.

4.3.3 Conclusions

A study on post-process WAAM heat treatments applied on Inconel 625 parts was performed. By combining hardness measurements with in-situ X-ray diffraction measurements, the following was concluded:

- The as-built samples presented an γ matrix with γ' , γ'' , MC carbides, and Laves phase as secondary phases;
- After the stress relief at 870°C, synchrotron X-ray diffraction showed the appearance of the δ -phase, and as it forms, it removes Nb from the matrix, thus decreasing the lattice parameter of the γ phase;
- Both annealings's performed at 1050 and 1150 °C for 1 hour fully dissolved the δ -phase. However, the time was short for dissolving both carbides and Laves. The annealing at 1050 °C did not affect the hardness measurements, but at 1150 °C, hardness decreased by approximately 10 %;
- The heat treatment performed at 750 °C for 4 hours showed γ'' (Ni_3Nb) precipitation and, therefore, an increase of hardness from 225 HV to 236 HV.

4.4 Summary

This chapter understood the behavior of different heat treatments performed on stainless steel 316L and Inconel 625 parts. Furthermore, this chapter was developed to establish appropriate heat treatments to dissolve undesirable phases that can form during the fabrication of functionally graded materials with Inconel 625 and stainless steel 316 parts, which will be further developed and presented in chapter 6.

5.

IMPROVEMENT OF PARTS PROPERTIES VIA INSERTION OF REFINEMENT PARTICLES

5.1 Introduction

Columnar grains are the most predominant microstructure in WAAM. Therefore, preventing them is one of the main challenges since they are considered unfavorable as they lead to anisotropic properties. In contrast, homogeneous equiaxed grains are more desirable as they improve fatigue life and resistance to crack propagation [10]. Achieving equiaxed grains during fusion-based additive manufacturing can be achieved by controlling the processing parameters and consequently manipulating the temperature gradient (G) and the growth rate (R) of the Solidus/Liquidus (S/L) interface. For a given alloy, it is well known that columnar to equiaxed grains are favored when R increases and G decreases [116]. WAAM presents lower cooling rates and temperature gradients than other fusion-based AM processes (LMD, SLM), however, the solidification type structure falls mostly in the columnar dendritic type. Another characteristic of this process is the excessive amount at high temperatures that increases the grain size. Thus, it becomes challenging to achieve both equiaxed and refined grains during WAAM.

Nevertheless, the generation of an equiaxed and refined grain morphology in WAAM-fabricated parts can be possible with grain refiners [44]. Effective nucleant particles are the ones that facilitate heterogeneous nucleation with small supercooling while segregating solute develops a constitutionally supercooled zone that restricts further growth of the primary dendrites enabling neighboring particles to actively form new grains [117].

5.1.1 High strength low alloy Steel

High strength low alloy (HSLA) steels are widely used for naval and automotive applications and in the tools and die industries. WAAM of HSLA steels is reported in the literature [12,118]. It was stated that the thermal cycles and the heat accumulation experienced can influence the microstructure, thus

1 influencing the local mechanical properties at different heights of the produced parts. One of the
2 effects of extended periods at high temperatures during WAAM of HSLA steels is grain growth,
3 leading to a hardness decrease.

4 One key strategy to counteract a decrease in hardness is by refining the grain size. This solution can
5 be accomplished by reducing the heat input used to deposit the material or using ceramic particles to
6 change the nucleation and growth sequence during solidification. Ceramic particles can promote grain
7 refinement, precipitation hardening, solid solution strengthening, and even adjust the material
8 composition [119]. Even though inoculation is a common practice in the metal casting industry, its use
9 on HSLA steel and its effectiveness is yet to be explored in WAAM.

10 One potential inoculant is silicon carbide (SiC). Due to their high hardness (around 2500 HV),
11 excellent corrosion resistance, and high melting point, these ceramic particles have been proposed to
12 be used. For example, Meredy et al. [120] used SiC during WAAM of a Titanium alloy, and its use was
13 seen to refine the as-deposited prior- β grains. Nevertheless, some columnar grains were still
14 observed. Interestingly, the width of the columnar grains was reduced when SiC was used during
15 deposition. This behavior was attributed to the lateral rejection of the Si-rich solute, which decreases
16 the growth rate in the perpendicular direction to the heat flow extraction, resulting in narrower grains.

17 To this date, studies, where SiC or other ceramic particles are used in WAAM, are still very scarce.
18 However, SiC has already been used to create a metal matrix composite during selective laser
19 melting. Song et al. [121] used sub-micron SiC powder (2.2 wt.%) with Fe to create Fe/SiC
20 composites. Partial dissolution of the particles occurred, which led to the formation of martensite and
21 pearlite. Additionally, mechanical testing showed that the ultimate tensile strength increased from 357
22 to 764 MPa with SiC additions. In another study, laser surface alloying of SiC onto a mild steel
23 substrate was performed. Even though multiple phases can form, it is believed that the increase in
24 hardness and wear resistance of the laser-processed material can be attributed to the presence of
25 cementite. Cementite is formed as a consequence of the high carbon content in solid solution due to
26 the partial dissolution of SiC [122].

27 As it can be perceived, the inoculation of SiC particles in steel could improve the mechanical
28 properties of the fabricated parts. Chapter 5.2 assesses the effect of the addition of SiC as inoculant
29 particles during the WAAM of an HSLA steel.

30 **5.1.2 Inconel 625**

31 Inconel alloys are an essential engineering alloys in multiple Industries. Therefore, WAAM of Inconel is
32 attracting significant attention. The presence of a highly textured microstructure, which results in
33 anisotropic properties, is common. Thus, removing these unwanted microstructure features is
34 necessary. In this work, titanium diboride (TiB_2) was chosen to be added to the Inconel's molten pool,
35 as this refractory compound has a melting point of 3225 °C [123]. It is also characterized by high
36 hardness, corrosion resistance, and wear resistance. Although TiB_2 has a very high melting point,

1 dissociation can occur upon contact with the liquid Inconel. Assuming that some of the TiB₂ will
2 dissociate, incorporating Ti can further enhance the solidified material's mechanical properties,
3 enabling the precipitation of γ' (Ni₃Ti) [124]. Furthermore, additions of B in solid solution can influence
4 the width of columnar grains of WAAM parts [117]. Such is attributed to the large solute rejection to
5 the interdendritic regions that accumulate between the columnar grains, restricting lateral columnar
6 growth and granting neighboring columnar grains the opportunity to nucleate and grow.

7 In the coating industry, nano-TiB₂ has been highly used in concentrations up to 40 wt.% with Inconel
8 625 to create metal matrix composites [125]. The authors stated that the low interface energy between
9 TiB₂ and γ (200-500 mJ/m²) produces a small contact angle and is good enough to maintain excellent
10 wettability and promote heterogeneous nucleation. In addition, TiB₂ has higher thermal diffusivity
11 (5.98×10^{-6} vs 2.08×10^{-6} m²/s) and higher thermal conductivity (25 vs 11.4 W/(m·K)) than the γ
12 phase. This suggests that the temperature of the particles will be lower during solidification than the
13 surrounding liquid, providing favorable conditions for heterogeneous nucleation. In laser metal
14 deposition, Inconel 625 powder was mixed with TiB₂ particles in a weight ratio of 97.5:2.5 to improve
15 fabricated parts' strength and wear resistance. The tensile strength improved from 840 to 1020 MPa,
16 and the elongation increased from 16 to 18 %. Moreover, a substantial hardness increase from 255 to
17 347 HV was observed [126].

18 Chapter 5.3 investigates the role of TiB₂ as a grain refiner agent during the WAAM of Inconel 625
19 parts. Moreover, the relationship between the concentration of TiB₂ and new phases and the resulting
20 mechanical properties were investigated by combining electron microscopy, high-energy synchrotron
21 X-ray diffraction, mechanical testing, and thermodynamic modeling. The mechanism for grain
22 refinement of the Inconel parts is presented and discussed.

23 **5.2 Refinement of High strength low alloy Steel WAAM 24 parts**

25 **5.2.1 Materials and methods**

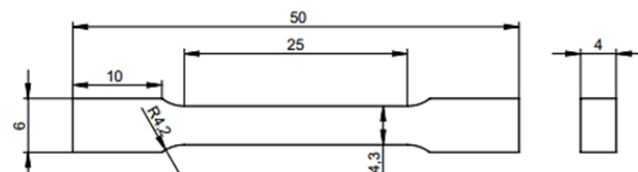
26 The HSLA steel (ER110S-G) was deposited onto a mild steel substrate using the GMAW-based
27 WAAM torch. A total of 50 layers were deposited, each one with a length of 180 mm. SiC particles in a
28 concentration of 0.66 wt.% were added between layers deposition, and its effect was compared to a
29 non-modified (SiC-free) sample after WAAM. SiC particles with a grain size ranging from 1 to 2 μm
30 were purchased from GetNanoMaterials-GNM. The wire feed speed was set to 3 m/min, while the
31 travel speed was 5 mm/s, the voltage was 19 V, and the current was 106 A. These parameters were
32 chosen based on the window of parameters recommendations from the welding wire supplier. The
33 subsequent layer's deposition started after the previous temperature reached approximately 100 °C.
34 This deposition strategy was used to stabilize the interpass temperature early on, avoiding the heat

1 accumulating throughout the deposition. This way, the mechanical properties would not be affected by
2 the different holding times and cooling rates, as seen in a previous work on HSLA steel. [12]

3 The geometry of the samples used for uniaxial tensile testing is depicted in Figure 5.1. Five specimens
4 were removed from deposition (Y-axis) and build-up directions (Z-axis). A schematic representation
5 of the extraction location of the samples used for each test is presented in Figure 5.2.

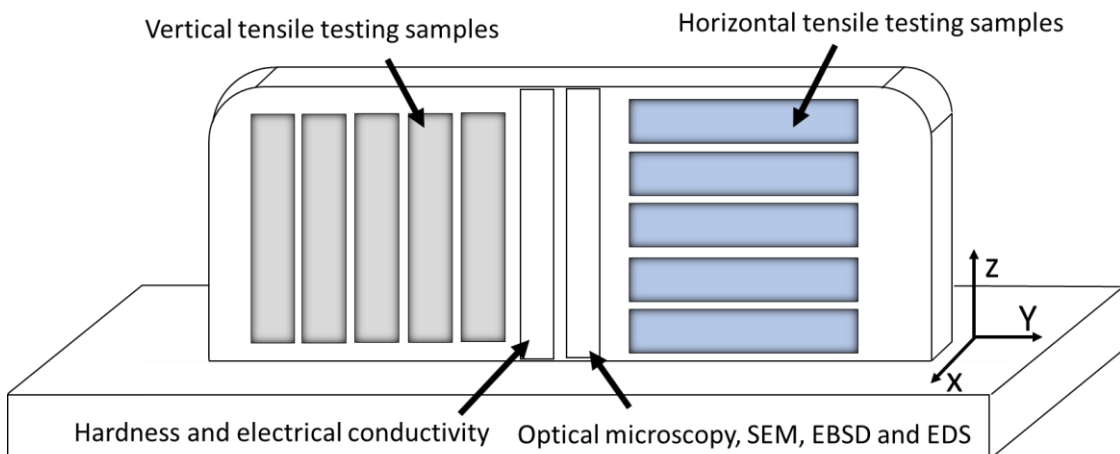
6

7



8 Figure 5.1 - Geometry and dimensions of the uniaxial tensile specimens removed from the HSLA steel sample.

9



10

11 Figure 5.2 - Representation of the sample extraction location for each characterization technique.

12

13 5.2.2 Results and Discussion

14

5.2.2.1 Microscopic characterization

15 Micrographs taken from the three orthogonal planes (X, Y, Z) from both samples are depicted in
16 Figure 5.3. Columnar grains are visible in both YZ and XZ planes of the non-inoculated (as-built
17 sample, refer to Figure 5.3 a). In the XY plane, an equiaxed morphology is found, as this is a
18 section view of the columnar grains. As for the SiC-inoculated sample, a smaller grain structure with
19 diverse growth directions in the three orthogonal planes is observed (Figure 5.3 b). According to Song
20 et al. [121], ferrite nucleation on the previous austenite grain boundaries hinders the formation of
21 massive columnar grains. Additionally, the presence of unmelted particles decreases the activation
22 energy required for ferrite nucleation [127].

23

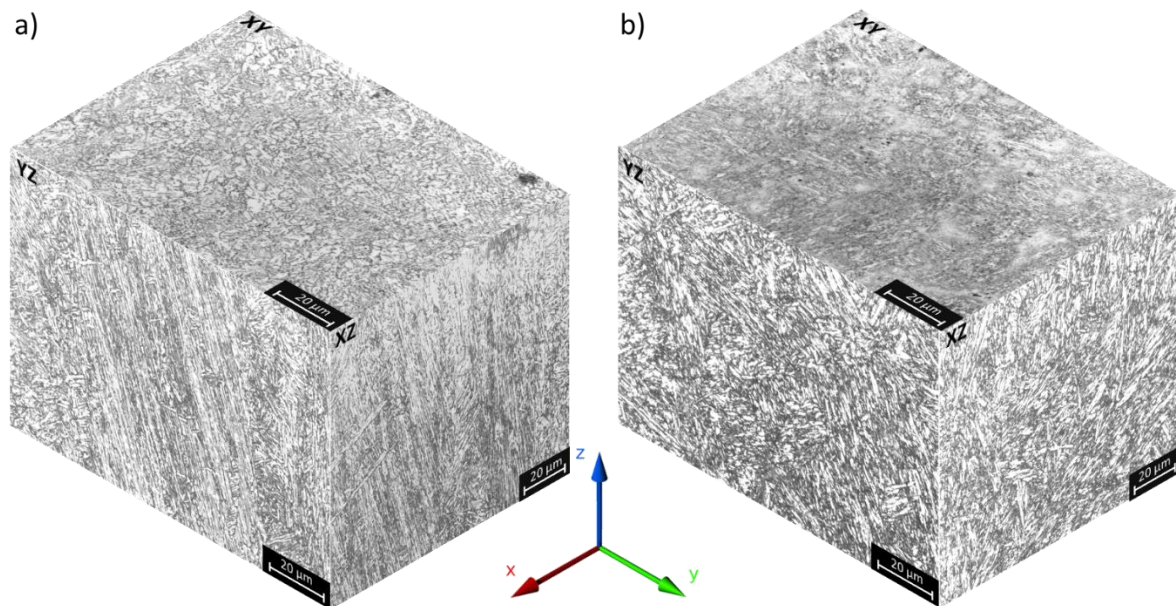


Figure 5.3 - Isometric micrographs of sample: a) HSLA as-built; b) HSLA with 0.66 wt.% SiC.

A more detailed analysis of the microstructure of the inoculated sample is presented in Figure 5.4. It is perceived the existence of multiple phases, including bainitic ferrite, martensite-austenite islands (M-A), and cementite (Fe_3C). The bainitic microstructure is expected due to several competing phenomena, such as the increased carbon content from the dissociated SiC particles and the inoculation effect due to eased heterogeneous nucleation from small SiC inclusions [127]. These M-A constituents are produced from an incomplete transformation from austenite upon cooling or after reheating to intercritical temperatures [128].

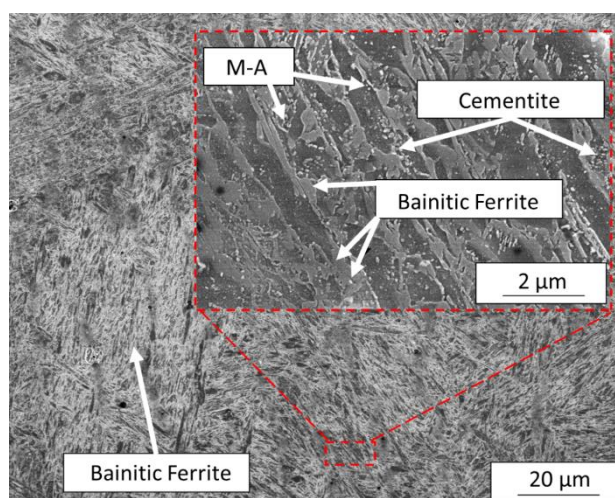
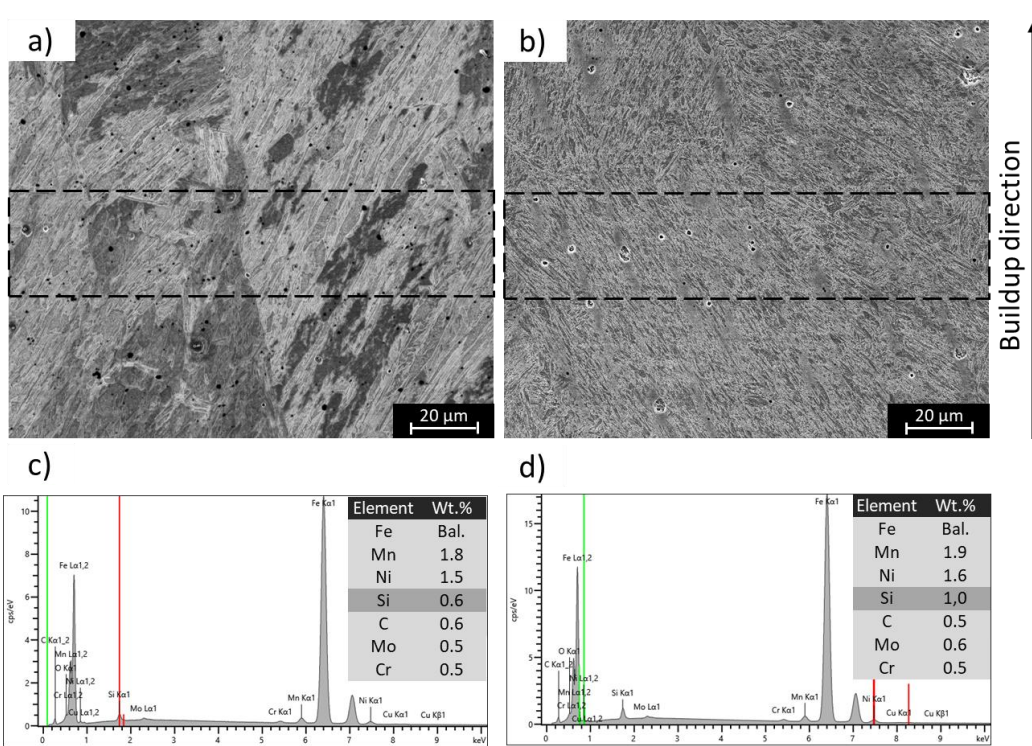


Figure 5.4 - Scanning electron microscopy image of the HSLA steel sample produced with SiC particles; M-A:martensite-austenite islands.

1 Figure 5.5 a) depicts an SEM micrograph of the non-inoculated WAAM part, revealing the presence of
 2 elongated columnar grains. In contrast, a refined grain structure is observed when SiC particles are
 3 added (Figure 5.5 b). These results are in good agreement with the previous light optical micrographs.
 4 Energy-dispersive X-ray spectroscopy (EDS) was performed to evaluate the effect of introducing SiC
 5 particles on part composition. The dashed boxes in Figure 5.5 a) and b) indicate the regions where
 6 compositional measurements were measured. The semi-quantitative Si content in the non-inoculated
 7 sample (Figure 5.5 c) was found to match that of the welding wire used (\approx 0.6 wt.%). For the SiC-
 8 containing sample, the Si content increased up to 1.0 wt.% (Figure 5.5 d). This increase indicates
 9 partial or complete dissociation of SiC particles into the molten pool.
 10 Nevertheless, some dispersed SiC particles were found in the WAAM part matrix. Figure 5.6 depicts
 11 an example of one of those non-dissociated particles with an EDS line scan performed over it. The
 12 length of the particle (\approx 1.5 μm) matches the original dimensions of the SiC particles used (ranging
 13 from 1 to 2 μm). As such, it can be inferred that the heat input was insufficient to melt SiC particles
 14 fully. Note that some of the black dots observed in Figure 5.5 a) and b) are caused by local pitting
 15 during the etching of the samples and not by residual SiC particles.
 16



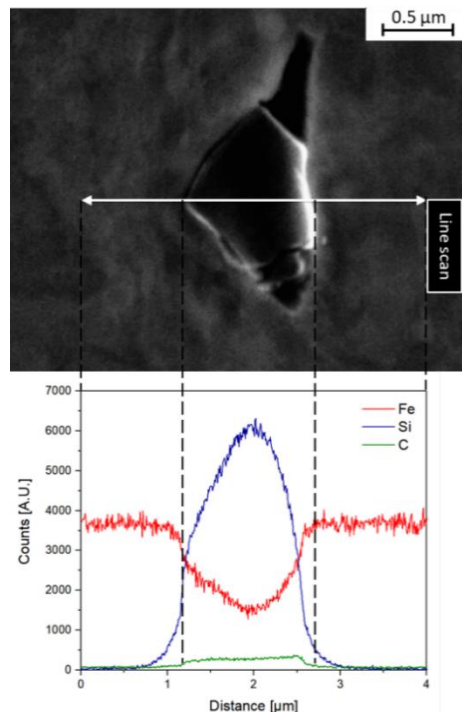
17
 18 Figure 5.5 - Scanning electron microscopy images of samples: a) HSLA as-built; b) HSLA with 0.66 wt.% SiC; c)
 19 and d), energy dispersive spectra and chemical composition of the SiC-free and SiC-added WAAM parts,
 20 respectively. The dashed rectangles in a) and b) show the area used to determine the overall composition of the
 21 produced parts.
 22

1 The partial dissociation of the SiC particles in the melt pool can be attributed to their melting point
2 (around 2800 °C), granulometric size, and relative location to the heat source. If the particles are right
3 below or near the heat source, the experienced peak temperature during the process will be higher;
4 therefore, melting the SiC particles is more likely to occur. In opposition, if the particles are located
5 toward the edges of the molten pool, the temperatures reached will be lower and complete dissolution
6 can be hindered.

7 EBSD analysis was performed in the non-inoculated and inoculated samples, and the results are
8 shown in Figure 5.7 a) and b), respectively. When SiC particles were not used, columnar grains with a
9 width of about 10 µm were observed. In contrast, the inoculated sample evidenced refined grains with
10 an average width of 2.5 µm.

11 Analysis of the misorientation angles of the ferritic grains was performed (Figure 5.8). Both conditions
12 exhibited a high content of low-angle grain boundaries (< 15°). The frequency for misorientation
13 angles between 15 and 50° is low, while it increases again for misorientation angles above 50°. The
14 existence of more boundaries with misorientation angles between 50 and 60° in the SiC-containing
15 sample is related to the grain refinement effect of the upper and lower bainite [129].

16



17

18 Figure 5.6 - Energy-dispersive X-ray spectroscopy line scan over a SiC particle in a WAAM sample inoculated
19 with 0.66 wt.% of SiC.

20

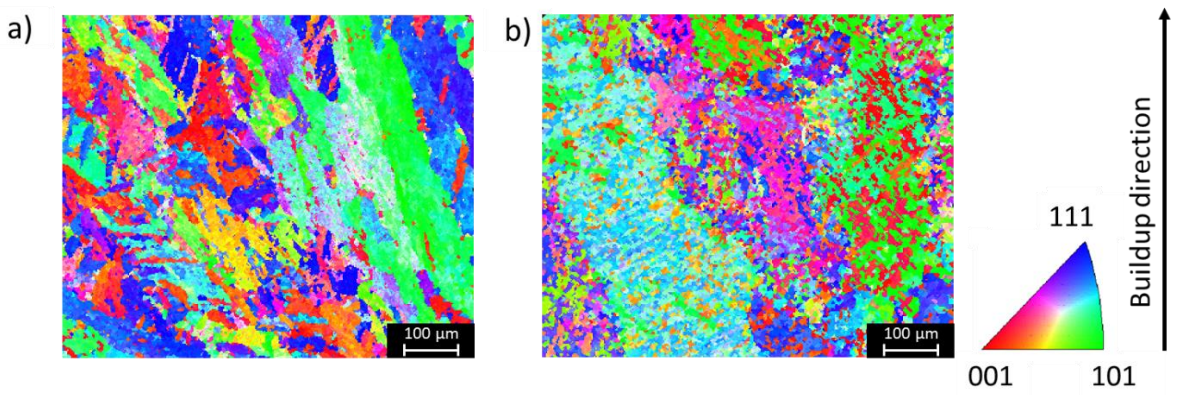


Figure 5.7 - Electron backscattered diffraction (EBSD) orientation maps of sample: a) HSLA steel as-built; b) HSLA steel with 0.66 wt.% SiC.

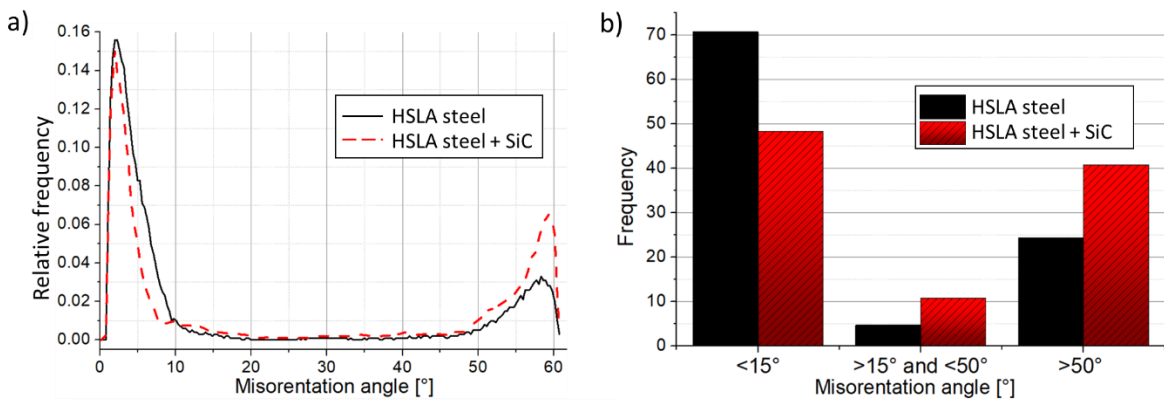


Figure 5.8 - Distribution of the misorientation angles of the ferritic grains in the as-built (HSLA steel) and inoculated (HSLA steel + SiC) WAAM parts: a) boundary distribution and b) frequency of low ($< 15^\circ$) and high angle ($> 15^\circ$ and $< 50^\circ$, and $> 50^\circ$) boundaries.

5.2.2.2 Synchrotron X-ray diffraction results

Figure 5.9 depicts the high-energy X-ray diffraction patterns of the two samples. Both exhibits retained austenite (γ) and ferrite (α) as the main volumetric phases.

The multi-peak fitting for the austenitic {111}, {200}, {220}, {311}; and ferritic {110}, {200} and {211} peaks evidenced the presence of retained austenite in volume percentages of 12 and 18 % for the non-inoculated and inoculated samples, respectively. This calculation was made according to equations (7), (8), and (9). The increased amount of retained austenite (M-A) with the addition of SiC particles can be attributed to the high carbon content incorporated into the welding pool and also to the retardant effect of Si in the precipitation of Fe_3C , favoring the formation of carbon-rich austenite [130].

Besides retained austenite, the most apparent difference between the two samples is the evident existence of cementite in the SiC-containing sample, as shown in blue arrows in Figure 5.9. The

1 formation of Fe₃C was favored since the parent phase was supersaturated in carbon [131]. No
2 evidence of SiC diffraction peaks is found in X-ray diffraction patterns, which is related to the very low
3 volume fraction of solid SiC particles found by scanning electron microscopy. Though synchrotron X-
4 ray diffraction can detect small volume fraction phases [132,133], such was not possible in this case.
5

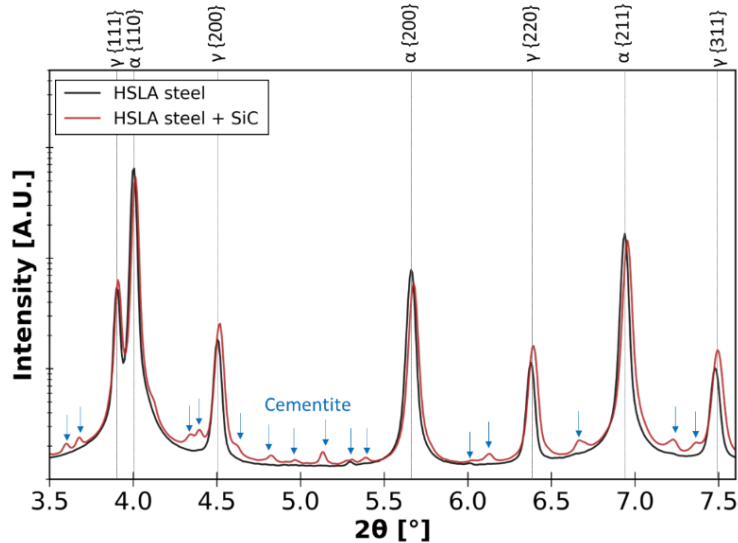


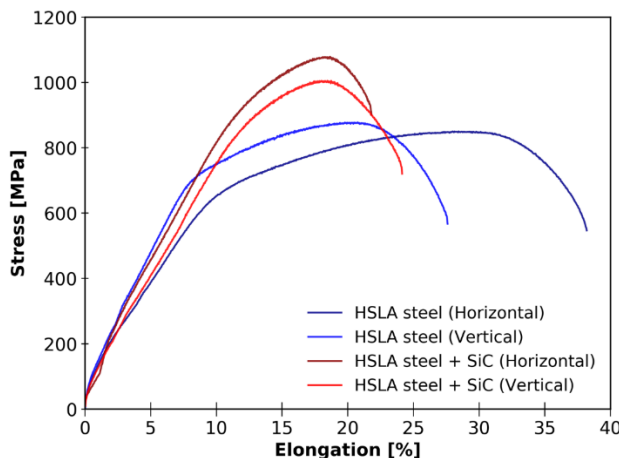
Figure 5.9 - Diffractogram of the sample: black) HSLA steel; red) HSLA steel with 0.66 wt.% SiC. γ – Austenite; α -Ferrite.

Si is an alloying element known to suppress the precipitation of Fe_3C from austenite during the bainitic transformation. The addition of Si reduces the driving force for forming Fe_3C when this phase is forced to inherit the Si present in the parent phase [134–136]. The rejected Si piled up at the carbide-matrix interface decreases the carbon flux from the matrix, thus slowing down the Fe_3C precipitation [137–139], causing the residual austenite to become carbon-enriched [139,140].

The effect of the SiC particles during the production of the HSLA steel parts was not solely observed on the solid-state transformation experienced by the material upon successive reheating cycles. It also impacted the grain morphology of the as-solidified material (refer to Figure 5.3). When SiC particles are dissociated, Si-rich solute promotes constitutional supercooling, which has a refinement effect in HSLA steels [120].

5.2.2.3 Mechanical Properties

21 The tensile curves of produced samples tested along different orientations (Figure 5.2) are depicted in
22 Figure 5.10. The elongation to fracture, yield, and ultimate tensile strength of both parts, obtained
23 along the vertical and horizontal directions, are summarized in Table 5.1.



1

2 Figure 5.10 - Tensile curves of SiC and non-SiC WAAM parts tested along the horizontal and vertical directions.

3

4 The introduction of the SiC particles and their massive dissociation resulted in an increase of the yield
5 strength by 195 and 179 MPa, in the horizontal and vertical directions, respectively. The ultimate
6 tensile strength of the SiC-containing samples increased by 200 MPa (23 %) and 146 MPa (16 %) in
7 the horizontal and vertical directions, respectively. Finally, the elongation to fracture of the inoculated
8 sample decreased by 16 % and 6 %, with the addition of SiC.

9

10 Table 5.1 - Summary of mechanical properties of the SiC-free and SiC-containing HSLA steel parts obtained from
11 uniaxial tensile testing.

Sample Reference	Yield Strength [MPa]		Ultimate Tensile Strength [MPa]		Elongation to Fracture [%]	
	Horizontal	Vertical	Horizontal	Vertical	Horizontal	Vertical
HSLA steel	681 ± 25	707 ± 33	870 ± 37	889 ± 16	39 ± 2.1	30 ± 2.8
HSLA steel + SiC	876 ± 22	886 ± 26	1070 ± 25	1035 ± 31	23 ± 1.2	24 ± 0.8

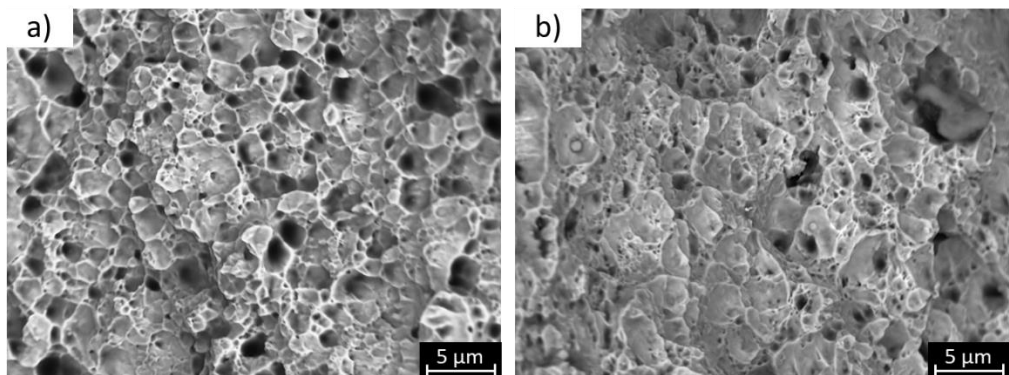
12 Overall, there was a significant increase in the mechanical strength of the SiC-inoculated samples.
13 However, this improvement came at the expense of reduced ductility. This effect can be attributed to
14 the microstructural differences between both samples. The strengthening mechanisms that justify the
15 higher mechanical strength of the SiC-added parts include dislocation pinning due to more grain
16 boundaries and the fine dispersion of Fe₃C particles. Following the Hall-Petch relation [141,142], it is
17 known that grain boundaries act as pinning points, hindering dislocation movement under service
18 conditions. A decrease in the grain size will increase the required stress necessary for dislocations to
19 move, thus, strengthening the material. Grain refinement of ferrite is one of steel's most common
20 strengthening methods [119]. Even though the volume fraction of austenite in the SiC-containing

1 sample was higher, the effect of ferrite grain size and Fe₃C precipitates prevails as another critical
2 factor regarding the improvement of the parts' mechanical strength.

3 Another strengthening mechanism for the inoculated samples is related to the differences in the
4 thermal properties between Fe₃C and the surrounding material matrix. The thermal expansion
5 coefficient mismatch between cementite and the surrounding matrix is high (4.1×10^{-5} vs 12×10^{-6} K).
6 As such, the multiple heating and cooling steps due to consecutive depositions lead to the generation
7 of dislocations [143,144]. This increased dislocation density also contributes to the increase in the
8 mechanical strength of the parts. It should be noted that the elongation to fracture in both horizontal
9 and vertical directions of the inoculated samples is similar, suggesting a significant decrease of the
10 anisotropy upon introducing SiC particles.

11 Fracture analysis of the tested samples (Figure 5.11) revealed the presence of dimples, in excellent
12 agreement with the high plasticity of both the inoculated and non-inoculated parts.

13



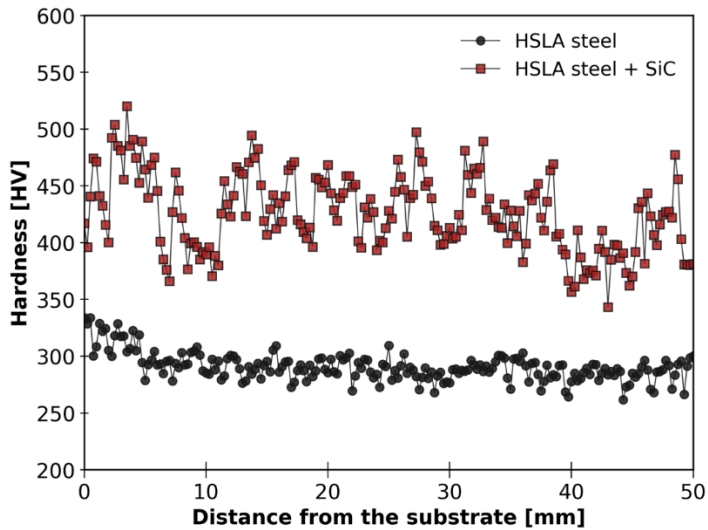
14

15 Figure 5.11 - Scanning electron microscopy image of a surface fracture of sample: a) HSLA steel; b) HSLA steel
16 with 0.66 wt.% SiC.
17

18 As HSLA steel can be used as structural parts, evaluation of the material's hardness is also essential.
19 The effect of SiC addition on the material hardness is depicted in Figure 5.12. The hardness of the
20 SiC-free sample was approximately 290 HV, whereas, for the SiC-added part, a massive increase to
21 ≈ 425 HV was measured. This significant hardness increase is attributed to the higher nominal carbon
22 content, higher presence of retained austenite (M-A), more refined grain structure, and the presence
23 of finely dispersed Fe₃C.

24 On the other hand, the hardness of the inoculated sample was higher than the expected martensite
25 hardness (approximately 350 HV) for the nominal content of 0.1 wt.% C. Therefore, carbon
26 dissociation toward the matrix must have occurred. Some oscillations in the hardness profile along the
27 part height can be justified based on the subsequent interpass tempering sequence and the irregular
28 distribution of SiC, which can influence the location where Fe₃C forms. This increase in hardness is
29 not expected to be due to the presence of SiC particles in the matrix but rather due to the small grain
30 size as observed in the EBSD measurements.

1



2

3 Figure 5.12 - Hardness values measurements across sample's height: non-inoculated sample (black)
4 and 0.66 wt.% SiC inoculated sample (red).

5

6 5.2.2.4 Electrical conductivity measurements

7 The electrical conductivity measurements along the sample's height are depicted in Figure 5.13.
8 Although electrical conductivity is sensitive to the chemical composition of the material, the effect of
9 grain size is predominant [145]. Variations in electrical conductivity, aside from allowing the detection
10 of defects or discontinuities, enable the detection of microstructural features, such as grain refinement
11 or coarsening, since more grain boundaries or precipitates hinder electron movement.

12 The electrical conductivity profiles depicted in Figure 5.13 agree with the microstructure analysis.
13 When the probe is moved from the substrate through the height of the sample, there is a sharp
14 decrease in the electrical conductivity, indicating the interface between the substrate and the first
15 deposited layer. As the substrate used in this work is mild steel, its carbon content is higher than the
16 wire feedstock used for the WAAM depositions, and thus a higher conductivity is found in the
17 substrate. Upon the particles' introduction, the inoculated part's electrical conductivity was reduced
18 from 3.5 to 3.0 % IACS. A refined grain structure of bainite and retained austenite with a high density
19 of dislocations and dispersed Fe₃C precipitates act as a barrier to electron movement, decreasing
20 electrical conductivity. Of particular interest is the inverse relationship between electrical conductivity
21 and hardness: a lower electrical conductivity translates into a higher material hardness, and vice-
22 versa. This correlation agrees with existing literature on the topic [48].

23

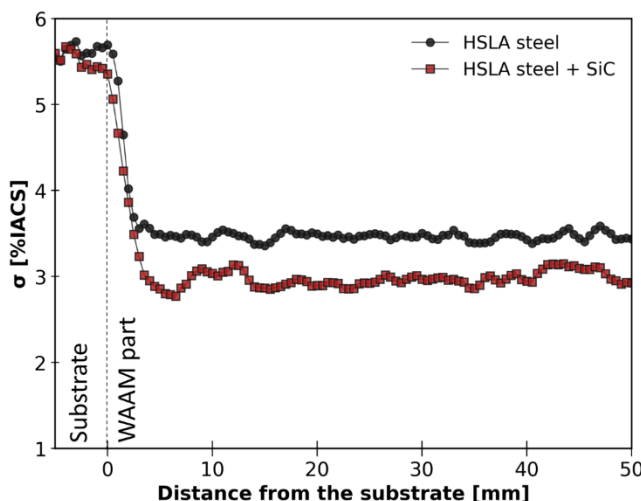


Figure 5.13 - Electrical conductivity measurements with a four-point probe.

5.2.3 Conclusions

In the present study, SiC particles were added in-situ to high-strength low alloy steel. The main findings include:

- Optical observations revealed the presence of a more homogenous microstructure in the sample refined with SiC particles. Near isotropic grains formed upon the introduction of SiC into the molten pool;
- The dissociation of the SiC particles in the molten pool led to an increased carbon content resulting in the coexistence of ferrite, retained austenite (M-A), and cementite (Fe_3C). The hardness increased, on average, from 290 up to 426 HV;
- Some SiC particles remained in the solid state, adding more nucleation sites, resulting in a refined and more equiaxed solidification structure;
- The tensile strength of the SiC-inoculated samples was significantly improved compared to the non-inoculated ones. This increase is attributed to the refined grain structure, higher carbon content, retained austenite, and Fe_3C precipitation in the SiC-containing samples;
- Electrical conductivity measurements exhibit an inverse relation with the hardness profiles: an increase in hardness reflected the decrease in grain size and electrical conductivity.

5.3 Refinement of Inconel 625 WAAM parts

5.3.1 Materials and methods

An ER NiCrMo-3 (Inconel 625) welding wire and the GMAW power source were used in these experiments. The wire feedstock composition can be found in section 3.6.1. TiB₂ particles ranging from 5 to 8 μm acquired from GetNanoMaterials were added using the device previously presented in

1 section 3.4.2 (Prototype 2). An interpass temperature of 150 °C was imposed and controlled with a
2 pyrometer. This deposition strategy was used to stabilize the interpass temperature early on, in order
3 to avoid significant heat accumulating throughout the deposition. This way, the heat accumulation
4 would not interfere with the process of adding particles.

5 The depositions were made using a 4 m/min wire feed speed. The travel speed was kept at 250
6 mm/min, the voltage was set to 19 V, and the current to 73 A. These parameters ensured defect-free
7 parts and were selected based on the window of parameters recommendations from the welding wire
8 supplier. A preliminary study was conducted where Inconel 625 was deposited together only with the
9 flux where the particles would be incorporated. By comparing the hardness and the microstructure of
10 an as-deposited sample against a sample deposited together with the soldering flux, it was concluded
11 that the flux would not interfere with the final properties nor with the geometric aspect of the
12 deposition.

13 Rectangular walls with a dimension of 120 × 50 × 9 mm were deposited on a mild steel substrate. One
14 control sample (0% of TiB₂) and two others (TiB₂ concentrations of 0.31 and 0.56 wt.%) were
15 deposited to evaluate the impact of the added TiB₂ on the microstructure evolution and resulting
16 mechanical properties.

17 A numerical model was developed using the commercial ESI SYSWELD finite element software to
18 estimate the weld pool temperature and evaluate the possibility of melting of the TiB₂ particles. The
19 model was validated via type-K thermocouples placed on the substrate. Two thermocouples were
20 used and measured the temperature 5 and 9 mm away from the centerline of the first layer to validate
21 the thermal model. The model used the geometrical dimensions of a 10-layer wall and the deposition
22 paraments. A double ellipsoidal volumetric heat source designed by Goldak et al. [146] was used to
23 simulate the heat source. The heat source dimensions were set via measurement of the final cross-
24 section dimensions. A LabVIEW design program was designed to measure both current and Voltage
25 during depositions to calculate the average arc power. The material physical properties (density,
26 specific heat, and thermal conductivity) and phase transformation data required for the numerical
27 model were obtained using the JMatPro thermodynamic simulation software, considering the Inconel
28 625 wire chemical composition presented in Table 3.1. The numerical simulations were performed
29 according to the work of Farias et al. [31].

30 The effects of the TiB₂ on the mechanical properties were evaluated via compression and hardness
31 testing. For compression testing, two specimens were removed in each sample's vertical and
32 horizontal directions. The specimens were manufactured in compliance with ASTM's E9-09 [147]
33 standard, using a length-to-diameter ratio of 2. Thus, samples measuring 6 mm in length and 3 mm in
34 diameter were used. The compression testing experiments were carried out using a displacement
35 speed of 1 mm/min.

1 **5.3.2 Results and discussion**

2 **5.3.2.1 Microscopic characterization**

3 Figure 5.14 shows the SEM images taken in the middle of each sample, both in a non-remelted/re-
4 heated area and in a remelted region of the walls. In the as-built Inconel 625 samples, the non-
5 remelted area (refer to Figure 5.14 a) presents the typical columnar dendrites with clear secondary
6 dendritic arms caused as a result of the relatively lower cooling rates during solidification of WAAM
7 components. Also, significant segregation in the interdendritic regions is visible (insert in Figure 5.14
8 a1). The remelted area of the as-built sample (Figure 5.14 b) presents columnar dendrites without
9 secondary arms due to higher temperature gradients, which is the first region of a layer that solidifies.
10 Figure 5.14 c) and d) depict the microstructure in the non-remelted and remelted regions in the sample
11 built with 0.31 wt.% TiB₂, respectively. The non-remelted and remelted region also exhibit columnar
12 dendrites with secondary arms and dendrites without secondary arms, respectively. Finally, when the
13 content of TiB₂ increased to 0.56 wt.%, the non-remelted region solidified as equiaxed dendrites, but
14 in the remelted area columnar dendrites are still present. The inserts a1, c1, and e1 in Figure 5.14,
15 correspond to higher magnifications SEM images. From those figures, it can be observed that upon
16 introducing the TiB₂ particles, the large segregation regions disappeared from the interdendritic
17 spaces. The inserts in the micrographs depict both a decrease of the Nb-rich Laves phase size and
18 the existence of Nb and Ti complex carbides/nitrides in the microstructure. Avoiding the long and
19 continuous Laves phase is beneficial as it improves the hot cracking resistance of Inconel [148].

20 Figure 5.15 details the Scheil solidification curve calculations for both Inconel 625 and Inconel 625
21 with additions of Ti and B, considering a complete dissolution of 0.56 wt.% TiB₂. It is perceived that the
22 solidification temperature range of Inconel 625 is 363 °C, but with additions of Ti and B, there is a
23 reduction to 257 °C. This smaller temperature range will benefit in avoiding/minimizing solidification
24 cracking that can develop in the final stages of solidification. The increase of the Ti content and the
25 existence of B in the alloy also change the phases that should form upon solidification. In the TiB₂-free
26 Inconel 625, Laves phase is formed within the 964-980 °C temperature range, but in the modified
27 alloy, the solidus temperature is 1050 °C, and Laves phase does not form. These results indicate that
28 the possible particle dissolution/melting during the process will not induce deleterious effects or reduce
29 the alloy weldability.

30

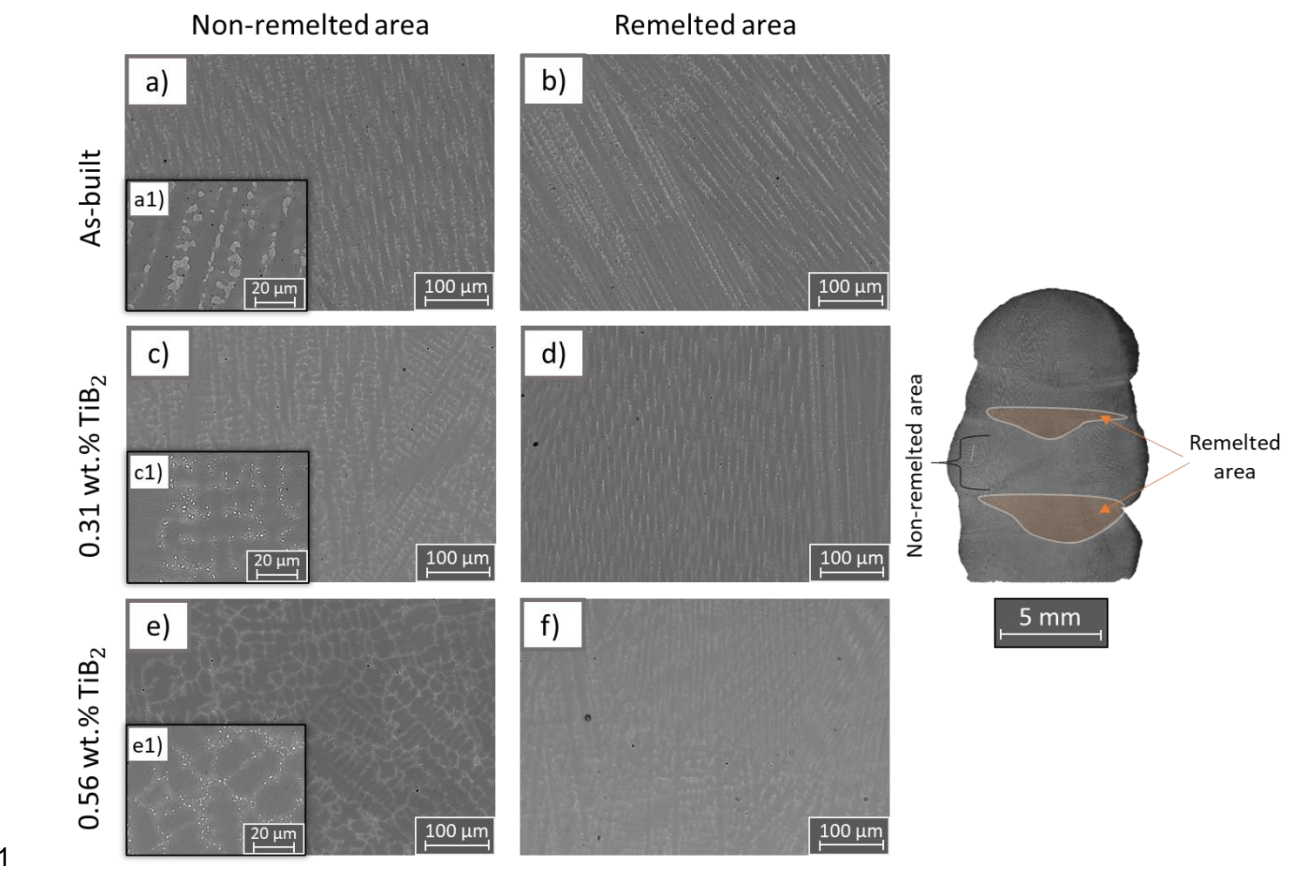


Figure 5.14 - SEM images taken from the non-remelted and remelted regions of samples: (a), (b) As-built; (c) (d) Inconel 625 with 0.31 wt.% TiB₂; (e) (f) Inconel 625 with 0.56 wt.% TiB₂. Inserts a1, c1, and e1 correspond to higher magnification SEM images.

The reduction in the size and fraction of Laves phase and segregated regions is explained by the increased nucleation rate that TiB₂ particles provide ahead of the S/L interface, which will provide less time for the solute to be rejected to interdendritic regions. Thermodynamic simulations (refer to Figure 5.15) confirmed that changes in the composition due to the dissolution of TiB₂ particles can also be beneficial in avoiding the formation of eutectic phases, such as Laves. Also, the formation of M₃B₂ (as predicted in the Scheil solidification simulation) can reduce the Mo and Nb concentration in the remaining liquid [149,150], which can also be beneficial in reducing the amount of Laves in the inoculated condition.

Since the addition of 0.56 wt. % TiB₂ resulted in significant solidification microstructure changes (compared to the 0.31 wt.% TiB₂ containing sample), the focus is mainly given to this condition, which is benchmarked against the as-built sample.

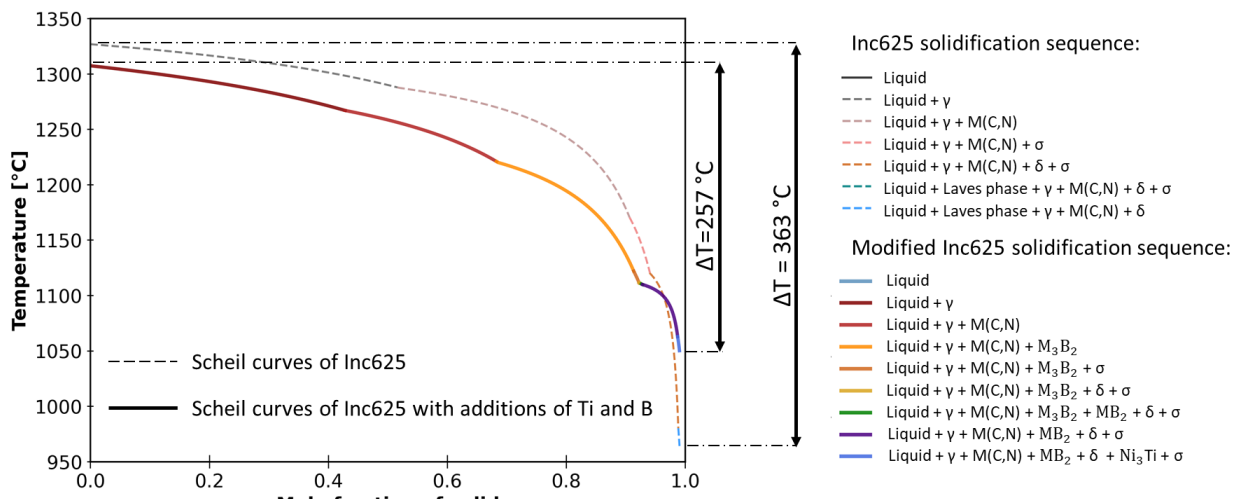


Figure 5.15 - ThermoCalc Scheil-Gulliver calculations for the Inconel 625 and modified Inconel 625 considering a complete dissolution of TiB_2 in the matrix.

Figure 5.16 a) and b) show the EBSD maps of the as-built Inconel 625 sample fabricated with 0.56 wt.% TiB_2 , respectively. In the as-built sample, the microstructure is mainly composed of columnar grains in both remelted and non-remelted regions. Some continuously grow from one region to the other (epitaxial growth). After adding TiB_2 particles, fully equiaxed grains in the non-remelted regions are observed. Moreover, there was a reduction in both the size and width of dendrites in comparison to the ones observed in the as-built sample ($39.1 \pm 4.3 \mu\text{m}$ vs $14.8 \pm 2.5 \mu\text{m}$, respectively). Besides the refinement effect during solidification providing heterogeneous nucleation sites ahead of the S/L interface in a supercooled zone, introducing TiB_2 particles refined the grain size, including the width of the columnar grains. Thus, there is a positive synergistic effect of the TiB_2 particles: they promote the columnar to equiaxed growth transition while simultaneously increasing the nucleation sites for the next layer to solidify.

As observed in Figure 5.16 c), the average grain area decreased from $1823 \mu\text{m}^2$, in the as-built condition, to approximately $583 \mu\text{m}^2$ for the TiB_2 -containing sample. As a result of the refinement and equiaxed grains formed with TiB_2 , the average shape factor was reduced from 1.53 to 1.46. In the non-remelted region, the shape factor reduced from 1.58 to 1.45. The division between grain boundary types is based on the principle that misorientation angles below 15° are referred to as low-angle grain boundaries (LAGB). In contrast, angles higher than 15° are considered high-angle grain boundaries (HAGB) [151]. Since grains come from the same formation mechanism (solidification), the number of LAGB and HAGB were similar between the samples.

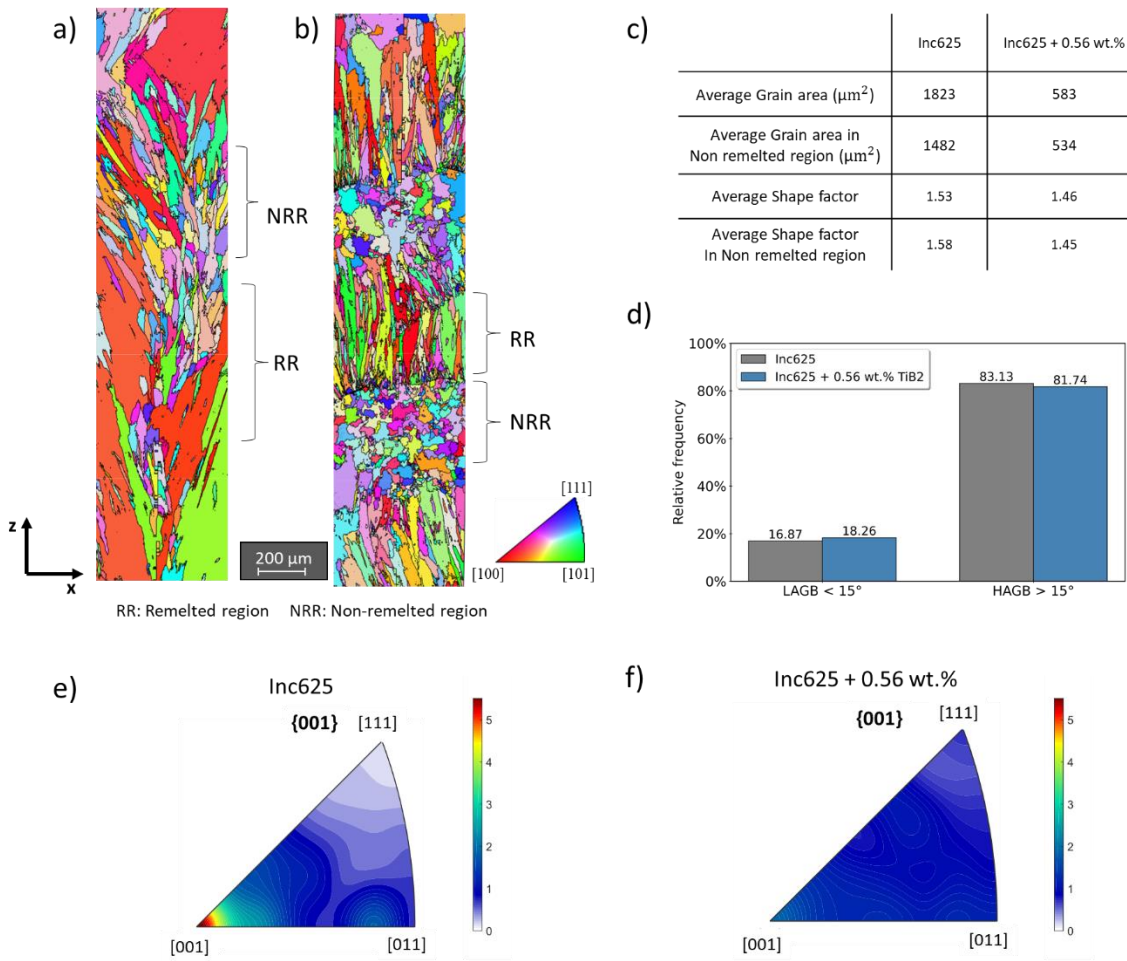


Figure 5.16 -a) EBSD map of the as-built Inconel 625 sample; b) EBSD map of the Inconel 625 with 0.56 wt.% TiB₂; c) Grain shape parameters obtained from the EBSD maps; d) Low and high grain boundaries angle density comparison; Comparison of inverse pole figures of texture for: e) as-built Inconel 625; f) Inconel 625 with 0.56 wt.% TiB₂.

Figure 5.16 e) shows that grains in the as-built sample have a <001> preferential orientation, parallel to the easy growth direction for metals with cubic structure, with the maximum density of grain orientation reaching 5.4. However, with the microstructure refinement upon introducing the TiB₂ particles, the orientation became almost random, with less cube orientation and the maximum grain orientation density reaching only 2.2 (Figure 5.16 f).

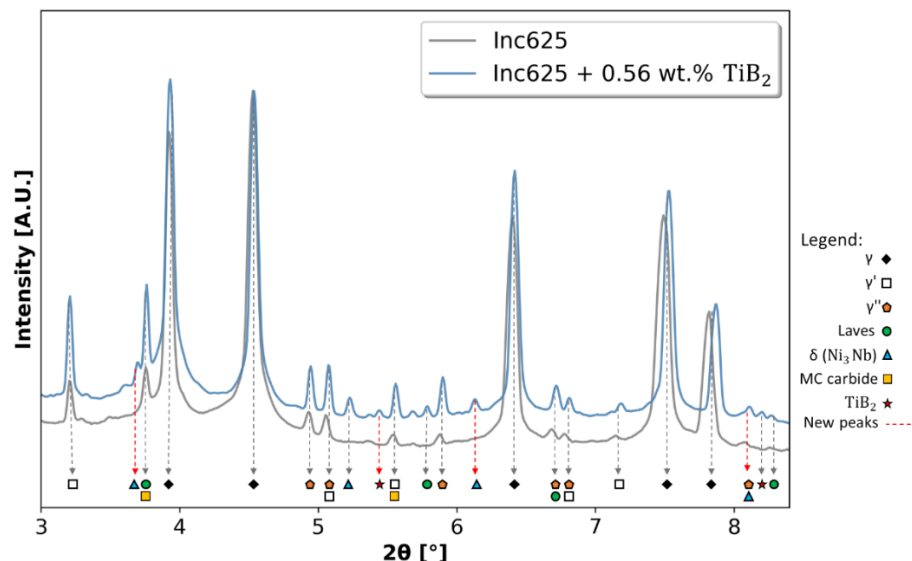
In the sample with TiB₂ additions, each new layer has a mixture of both columnar and equiaxed grains. This scenario is explained by the thermal gradients (G) that are not constant across the molten pool within a single deposited layer. Dynamically, there is a thermal gradient reduction from the bottom to the top of each layer [10]. During solidification ahead of the growing columnar dendrites, G is too high to allow nucleation from the dispersed particles. With further grain growth, G continues to decrease to a point where constitutional supercooling (ΔT) equals or exceeds the temperature at which nucleation will occur (ΔT_N). Hence, nucleation can occur from nearby particles. From this point

on, the existing thermal gradients allow constitutional supercooling to develop, triggering nucleation events within the supercooled zone from the dispersed TiB_2 particles [44,152]. The fact that the density of TiB_2 is smaller than that of liquid Inconel (4.52 vs 7.39 g/cm^3) [153] will also be beneficial for the heterogeneous nucleation, as the TiB_2 particles will tend to be in the top regions of each layer [154].

5.3.2.2 Synchrotron X-ray diffraction

Figure 5.17 presents the synchrotron X-ray diffraction patterns for the fabricated samples. The as-built Inconel presents γ , γ' , γ'' , Laves phase, and MC carbides. When TiB_2 is added to the molten pool of Inconel, new diffraction peaks associated with the δ (Ni_3Nb) phase and TiB_2 are indexed. The formation of new peaks corresponding to the δ -phase suggests that partial dissolution of TiB_2 occurred, as indicated by the Scheil solidification simulation, reducing the potency of these inoculants to start nucleation and the number of potent nucleants. The partial dissolution of TiB_2 resulted in the segregation of Ti to the interdendritic spaces. It is stated in the literature that increasing the amount of Ti with respect to Al and Nb will increase the amount of δ -phase nucleating along grain boundaries and will slow the γ' precipitation rate [155]. Moreover, decreasing the Al/Ti ratio will also increase the mismatch between the γ matrix and γ' precipitates, that further enhances the strength of the γ' phase but will also lower its thermal stability, encouraging the precipitation of the δ -phase [89,155,156]. The increased content of Ti in the matrix also presents some advantages as it restricts the dendrite growth of prior austenite grains and consequently promotes heterogeneous nucleation ahead of the S/L interface [157].

21



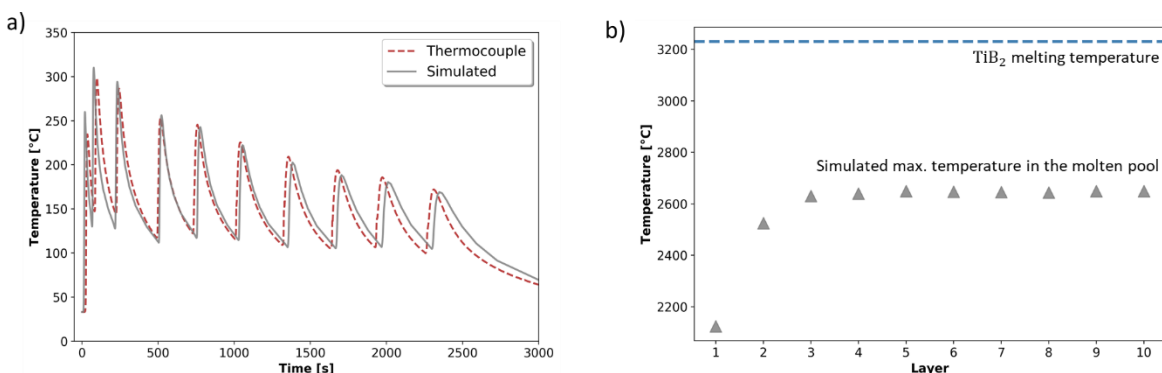
22

23 Figure 5.17 - Synchrotron X-ray diffraction measurements for the WAAM fabricated parts with and without the
24 introduction of TiB_2 .

25

1 The different microstructure features when Inconel 625 is deposited with and without the TiB₂ particles
2 can be justified with the thermal model implemented in this work. A good match exists between the
3 temperatures simulated by the implemented numerical simulation and experimental data obtained with
4 thermocouples, as shown in Figure 5.18 a), validating the heat source and the boundary conditions of
5 the FEM model. The numerical simulation of 10 deposited layers (Figure 5.18 b) simulated the
6 maximum temperature that would develop inside the molten pool considering an interpass
7 temperature of 150 °C. The deposition strategy of regulating the subsequent layer deposition based
8 on the interpass temperature showed that the maximum temperature of the molten pool was 2646 °C,
9 which was stabilized after the 5th layer.

10 It is worth noting that the maximum temperature developed in the melt pool never reaches the melting
11 temperature of TiB₂ (3225 °C). Nevertheless, as inferred from the synchrotron diffraction data, partial
12 dissolution of the particles occurred, which aided in the formation of δ-phase (Ni₃Nb) when 0.56 wt.%
13 of TiB₂ was added. Also, it was detected a diffraction peak associated with TiB₂, confirming that these
14 particles remain, at least partially, in the solid state during the WAAM process. The partial dissolution
15 of the TiB₂ can occur not only when these are in contact with the molten pool but also when they enter
16 contact with the electric arc that typically has temperatures above 6000 °C.
17



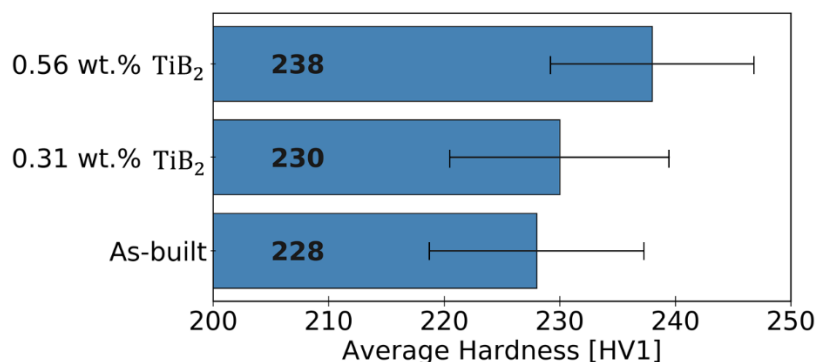
18
19 Figure 5.18 - a) Temperature simulated and measured by thermocouples during the deposition of the 1st layer of
20 the WAAM-fabricated wall; b) Simulation of the maximum temperature of the molten pool at each deposited layer
21 vs the melting temperature of TiB₂.
22

23 5.3.2.3 Mechanical Properties

24 The average hardness of the fabricated samples is depicted in Figure 5.19. Hardness in the as-built
25 sample is, on average, 228 HV, which is in good agreement with the literature of WAAM of Inconel
26 625, which showed variations between 220 and 240 HV [158,159]. With a content of 0.31 wt.% TiB₂,
27 the increase in hardness was only 2 HV which is almost negligible. Only when the TiB₂ content
28 increases to 0.56 wt.%, a more notorious hardness increase to 238 HV occurs. As reported by Hu et
29 al. [160] and Jena et al. [161], additions of Ti between 0 and 3 wt.% have an almost insignificant effect
30 on the hardness, indicating that the effect of solid solution strengthening of Ti on the hardness is

1 relatively small. Only when the amount of Ti was increased to 5 wt.% did the hardness significantly
2 improve, which was attributed to the increased Laves phase content. Since the welding wire used in
3 this study only has 0.4 wt.% of Ti, adding 0.56 wt.% of TiB₂ will not affect the material's hardness by
4 solid solution strengthening. However, as seen in the microstructure images of Figure 5.14, the
5 density and size of the interdendritic segregation regions decreased with the introduction of TiB₂
6 particles. Thus the matrix will be enriched with solid solution strengtheners (Nb, Mo), promoting an
7 increased hardness. This increase is, therefore, attributed to a synergistic effect of the grain size
8 refinement effect (by Hall-Petch strengthening) and solid solution strengthening the matrix. The
9 hardness measurements were not affected by the formation of the δ-phase, as this orthorhombic
10 phase (in amounts < 1.38 vol.%) does not contribute to changes in the tensile strength, yield strength,
11 and hardness at room temperature [162].

12



13

14 Figure 5.19 - Average hardness measurements taken by mapping an area of 5 x 5 mm with a step size of
15 250 μm.

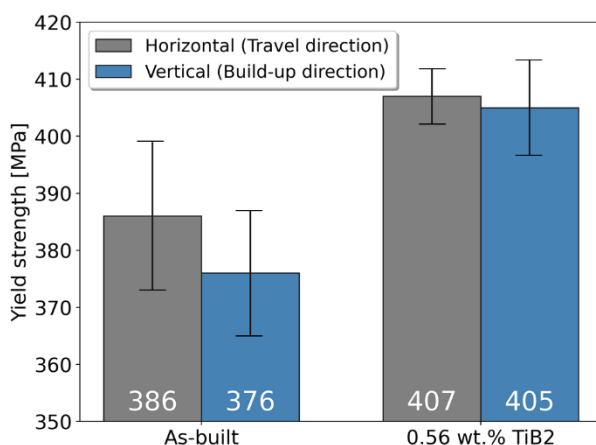
16

17 The average values of yield strength (σ_c) in the vertical and horizontal directions are shown in Figure
18 5.20. According to the literature, the yield strength values in the vertical direction of Inconel 625 parts
19 range between 373 MPa and 384 MPa, while in the horizontal direction, the values reach
20 approximately 380 MPa [13,159,163]. In Figure 5.20, the yield strength of the as-built Inconel is 386
21 and 376 MPa in the horizontal and vertical directions, respectively. Therefore, it can be concluded that
22 these values are within those expected for WAAMed Inconel 625.

23 The introduction of 0.56 wt.% TiB₂ increased the yield strength in the horizontal and vertical directions
24 to 407 and 405 MPa, respectively. Moreover, the values between principal directions had only a
25 difference of 2 MPa on average, while for the control sample the difference was 10 MPa. Thus, it can
26 be concluded that the mechanical properties became more isotropic upon introducing TiB₂ particles.
27 This isotropy can be directly correlated with the EBSD data (refer to Figure 5.16), where the TiB₂
28 particles induced an almost-random texture since the columnar dendrites were replaced mainly by
29 refined equiaxed grains in the non-remelted areas. Gao et al. [151] studied the effect of five
30 strengthening contributions (lattice friction stress, solid solution strengthening, grain boundary
31 strengthening, twin boundary strengthening, and dislocation strengthening) on the yield strength of

1 Inconel 625. The authors found that the predominant mechanism for strengthening is increasing the
2 number of dislocations and twin boundary strengthening. Additionally, grain refinement was the factor
3 that less contributed to the strength (up to 27 % increase). These results explain the only moderate
4 increase in yield strength observed in this work, around 5.4 % in the horizontal specimens and 7.7 %
5 in the vertical specimens. However, the near isotropic properties are relevant since these are typically
6 preferred for structural applications subjected to multi-axial loadings. Thus, it can be concluded that
7 adding TiB₂ to Inconel 625 increased the material's strength and provided near-isotropic properties to
8 the fabricated parts.

9



10

11 Figure 5.20 - Summary of yield strength obtained from compression tests taken from the travel and build-up
12 direction. Three specimens of each condition were tested.

13

14 5.3.3 Conclusions

15 In this study, Inconel 625 with additions of 0.31 and 0.56 wt.% TiB₂ particles were successfully
16 fabricated with WAAM. A new feeding mechanism was developed to introduce particles to the molten
17 pool with a solder flux that evaporates before reaching the electric arc, thus leaving the particles to
18 adhere to the welding wire or flow together with the shielding gas. The mechanism can also introduce
19 particles with lower melting points in the molten pool to perform compositional adjustments for each
20 alloy at specific regions of a part.

21 FEM simulations confirmed that the deposition strategy used to maintain a constant interpass
22 temperature would not result in peak temperatures in the molten pool above the melting point of TiB₂.

23 Microstructural analysis showed a reduction in the size of the interdendritic segregation regions with
24 the introduction of TiB₂ particles, thus enriching the matrix with solid solution strengtheners. Electron
25 microscopy revealed that the content of TiB₂ (0.56 wt.%) replaces columnar grains with equiaxed
26 grains. The average grain area was substantially reduced from 1823 μm² to 583 μm² after adding a
27 TiB₂ content of 0.56 wt.%. Besides promoting the formation of equiaxed grains, EBSD revealed that
28 these refined equiaxed grains were also the starting point for the next layers to grow from, resulting in

1 finer columnar grains. These columnar grains were unavoidable due to the differences in the
2 temperature gradient, G, and growth rate, R, during the solidification of one layer, which resulted in
3 columnar grains in the lowest part of each layer.

4 In the sample that contained additions of TiB₂, synchrotron X-ray diffraction revealed the existence of
5 peaks associated with δ-phase (Ni₃Nb) that were not present in the as-built sample. The existence of
6 this new phase is attributed to the partial dissolution of Ti in the interdendritic spaces, which favors δ-
7 phase precipitation. The introduction of 0.56 wt.% of TiB₂ particles increased the material yield
8 strength (from 386 to 407 MPa in the horizontal direction and from 376 to 405 MPa in the build-up
9 direction) and hardness (from 228 to 238 HV). Introducing TiB₂ can affect the final microstructure
10 depending on the particle's dissolution. In the case of dissolution, the increase of Ti and B content in
11 the molten pool will enable the formation of the δ-phase, restricting the growth of prior austenite grains
12 and enhancing nucleation ahead of the solid/liquidus interface. If the particles do not fully dissolve,
13 TiB₂ particles will trigger nucleation events within the supercooled zone, resulting in equiaxed grains
14 and the refinement of the unavoidable columnar grains.

15 **5.4 Summary**

16 Chapter 5 demonstrates two ways to introduce refinement particles to the molten pool during WAAM.
17 In both studies, the fabricated material's properties were improved compared to the as-built condition.
18 Moreover, manipulating the microstructure was possible since columnar grains were avoided and
19 replaced by equiaxed ones. Besides tailoring the microstructure and resulting properties, introducing
20 particles gradually to the molten pool of fusion-based processes can also be used to create
21 functionally graded materials. In the next chapter, functionally graded materials will be developed by
22 varying the amount of each deposited material.

23

6.

FUNCTIONALLY GRADED MATERIALS

6.1 Introduction

The concept of Functionally Graded Materials (FGMs) was proposed in an attempt to develop high-performance heat-resistant materials, in which heat-resistant ceramics were blended with metals [164]. FGMs are an advanced class of heterogeneous materials that exhibit a controlled spatial variation of their composition and properties, leading to gradual changes in their performance (thermal/electric conductivity, corrosion resistance, mechanical, biochemical, and so on). The main idea behind FGMs consists of a material that cannot deliver all design requirements and a different material suitable for specific locations and operational conditions. Due to this synergic effect, FGMs can be applied in different fields, e.g., biomedical, automotive and aerospace, electronics, optics, nuclear applications, reactor components, and energy conversion [165]. FGMs can be characterized either by a gradual or a discontinuous/abrupt transition between materials. The abrupt transitions (direct interface), parts can experience significant stresses and chemical incompatibility. In contrast, a continuous/gradual transition could minimize these issues, enhancing the mechanical properties, as shown by Pietrzak et al. [166].

Arc-based directed energy deposition, commonly called Wire and Arc Additive Manufacturing (WAAM), is a valuable manufacturing technique for the fabrication of FGMs. Its production can be easily employed with a machine equipped with multiple and independent wire feeders, which allows the creation of parts with gradients of composition and properties in multiple directions. Using two wires simultaneously is designated as Twin-Wire and Arc Additive Manufacturing (T-WAAM). Nonetheless, combining two materials in the same molten pool brings forth perplexing challenges, including the potential formation of undesirable intermetallic compounds, which can reduce the weldability/printability (e.g. due to the formation of hot cracks and high hardness regions) and induce premature failure [165]. Moreover, mismatches in the thermal expansion coefficients, differences in the melting temperature, and lack of solubility can cause cracking and embrittlement [167]. The different thermophysical properties of each wire can also imply significant disparities in the process parameters needed to ensure defect-free parts.

In this section, abrupt and gradual transitions between two different combinations of materials were tested: i) High strength low alloy steel and Cu-Al alloy; ii) Stainless steel 316L and Inconel 625. The properties in the interface between the set of materials are expected to differ from the base materials. Therefore, different characterization techniques have been conducted to study each interface.

6.1.1 HSLA Steel to Copper alloy

Among the metals that can be fabricated with T-WAAM, copper to steel multi-metallic parts has a significant interest in the power generation industry, heat transfer components, electric conductors, cryogenic sector, and dies-casting industries [168]. If used in dies, the higher thermal conductivity of copper grants an intense heat extraction from the castings, reducing production times and manufacturing costs. It can also refine the microstructure by promoting faster cooling rates. Moreover, copper and its alloys often offer good wear and corrosion resistance, whereas steel provides excellent toughness and fatigue resistance.

Despite the above advantages and large applications field for the copper-steel FGM, joining these materials is difficult. The mismatch in the thermal expansion coefficient ($10 \text{ vs. } 17 \times 10^{-6} /^\circ\text{C}$) originates large misfit strains and high residual stresses, which can lead to cracking. Also, the difference in the crystal structure and the low solubility of Cu in Fe is the reason for the lack of solid solution phases in the Fe-Cu phase diagram at low temperatures. In addition, the liquid Cu can penetrate the steel grain boundaries causing hot cracking (liquid metal embrittlement phenomena) [169]. Moreover, the Fe-Cu system exhibits a miscibility gap in which a metastable liquid-phase separation occurs by undercooling the melt pool. This liquid-phase separation greatly weakens the microstructure and may negatively influence the mechanical properties at the interface of the two materials [170].

Attempts to obtain components based on steel and copper-based alloys have been primarily tried via fusion-based welding [169,171,172]. However, weldability issues (hot cracks and brittle constituents) required the development of welding strategies capable of obtaining sound and high-performing structures. For example, a nickel interlayer has been proposed as a solution to make this dissimilar joint [173]. Later, this solution was employed during powder-based additive manufacturing, in which a Ni-based powder was used to create an interlayer between an H13 steel substrate and the top Cu layers. Without the interlayer of Ni, the abrupt transition from Cu to steel resulted in micro-cracks at the interfacial area. The authors attributed this to the combined effect of solidification cracking and high residual stresses, which were caused by the mismatch in the coefficients of thermal expansion and by consecutive cycles of expansion and shrinkage during subsequent layer depositions [174]. Another solution to successfully join these materials is using a pulsed welding heat source (e.g. electric arc or focused laser beam), which will avoid a deeper penetration of Cu onto the steel, i.e., low dilution [169].

Nevertheless, Cu to steel FGM has already been obtained with different additive manufacturing technologies. For example, with Laser Engineered Net Shaping TM (LENS) [175], a crack-free smooth

transition was possible but with several pores observed. Similarly, a controlled gradient was possible with electron beam freeform fabrication (EBF³) [176]. The authors determined that no iron constituents could be found after three layers were deposited on top of a steel layer. X-ray diffraction results showed the presence of the metastable FeCu₄ in the first deposited copper layers due to the slow cooling rates of EBF³. Regarding arc-based additive manufacturing, structural components based on these materials have not been reported yet.

6.1.2 Stainless steel 316L to Inconel 625

FGM of stainless steel 316L (SS 316L) to Inconel 625 (Inc625) is used in chemical plants, oil and gas, and nuclear industry applications. Especially in cladded pipes and valves where parts are inserted in two different environments, which require different corrosion and wear resistances (inner contact to corrosive fluids, e.g., crude oil with high CO₂ and H₂S content, and outside contact with the atmosphere [177–179]). Although these properties are superior in Inconel 625, replacing Inconel with stainless steel in strategic regions of structural parts can reduce the associated component costs. Both alloys exhibit as a matrix a single face-centered cubic (FCC) phase (γ), and their principal alloying elements are Fe, Cr, and Ni. Depending on the process and building strategy, some problems can occur, where hot cracks are especially prevalent.

Shah et al. [180], using laser-directed energy deposition (L-DED), analyzed the influence of the process parameters on the fabrication of a 316 stainless steel to Inconel 718 FGM. The authors demonstrated no evidence of cracks induced by thermal stresses, regardless of the process parameters used. Since the susceptibility for liquation cracking increases with grain size [181], the fine microstructure of the bimetallic structure protects against this type of defect. X-ray diffraction detected Niobium carbides (NbC) and Laves (Fe₂Nb) at the interface. Chen et al. [182] studied a direct interface deposition of Inconel 625 on top of 316 stainless steel (type I-interface) and stainless steel 316 on top of Inconel 625 layers (type II-interface). The authors found that the type I interface is more favorable since a gradual compositional transition can be obtained due to the lower density and viscosity of stainless steel compared to Inconel 625, which aids in promoting a good mixing of the two materials. In the type II interface, the higher density and higher viscosity of Inconel hindered the compositional mixing and thus generated a compositional sudden-change zone, causing cracks to appear in the interface. Through laser DED, Carroll et al. [183] fabricated an FGM of 304L stainless steel to Inconel 625 with 24 layers as the transition region, where the composition was changed in 4 vol.% steps. Large cracks (> 200 μm) were found in approximately 79 wt.% stainless steel and 21 wt.% Inconel 625. Further characterization and thermodynamic calculations allowed the authors to confirm that cracks were promoted by the formation of Nb and Mo-based eutectics, which have a large stability region between 500 °C and 1045 °C.

Despite the direct transition zone (absence of gradually mixed filler metal) commonly observed in stainless steel (used as base metal) arc welded with Inconel 625 (used as filler metal), the WAAM literature on 316L stainless steel to Inconel 625 FGMs is still scarce and divergent. Thus, section 6.3

attempts to optimize and compare the FGMs' properties built with different deposition strategies. Moreover, it will be demonstrated that with WAAM, a completely smooth transition can be obtained without defects, which is yet to be obtained with other fusion-based additive manufacturing processes.

6.2 HSLA Steel to Copper alloy

6.2.1 Materials and design

In this section, an FGM was made using the GTAW power source and the multiple-wire feed system previously presented in section 3.5. The wires used to fabricate the multi-material metallic part were the ERCuAl-A2 (Cu-Al alloy) and the ER-120S-G (HSLA steel). Besides, control samples of the Cu-Al alloy and HSLA steel were fabricated.

Preliminary parameter selection enabled to obtain process parameters that resulted in a similar height and width for both materials and were chosen to fabricate three different samples: i) 40 layers of HSLA steel; ii) 40 layers of Cu-Al alloy; iii) 25 layers of HSLA steel covered by 20 layers of Cu-Al alloy (Figure 6.1). The fabricated parts were single walls 120 mm in length. The process parameters used are detailed in Table 6.1. Notice that the current was set at 100 A for the steel layers and increased to 120 A for the Cu-Al alloy. The need to increase the welding current to deposit the copper-based wire is related to its high thermal conductivity, which tends to dissipate the heat and rapidly create a small molten pool. Starting from the process parameters given by the welding wire supplier and depositing samples with both materials, these parameters were chosen since they resulted in similar heights and widths for both materials. An interpass temperature between 100-150 °C was used and controlled with a pyrometer, as this range of temperature results in a more stable and repeatable shape of the deposit, with less waviness [184]. The terminology used for phase identification in the Cu-Al alloy was taken from the work Wang et al. [185]. Only vertical specimens (aligned with the Z-axis direction) were tested by uniaxial tensile testing.

Table 6.1 - Process parameters used in the experiments.

Process	Gas tungsten arc welding (GTAW)
Travel speed	100 mm/min
Wire feed speed	1 m/min
Current	100 A for steel; 120 A for Cu alloy
Shielding gas	Argon 99.99 %
Shielding gas flow rate	18 L/min

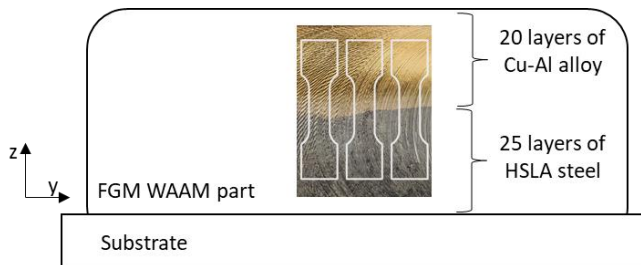


Figure 6.1 - Schematic representation of the functionality graded material of HSLA-steel to Cu-based alloy.

6.2.2 Results and discussion

6.2.2.1 Macroscopic characterization

A defect-free HSLA steel/Cu-Al alloy FGM part with no cracks or pores was obtained. Figure 6.2 a) depicts the macrograph of the cross-section of the FGM part. Figure 6.2 b) illustrates the region only composed of the Cu-Al alloy, in which a mixture of a predominant Cu (FCC) phase (white areas) with β phase at the intercellular regions (dark regions) can be noticed. The size of the Cu (FCC) constituents ranges from 15 to 110 μm . The micrograph of Figure 6.2 c) is taken from an area with only HSLA steel and presents the characteristic ferrite grain boundaries with a grain size ranging from 1 to 4 μm . Scanning Electron Microscope images of the microstructure at the interface region are detailed in Figure 6.2 d), e), f), and g). In region D, both β phase and small Fe (BCC) constituents in a Cu (FCC) matrix were observed. In regions E, F, and G (higher Fe content regions), it can be perceived the existence of both Fe (BCC) (grey features) with Cu (FCC) (light features) in the intercellular regions. Since both wires were not deposited simultaneously, this mixture arises from intense convective motion in the molten pool created by the Lorentz force, Buoyancy Force, Surface Tension gradient, and arc shear stress [11]. When moving upwards from region G to D, a reduction in the Fe (BCC) constituents can be perceived as we move closer to the region unaffected by the steel elements (region D). The morphologies of the Fe constituents in regions D and E are of a dendritic type and a globular type in regions F and G.

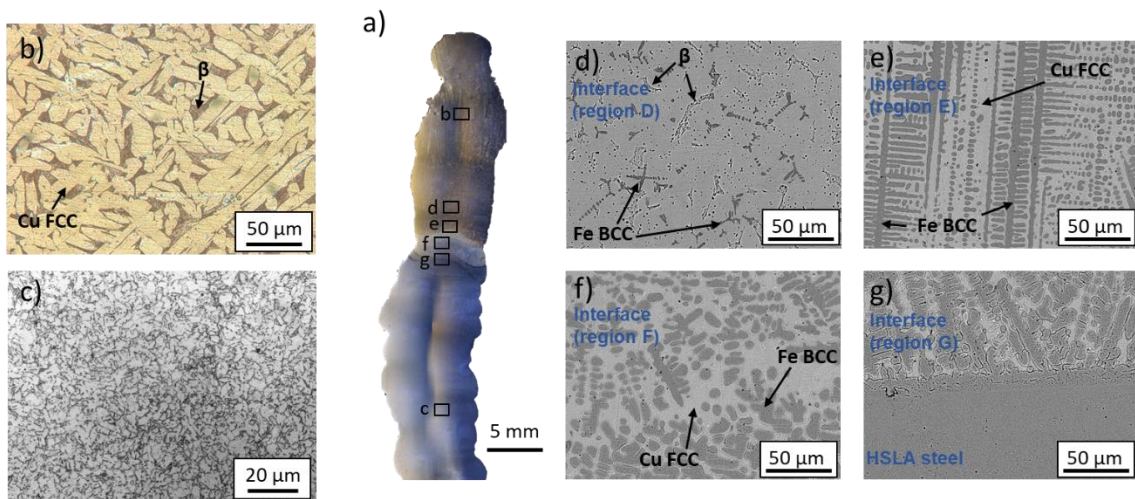


Figure 6.2 - a) Cross-section overview of the as-built FGM part; Detail of the region with: b) 100% HSLA steel, c) 100% Cu-Al alloy, d), e), f) and g) interfacial regions.

6.2.2.2 Synchrotron radiation measurements

Figure 6.3 details the synchrotron X-ray diffraction patterns taken from the cross-section of the FGM. The diffraction patterns reveal that the HSLA steel region is composed of Fe (BCC) and Fe (FCC), corresponding to ferrite and austenite. In the Cu-Al alloy region, a mixture of several crystalline phases, including Cu (FCC), AlCu₃ (D0₁₉), Al₄Cu₉ (γ_1), and AlCu₃ (β), are observed. At the joining interface, no intermetallics were found. The main phases of each alloy were observed in the diffraction patterns obtained from the interfacial region: Fe (BCC), and Fe (FCC), together with Cu (FCC). This result agrees with the interface micrographs previously depicted in Figure 6.2 d), e), f), and g), where no other intermetallics were discernible at this location. This result indicates that these two alloys used can be used together with GTAW-based WAAM without the appearance of potentially undesirable phases in the bonding area.

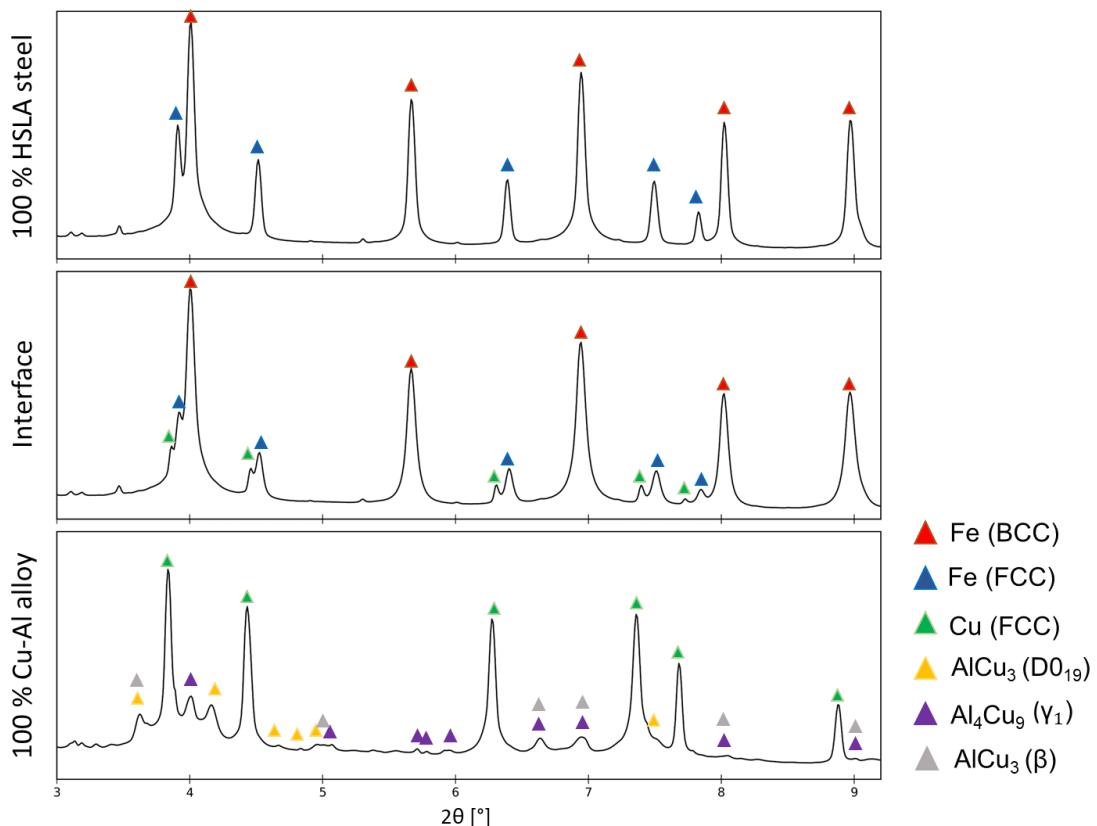


Figure 6.3 - Synchrotron X-ray diffraction analysis performed in regions comprising only HSLA steel, Cu-Al alloy, and the interface (region E, previously depicted in Figure 6.2 e).

6.2.2.3 Scanning electron microscopy analysis

The results of the elemental mapping compositions measured by SEM-EDS in the region of HSLA steel, Cu-Al alloy, and at the interface are given in Figure 6.4, Figure 6.5, and Figure 6.6, respectively.

The content in the steel region is mainly composed of Fe, but Mo and Ni were also measured (refer to Figure 6.4 b,c). The EBSD map along the build-up direction (Figure 6.4 d) revealed a near-equiaxed microstructure at the HSLA steel region of the FGM, unlike the typical columnar grains found during WAAM of other engineering alloys [186]. Such equiaxed grains are commonly seen in WAAM of HSLA steel [12] and are a consequence of the solid solution transformations of Fe (FCC) to Fe (BCC).

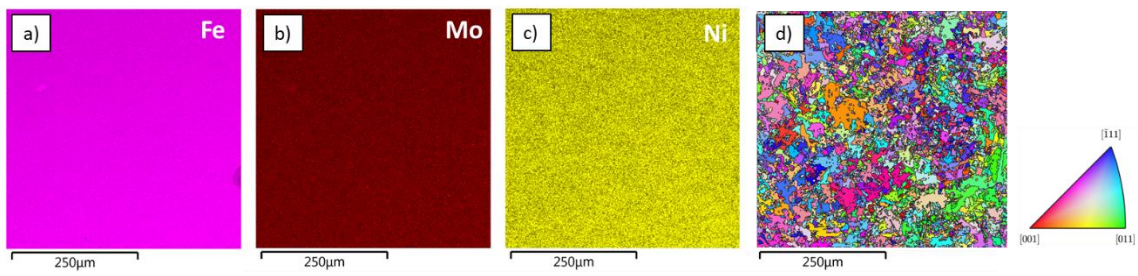


Figure 6.4 - Energy-dispersive X-ray spectroscopy (EDS) mapping of the as-built HSLA steel region: a) Fe; B) Mo, c) Ni, d) Electron Backscatter Diffraction (EBSD) inverse pole figure.

EDS measurements in the Cu-Al base material (Figure 6.5) revealed compositional changes between the β -phase and the remaining Cu (FCC) matrix. Besides Cu and Al, the Cu-Al wire also has a considerable amount of Fe (0.8 wt%) in its composition. Therefore the quantity of these three elements was evaluated. A reduction in the amount of Cu along the grain boundaries (Figure 6.5 a) was found, contrasting with the larger amount of Fe which migrated to these regions during solidification (Figure 6.5 c). Al was found in higher amounts within the β regions (Figure 6.5 b) and depleted at the Cu (FCC) regions. This is a consequence of the precipitation of Al-rich (Al_4Cu_9) in the β (AlCu_3) regions, which are Al-rich regions. At higher magnification, it is possible to observe the existence of different precipitates inside the β regions (Figure 6.5 d). The EDS scan line across the β regions (Figure 6.5 e) showed a decrease in the Cu content and an increase in the Al, as the stoichiometry of these regions follows the composition of the constituents identified by X-ray diffraction (Al_4Cu_9). EBSD mapping of the Cu-alloy (Figure 6.5 f) shows equiaxed grains without any preferential orientation.

Although SEM-EDS is a semi-quantitative analysis technique, it still enables the evaluation of the tendency of the element's distribution along the interface region of the FGM part. Figure 6.6 presents two EDS maps taken at the interfacial area. Figure 6.6 a), b), and c) depict the first EDS map scan between the interface region G and the HSLA-steel. No Cu and Al were found in the HSLA-steel section. However, both are present in region G, previously identified by a mixture of Fe (BCC) with Cu (FCC) constituents at the intercellular regions (refer to Figure 6.2 g). In contrast, the amount of Fe decreases in the interfacial area when Cu and Al start to blend in with the steel. In the second EDS map scan (Figure 6.6 d, e, and f), taken from the interface between regions E and F (refer to Figure 6.2 e,f), an inverse relationship between the amount of Fe and Cu can be perceived, i.e., with the increase in the amount of Cu (as we move closer to the region of 100 % Cu-Al alloy), the amount of Fe decreases.

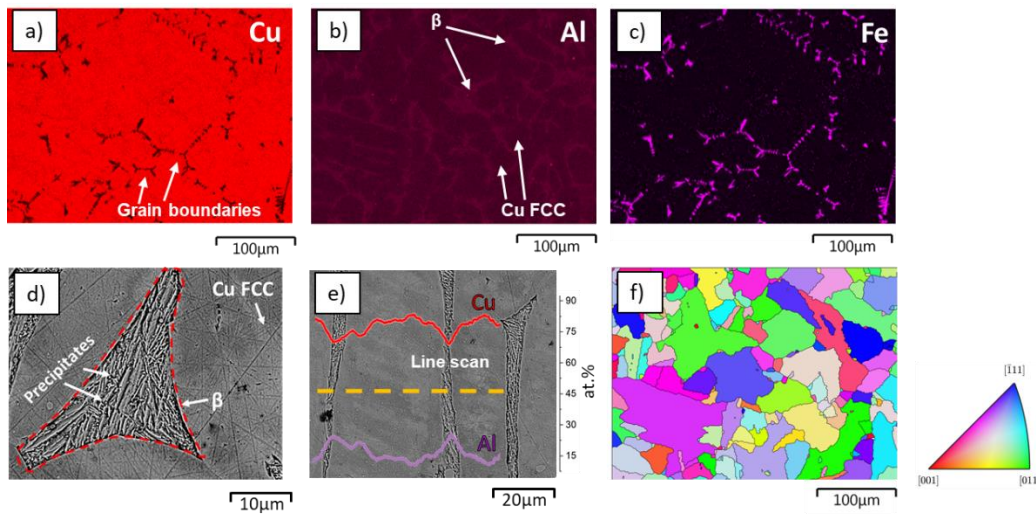


Figure 6.5 - Elemental mapping of the as-built copper microstructures obtained by scanning electron microscopy coupled with energy dispersive X-ray spectrometry (SEM-EDS): a) Cu, b) Al, c) Fe; d) Scanning electron microscopy (SEM) image of the secondary phases and precipitates found in the as-built copper alloy; e) EDS line scan across Cu-based alloy secondary phases; f) EBSD orientation maps.

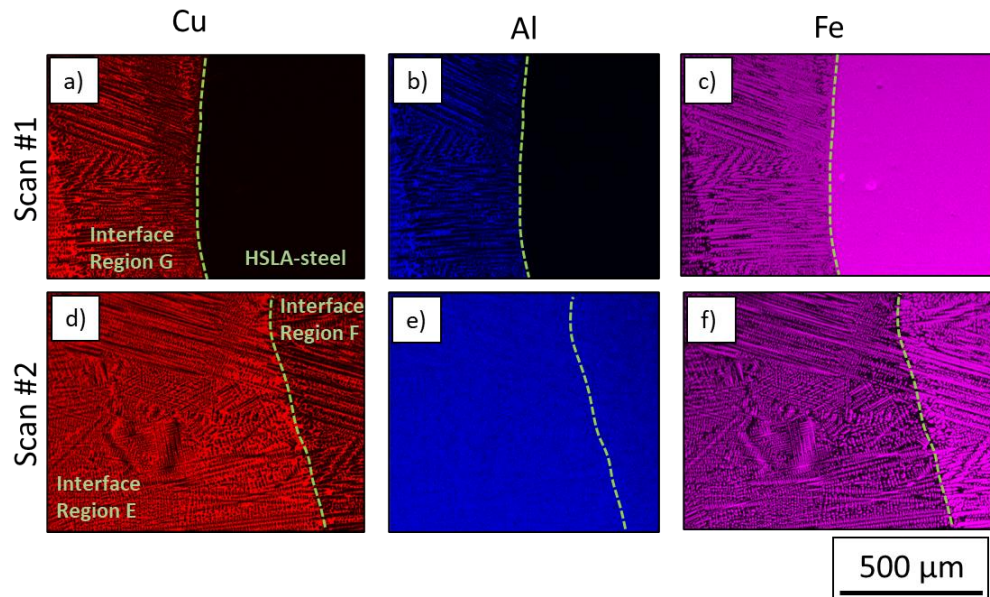


Figure 6.6 - EDS mapping of the HSLA-steel to Cu-Al interface region analysis: Scan #1: a) Cu, b) Al, c) Fe; Scan #2: d) Cu, e) Al, f) Fe.

Figure 6.7 a) depicts an EBSD phase map taken at the FGM interface. The region of HSLA steel is mainly composed of small equiaxed grains of BCC-type (Ferrite). At the same time, the interface shows a columnar-dendritic microstructure, highly oriented perpendicularly to the fusion line. Moreover, the coarse elongated grains are of BCC-type, indicating an incomplete transformation of δ -ferrite to γ . Higher magnification SEM images in the interface region (Figure 6.7 b,c) revealed that

the Fe (BCC) constituents in the HSLA steel and the interface regions have different morphologies. In the region of the HSLA steel, it was observed the presence of MA (Martensite-Austenite) constituents and α -ferrite. In the interface region, the elongated Fe-dendrites are δ -ferrite. EDS point analysis (Figure 6.7 d) was conducted to determine the chemical composition of the Fe and Cu constituents in the interface region. It was determined that δ -ferrite contains up to 11 % of Cu, and the Cu (FCC) constituents hold up to 5% of Fe. This change in the composition of the Fe constituents might be responsible for hindering the complete transformation of δ -ferrite during solidification.

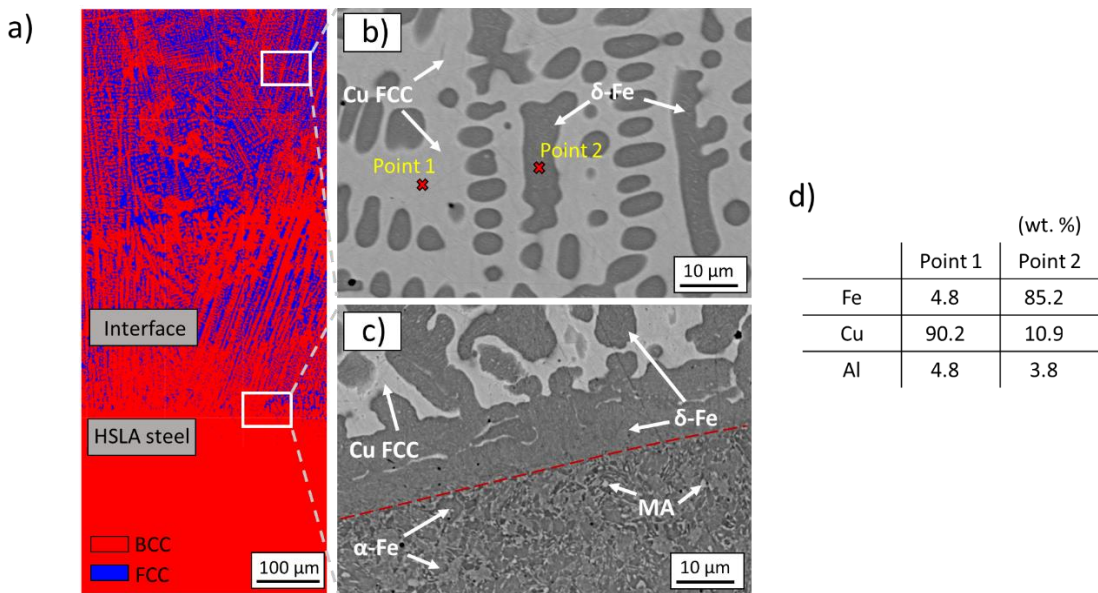


Figure 6.7 - a) EBSD phase mapping of the interface region; b) SEM morphologies of δ -ferrite in a Cu FCC matrix; c) SEM morphologies of MA constituents in an α -Fe matrix; d) EDS point analysis at positions marked in b). MA: Martensite-austenite.

6.2.2.4 Hardness, electrical conductivity, and electrical impedance measurements

Figure 6.8 depicts the hardness measurements along the height of the FGM. A good agreement exists between the macrograph presented in Figure 6.2 a) and the hardness measurements. In particular, the region identified as being only composed of HSLA-steel (height < 15 mm) has an average hardness of 250 HV. As we move closer to the interface region, the hardness decreases to 197 HV, approximately. This decrease was attributed to increased Cu content and the α -Fe (BCC) grain size near the interface. The Cu-alloy layers were deposited with higher energy than the steel layers, reducing the cooling rate and promoting larger polygonal α -ferrite to form and grow. In region G, the hardness drops to around 180 HV. This result is associated with the change of HSLA steel constituents from polygonal α -ferrite + MA islands to a majority of coarse dendritic δ -ferrite. The slight hardness increase to 200 HV in regions F and E was attributed to the dual-phase microstructure (δ -Ferrite + Cu (FCC) constituents) and its multiple iterations, similar to what occurs in duplex stainless

steel [187–189]. Towards the end of the interface, a smooth hardness transition exists due to the continuous decrease in the amount of Fe (BCC constituents). This gradual hardness transition agrees with the SEM images previously depicted in Figure 6.2 d), e), f), and g), which depicts a gradual variation in the number and size of Fe (BCC) constituents along the interface region, and the inexistence of high hardness constituents (e.g., martensite), characteristic of dissimilar welding [190–192].

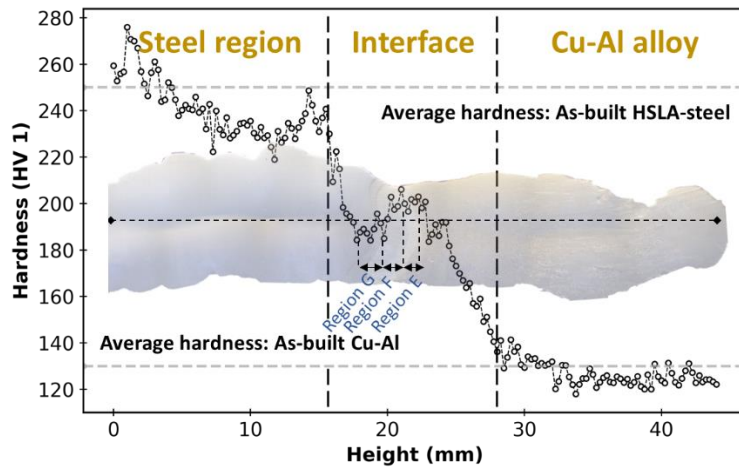


Figure 6.8 - Hardness measurements taken from the substrate to the last deposited layer of the FGM cross-section.

The electrical conductivity and electrical impedance measurements are presented in Figure 6.9. In the steel region, the electrical conductivity is, on average, 5.2 % IACS and increases to 11.1 % IACS in the region that is only composed of Cu-Al alloy. Both techniques used to characterize electrical properties are very sensitive to the amount of each alloy, which allows quantifying the extension of the interfacial region. With these techniques and hardness measurements, a length of 12 mm was measured for the interface region. This large interface region is due to the diffusion of elements between both materials that occurs during the deposition of subsequent layers and is not confined between the last steel and first Cu-Al alloy deposited layers.

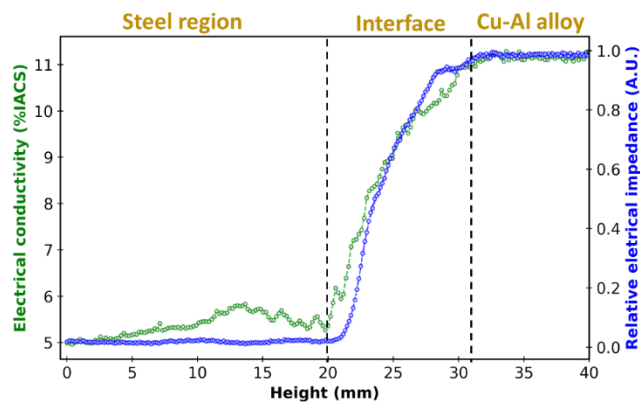


Figure 6.9 - Electric conductivity and electrical impedance measurements taken from the first to the last deposited layer of the FGM cross-section.

6.2.2.5 Uniaxial tensile testing

Representative stress-strain curves of both single HSLA steel, Cu-Al, and FGM samples are detailed in Figure 6.10. It can be observed that the tensile strength of the HSLA-steel is significantly higher than the Cu-Al alloy base material (753 vs 502 MPa). The elongation to fracture between the base materials is higher in the Cu-Al alloy (35.2 vs 24.6 %). As for the FGM part, it can be observed that the tensile strength is between that of the two base materials (690 MPa), while the fracture strain is lower than both base materials (16.6 %). The fracture surface of the functionality graded material indicates a mixture of a ductile-like fracture, with dimples, and a quasi-cleavage type fracture, with cleavage facets (Figure 6.10 b). The fracture surface of the control HSLA steel sample is mainly composed of dimples, indicating a ductile-like type of fracture (Figure 6.10 c). The fracture appeared on the Cu-Al side in region D (refer to Figure 6.2 d) in all tested samples taken from the FGM. As for the as-built Cu-Al alloy (Figure 6.10 d), SEM images show a predominant existence of dimples with small regions of cleavage facets, which indicates that a ductile fracture predominantly dominates the fracture.

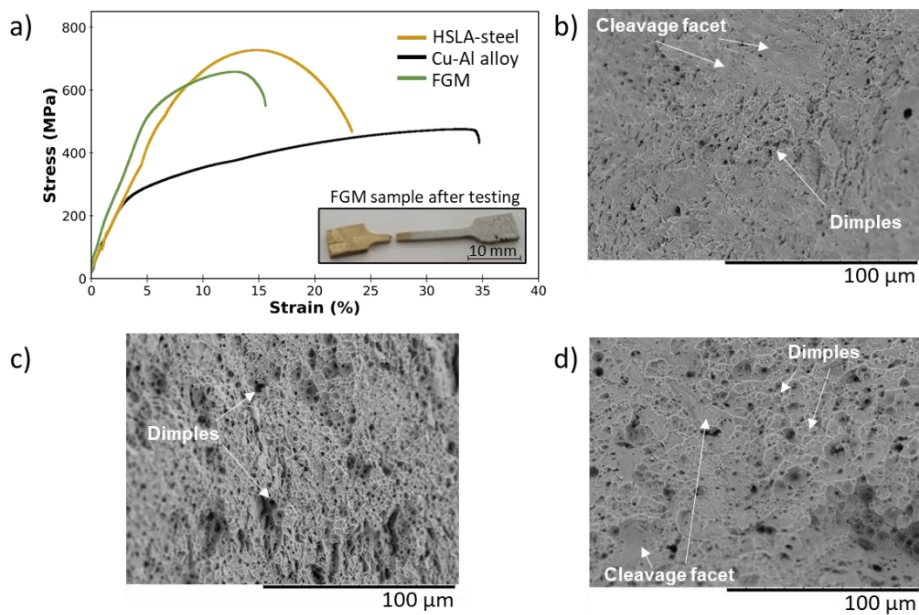


Figure 6.10 - Representative stress-strain curves of the HSLA-steel and Cu-Al alloy parts and their dissimilar multi-metallic part; SEM image of the fracture surface of b) Functionality graded material; c) As-built HSLA steel; d) As-built Cu-Al alloy. Three specimens of each condition were extracted and tested.

6.2.3 Discussion

The Cu-Fe phase diagram (Figure 6.12 a) shows that joining Cu to steel is challenging. The Fe-Cu system possesses a nearly flat liquidus line. Therefore, a submerged miscibility gap can be accessed by undercooling the melt. A large enthalpy of mixing characterizes Cu-Fe, i.e., if the melt in the interface area cools rapidly, the weld pool will undercool, causing a separation of the liquid phase into a Fe-rich melt (L1) and Cu-rich melt (L2). Thus, leading to solidification below the liquid metastable miscibility gap. In the binary Cu-Fe phase diagram, the position of this miscibility gap is right below the liquidus line.

Consequently, small undercooling is sufficient to promote this separation of liquid phases [193]. After the liquid-phase separation, both liquid phases are in an undercooled state. Thus, the L1 (Fe-rich) phase solidifies as the leading phase since it will be the phase possessing a higher undercooling, which will be the preferential nucleation site [170]. Based on the Cu-Al binary phase diagram (Figure 6.11 b) it can be perceived that the depletion of Al content in the Cu FCC constituents located at the interface region (refer to Figure 6.7), from 8.5 wt.% in the Cu-Al alloy down to 4.8 wt.%, resulted in a change in the alloy composition, which prevents the solidification reaction liquid → β, leading to the absence of solid-state transformations. This fact corroborates the non-existence of β and other phases in the regions E, F, and G since the liquid directly transforms to Cu-FCC.

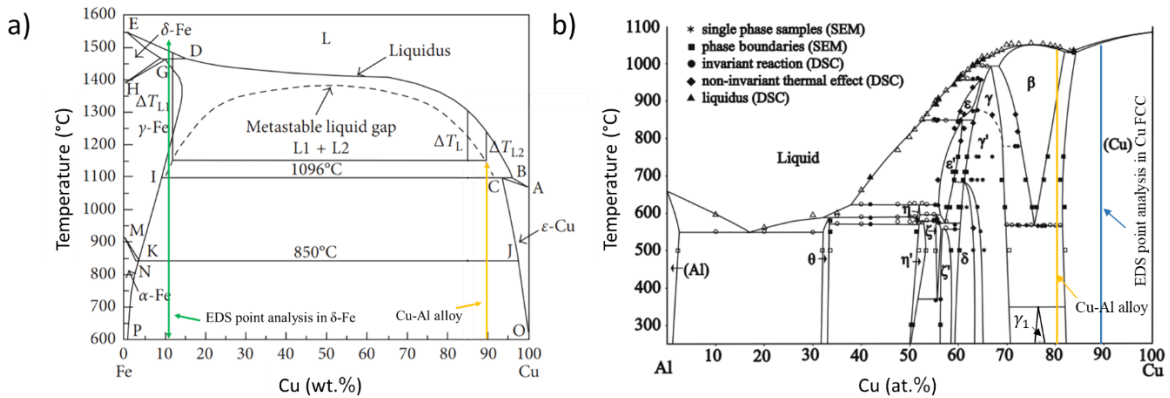


Figure 6.11 - Cu-Fe Phase diagram with the metastable miscibility gap (dotted curved line) (adapted from [194]), pointing to the composition of the δ -Fe constituent; b) Cu-Al binary phase diagram highlighting the composition in the Cu-FCC constituents in the interface (adapted from [195]).

In the SEM images (Figure 6.2 d, e, f, g), the Cu and Fe solute distributions at the interface are visible, without forming Fe-rich or Cu-rich spheres that would form if the material entered the metastable miscibility gap [196]. The existence of highly aligned Fe columnar dendrites (EBSD, Figure 6.7 a) also suggests that the melt at the interface did not experience sufficient undercooling to enter the metastable liquid miscibility gap, resulting from the normal liquid-solid phase transformation [197]. Due to a low ΔT before nucleation, the δ -ferrite (Fe-BCC) in the interface region is the first to solidify without entering the metastable miscibility gap. Then, the Cu-rich region (FCC) will solidify due to the continuous solute segregation of the remaining liquid during solidification [194]. Following, around 800-900 °C, the Fe (BCC) will experience transformation into Fe (FCC). Similar behavior has been found in the literature, where the mixture of a Fe with a Cu alloy did not enter the miscibility gap [194,196]. Figure 6.12 details a thermodynamic calculation considering a conservative dissolution of only 30 % of the Cu-Al alloy in the HSLA steel. In the equilibrium phase diagram, it can be noticed that δ -ferrite does not completely transform during cooling. In addition, due to the higher cooling rate of WAAM, the δ -ferrite to austenite transformation is suppressed [198]. These results, alongside the EBSD data (Figure 6.7 a), with highly oriented columnar dendrites in the interface, corroborate the thesis that the increase of the Cu-Al content stabilized the δ -ferrite in the transition zone.

From the synchrotron X-ray diffraction measurements, different phases were revealed in the Cu-Al alloy: Cu (FCC), AlCu_3 (D_{019}), Al_4Cu_9 (γ_1), AlCu_3 (β). These results are in good agreement with the SEM image of the Cu-Al base material (Figure 6.5) since Al was found in higher quantity within the β (AlCu_3) regions. When the X-ray beam was focused on the interface area, the intermetallics of the Cu-Al base material (AlCu_3 (D_{019}), Al_4Cu_9 (γ_1), AlCu_3 (β)) were not found, and neither Cu-Al-Fe nor Fe-Al intermetallics, as found in others studies [199,200]. Nevertheless, in region D, far from the last deposited steel layers, both AlCu_3 (β) and Fe (BCC) phases were found, but in small quantities.

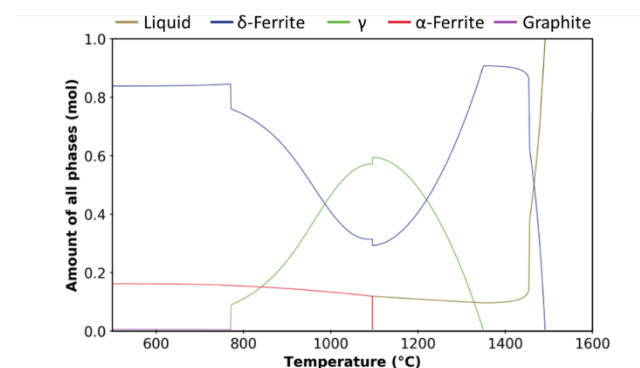


Figure 6.12 - Calculated equilibrium phase diagram considering an alloy with 70 % of the HSLA steel and 30 % of the Cu-Al alloy elements (wt.%) in the molten pool.

Tensile test specimens' fracture occurred on the Cu side near the interface region with two distinct fracture modes: ductile-like and quasi-cleavage fracture. The fact that the FGM part had less elongation to fracture than both base materials indicates that these have a larger deformation ability than the material near the interface, which cannot maintain high strain. This behavior is related to this region microstructure (Figure 6.2 d and e), which combines a dendritic-type structure of Fe phases and β precipitates in a Cu matrix. The incoherent microstructures can create several potential crack nucleation and propagation points, decreasing the ductility near the interface. Despite this, the absence of a hardness peak in the interface region allowed considerable ductility (16.6 %). The increase in the tensile strength compared to the Cu-Al base material is attributed to the Fe-constituents mixed in the Cu matrix. During the tensile testing, the stresses will be first accommodated by the softest material (Cu-Al). The stress will be transferred to a harder and more brittle region, and deformation will no longer be possible from that point on, resulting in the fracture surface as depicted in Figure 6.10 b). These results confirmed that with WAAM, an effective soft transition from HSLA-steel to Cu-Al alloy is possible, without defects and with excellent strength and ductility.

6.2.4 Conclusions

In this section, an HSLA-steel to copper-aluminum alloy functionally graded material was fabricated using the twin-wire and arc additive manufacturing (T-WAAM) technique. The FGM revealed no defects and had excellent strength and ductility in the interface. The major conclusions can be drawn:

- A mixture of Cu (FCC) and Fe (BCC) phases was visible in the interface region by scanning electron microscopic analysis. These Fe (BCC) phases were found to be residual δ -ferrite by EDS, thermodynamic calculation, and EBSD;
- Synchrotron X-ray diffraction measurements showed no brittle intermetallic phases in the interface;
- A gradient of composition, hardness, electrical conductivity, and electrical impedance was obtained at the interface. Even though an abrupt transition was made with these two

materials, the consequent remelting and heating of previously deposited layers, when a new one is added, resulted in a large interface region (≈ 12 mm). This fact demonstrates the potential of WAAM to be used for FGM's fabrication;

- Ultimate tensile strength of 690 MPa and an elongation at fracture of 16.6 % were achieved in the FGM, thus allowing the use of such components in structural applications. The fracture occurred in the Cu region near the interface, in which the microstructure involves a combination of a dendritic-type structure of Fe (BCC) phases and β precipitates in a Cu matrix, demonstrating that the interface strength is higher than the only copper region.

6.3 Stainless steel 316L to Inconel 625

6.3.1 Materials and design

The stainless steel 316L to Inconel 625 FGM was made using AWS A5.9 ER 316LSi (stainless steel 316L) and AWS ERNiCrMo-3 (Inconel 625) welding wires, whose composition can be found in section 3.6.1. The GTAW power source and the multiple-wire feed system presented in sections 3.2 and 3.5 were used for these experiments. The process parameters are detailed in Table 6.2. The fabricated parts were single walls, 130 mm in length, and the current was set at 65 A for every layer of each sample. Preliminary parameter selection enabled to obtain process parameters that resulted in a similar height and width for both materials. The starting point for the determination of the process parameters was made based on the recommendations provided by the welding wire supplier. An interpass temperature between 100-150 °C was used and controlled with a pyrometer, as this range of temperature results in a more stable and repeatable shape of the deposit, with less waviness [184].

Table 6.2 - Process parameters used to fabricate the different FGMs.

Process	Gas tungsten arc welding (GTAW)
Travel speed	120 mm/min
Wire feed speed	1 m/min
Current	65 A
Shielding gas	Argon 99.99 %
Shielding gas flow rate	16 L/min

The previously mentioned process parameters were used to fabricate the following samples: (i) A 40-layers sample of stainless steel 316L (as-built Stainless Steel, Figure 6.13 a); (ii) A 40-layer sample of Inconel 625 (as-built Inconel, Figure 6.13 b); (iii) An FGM with a direct interface of 20 layers of 316L stainless steel to 20 layers of Inconel 625 (FGM 100-100, Figure 6.13 c); (iv) An FGM with a direct

interface of 20 layers of 316L stainless steel to 20 layers of Inconel 625 subjected to a heat treatment of 1050 °C for 2 hours + air quenching (FGM 100-100 HT, Figure 6.13 d); (v) An FGM with a smooth transition (FGM 5; Figure 6.13 e), i.e., 15 layers of 316L stainless steel, 19 layers mixing the filler wires made in steps of 5 wt.% at each layer, and 15 layers of Inconel 625; (vi) An FGM with a smooth transition achieved in steps of 5 layers and compositional changes of 20 wt.% (FGM 20, Figure 6.13 f); (vii) smooth FGM created to avoid unwanted secondary phases in the mixing zone (FGM 90-10 Figure 6.13 g), i.e., the transition between materials is made between a weight percentage of 90 wt.% 316L stainless steel to 90 wt.% Inconel 625. Samples (i) and (ii) were used to benchmark 316L stainless steel and Inconel 625, respectively.

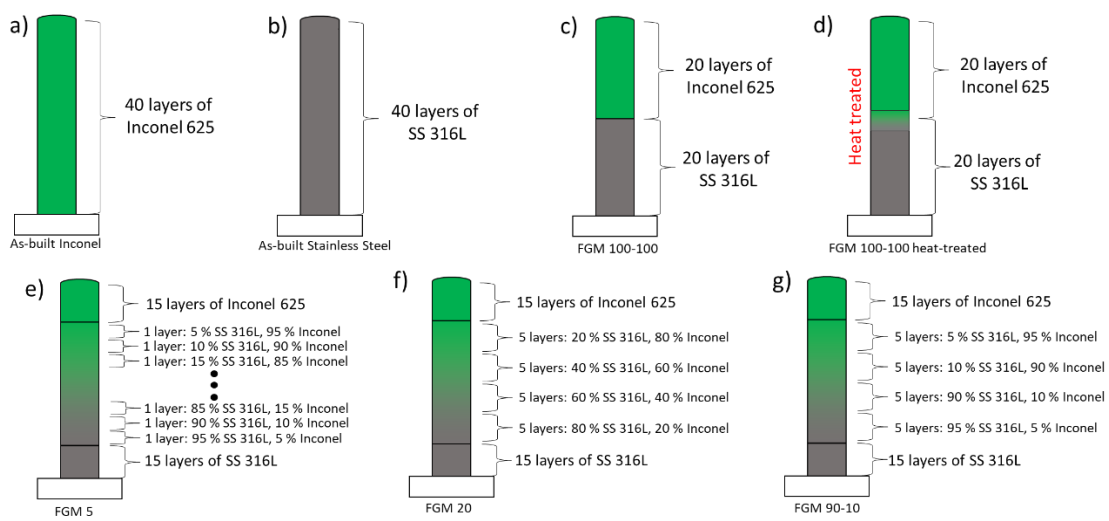


Figure 6.13 - Build strategies employed to fabricate different FGMS: a) and b) As-built control samples of Inconel 625 and 316L stainless steel, respectively; c) Direct interface from stainless steel to Inconel (FGM 100-100); d) Direct interface from stainless steel to Inconel with post-WAAM heat treatment of 1050 °C for 2 hours (FGM 100-100 HT); e) Smooth transition by varying the percentage of filler material within each layer in concentration steps of 5 wt.% (FGM 5); f) Smooth transition in steps of 5 layers and 20 wt.% (FGM 20) and g) Smooth transition intended to avoid undesirable phases, built-in steps of 5 layers and 5 wt.% (FGM 90-10).

The equations used to calculate the residual stresses in the principal directions are previously presented in section 3.6.6. Two lattice constants (d_0), one for the stainless steel and the other for the Inconel regions, of the stress-free condition were measured by synchrotron X-ray diffraction on the sample heat-treated at 1050 °C for 2 hours following air cooling. Young's modulus (E) and Poisson's ratio (ν) values are required for each compositional ratio. Thus, it was used 193 GPa as $E_{SS\ 316L}$ and 0.27 as $\nu_{SS\ 316L}$ when the amount of stainless steel was higher in the FGM, and 208 GPa as $E_{Inconel}$ and 0.27 $\nu_{Inconel}$ were used when the amount of Inconel was higher. Although these constants could be slightly different in the intermediate regions, when both materials are mixed, such considerations would result in marginal differences. Only vertical specimens for the tensile test were prepared and the transition between materials was exactly in the middle of the specimens.

6.3.2 Results and discussion

6.3.2.1 Macroscopic characterization

Macroscopic and higher magnification SEM images were taken at different regions of each FGM and are depicted from Figure 6.14 to Figure 6.16. Each multi-layer FGM showed good bonding between layers, with a columnar dendritic growth almost parallel to the building direction, mainly determined by the heat extraction direction. Despite the different compositional ratios tested in each sample, no evidence of cracks induced by the thermal stresses associated with the WAAM process was observed in the different transversal and longitudinal cuts made and during face milling of the parts to build tensile testing samples.

Figure 6.14 compares the microstructure between the FGM 100-100 and the FGM 100-100 HT. In the top layers (Figure 6.14 b, c, f, and g), the microstructure mainly consists of a Ni-FCC matrix solidified in a columnar-dendritic mode. The mixture region of sample 100-100 (Figure 6.14 d) microstructure is of columnar dendritic type with segregants embedded in the interdendritic regions, as marked by blue arrows.

The changes in the microstructure depicted in Figure 6.14 d) in comparison with Figure 6.14 c) are due to the complex cyclic thermal history during deposition which resulted in elemental migration in the interface. According to Silva et al. [201], the increase in the Fe content (transition zone; interface) enhances the interdendritic segregation of Mo and Nb (reducing the partition coefficient), which favors the formation of Laves phase in the interdendritic regions (eutectic transformation) corroborating the observed results. Due to the participation of Ni, the solidification mode was altered from FA to A and no evidence of δ -ferrite was observed at the interface. It is worth noting that the Laves phase content should be minimized since it can reduce the material ductility and corrosion resistance [202,203]. By performing PWHT, partial dissolution of the eutectic phases into the matrix occurred, which can be observed in Figure 6.14 f), g), and h) in comparison with Figure 6.14 b, c), and d). In the bottom regions corresponding to the 316L stainless steel (Figure 6.14 e and i), the bright regions correspond to austenite (γ) while the dark areas are retained δ -ferrite. The stainless steel feedstock wire in this work has a $\text{Cr}_{\text{eq}}/\text{Ni}_{\text{eq}}$ ratio of 1.69 and, which considering the WRC-1992 constitution diagram corresponds to a ferritic-austenitic (FA) solidification mode (Liquid \rightarrow Liquid + δ \rightarrow Liquid + δ + γ \rightarrow δ + γ) [97]. Still, in the sample that underwent heat treatment, the amount of δ -ferrite constituents decreased as they were dissolved into the matrix.

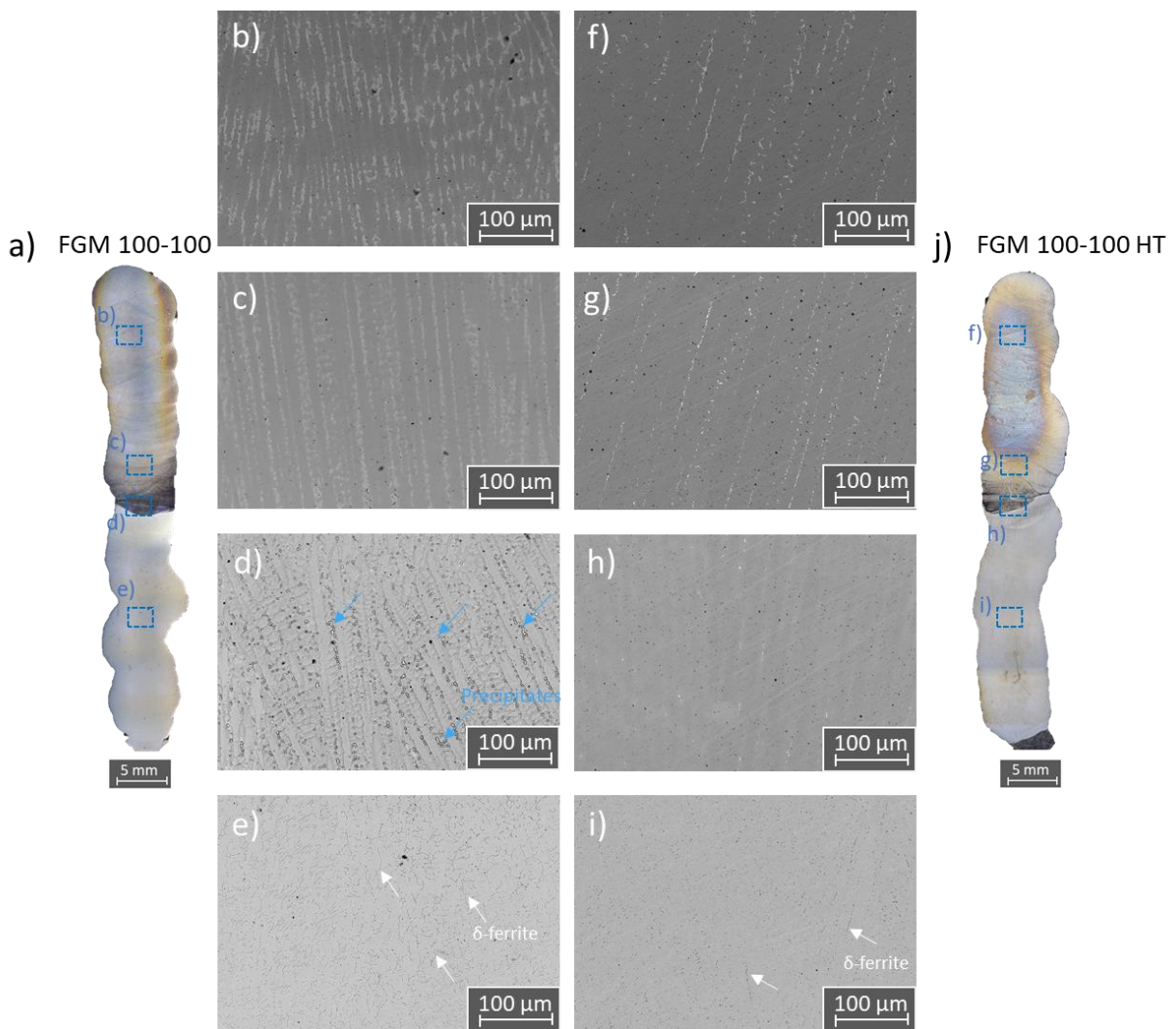


Figure 6.14 –Comparison of the cross-section overview of the samples built with a direct interface with and without heat treatments, respectively, (FGM 100-100 (a), FGM 100-100 HT (j)); Details of the regions with: (b),(c),(f) and (g) 100 wt.% Inconel 625, (d) and (h) interfacial region, and (e) and (i) 100 wt.% 316L Stainless steel.

The microstructure at six different locations of the FGM 90-10 designed to avoid undesirable concentrations is illustrated in Figure 6.15. In the range of 0 to 10 wt.% of stainless steel, the microstructure is mainly composed of columnar dendrites without secondary arms (Figure 6.15 b,c). At interface #1 (Figure 6.15 d), a unique microstructure of columnar dendrites with secondary arms with precipitates in the interdendritic regions is presented. In interface #2 (refer to Figure 6.15 e), the sudden microstructure changes from dendritic-type to the typical microstructure found in the stainless steel areas can be visible. From this point on, down to 100 wt.% of stainless steel light areas are austenite, and dark are δ-ferrite.

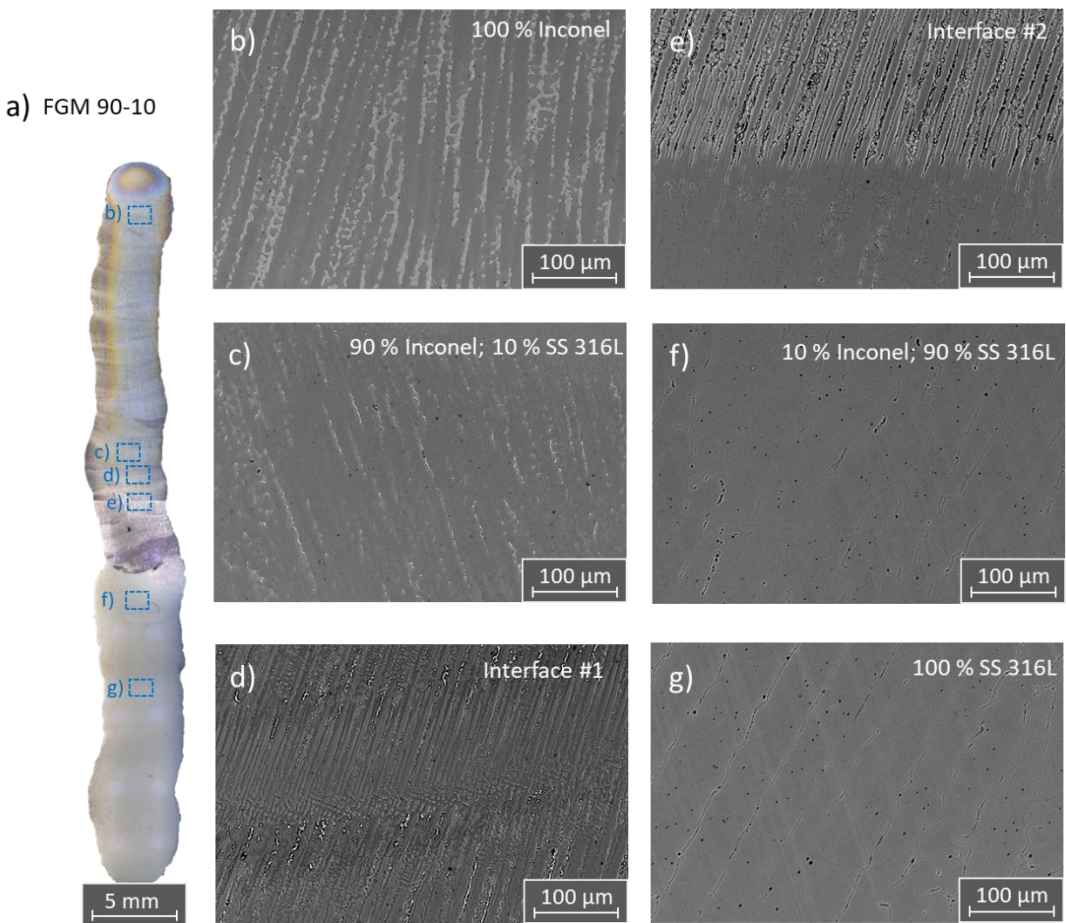


Figure 6.15 - a) Cross-section overview of the FGM 90-10 built to avoid unwanted concentrations; Detail of the region with: b) 100 wt.% Inconel, c) 90 wt.% Inconel, d) interface region #1, e) interface region #2, f) 10 wt.% Inconel and g) 100 wt.% 316L Stainless steel.

The microstructure of the FGM made in compositional steps of 5 wt.% is detailed in Figure 6.16. It can be perceived a gradient of microstructures without sudden/abrupt changes, in the range of 0 to 15 wt.% of stainless steel (Figure 6.16 b to d), the microstructure resembles that of as-built Inconel 625, which presents dendrites (white features) aligned with the build direction in a γ -matrix. From 35 to 55 wt.% of stainless steel (Figure 6.16 e to g), the microstructure contains dendrites with some precipitates inside both primary and secondary arms. When the stainless-steel composition increases to 75 wt.% (Figure 6.16 h), still no δ -ferrite was found, but it is visible the presence of other precipitates. Regions with more than 85 wt.% of stainless steel (Figure 6.16 h to j) presented δ -ferrite dendrites as dark regions in an austenite matrix. The precipitates at different locations of the FGM will be further discussed, considering the synchrotron X-ray diffraction analysis performed at the same locations. From the pseudo-binary diagram of stainless steel with 70 wt.% Fe (refer to Figure 6.17), it can be perceived that below a weight percentage of 90 wt.% of stainless steel, assuming a homogeneous composition, the FGM microstructure is expected to be depleted of δ -ferrite.

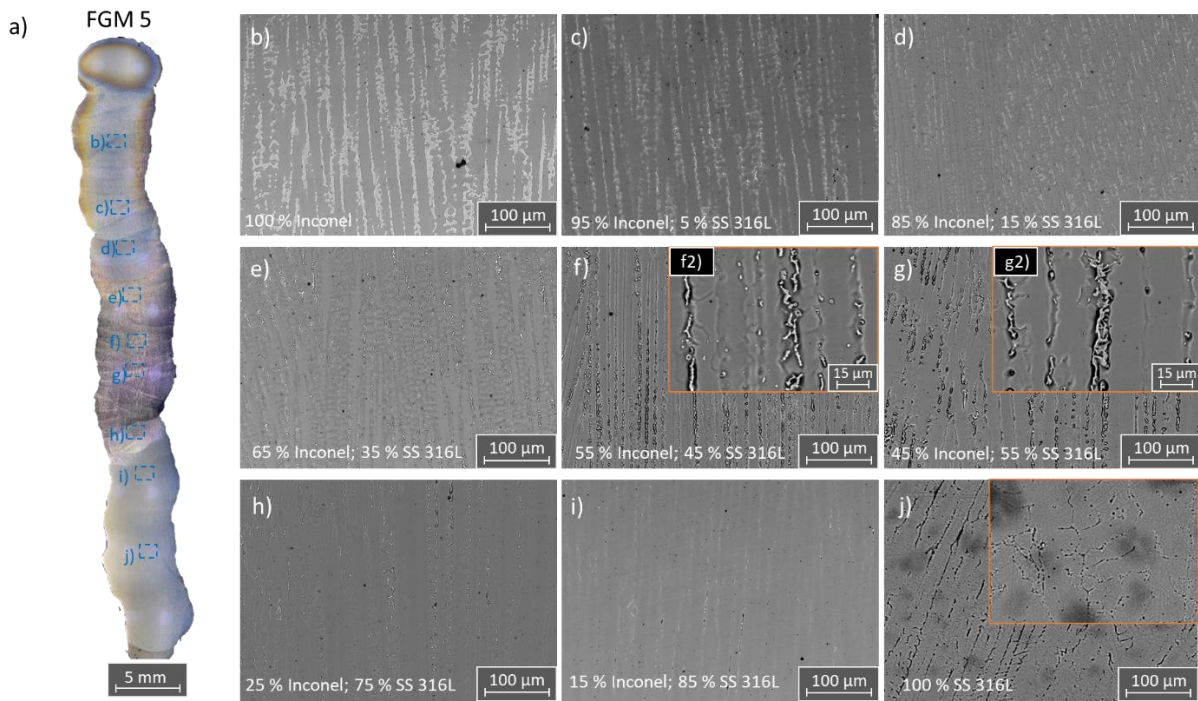


Figure 6.16 - Microstructure of the: a) Cross-section of the FGM made in weight percentage steps of 5% (FGM 5); Details of the region with: b) 100 wt.% Inconel, c) 95 wt.% Inconel, d) 85 wt.% Inconel, e) 65 wt.% Inconel, f) 55 wt.% Inconel, g) 45 wt.% Inconel, h) 25 wt.% Inconel, i) 15 wt.% Inconel and j) 100 wt.% 316L Stainless steel.

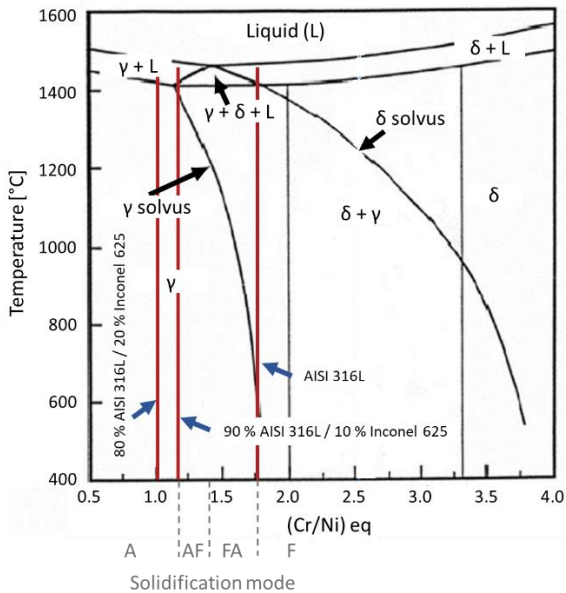


Figure 6.17 - Pseudo-binary FeCrNi diagram (adapted from [204]).

After surface finishing, cracks of hundred microns in length were found in a region of 40 wt.% stainless steel in the sample FGM 20 (Figure 6.18). These features might be attributed to the deposition

strategy used, which repeated the deposition of the same compositions (5 layers for each compositional ratio) to obtain the FGM. Near the cracks, several carbides were found due to the excess carbon in these regions, which might be the primary cause of failure.

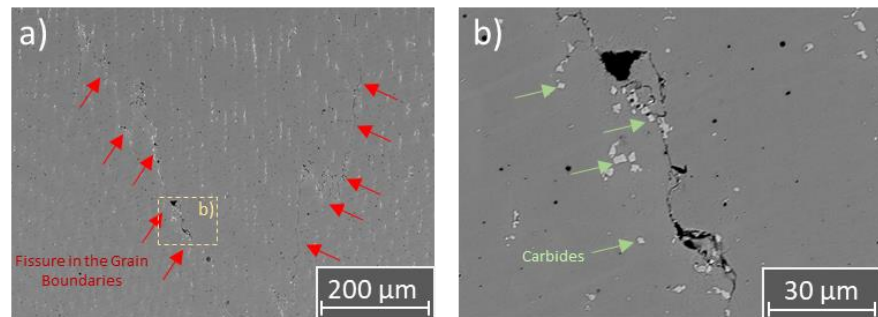


Figure 6.18 - Cracks in sample FGM 20 in the region containing 60 wt.% Inconel and 40 wt.% Stainless steel.

The calculated $\text{Cr}_{\text{eq}}/\text{Ni}_{\text{eq}}$ ratio as a function of the weight percentage of stainless steel 316 is shown in Figure 6.19 in steps of 5 wt.% with the corresponding solidification mode. The red region marks the hot-cracking region where the cracking occurred in the sample designated as FGM 20. According to the literature, the dashed lines with the stainless steel's solidification modes were drawn [205]. Several authors attribute the main cause for micro-fissures during the deposition of superalloys to the constitutional liquation of the Nb-rich Laves phase and carbides caused by fast cooling, which does not allow sufficient time for dissolution of the secondary phases within the matrix to occur [206]. Laves and carbides will form at the final steps of solidification, having lower melting points, and broadening the solidification range. During a subsequently deposited layer, these eutectic products will have their temperature increased, and some of them might melt. This melting follows the inherent residual stresses imparted by the material due to the non-equilibrium heating and cooling conditions that make liquation cracking prone. The material was more prone to cracks in a region with a compositional ratio between 40-70 wt.% of Inconel, since the amount of impurity elements (such as MC carbides and Laves) increases in those regions and accumulate along the inter-dendritic spaces.

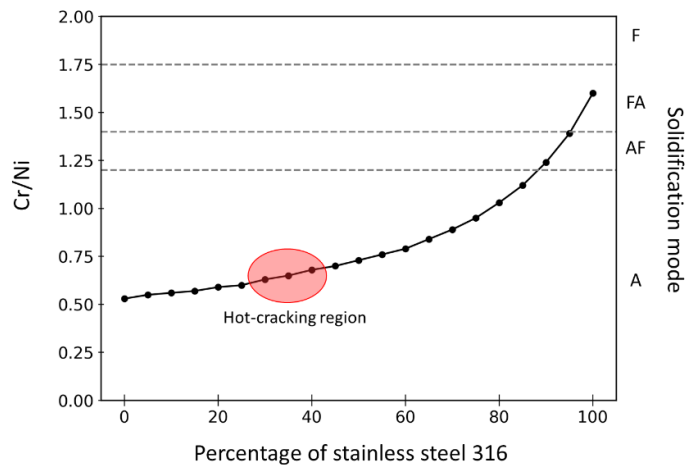


Figure 6.19 - Representation of the $\text{Cr}_{\text{eq}}/\text{Ni}_{\text{eq}}$ ratio of the region where the fracture at sample FGM 20 was found.

6.3.2.2 Synchrotron X-ray diffraction measurements

The synchrotron X-ray diffraction measurements performed in the FGM 100-100 and FGM 100-100 with heat treatment are compared in Figure 6.20. Both samples displayed FCC austenite (γ) as the primary phase, but both base materials had different secondary phases. The Inconel 625 regions presented γ' , γ'' , MC carbides, and Laves phase, while the stainless steel has both δ -ferrite and σ -phase. In the middle region, where the two materials are mixed, no other phases were discernible besides those already identified in the base materials. The heat treatment allowed to reduce the overall intensity of the δ -ferrite peaks, which is an indirect measure of their volume fraction, which is in good agreement with the reduction of these constituents as detailed in the microstructures depicted in Figure 6.14.

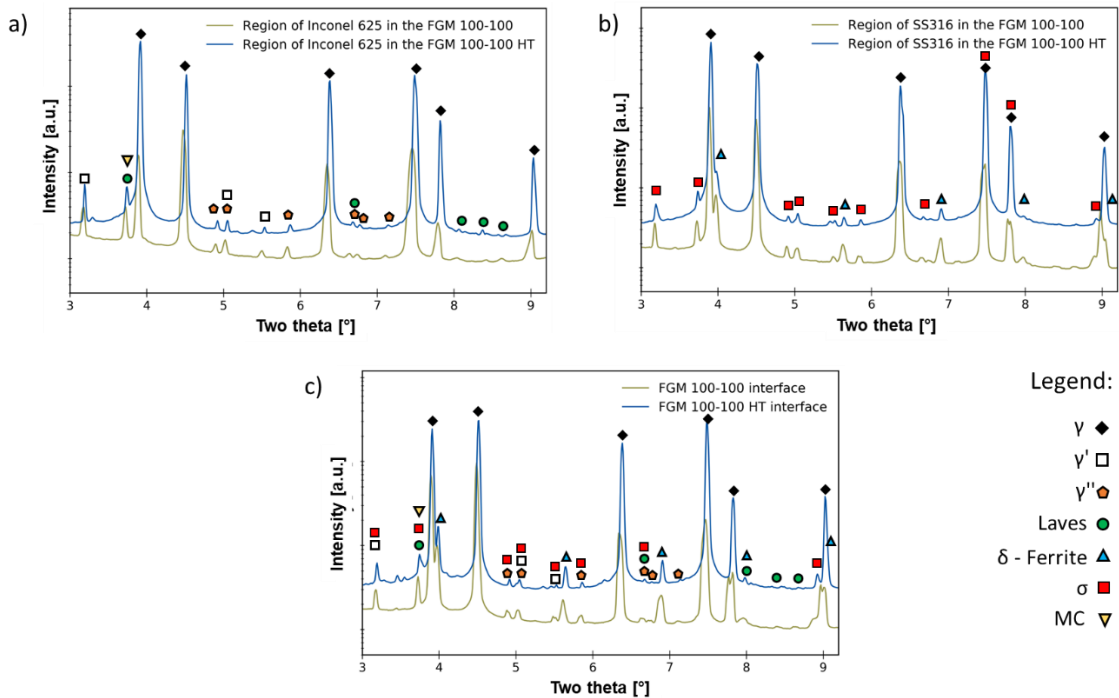


Figure 6.20 - Synchrotron X-ray diffraction analysis performed in samples FGM 100-100 and FGM 100-100 HT in regions comprising: a) Inconel 625, b) Stainless steel 316L, c) Interface.

The synchrotron X-ray diffraction measurements (detailed in Figure 6.21) in the FGM 5 (smooth-type interface) qualitative show that with the increase of Fe, new phases (δ -phase (Ni_3Nb), σ , and MC carbides) are formed between the regions with 60 to 80 wt.% of Inconel. This result is in accordance with Silva et al. [18], who found that an increase in the Fe content in Inconel 625 increases the fraction of δ -phase (Ni_3Nb) precipitates. Solidification of Inconel 625 is complex and largely dependent on the amount of each alloying element. Cieslak et al. [207] studied the influence of different elements on the solidification modes of Inconel 625 and verified that Nb significantly impacted the melting temperature range. Moreover, the solubility of Nb in the γ matrix is reduced with the increased presence of Cr, Mo, and Fe, which reduces its distribution coefficient and increases the amount of eutectic phases (especially carbides) in the interdendritic regions. The excess of Fe also favors the formation of topologically close-packed (TCP) phases, such as Laves phase during solidification with a stoichiometry rich in iron, Fe_2Nb , or Fe_2Mo [207], and the precipitation of σ -phase [155], as verified in Figure 6.21 a).

In the regions with 50 wt.% of each material, since the Inconel secondary phases (γ' , γ'' and Laves phase) diffract at the same angles as the σ -phase, it is impossible to characterize this region accurately. At 40 wt.% of Inconel, some MC carbides were observed. After that, only when the amount of Inconel was decreased below 30 wt.% δ -ferrite was present.

By removing the defective compositional ranges by designing the FGM 90-10, the concentration ratios from 80 wt.% Inconel down to 20 wt.% were avoided, and therefore no eutectic phases besides the

ones already found in the base materials were present in the interface region. This strategy also reduced the number of layers with segregants in the inter-dendritic regions, as depicted in Figure 6.15.

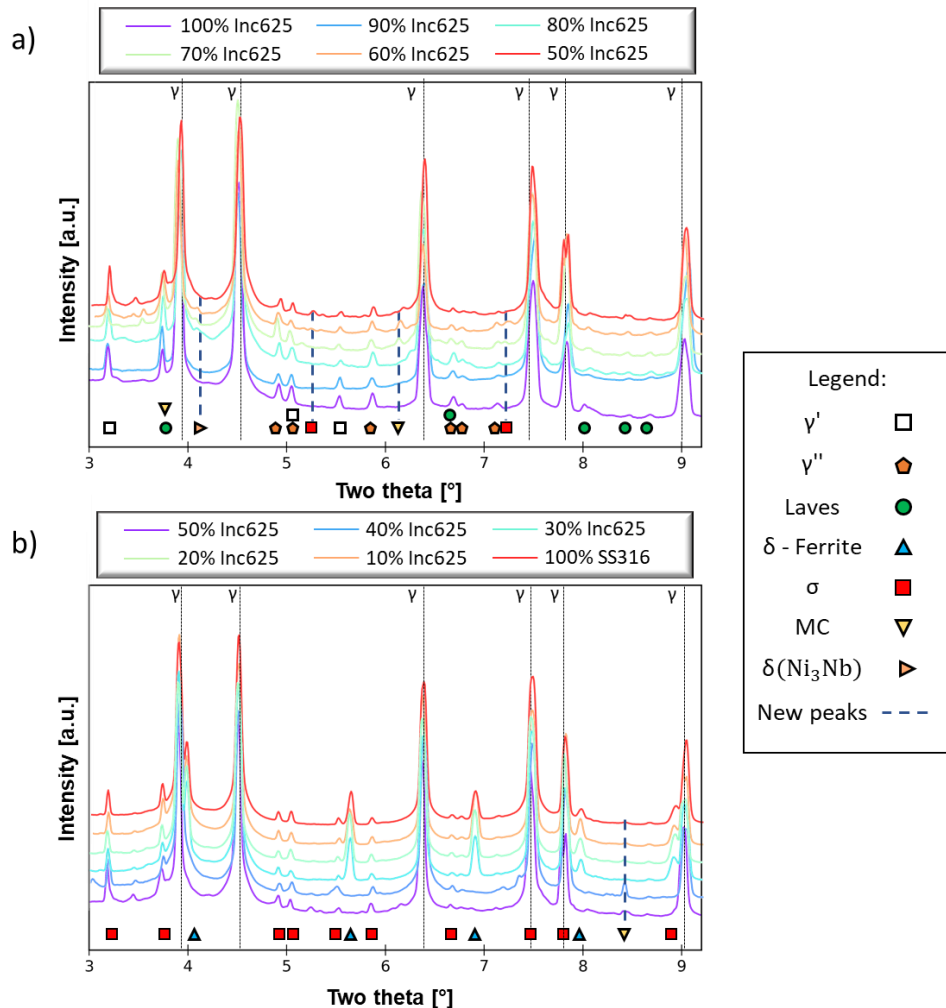


Figure 6.21 - Synchrotron X-ray measurements taken from the substrate to the last deposited layer in FGM 5.

Thermodynamic calculations considering a weight percentage of 85, 70, 60, and 50 wt.% of stainless steel were computed and are presented respectively in Figure 6.22 a), b), c), and d). For 85 wt.% of stainless steel, the solidification path predicts austenite formation, followed by M_6C , the first eutectic phase to form along the interdendritic boundaries. With further cooling, Laves phase forms, but δ -ferrite does not.

When the weight percentage of stainless steel decreases to 70 and 60 wt.%, the Scheil-Gulliver calculations, besides the hexagonal Laves phase and M_6C carbides, predict the precipitation of σ , $M_{23}C_6$, and δ -phase (Ni_3Nb). These results are corroborated by the synchrotron X-ray diffraction results, which indicated the presence of carbides and σ -phase between the regions with 40 and 60 wt.% of stainless steel. From Figure 6.22 a) to c), an increase in the solidification range can be noticed, making the material more likely to experience solidification cracking as the different

concentrations make the material more prone to segregation and precipitation of secondary phases as Nb-rich laves, which have a low melting point [208,209].

Figure 6.22 d) shows the equilibrium phase diagram for a weight percentage of 50/50 wt.%. This diagram considers the hypothetical situation of an infinitely slow cooling condition in which the composition was allowed to reach an equilibrium condition at each temperature step. Austenite is the first to solidify from the liquid at around 1340 °C, followed by σ that started to form at 1045 °C, increasing in amount until 790 °C, and then suddenly dropped off at 656 °C. Following these occurrences, δ -phase (Ni_3Nb) was in equilibrium between 500 and 1023 °C in amounts up to 4 at.%. Laves began to precipitate at 770 °C and should represent around 10 at.%, while α -ferrite (BCC) began to precipitate at 656 °C, resultant of the direct transformation of $\sigma \rightarrow \alpha$ -ferrite.

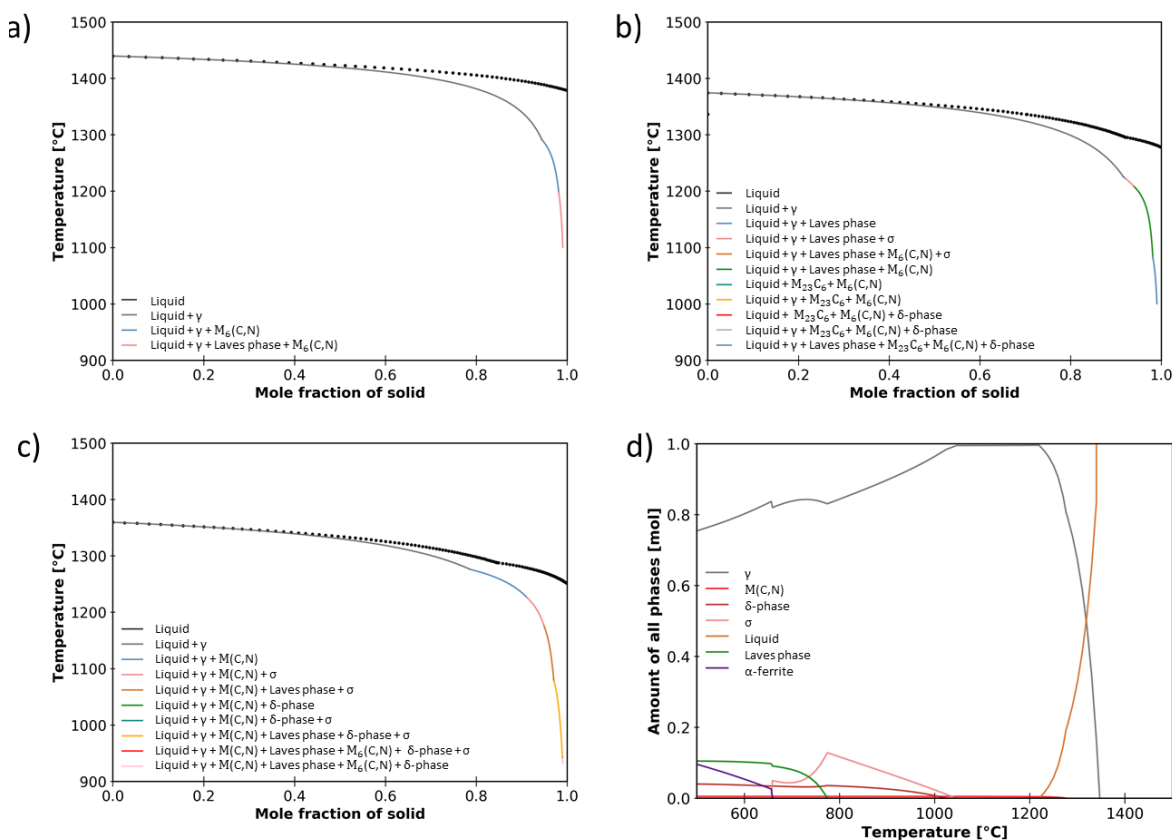


Figure 6.22 - Scheil-Gulliver calculations for stainless-steel wt.% concentrations of: a) 85 %, b) 70%, and c) 60%; d) Thermodynamic equilibrium calculations considering 50 wt.% of Inconel and stainless steel.

6.3.2.3 Scanning Electron Microscopy with Energy Dispersive Spectroscopy

The distribution of elements on the cross-section of the FGM 100-100 and FGM 100-100 HT samples was investigated by SEM/EDS. As shown in Figure 6.23, moving from the regions of Inconel to the stainless steel side, the Fe content increased, but Ni, Mo, and Nb contents decreased, in agreement with the amount of each element in the feedstock wires. The segregated regions in Inconel are

enriched with Nb, favoring the presence of γ'' in these areas. In Figure 6.23 a), it is observed that the interface between materials is sudden (absence of macrosegregation [210]) without any gradient and an evident transition of grain structure with negligible elemental diffusion. The microstructure in both sides of the FGM 100-100 HT sample was homogenized after heat treatment as the dendrites fully disappeared, and elements such as Mo and Nb could diffuse to the matrix (Figure 6.23 b).

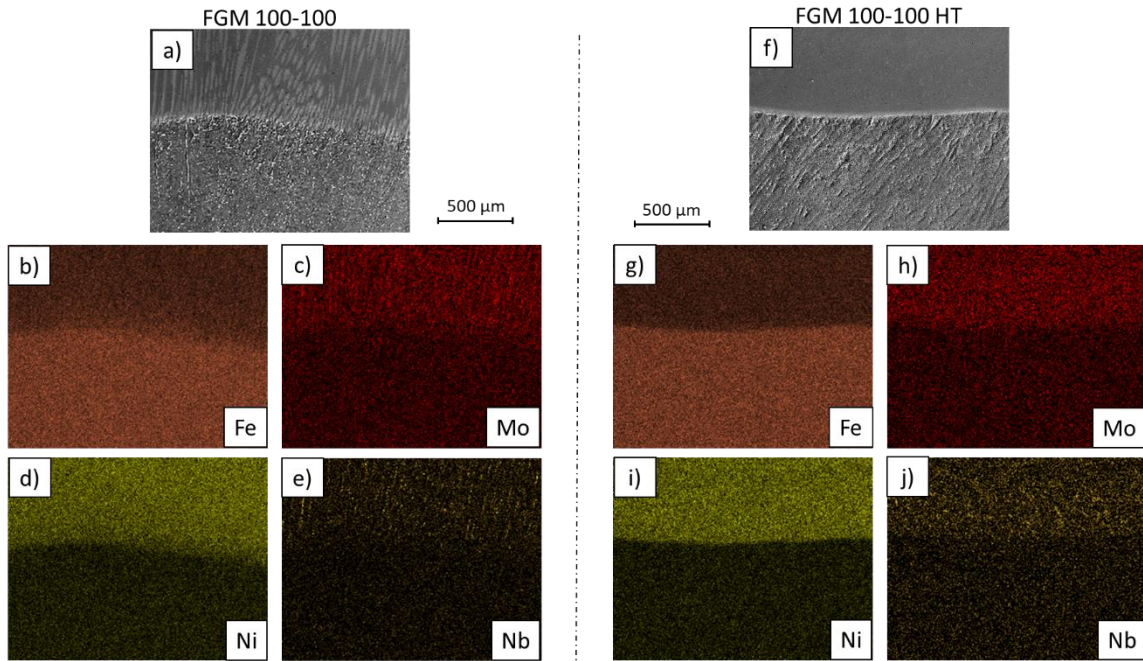


Figure 6.23 - Scanning electron microscopy (SEM) and Energy-dispersive X-ray spectroscopy (EDS) mapping of the interface of: a) to g) FGM 100-100; f) to j) FGM 100-100 HT.

Figure 6.24 shows the distribution of elements across the precipitates found in the interdendritic regions of the FGM 5 sample around the compositional region with 50 wt.% stainless steel/50 wt.% Inconel 625. Severe segregation of Nb and Mo into these interdendritic spaces might indicate the presence of Laves phase (Cr_2Mo) and carbides (NbC).

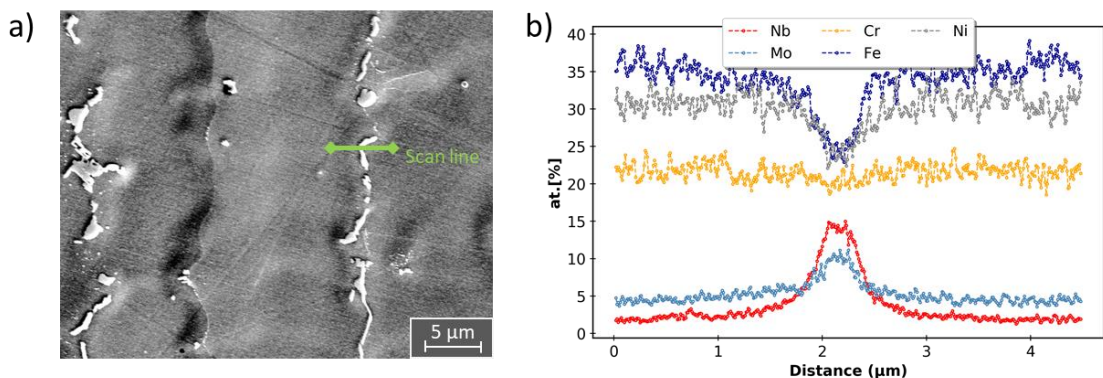


Figure 6.24 - Energy-dispersive X-ray spectroscopy (EDS) line scan across the precipitates in the compositional region with 50 wt.% stainless steel/50 wt.% Inconel.

6.3.2.4 Residual stresses measurements

Figure 6.25 compares the residual stresses in the three orthogonal directions (X, Y, Z) measured along a central line across the FGM 100-100 and FGM 5 walls. The results show compressive stresses in the region where the two materials are mixed of FGM 100-100 with a magnitude up to 180 MPa in the building direction (Figure 6.25 a). In the other two directions, the magnitude was not higher than 80 MPa throughout the height of the sample. FGM 5 experienced considerably more residual stresses than FGM 100-100 (Figure 6.25 b). The neutron diffraction results depict tensile stresses at the interface, near a concentration of 55 wt.% Inconel, with magnitudes up to 314, 348, and 468 MPa in the X, Y, and Z directions, respectively. The residual stress being higher in the FGM 5 might be attributed to the potential deleterious concentrations resulting in the precipitation of δ -phase (Ni_3Nb), σ -phase, and carbides. The existence of multiple precipitates with different stoichiometries and properties might result in strong volume mismatches and significant stresses that the material must accommodate. These results go against the common assumptions that a smooth gradient might be desirable for reducing internal stresses [211]. Such graded structures can indeed be of interest to decrease residual stresses provided that no detrimental phases are formed.

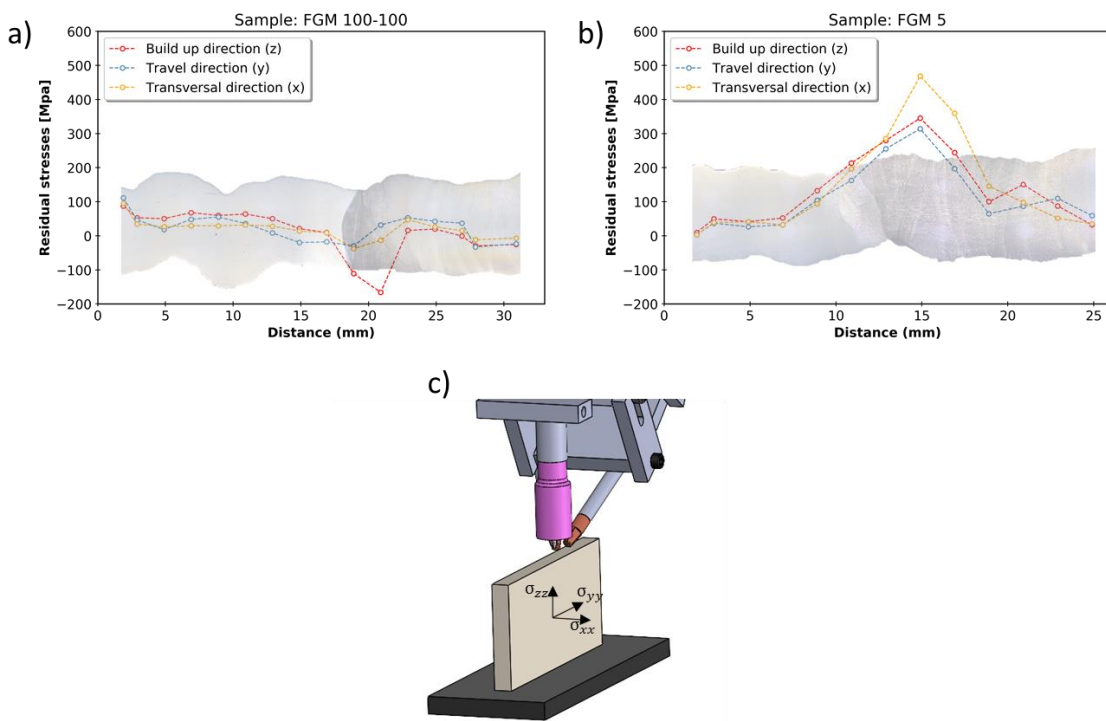


Figure 6.25 - Residual stresses in the three principal directions (c) of the sample: a) FGM 100-100 (direct interface); b) FGM 5 (smooth transition).

6.3.2.5 Mechanical Properties and electrical conductivity measurements

Hardness measurements

Figure 6.26 a) and b) depict the micro-hardness measurements made along the walls' height from the bottom to the top of the FGMS with smooth and direct interfaces, respectively.

Figure 6.26 a) shows similar hardness and tendencies in both samples (FGM 5 and FGM 90-10). In the first layers, the hardness is approximately 200 HV, then decreasing to around 173 HV at around 35 to 40% of the total height. From this point onwards, it increases almost linearly until reaching the region with only Inconel 625 (> 80% total height) with a maximum hardness of 220 HV. The increased hardness in the first layers of both samples is attributed to the high carbon content in the substrate and to the faster cooling rates that the first layers undergo which results in a finer microstructure and less elemental segregation [31,212]. Only at around 18% of the parts' total height do the hardness values reach values similar to the average value of the as-built stainless steel 316 (≈ 183 HV). However, near the region between 35 to 40 % of total height, the FGM 5 sample experiences a hardness decrease to 169 HV. This decrease is attributed to the decrease of the δ -ferrite content in the weight percentage of 70 wt.% stainless steel/30 wt.% Inconel, since δ -ferrite is known to provide increased hardness in stainless steel [213]. This depletion of ferrite is explained by the increased content of Ni content in steel that shifts the $\text{Cr}_{\text{eq}}/\text{Ni}_{\text{eq}}$ ratio to the left in the pseudo-binary diagram (refer to Figure 6.17) changing the solidification mode. It is perceived that the as-built AISI 316

stainless steel composition solidification starts with δ -ferrite from the liquid (Liquid \rightarrow Liquid + δ), which due to interdendritic segregation induces the formation of austenite, resulting in a ferritic-austenitic solidification (FA) mode (Liquid \rightarrow Liquid + δ \rightarrow Liquid + δ + γ \rightarrow δ + γ). However, below an 80 wt.% of stainless steel, the solidification mode changes to mode A – single phase austenite (Liquid \rightarrow Liquid + γ \rightarrow γ), depleting δ -ferrite formation, which decreased the material's hardness. Such similarities were found in AISI 904L superaustenitic stainless steel welded joints, which had higher Ni, Cr, and Mo contents (solidification mode A, i.e., absence of δ -ferrite) than the AISI 316L stainless steel [214]. Moreover, the AISI 904L superaustenitic stainless steel welded joints had comparable hardness (172 HV) with the FGM's minimum (169 HV), due to the matching microstructure (only austenite). In addition, similarly to the AISI 904L superaustenitic stainless steel the increase in alloying elements (solid solution strengthening) does not translate into higher hardness in the AISI 316L stainless steel since the microstructure (austenite + δ -ferrite, and phase boundary effects) has a stronger effect than the solid solution strengthening effect. Kim et al. [215] also reported that the gradual chemical composition induces a soft region (\approx 170 HV) in an FGM (70 wt.% Inconel 718/30 wt.% stainless steel 316) fabricated by laser-DED, which also relates to the microstructure changes (absence of δ -ferrite), further corroborating the present discussion. As the Inconel 625 content increases with height (region with 50 wt.% = 50 % total height), more Nb and Mo are added to the molten pool, allowing more secondary precipitates to form, which increases the material's hardness. Despite no MC carbides or δ -phase (Ni_3Nb) being identified in the interface of the FGM 90-10, the hardness measurements were identical between samples. However, by removing the compositional range of 70 wt.% stainless steel/30 wt.% Inconel from the FGM 90-10, the minimum hardness value was 177 HV instead of 165 HV, as measured in the FGM 5.

Figure 6.26 b) shows the hardness results of the FGM made with a direct interface deposition strategy (FGM 100-100 and FGM 100-100 HT). It can be noticed that the values of the FGM 100-100 present a similar behavior as the smooth-type gradient FGM. In the first layers, the hardness decreases until reaching 35 to 40% of the total height and then gradually increases until reaching the region with only Inconel. No differences were measured in the regions with only Inconel. However, in the stainless steel region, the minimum value decreased from 174 to 150 HV after heat treatment, instead of 174 HV, due to δ -ferrite dissolution.

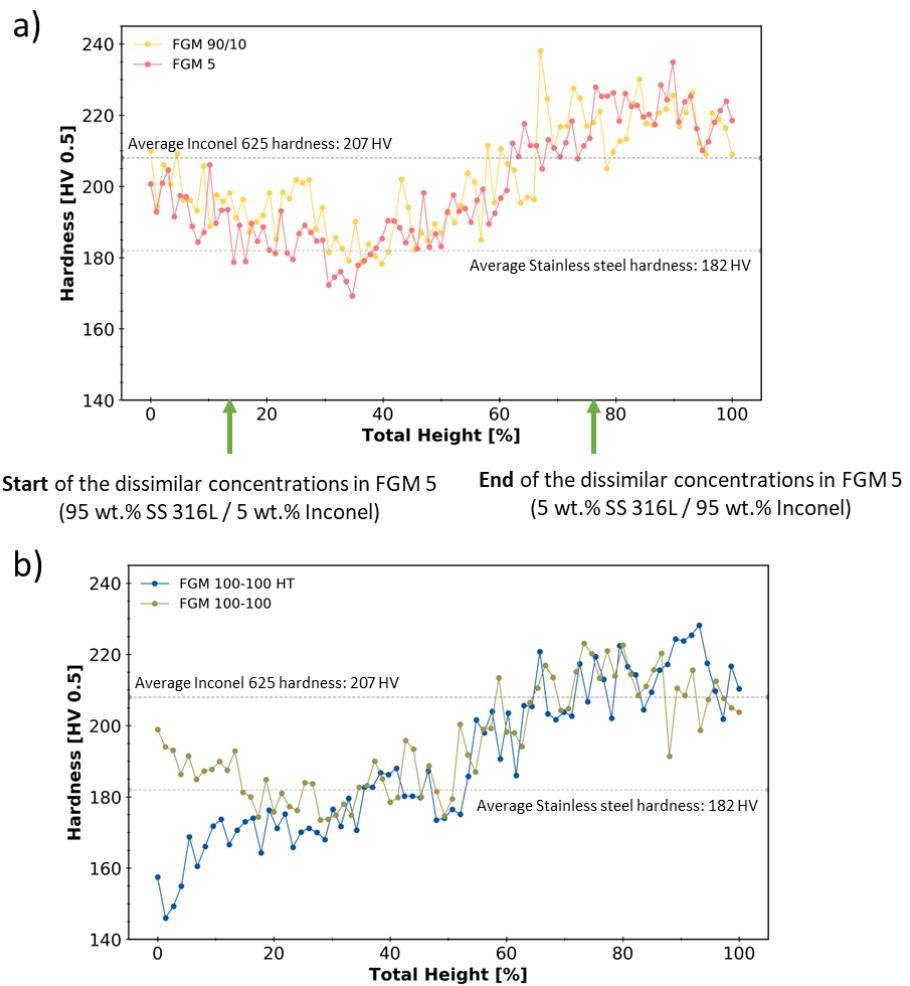


Figure 6.26 - Comparison of hardness measurements between samples: a) FGM 90-10 vs FGM 5 (smooth transition); b) FGM 100-100 vs FGM 100-100 HT.

Electrical conductivity measurements

The electrical conductivity measurements are presented in Figure 6.27. In the stainless-steel region, the electrical conductivity is, on average, 2.19 % IACS and gradually decreases in every sample to approximately 1.31 % IACS in the region that is only composed of Inconel 625. This technique allowed to quantify the extension of the interfacial region in the samples made with a direct interface. Both FGM 100-100 and FGM 100-100 HT had dissolution of elements in the interfaces up to a height of 12 mm, which corresponds approximately to 9 layers in length. These results also indicate the successful fabrication of the gradient materials.

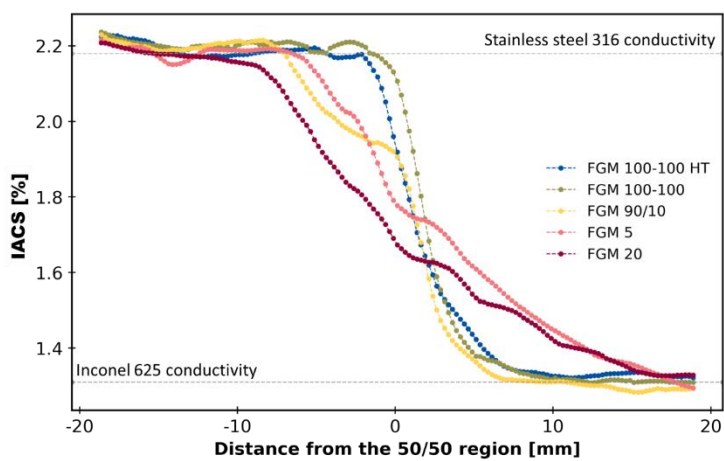


Figure 6.27 - Electric conductivity measurements made starting in the first layer and ending on the last deposited one.

Uniaxial tensile strength test

Specimens for tensile testing with the load direction aligned with the build-up direction (Z-axis) were made to evaluate the properties with different depositions strategies. A summary of the average mechanical properties of the fabricated material, namely the ultimate tensile strength (UTS) and extension at fracture, is presented in Figure 6.28. It can be perceived that the best overall results were obtained when using the direct deposition transition-built strategy. The sample FGM 100-100 had an average UTS of 542 MPa and an elongation at fracture of 61.6 %, but with heat treatment (FGM 100-100 HT), both properties were improved to 566 MPa and 69.3 %, respectively. These UTS values are within the range of those obtained in the as-built control samples (501 and 718 MPa, for stainless steel and Inconel, respectively). The increase in the UTS and ductility in the FGM 100-100 HT compared to the FGM 100-100 is attributed to the dissolution of the eutectic phases, whose elements can go back to the matrix to strengthen the matrix by solid solution.

When using a smooth transition deposition strategy, the average UTS was within 470–503 MPa, and the elongation was between 28.9–32.4 %. These values are similar to those found in the as-built control stainless steel 316 samples (501 MPa and 41.6 %), which was expected since the fracture in these samples occurred near the region of stainless steel. The decreased extension of the FGM can be attributed to the existence of interdendritic phases (both δ -phase and carbides) in the region where the fracture occurred, i.e., the mixing of the two metals induced a deleterious microstructure which causes a smaller ductility in comparison with the FGM 100-100 whose fracture occurred right at the middle of the specimens (50 wt.% stainless steel/50 wt.% Inconel 625). Similar behavior was found in the literature where a larger gradient between materials resulted in lower tensile strength and elongation at fracture. The existence of more layers with various mixing ratios made the material more prone to the existence of precipitates and inclusions [216].

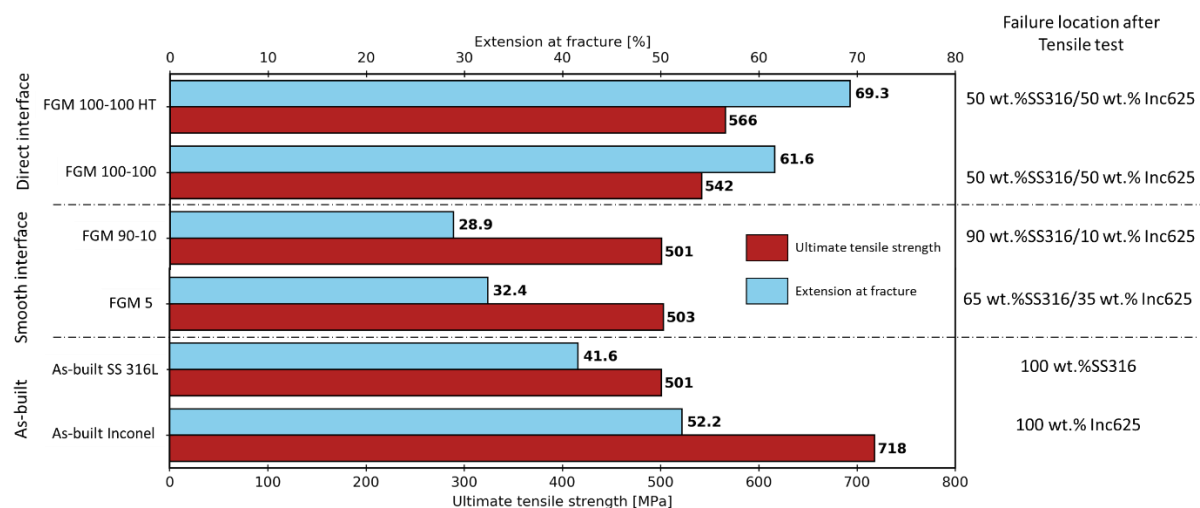


Figure 6.28 - Average mechanical strength test results after tensile loading three specimens from each condition and respective fracture location. Four tensile specimens of each condition were extracted from the samples to obtain mean and standard deviation values for the ultimate tensile strength and extension at fracture.

Digital image correlation

During uniaxial tensile testing, the deformation distribution along the load direction (z) was evaluated at different zones of the joining interfaces using digital image correlation (DIC). The elongation stages for different nominal elongations are given in Figure 6.29. The elongation distribution in the FGM 5 and 90-10 was heterogeneous due to the combination of different compositional regions. At 5 % elongation, the maximum strain was observed in a region containing about 65 wt.% of stainless steel. It is perceived that with stainless steel being softer than Inconel, the deformation will start at this region, and then at around 15 % of deformation, the loads start to be transferred to Inconel. The failure occurred in FGM 5 at around 65 wt.% of stainless steel and around 90 wt.% of stainless steel in FGM 90-10. The lack of δ -ferrite and consequently a downturn of hardness may be responsible for the location of the failure. It must be noticed that in every specimen of each condition, failure occurred in these regions.

Concerning the specimens taken from samples FGM 100-100 and FGM 100-100 HT, fracture always occurred in the direct interface between the two materials with elongations up to 65 %. Until an elongation of 20 % deformation, deformation remained almost symmetrical in both as-built materials. At 40 %, deformation started to increase near the interface, then failure occurred.

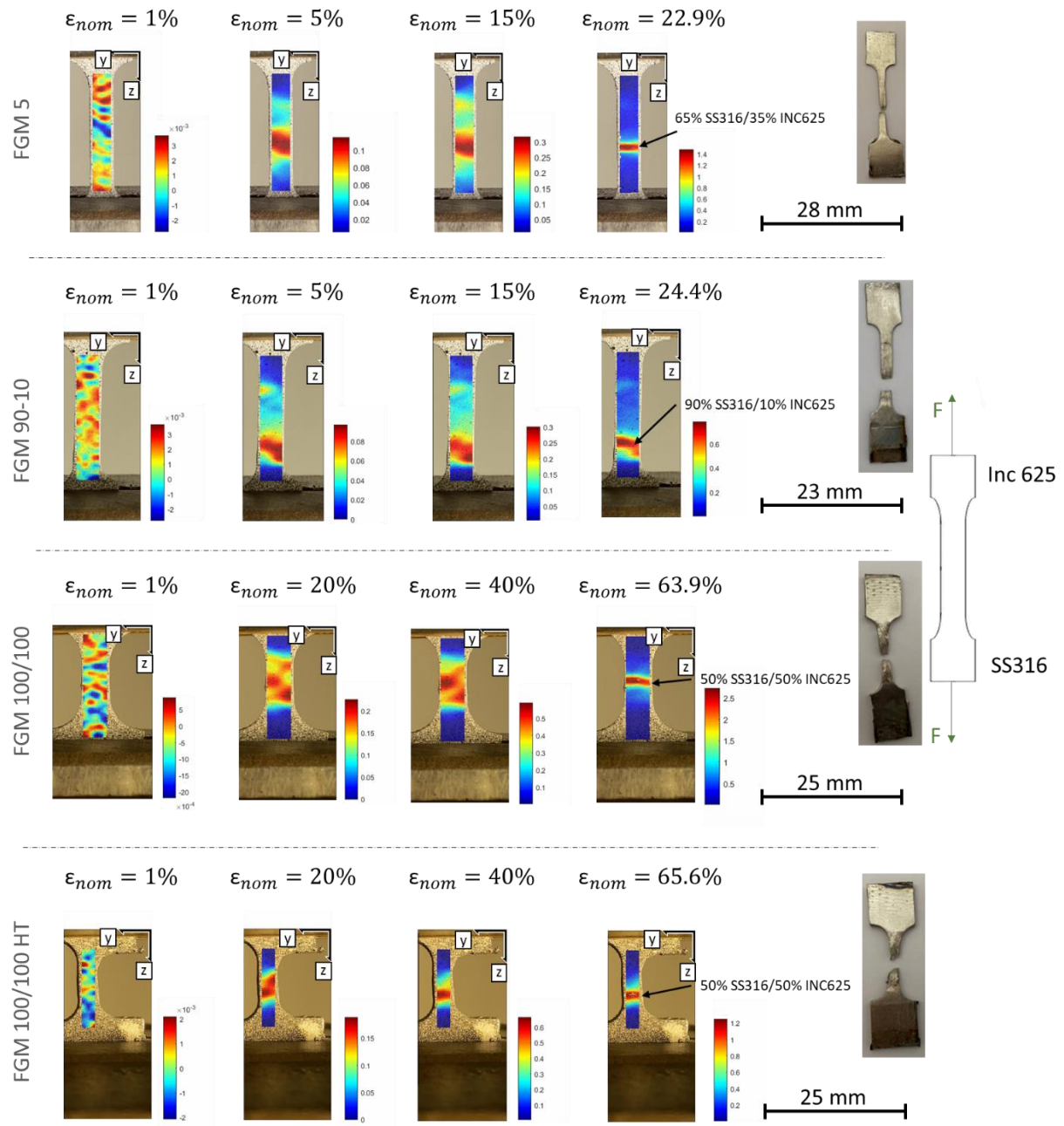


Figure 6.29 - Strain measurements along the X-axis distribution during tensile testing for specimens: FGM 5, FGM 90-10, FGM 100-100, and FGM 100-100 HT.

Fracture Surface

Fractography of the FGM 100-100 (Figure 6.30 a) and FGM 100-100 HT (Figure 6.30 b) samples had a ductile aspect with a fracture surface mainly composed of homogeneously distributed fine dimples, which correlates well with the high elongation at fracture exhibited in this samples. The fracture surface of the FGM 5 (Figure 6.30 c) and the FGM 90-10 (Figure 6.30 d) samples indicate a mixture of fracture aspects, with dimples and quasi-cleavage facets. Despite this, the FGM with a smooth interface still had a high elongation at fracture. The quasi-cleavage aspect was attributed to the

presence of TCP phases [202]. The fractography of both control samples (stainless steel 316L and Inconel 625) showed a ductile-like aspect composed mainly of large and homogenously dispersed dimples.

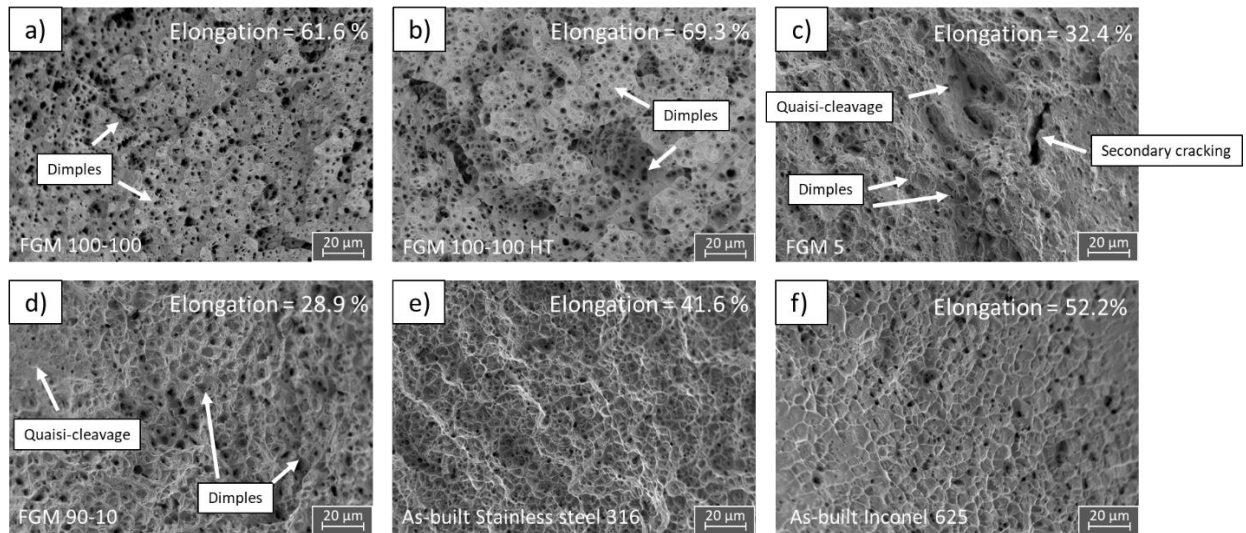


Figure 6.30 - Scanning electron microscope (SEM) image of the fracture surface of sample: (a) FGM 100-100; (b) FGM 100-100 HT; (c) FGM 5; (d) FGM 90-10; (e) As-built stainless steel 316; (f) As-built Inconel 625.

6.3.3 Conclusions

The present work attempts to optimize and compare properties of FGMS of stainless steel 316L and Inconel 625 built with different deposition strategies (direct and smooth-type interfaces). At the interface of the smooth transition FGMS, secondary phases that were not present in the as-built materials, such as the δ -phase (Ni_3Nb) and MC carbides, were detected by synchrotron X-ray diffraction. However, none of these phases were formed when using a direct interface.

The FGMS built with a direct interface showed strengths, on average, higher than 542 MPa and elongation higher than 61.6 %. The smooth transition FGMS had strengths up to 503 MPa and elongations up to 32.4 %. The specimens underwent a predominantly ductile-like fracture with considerable plastic deformation in all the tensile tests.

The residual stresses measurements, as determined by neutron diffraction, showed stresses in the interface of the FGM 100-100 only up to a magnitude up to 180 MPa, while the FGM 5 experienced stresses up to 314, 348, and 468 MPa in the X, Y, and Z directions, respectively.

6.4 Summary

The objective of this chapter was to investigate the feasibility of fabricating functionally graded materials with WAAM. The first FGM study joined an HSLA steel with a copper alloy without defects

and excellent strength and ductility in the interface. A direct interface between materials was adequate for joining these two materials. The process characteristics that involve remelting a large portion of the preceding layer and re-heating the previous layers created a gradient of composition, hardness, and electrical conductivity of around 12 mm. The next sub-chapter optimized the preferred building strategy for stainless steel 316L/Inconel 625 FGM. It was concluded that a direct interface was preferred over a gradient transition, with the two materials being fed simultaneously to the molten pool. The FGM built with a direct interface showed higher strengths and elongations, and no precipitates were found beside the phases already present in the base materials.

7.

DEVELOPMENT OF A NEW WIRE AND ARC ADDITIVE MANUFACTURING VARIANT

7.1 Introduction

In WAAM, the electric arc is established between the wire feedstock material and the substrate. As well-known, the thermal cycles during the deposition sequence significantly affect the microstructure evolution of the fabricated parts. As such, control of the heat input and, therefore, the cooling rates is of significant importance as these can drastically change the solidification conditions and solid-state transformations experienced by the material. Variants such as cold metal transfer (CMT) and hot wire WAAM (HWAAM) have been proposed to decrease the heat input [39]. Moreover, Chen et al. [217] combined two electric arcs during welding to control the material deposition, naming this new variant arcing wire-gas tungsten arc welding (AC-GTAW). While the main arc was established between the tungsten electrode and the substrate to assist the detachment of the filler material, an auxiliary side arc created between the tungsten electrode and the filler wire was used to melt the filler material. Higher deposition rates were possible by decoupling the deposition rate from the arc energy. However, this method fails in reducing the overall energy and costs involved, as an additional power source is required, increasing the system's complexity.

Consumable and Non-Consumable Indirect Arc Welding Process (CNC-IADW) was introduced by Wang et al. [218]. Here, the electric arc is established between the non-consumable tungsten electrode and the filler material, preventing the current from passing through the workpiece, thus reducing the process heat input. Liu et al. [219] recently developed a compulsively constricted WAAM (CC-WAAM) method, in which the electric arc established between the wire feedstock material and the tungsten electrode is confined to a narrow space inside a ceramic nozzle. During CC-WAAM, the material is ejected from the ceramic nozzle due to mechanical and thermal compression. Figure 7.1 illustrates the different arc welding and arc-based AM methods described above.

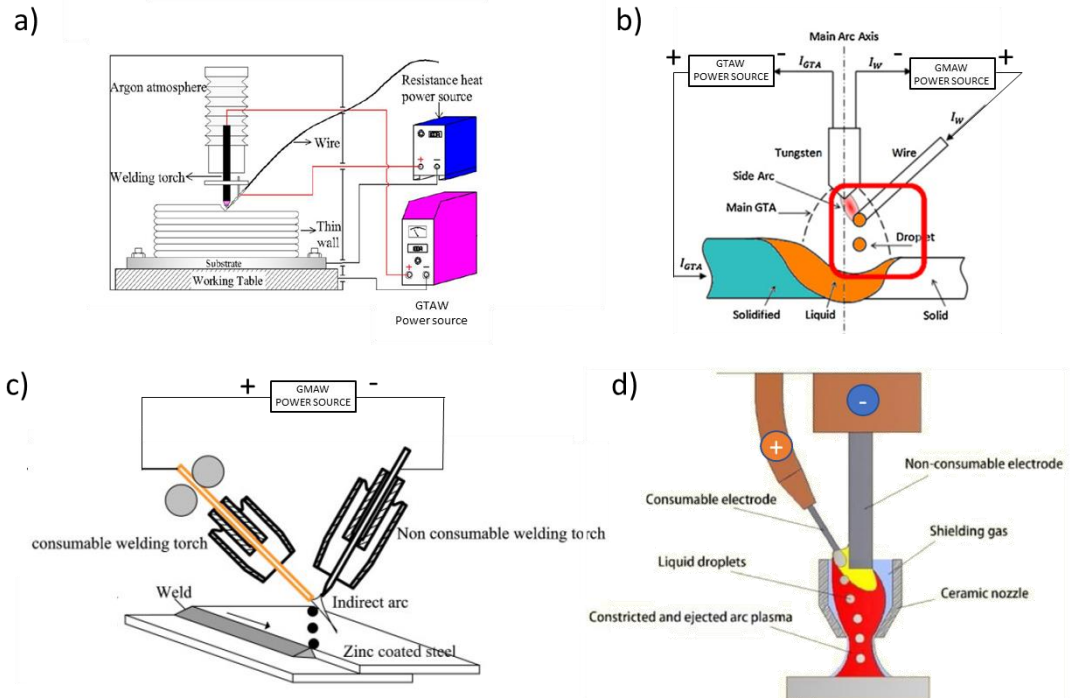


Figure 7.1 - WAAM variants: a) hot-wire GTAW b) arcing wire GTAW, c) Consumable and Non-consumable Indirect Arc Welding Process, d) Compulsively constricted WAAM (adapted from [39,218–220]).

In the next section, a new WAAM variant, named Ultracold-Wire and Arc Additive Manufacturing (UC-WAAM), is presented. UC-WAAM setup is the same as already used in the variant CNC-IADW introduced by Wang et al. [218], but it has never been used in an additive manufacturing application. UC-WAAM aims to reduce the heat transferred to the part during build-up without compromising the deposition rate. The effect of different process parameters on the deposited beads is assessed. After process optimization, single walls of HSLA steel were built. Microstructure and mechanical characterization of the fabricated samples were performed and compared to conventional GMAW-based WAAM.

7.2 Materials and design

The GMAW-based WAAM torch previously described in section 3.3 was used to fabricate the control samples, and the multi-wire torch described in section 3.5 was used to deposit the material with this new process variant. The GMAW power source was used in both processes. Both processes connected the positive pole (anode) to the wire feedstock. The negative pole (cathode) was connected to the substrate in the GMAW-based variant and to the tungsten electrode in UC-WAAM. The schematic representation of GMAW-based WAAM and UC-WAAM is depicted in Figure 7.2 a) and b), respectively, whereas Figure 7.2 c) presents the customized UC-WAAM torch. The wire feedstock used was the ER110S-G.

A multiparametric study was developed to determine suitable process parameters capable of creating defect-free parts. Single-layer beads were performed with UC-WAAM varying the following parameters: wire feed speed from 1 to 10 m/min in 1 m/min steps; travel speed from 50 to 400 mm/min with intervals of 50 mm/min. The voltage was set to 17 V in every experiment, and the welding machine would adjust the current depending on the wire feed speed. The depositions were evaluated regarding shape, forming quality, and feasibility for arc-based AM.

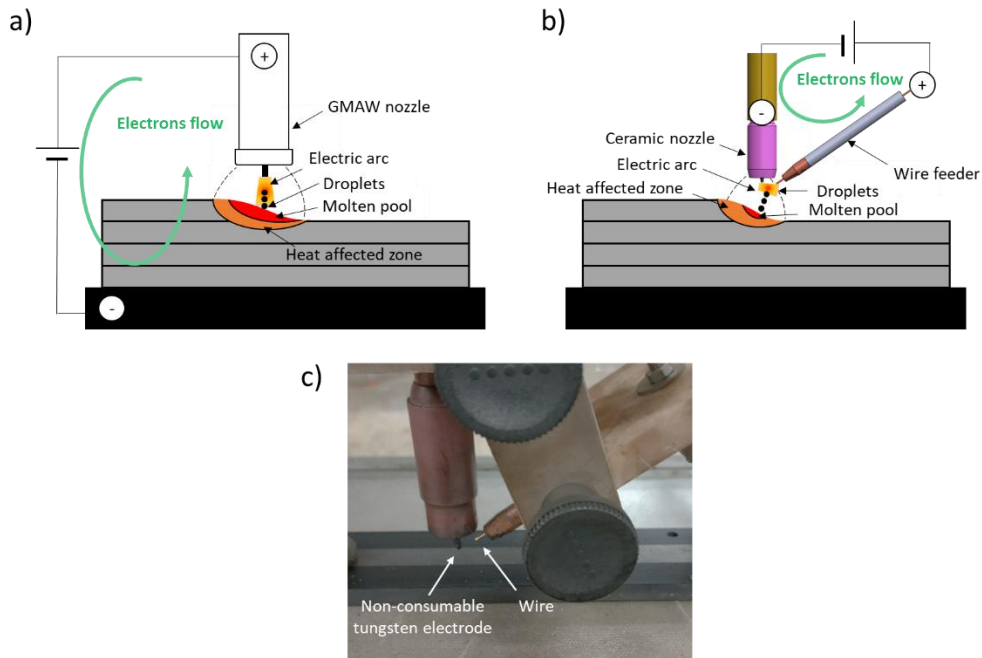


Figure 7.2 - Schematic comparison of the electric arc location, electrons flow, and the setup used with a: a) GMAW-based WAAM torch, b) UC-WAAM torch, c) Customized UC-WAAM torch.

After testing each set of process parameters, some were not well suited for UC-WAAM. Therefore from the obtained processing feasibility window (further detailed in Figure 7.4), two sets of process parameters were selected for a more in-depth analysis of the microstructure and mechanical properties of the as-built parts. It should be stated that the selection of these sets of parameters encompassed a two-step decision process: i) it should fall within the feasibility parameter range for UC-WAAM; ii) it should guarantee defect-free and well-formed beads. The selected process parameters are detailed in Table 7.1. The first set comprises a wire feed speed of 3 m/min and a travel speed of 150 mm/min. The second set used a wire feed speed of 4 m/min and a travel speed of 200 mm/min. The voltage and the shielding gas were the same as previously used in the preliminary experiments. A total of 9 layers were deposited, with a length of 100 mm. The time between subsequent depositions was set to 2 minutes. This way, the temperatures that would develop during both processes could be compared.

Since this is a proof-of-concept of a novel WAAM variant, only nine layers per condition were deposited. To fully demonstrate the wall appearance ability of UC-WAAM, a three-layer wall was made with a different set of parameters (named sample P5), chosen from the feasibility window assessed. The wire feed speed was 5 m/min, and the travel speed was 150 mm/min.

Table 7.1 - Process parameters of single-wall samples built.

Process Variant (Sample reference)	Wire feed speed [m/min]	Travel speed [mm/min]	Voltage [V]	Gas
GMAW-based WAAM (P1) and UC-WAAM (P2)	3	150	17	Argon 99.99 %
GMAW-based WAAM (P3) and UC-WAAM (P4)	4	200	17	Argon 99.99 %
UC-WAAM (P5)	5	150	17	Argon 99.99 %

Process instrumentation was used while performing the depositions. Four thermocouples were mounted on the substrate (Figure 7.3), and a thermographic infrared camera was used to evaluate the temperatures during the depositions. Two tensile specimens obtained along the deposition direction (horizontal) were tested for each sample.

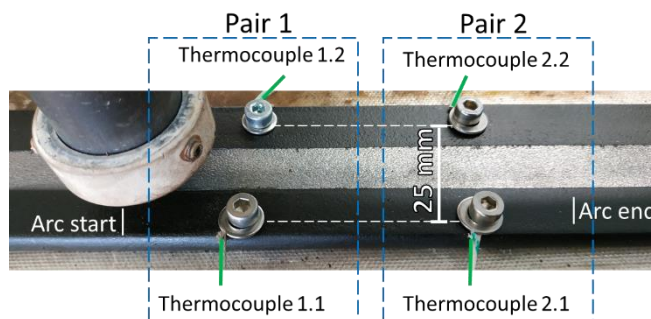


Figure 7.3 - Location of the position of the arc start, arc end, and the position of the four thermocouples used to measure the temperatures experienced in the substrate.

7.3 Results and discussion

7.3.1 Preliminary UC-WAAM single-beads experiments

Figure 7.4 depicts a contour fill plot of this new variant's most feasible process parameters (wire feed speed and travel speed). Based on the single-beads appearance, arc characteristics, and penetration, the window of parameters was divided into four zones.

In zone 1, corresponding to low travel speeds, an excessive amount of material was deposited, which ultimately led to a large amount of material being piled up that contaminated the tungsten electrode. The resultant beads were too large for application in additive manufacturing (widths > 10 mm).

Zone 2 corresponds to the region of high wire feed speed. The increase in wire feed speed directly influences the current involved, i.e., higher wire feed speeds require more current, which leads to an increase in the heat input. The resulting beads were significantly large (8 to 10 mm), with an inconsistent width and height along their length (refer to Figure 7.4 b). This result can be explained as follows: as a result of the heat input, the center of the molten pool was too far (> 15 mm) from the extension line of the tungsten electrode. This elongated molten pool is more susceptible to deviations induced by the arc force. As a result, the droplets of molten material are shifted from side to side along the center of the molten pool, thus resulting in irregular-shaped beads.

In zone 3, corresponding to the zone of wire feed speed to travel speed (WFS/TS) ratios lower than 15, the welding arc was unstable, and the resultant beads had visible humps and discontinuities (refer to Figure 7.4 b). These results can be explained by considering that when the travel speed increases, the molten pool extension decreases, and solidification occurs faster. The solidification of the molten pool occurs before a new drop of material is detached from the wire feedstock. As such, when a new drop is finally released, it will be deposited onto an already solidified layer promoting the formation of these humps.

Zone 4 is delimited by WFS/TS ratios between 15 and 80, corresponding to the suitable process parameters for UC-WAAM. When the travel speed increased, the beads became thinner and higher since the molten pool size decreased, solidifying rapidly. Beads became larger upon increasing the wire feed speed, and the penetration increased since higher values of wire feed speed required higher current. Figure 7.4 a) depicts cross-sections of different samples produced with parameters selected from zone 4.

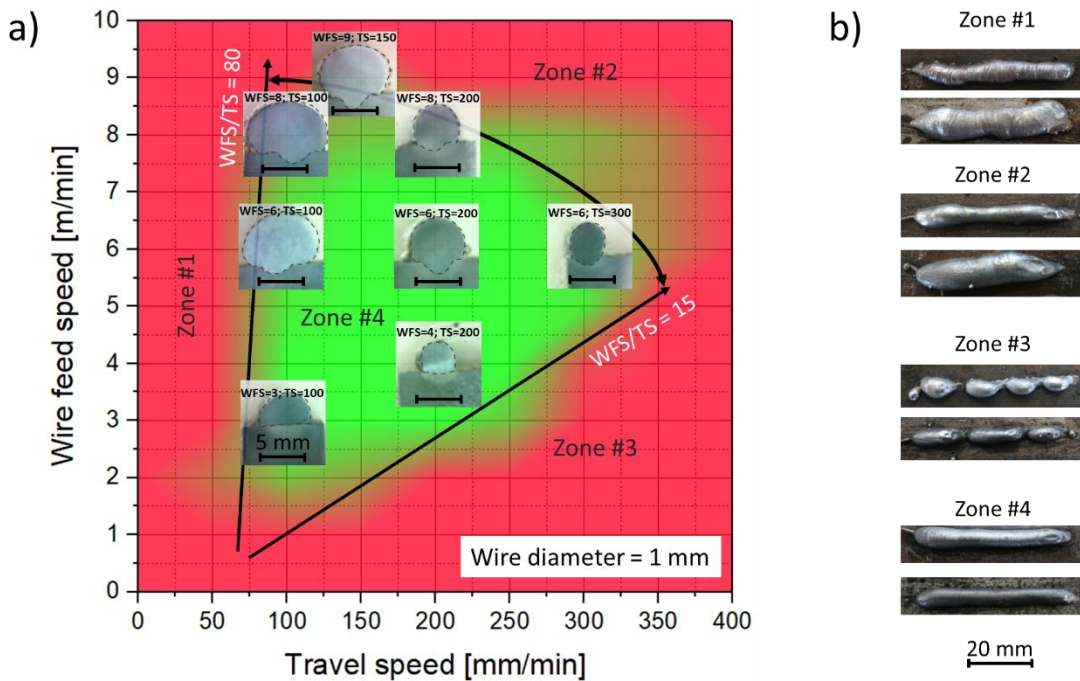


Figure 7.4 - Ultracold-Wire and Arc Additive Manufacturing: a) Process parameters window with single-beads cross-sections of samples within the feasible process parameters; b) Single-beads appearance of each identified zone.

7.3.2 GMAW-based WAAM and UC-WAAM single walls

In section 7.3.1, a range of suitable process parameters was obtained for the novel UC-WAAM variant. Two sets of process parameters were selected to directly compare UC-WAAM with GMAW-based WAAM (refer to Table 7.1). Figure 7.5 details the cross-sections of the produced samples, with the cross-section micrographs of the produced samples, while Table 7.2 resumes their geometric characteristics. Due to excessive waviness in samples P2 and P4 made with UC-WAAM, a wall with a set of parameters more suitable ($WFS = 5 \text{ m/min}$; $TS = 150 \text{ mm/min}$) was created (Figure 7.6). It can be concluded that UC-WAAM's excessive waviness can be reduced using optimal process parameters. However, if these parameters were to be used with traditional GMAW-based WAAM could result in an unstable deposition. It should be emphasized that even with the excessive waviness in samples P2 and P4, no defects such as cracks or pores occurred in the as-built parts. The red dashed lines in Figure 7.5 marked the region between the non-remelted and remelted area of a previous layer onto the next one.

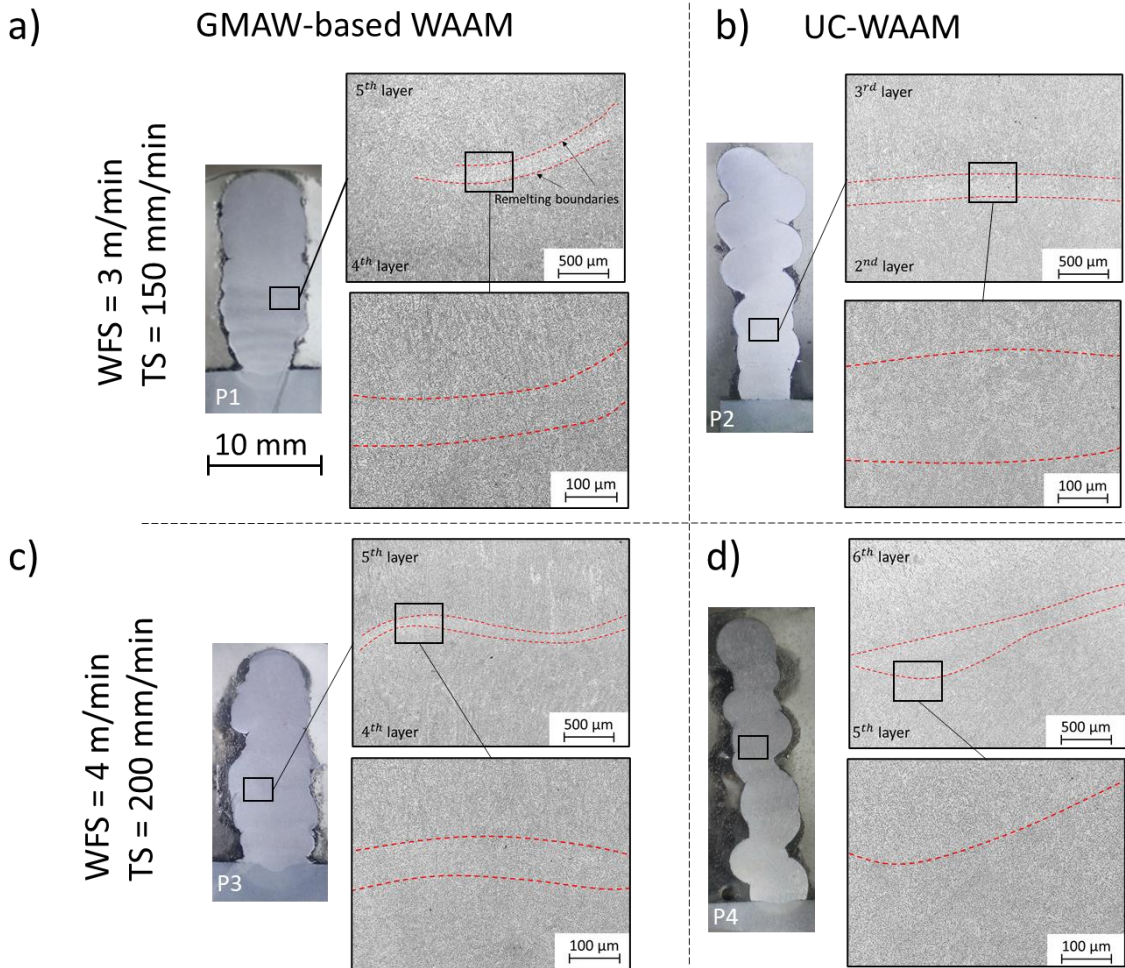


Figure 7.5 - Cross-section images and micrographs of the interlayer region of samples: a) P1, b) P2, c) P3, and d) P4.

While the heat input for the samples produced by GMAW-based WAAM and UC-WAAM is the same for the same process parameters, the electric arc created between the tungsten electrode and the wire feedstock in UC-WAAM is further away from the molten pool. As a result, more heat is lost between the detachment of a liquid droplet and its incorporation into the molten pool. This heat loss results in a smaller penetration depth and faster solidification. Nonetheless, this did not prevent the different layers from adhering to the substrate or already deposited layers. The faster solidification can be helpful during arc-based additive manufacturing as it prevents the collapse of the molten pool towards the sides, thus leading to the formation of layers with reduced width but increased height. This low penetration obtained during UC-WAAM can also be of interest to control the dilution that occurs during arc-based additive manufacturing, especially for producing FGMs.

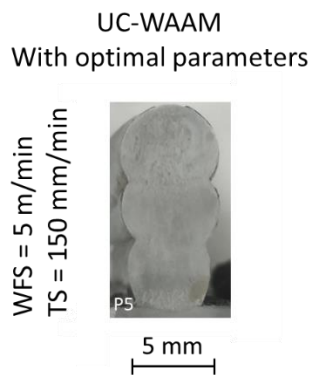


Figure 7.6 - Cross-section of the sample built with UC-WAAM using optimal process parameters.

Table 7.2 - Single walls cross-section characteristics.

Sample	Process	Width [mm]	Height [mm]	Penetration depth of the first layer [mm]	Penetration area of the first layer [mm ²]
P1	GMAW-based WAAM	8.6	18.8	0.6	1.1
P2	UC-WAAM	7.7	22.2	≈ 0	≈ 0
P3	GMAW-based WAAM	7.9	18.1	0.7	1.5
P4	UC-WAAM	7.2	24.2	0.2	0.3

During UC-WAAM, the current can only flow between the non-consumable tungsten electrode and the wire feedstock material. Thus, the heat contribution comes only from the detachment of the droplets, aided by the coaxial shielding gas. One of the significant advantages of UC-WAAM is the possibility to adjust the heat input, not only by selecting the process parameters (wire feed speed, travel speed, and voltage) as it occurs in GMAW-based WAAM. But also by modifying the distance between the non-consumable tungsten tip and the substrate. However, this procedure must be applied with caution as the higher distance between the tungsten tip and the electrode, the easier it is for the detached droplets to split to the sides of already deposited beads.

7.3.3 Electrical current measurements

The GMAW power supply has a self-regulation mode, which adjusts the current according to the arc characteristics by setting the voltage to maintain the arc length. The current waveform during the deposition of samples P3 (GMAW-based WAAM) and P4 (UC-WAAM) is depicted in Figure 7.7. Some striking differences can be observed in the set of parameters used to fabricate samples P3 and P4. The most obvious is the current intensity range in both processes: with GMAW-based WAAM, the current varied between 0 and 370 A, while in UC-WAAM, it varied between 80 and 140 A. As shown in

the following sub-section, these differences can be explained based on the different material drop mechanisms.

Moreover, by integrating the current over time, it was determined that the average current of both process variants differed by less than 1%. The average current for the UC-WAAM fabricated sample P3 was 119.8 A, while for the GMAW-based WAAM P4 sample, it was 121.3 A. Overall, the heat input is almost the same used in both processes. Nonetheless, the temperature profiles experienced by the material in each process significantly differ, which will be discussed in a further sub-section. The average currents were 90, 92, 119, and 121 A for samples P1, P2, P3, and P4, respectively, illustrating that the current is only a function of the wire feed speed rather than the process used.

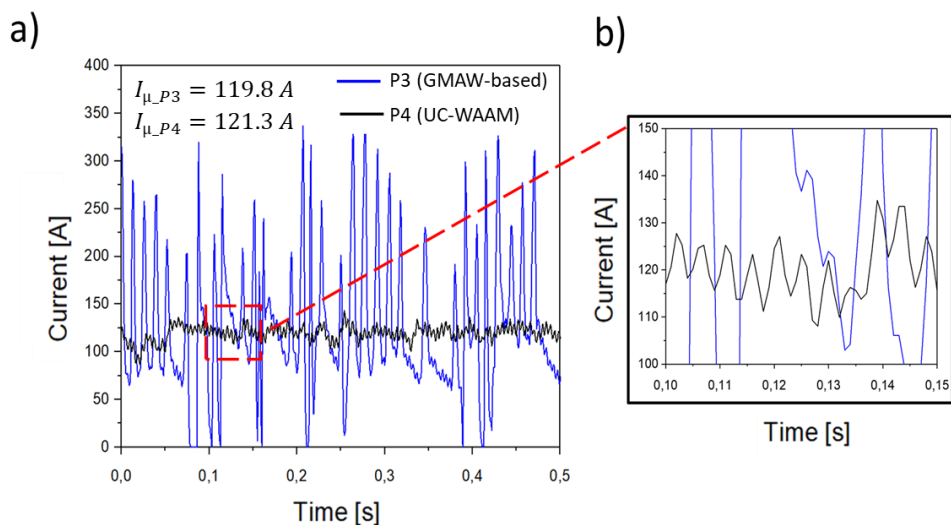


Figure 7.7 - Current measurements of the second layer of samples P3 and P4 during: a) 0.5 seconds; b) 0.05 seconds. The average current during the fabrication of samples P3 and P4 was 119.8 A and 121.3 A, respectively.

7.3.4 UC-WAAM droplet transfer mechanism

Typically in GMAW welding, therefore, in GMAW-based WAAM, the current waveform is as follows: ignition of the electric arc is established with a specific background current. This background current is enough to maintain the electric arc stable and promotes the melting of the wire feedstock. Eventually, the melted material will grow and turn into a droplet. The liquid droplet will contact the molten pool, and a short circuit occurs. This short circuit causes a sharp increase in the current while the voltage drops to zero. Once this happens, the droplet is finally detached. The cycle is then repeated until the extension of the electric arc.

Before describing the waveform characteristics of the UC-WAAM process, we first need to analyze the arc behavior. The arc morphology and droplet transition process during the fabrication of sample P4 are shown in Figure 7.8. From this dynamic analysis, it can be perceived that the droplet transfer

frequency is 4 Hz. During the first 200 ms (Figure 7.8 b-d), the droplet began to form and grow. Eventually, the force of gravity and the shielding gas will overcome the surface tension, promoting the droplet's detachment (Figure 7.8 e). When the detachment of the droplet occurs, the previously elongated arc will return to its normal size, associated with the voltage prescribed, due to the self-regulation mechanism of the power source used. When the droplet reaches the molten pool, there is a slight deviation toward the left where the molten pool is located. During UC-WAAM, the droplet is detached below the tungsten electrode and the wire feedstock material, avoiding direct contact with the tungsten electrode. Therefore no current or voltage peaks occur. This distinct transfer mechanism justifies the differences between the current waveform of UC-WAAM and GMAW-based WAAM processes.

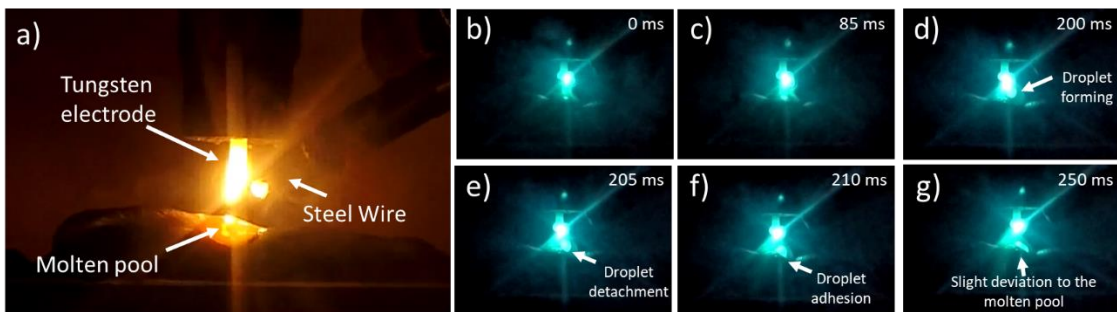


Figure 7.8 - a) High-speed camera image of the arc morphology and molten pool size, b-g) Steps of the droplets transfer mechanism.

7.3.5 Thermal analysis comparison between GMAW-based WAAM and UC-WAAM

By observing the macrographs of the GMAW-based WAAM and UC-WAAM produced parts (Figure 7.5), it can be inferred from the differences in the height and width of the samples that the UC-WAAM process promotes a faster solidification. To confirm those results, multiple temperature profiles (in the substrate via thermocouples and at the first and fifth deposited layers via infrared camera measurements) were obtained.

7.3.5.1 Thermocouple's temperature measurements on the substrate

The temperature history measured by the thermocouples placed in the substrate is given in Figure 7.9. Regardless of the process parameters, the temperature at any given instant during the process is higher with GMAW-based WAAM than with UC-WAAM. This fact demonstrates the effectiveness of UC-WAAM in reducing the heat transfer to the workpiece for the same set of wire feed speed, travel speed, and voltage.

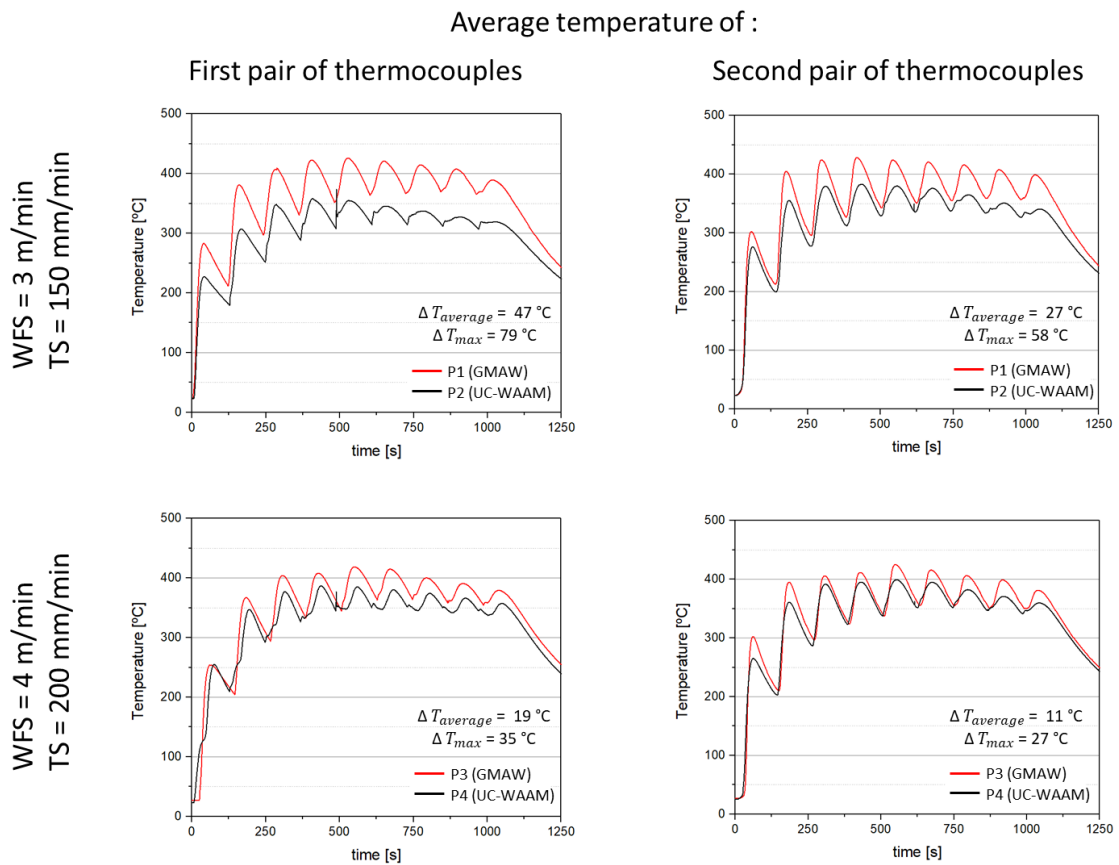


Figure 7.9 - Comparison of the temperature measurements obtained from the pairs of thermocouples placed in the substrate during the deposition of each sample.

7.3.5.2 temperature measurements with an infrared camera

Figure 7.10 depicts the thermographic images obtained during the last (ninth) deposited layer of samples P1 and P2. The 600 and 800 °C isothermals are marked in Figure 7.10 as dashed and continuous lines, respectively.

In good agreement with previous observations, it can be observed that for sample P1, both the 600 and 800 °C isothermals occur deeper within the deposited layers and covers a larger area, which further corroborates the hypothesis that in UC-WAAM the heat transferred is lower. The material melts outside the already deposited part through an external electric current that flows between the tungsten electrode and the wire feedstock without affecting the previously deposited layers. Also, another effect that can explain the differences in the temperature profiles can be attributed to the current peaks during GMAW-based WAAM (Figure 7.7). As seen in the last sub-section, during UC-WAAM, a maximum current value of 140 A is achieved, while during GMAW-based, a maximum peak of 370 A is observed. Therefore, during GMAW-based WAAM, higher temperatures can also be developed as a result of these high-intensity current peaks.

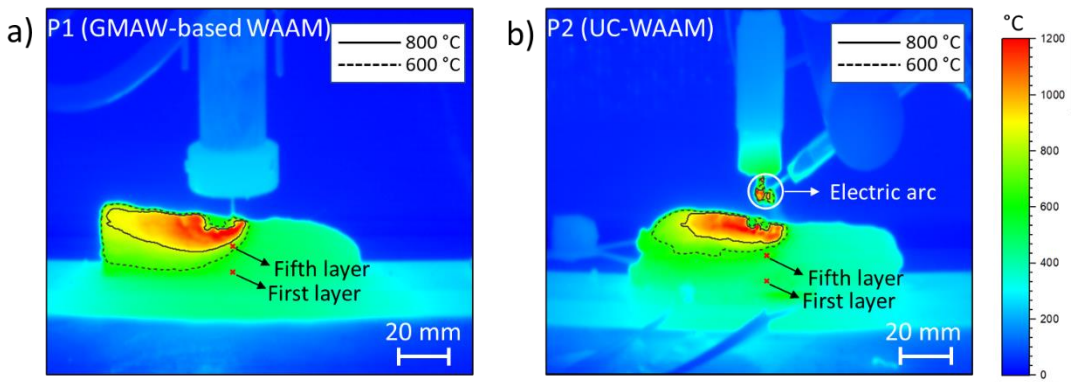


Figure 7.10 - Thermographic image taken during the deposition of the last layer of: a) P1 (GMAW-based WAAM), b) (UC-WAAM).

From the thermographic data, two regions of interest (marked in Figure 7.10) corresponding to the first and fifth deposited layers were analyzed to determine the cooling rates within the 800-500 °C range. The cooling rates for the layers of interest are detailed in Figure 7.11, and were only determined when the maximum peak temperature was above 600 °C.

The measured temperatures of samples P1 and P2 confirmed that less heat is transferred onto the substrate or previously deposited material with UC-WAAM, as the maximum peak temperatures are always lower than the GMAW-based WAAM process, while the cooling rates are always higher. Achieving higher cooling rates is desirable as it can reduce grain size and increase the material strength of an HSLA steel, as indicated by Thompson et al. [221]. One of this work's major outcomes is that with UC-WAAM, the interpass temperatures are lower than in conventional GMAW-based WAAM, considered one of the most important parameters to ensure constant cooling rates and decrease residual stresses [33,34]. With the increase in heat accumulation during parts fabrication, it becomes essential the use active cooling methods to avoid dwell times between layers of several minutes. Therefore UC-WAAM is a non-intrusive/passive technique that reduces heat accumulation and thus the time for the previous layers to reach a pre-established temperature. As a result, UC-WAAM also aids in reducing the lead times in production and overall costs.

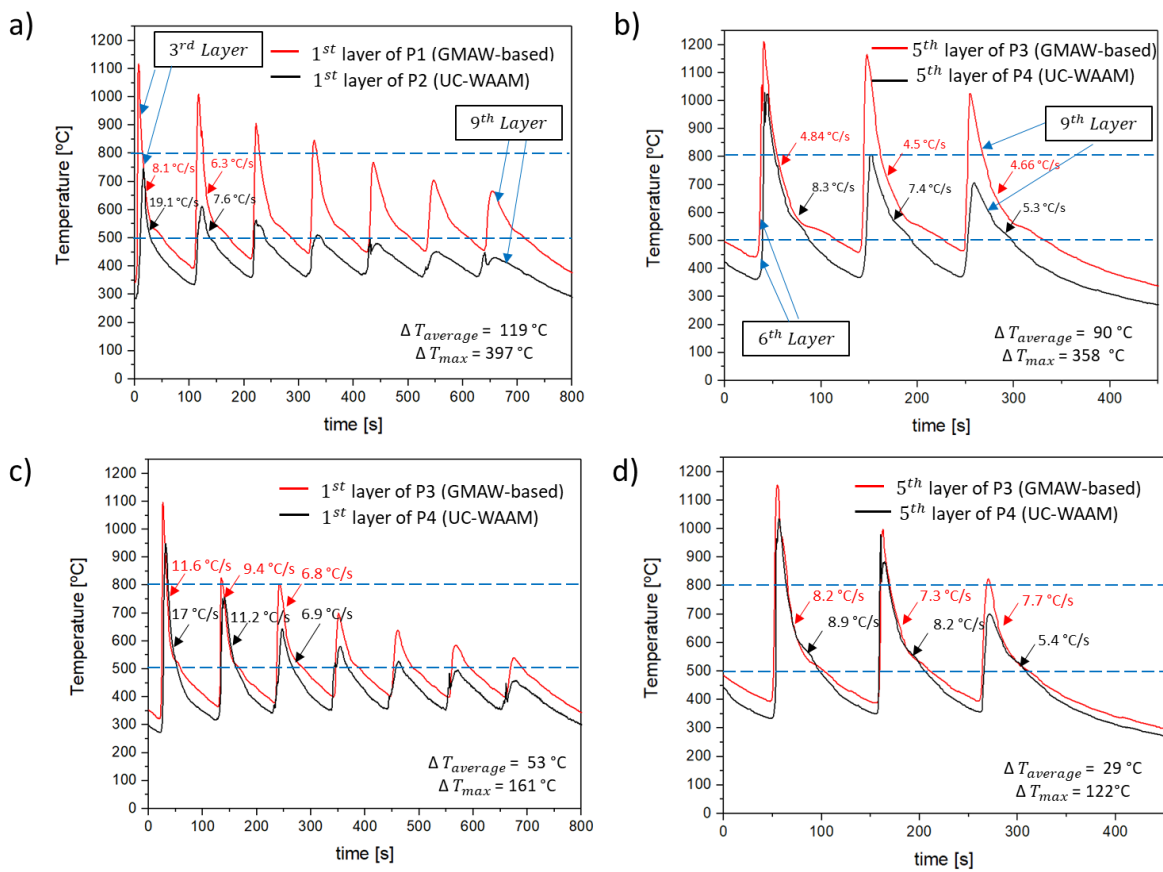


Figure 7.11 - Results of the temperature measured in: a) the first layer of samples P1 and P2; b) the fifth layer of samples P1 and P2; c) the first layer of samples P3 and P4; d) the fifth layer of samples P3 and P4.

7.3.6 Microstructure analysis of the single walls

Representative optical micrographs of the produced samples are depicted in Figure 7.12. The samples are composed of polygonal and acicular ferrite, and the grain size ranged between 1 and 20 μm . No significant microstructural differences were observed despite the differences in the thermal cycles between the processes used. Such is related to the small influence of cooling rates on this particular wire feedstock material and the small number of layers built.

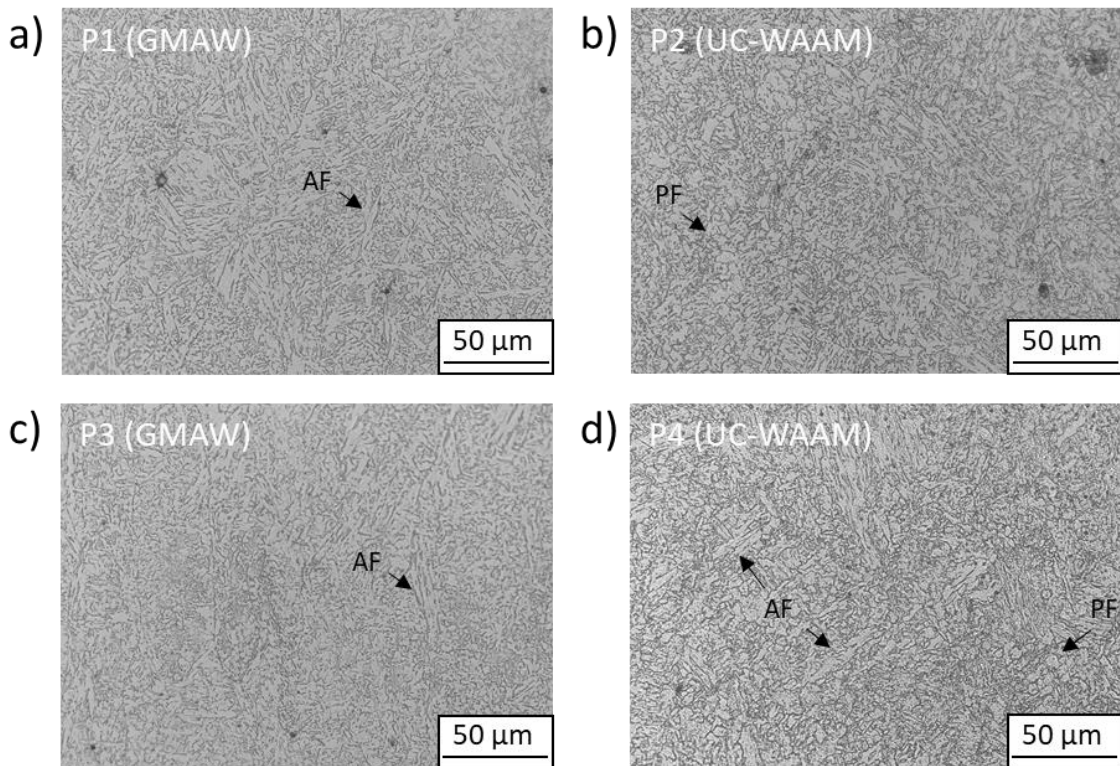


Figure 7.12 - Cross-section micrographs of samples: a) P1, b) P2, c) P3, and d) P4; (AF: acicular ferrite; PF: Polygonal ferrite).

7.3.7 Mechanical properties of the single walls

Figure 7.13 illustrates the hardness profile measurements. The mild steel substrate presents a low (~ 175 HV) hardness. The higher values in the first layers of the produced samples are due to the low temperature of the substrate at the beginning of the process, which promotes higher cooling rates, resulting in harder structures. Towards the top of the walls, the hardness fluctuated between 230 and 318 HV, with no apparent trend. This large disparity in hardness can be related to the heterogeneous grain size (1 to 20 μm) formed within the deposited parts (refer to Figure 7.12).

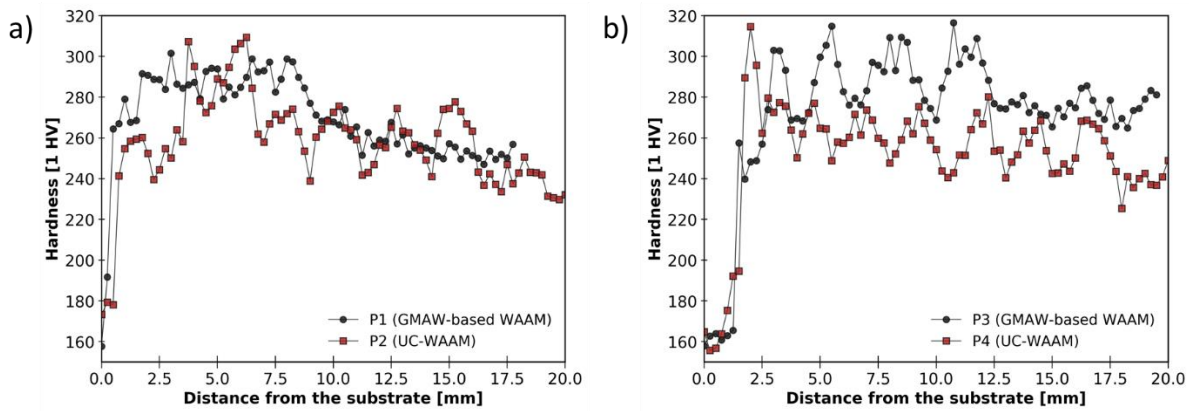


Figure 7.13 - Hardness values measurements across the sample height: a) P1 and P2; b) P3 and P4.

Stress-strain curves obtained across the deposition direction are depicted in Figure 7.14. Overall, all samples exhibited high strength (>700 MPa) and excellent ductility (>25 % for GMAW-based WAAM and >30 % for UC-WAAM samples). These results show that the novel UC-WAAM process variant is not detrimental to the parts' mechanical properties. Future studies will address the orientation dependence of the mechanical properties with the building and deposition directions.

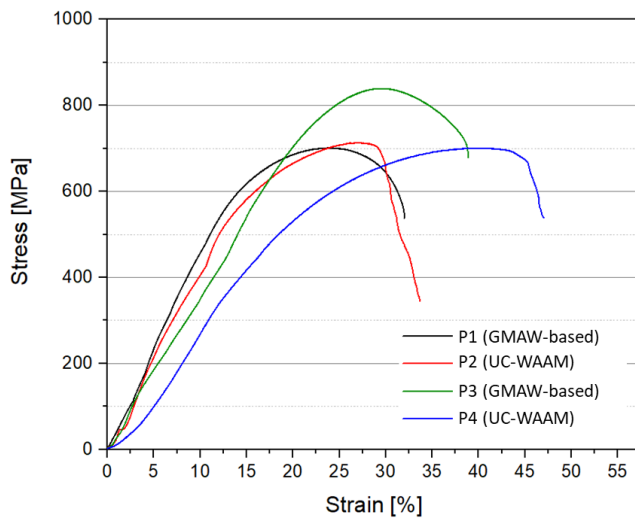


Figure 7.14 - Uniaxial tensile Stress-Elongation curves of the samples built.

7.4 Potential applications

Although WAAM is suitable for producing large parts with high deposition rates, some drawbacks still exist. One major issue in WAAM is the ability to produce overhang structures or self-supported ones. Kazanas et al. [222] and Yuan et al. [223] used CMT to create parts along the horizontal direction on a vertically fixed substrate. Another potential solution is having the substrate mounted on a 5-axis

machine, which allows it to rotate the part as it is being deposited, facilitating and increasing the possibility of WAAM for industrial applications [224]. UC-WAAM offers a new expedite solution for creating self-supporting or overhang structures, as will be demonstrated. To do so, a non-conductive/non-metallic material is used. This block of material acts as a support and can be easily removed during or after the UC-WAAM process.

A graphite block was used to show the ability of UC-WAAM to create supportless structures. A schematic representation of the part build procedure is depicted in Figure 7.15 a), while the building sequence is shown in Figure 7.15 b). The graphite block was inserted after the deposition of the 6th layer between the already deposited beads. Subsequently, with the UC-WAAM process's restart, the feedstock material droplets started to be detached, landing on the graphite block. It must be emphasized that there is no disruption of the electric arc since the current does not flow through the graphite block. After the deposition of the 10th layer, the graphite block was removed. The final UC-WAAM part is depicted in Figure 7.15 b).

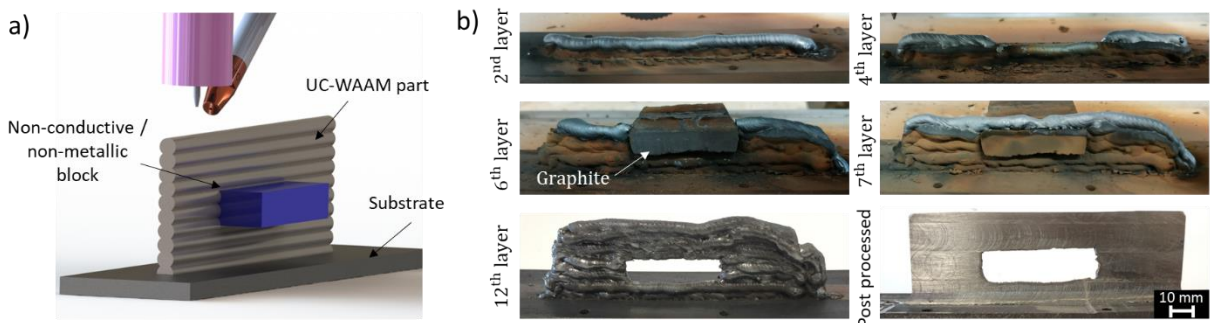


Figure 7.15 - a) Schematic 3D view of the setup used to build overhang structures; b) UC-WAAM building sequence steps for the overhang structures.

7.5 Conclusions

A novel variant of the WAAM process was developed and experimentally validated. UC-WAAM differs from conventional GMAW-based and GTAW-based WAAM by using the wire feedstock material as the positive pole and the non-consumable tungsten electrode as the negative pole. The main findings of this work include:

- UC-WAAM is a valuable alternative for arc-based AM, as it offers good arc stability and avoids spatter formation. Moreover, the deposition rates of UC-WAAM are similar to those obtained via GMAW-based WAAM. Still, the layers are narrower and higher due to higher solidification rates, with a small dilution of the precedent layer;

- Despite the process heat input being the same, by thermal analysis, it was observed that higher cooling rates, up to $11\text{ }^{\circ}\text{C/s}$, and a peak temperature difference, up to $\approx 400\text{ }^{\circ}\text{C}$, are achieved with UC-WAAM. This result can have a significant microstructural impact on materials where the thermal cycle plays a significant role;
- In UC-WAAM and GMAW-based WAAM, fine grain size structures were developed, and the produced parts presented high mechanical strength and ductility;
- An overhang structure was fabricated using a non-conductive/non-metallic block, highlighting the potential for UC-WAAM to be used for overhang 3D structures.

7.6 Summary

This chapter tested a welding technique yet to be used in Additive Manufacturing. Even though the process parameters need to be carefully chosen to avoid excessive waviness, this variant was seen to be able to reduce the temperatures that developed during parts' fabrication.

1
2
3 **8.**

CONCLUSIONS AND FUTURE WORKS

4

8.1 Introduction

5 The main conclusions of the entire work are presented in this chapter. It summarizes the results of the
6 different heat treatments performed, the effect of the introduction of particles during Wire and Arc
7 Additive Manufacturing of Inconel 625 and HSLA steel, the production, and characterization of
8 Functionally Graded Materials, and finally, the results of the developments made using concerning a
9 new WAAM variant to reduce the heat transferred to the parts during fabrication.

10

8.2 Major conclusions

11 This thesis aimed to develop technological advances capable of enhancing and tailoring the
12 microstructure and mechanical properties of metal parts produced with WAAM, contributing to its
13 industrialization. At the end of each chapter, the key conclusions were reported in detail, but in this
14 section, only the most relevant ones are summarized.

15 Regarding technological advances, every customized torch and the 3D printing apparatus (XYZ-
16 motion equipment) were suitable for the developed research, with accuracy and repeatability to be
17 used in production with different materials.

18

19

Heat treatments performed on Wire and Arc Additive Manufacturing Parts

20

Stainless steel 316L

- 21 • The as-built samples presented an austenitic matrix with skeletal and lathy δ-ferrite
22 morphologies aligned with the solidification direction;
- 23 • After the stress relief at 400°C, the microstructure retained similar characteristics to that of the
24 as-built condition, but the average hardness decreased by 4 HV;
- 25 • The heat treatment performed at 950 °C for two hours led to the transformation of δ-ferrite in
26 the σ-phase. The hardness decreased by 5 HV compared to the as-built sample;

- 1 • The temperature of 1050 °C showed to be enough to promote δ-ferrite dissolution, avoiding
2 the precipitation of the metastable σ-phase. Efficient dissolution of δ-ferrite dendrites can be
3 achieved with higher solubilization temperature, as heat treatments performed at 1050 and
4 1200 °C resulted in a retained amount of δ-ferrite of approximately 6.5 % and 0.4,
5 respectively.

6

7 **Inconel 625**

- 8 • The as-built samples presented an γ matrix with γ',γ'', MC carbides, and Laves as secondary
9 phases;
- 10 • During the stress relief heat treatment performed at 870°C, in-situ synchrotron X-ray
11 diffraction revealed δ-phase precipitation;
- 12 • Both annealings performed at 1050 °C and 1150 °C for 1 hour fully dissolved the δ-phase.
13 However, the time was short for dissolving both carbides and Laves phase. The annealing at
14 1050 °C did not affect the hardness measurements, but at 1150 °C, hardness decreased by
15 approximately 10 % (21 HV);
- 16 • The heat treatment performed at 750 °C for 4 hours resulted in the precipitation of γ'' (Ni₃Nb),
17 causing an increase of hardness from 225 HV to 236 HV.

18

19 **Improvement of Parts Properties via Inoculation of Refinement Particles**

20 **High strength low alloy steel**

- 21 • The introduction of SiC particles in HSLA steel parts promoted the formation of a more
22 homogenous microstructure with a nearly isotropic grains structure;
- 23 • The partial dissociation of the SiC particles in the molten pool led to an increase in the carbon
24 content, which resulted in the coexistence of ferrite, retained austenite (M-A), and cementite
25 (Fe₃C). The hardness increased, on average, from 290 to 426 HV;
- 26 • The ultimate tensile strength of the SiC-containing samples increased by 200 MPa (23 %) and
27 146 MPa (16 %) in the horizontal and vertical directions, respectively. The elongation to
28 fracture with particles decreased by 16 and 6 % in the same directions.

29

30 **Inconel 625**

- 31 • The proof of concept prototype showed that is possible to add particles to the molten pool via
32 the new feeding mechanism where the particles are mixed with a solder flux that evaporates
33 before reaching the electric arc. Thus, this new variant is relevant and can be used with
34 different materials and particles to be further incorporated into XYZ-motion equipment or a
35 conventional robotic arm to produce parts;

- 1 • FEM simulations confirmed that the deposition strategy used of keeping a constant interpass
2 temperature would not result in peak temperatures above the melting point of TiB₂;
- 3 • Microstructural analysis showed a reduction in the size of the interdendritic segregation
4 regions with the introduction of TiB₂ particles, thus enriching the matrix with solid solution
5 strengtheners;
- 6 • The average grain area was substantially reduced in the sample with TiB₂ addition. Besides
7 replacing columnar grains with equiaxed ones, EBSD results revealed that these refined
8 equiaxed grains were also the starting point for the next layers to grow, resulting in finer
9 columnar grains at the remelted regions;
- 10 • In the sample that contained additions of TiB₂, synchrotron X-ray diffraction revealed the
11 existence of peaks associated with δ-phase (Ni₃Nb) that were not present in the as-built
12 sample.
- 13

14 **Functionally Graded Materials**

15 **High strength low alloy steel to Copper alloy**

- 16 • A mixture of Cu (FCC) and Fe (BCC) phases was visible at the interface region. The Fe (BCC)
17 phase was found to be residual δ-ferrite. No brittle intermetallic phases were found in the
18 interface;
- 19 • At the interface, a gradient of composition, hardness, electrical conductivity, and electrical
20 impedance was obtained. Even though an abrupt transition was made with these two
21 materials, the consequent remelting and heating of previously deposited layers, when a new
22 one is added, resulted in a large interface region (≈ 12 mm);
- 23 • An ultimate tensile strength of 690 MPa and an elongation at fracture of 16.6 % were achieved
24 in the FGM;
- 25 • The fracture occurred in the Cu region near the interface, in which the microstructure involves
26 a combination of a dendritic-type structure of Fe (BCC) phases and β precipitates in a Cu
27 matrix, demonstrating that the interface strength is higher than the region composed only by
28 copper.
- 29

30 **Stainless steel 316L to Inconel 625**

- 31 • Direct and smooth transition interfaces were tested and characterized;
- 32 • Microstructure analysis revealed that all interfaces and base materials samples had an
33 austenitic matrix, and parts were well bonded and free of defects;

- The FGMs built with a smooth-type transition had phases at the interface that were not present in the as-built materials, such as the δ -phase (Ni_3Nb) and MC carbides. None of these was formed within the FGMs built with a direct interface;
- The FGMs built with a direct interface showed strengths higher than 542 MPa and elongations higher than 61.6 %. The smooth transition FGM-types only showed strengths up to 503 MPa and elongations up to 32.4 %;
- The fracture location in the direct and smooth-type interface FGMs were located at the 50 and 65 wt.% of 316L stainless steel regions, respectively;
- The FGMs built with a smooth-type transition showed a gradual increase of hardness but only after the composition ratio of 70 wt.% 316L stainless steel/30 wt.% Inconel 625. Before that, the hardness had decreased from the stainless steel region due to the depletion of δ -ferrite.

Developments of a new WAAM variant (UC-WAAM)

- Ultra Cold-Wire and Arc Additive Manufacturing (UC-WAAM) is a valuable alternative for arc-based AM, as it offers good arc stability and avoids spatter formation;
- By using the same process parameters with UC-WAAM and GMAW-based WAAM, higher cooling rates with UC-WAAM, up to 11 °C/s, and a maximum peak temperature difference, up to ≈ 400 °C was achieved;
- An overhang structure was fabricated using a non-conductive/non-metallic block, highlighting the potential for UC-WAAM to be used for fabricating overhang structures.

8.3 Recommendations for future works

Due to the available resources, this thesis did not further investigate various topics. This section briefly summarizes suggestions to extend this work into different topics of interest.

Concerning the heat treatments performed on Inconel 625 parts, further microstructural characterization after the heat treatments is required to understand the microstructural changes. Furthermore, increasing soaking times at high temperatures should be tested to evaluate the possibility of completely dissolving the secondary phases in the as-built material.

Concerning the introduction of ceramic particles on Inconel 625, tensile testing should be made to further mechanically characterize the samples. It is suggested that a design of experiments before using grain refinement particles to determine the optimized process parameters that minimize the region with columnar grains, enhancing the effectiveness of using such particles. Also, the influence of the process parameters on the growth rate, R, and thermal gradients, G, should be measured. Concerning technological developments, it should be established what percentage of the extruded particles are added to the molten pool to assess the process efficiency. It should also be determined if

1 the added particles or the flux influence the amount of energy transferred to the fabricated part and
2 what effect it has on the developed temperatures. The refinement of Inconel 625 can be tested with
3 different particle sizes and consequently correlated with its effect on the grain size and mechanical
4 properties. It is also important to develop finite element models that can predict microstructure
5 evolution when ceramic particles are added to the molten pool. By combining two of the results of this
6 thesis, the optimized heat treatments that dissolved the δ -phase can be used to dissolve this phase
7 that was present on the Inconel 625 samples that had additions of TiB_2 .

8 Regarding the Functional Graded Materials, Copper layers can be processed using pulse or AC
9 welding modes to achieve better penetration and surface finishing. When building FGMS with a direct
10 interface, further studies can focus on changing the process parameters, correlating the heat input
11 with the dilution between the two materials, and further understanding its effect on the final properties.
12 Complex geometries design should be developed to demonstrate the potential of copper and steel
13 combinations for injection mold applications with higher complexity, including the existence of cooling
14 channels. It is also necessary to design other heat treatments with higher temperatures and soaking
15 times to dissolve the large, segregated regions with secondary precipitates on the 316L stainless
16 steel-Inconel 625 FGM. Since the materials in the 316L stainless steel-Inconel 625 FGM will behave
17 differently, further research should be developed to understand the behavior of each heat treatment at
18 different compositional ratios.

19 Concerning the Ultra Cold Wire and Arc Additive Manufacturing (UC-WAAM) process variant, it should
20 be further emphasize the thermal effect that this new variant can have during build parts by
21 establishing the time needed to stabilize the interpass temperature against other technologies.
22 Moreover, this variant should be tested to build parts with more layers and with different designs
23 containing overhang structures.

24

Bibliography

- [1] International Organization for Standardization. Additive manufacturing — General principles — Fundamentals and vocabulary (ISO/ASTM : 52900), (2021).
- [2] O. V. Panchenko, L.A. Zhabrev, D. V. Kurushkin, A.A. Popovich, Macrostructure and Mechanical Properties of Al – Si, Al – Mg – Si, and Al – Mg – Mn Aluminum Alloys Produced by Electric Arc Additive Growth, Met. Sci. Heat Treat. 60 (2019) 749–754. <https://doi.org/10.1007/s11041-019-00351-z>.
- [3] F. Martina, J. Ding, S. Williams, A. Caballero, G. Pardal, L. Quintino, Tandem metal inert gas process for high productivity wire arc additive manufacturing in stainless steel, Addit. Manuf. 25 (2019) 545–550. <https://doi.org/10.1016/j.addma.2018.11.022>.
- [4] S.W. Williams, F. Martina, A.C. Addison, J. Ding, G. Pardal, P. Colegrove, Wire + Arc Additive Manufacturing, Mater. Sci. Technol. 32 (2016) 641–647. <https://doi.org/10.1179/1743284715Y.0000000073>.
- [5] M.. Easton, D.. StJohn, A model of grain refinement incorporating alloy constitution and potency of heterogeneous nucleant particles, Acta Mater. 49 (2001) 1867–1878. [https://doi.org/10.1016/S1359-6454\(00\)00368-2](https://doi.org/10.1016/S1359-6454(00)00368-2).
- [6] W. Kurz and D.J. Fisher, Fundamentals of Solidification, 3rd ed., Trans Tech Pubn, 1990.
- [7] J.C. Lippold, Welding Metallurgy and Weldability, John Wiley & Sons, Inc., 2015.
- [8] J. Donoghue, A.A. Antonysamy, F. Martina, P.A. Colegrove, S.W. Williams, P.B. Prangnell, The effectiveness of combining rolling deformation with Wire–Arc Additive Manufacture on β -grain refinement and texture modification in Ti–6Al–4V, Mater. Charact. 114 (2016) 103–114. <https://doi.org/10.1016/J.MATCHAR.2016.02.001>.
- [9] C.R. Cunningham, J.M. Flynn, A. Shokrani, V. Dhokia, S.T. Newman, Invited review article: Strategies and processes for high quality wire arc additive manufacturing, Addit. Manuf. 22 (2018) 672–686. <https://doi.org/10.1016/j.addma.2018.06.020>.
- [10] H. Li, Y. Huang, S. Jiang, Y. Lu, X. Gao, X. Lu, Z. Ning, J. Sun, Columnar to equiaxed transition in additively manufactured CoCrFeMnNi high entropy alloy, Mater. Des. 197 (2021)

109262. <https://doi.org/10.1016/j.matdes.2020.109262>.

- [11] S. Kou, Welding Metallurgy, John Wiley & Sons, Inc., Hoboken, NJ, USA, 2002. <https://doi.org/10.1002/0471434027>.
- [12] T.A. Rodrigues, V. Duarte, J.A. Avila, T.G. Santos, R.M. Miranda, J.P. Oliveira, Wire and arc additive manufacturing of HSLA steel: Effect of thermal cycles on microstructure and mechanical properties, *Addit. Manuf.* 27 (2019) 440–450. <https://doi.org/10.1016/j.addma.2019.03.029>.
- [13] W. Yangfan, C. Xizhang, S. Chuanchu, Microstructure and mechanical properties of Inconel 625 fabricated by wire-arc additive manufacturing, *Surf. Coatings Technol.* 374 (2019) 116–123. <https://doi.org/10.1016/j.surfcoat.2019.05.079>.
- [14] D.G. McCartney, Grain refining of aluminium and its alloys using inoculants, *Int. Mater. Rev.* 34 (1989) 247–260. <https://doi.org/10.1179/imr.1989.34.1.247>.
- [15] D.H. Stjohn, M. Qian, M.A. Easton, P. Cao, The Interdependence Theory: The relationship between grain formation and nucleant selection, *Acta Mater.* 59 (2011) 4907–4921. <https://doi.org/10.1016/j.actamat.2011.04.035>.
- [16] D.H. Stjohn, M.A. Easton, M. Qian, J.A. Taylor, Grain refinement of magnesium alloys: A review of recent research, theoretical developments, and their application, *Metall. Mater. Trans. A Phys. Metall. Mater. Sci.* 44 (2013) 2935–2949. <https://doi.org/10.1007/s11661-012-1513-x>.
- [17] M.A. Easton, M. Qian, A. Prasad, D.H. StJohn, Recent advances in grain refinement of light metals and alloys, *Curr. Opin. Solid State Mater. Sci.* 20 (2016) 13–24. <https://doi.org/10.1016/j.cossms.2015.10.001>.
- [18] B. Wu, Z. Pan, D. Ding, D. Cuiuri, H. Li, J. Xu, J. Norrish, A review of the wire arc additive manufacturing of metals: properties, defects and quality improvement, *J. Manuf. Process.* 35 (2018) 127–139. <https://doi.org/10.1016/j.jmapro.2018.08.001>.
- [19] P.A. Colegrove, H.E. Coules, J. Fairman, F. Martina, T. Kashoob, H. Mamash, L.D. Cozzolino, Microstructure and residual stress improvement in wire and arc additively manufactured parts through high-pressure rolling, *J. Mater. Process. Technol.* 213 (2013) 1782–1791. <https://doi.org/10.1016/j.jmatprotec.2013.04.012>.
- [20] F. Martina, M.J. Roy, B.A. Szost, S. Terzi, P.A. Colegrove, S.W. Williams, P.J. Withers, J. Meyer, M. Hofmann, Residual stress of as-deposited and rolled wire+arc additive manufacturing Ti–6Al–4V components, *Mater. Sci. Technol.* 32 (2016) 1439–1448. <https://doi.org/10.1080/02670836.2016.1142704>.
- [21] J.L. Gu, J.L. Ding, B.Q. Cong, J. Bai, H.M. Gu, S.W. Williams, Y.C. Zhai, The Influence of Wire Properties on the Quality and Performance of Wire+Arc Additive Manufactured Aluminium

- Parts, Adv. Mater. Res. 1081 (2014) 210–214.
<https://doi.org/https://doi.org/10.4028/www.scientific.net/amr.1081.210>.
- [22] V.I. Murav'ev, R.F. Krupskii, R.A. Fizulakov, P.G. Demyshev, Effect of the quality of filler wire on the formation of pores in welding of titanium alloys, Weld. Int. 22 (2008) 853–858. <https://doi.org/10.1080/09507110802650610>.
- [23] J. Ding, P. Colegrove, F. Martina, S. Williams, R. Wiktorowicz, M.R. Palt, Development of a laminar flow local shielding device for wire + arc additive manufacture, J. Mater. Process. Technol. 226 (2015) 99–105. <https://doi.org/10.1016/j.jmatprotec.2015.07.005>.
- [24] J.N. DuPont, J.C. Lippold, S.D. Kiser, Welding Metallurgy and Weldability of Nickel-Base Alloys, John Wiley & Sons, Inc., Hoboken, NJ, USA, 2009. <https://doi.org/10.1002/9780470500262>.
- [25] F. Martina, P.A. Colegrove, S.W. Williams, J. Meyer, Microstructure of Interpass Rolled Wire + Arc Additive Manufacturing Ti-6Al-4V Components, Metall. Mater. Trans. A. 46 (2015) 6103–6118. <https://doi.org/10.1007/s11661-015-3172-1>.
- [26] X. Xu, S. Ganguly, J. Ding, C.E. Seow, S. Williams, Enhancing mechanical properties of wire + arc additively manufactured INCONEL 718 superalloy through in-process thermomechanical processing, Mater. Des. 160 (2018) 1042–1051. <https://doi.org/10.1016/j.matdes.2018.10.038>.
- [27] V.R. Duarte, T.A. Rodrigues, N. Schell, R.M. Miranda, J.P. Oliveira, T.G. Santos, Hot forging wire and arc additive manufacturing (HF-WAAM), Addit. Manuf. 35 (2020) 101193. <https://doi.org/10.1016/j.addma.2020.101193>.
- [28] V.R. Duarte, T.A. Rodrigues, N. Schell, R.M. Miranda, J.P. Oliveira, T.G. Santos, In-situ hot forging directed energy deposition-arc of CuAl8 alloy, Addit. Manuf. 55 (2022) 102847. <https://doi.org/10.1016/j.addma.2022.102847>.
- [29] R. Sun, L. Li, Y. Zhu, W. Guo, P. Peng, B. Cong, J. Sun, Z. Che, B. Li, C. Guo, L. Liu, Microstructure, residual stress and tensile properties control of wire-arc additive manufactured 2319 aluminum alloy with laser shock peening, J. Alloys Compd. 747 (2018) 255–265. <https://doi.org/10.1016/j.jallcom.2018.02.353>.
- [30] J.R. Hönnige, P. Colegrove, S. Williams, Improvement of microstructure and mechanical properties in Wire + Arc Additively Manufactured Ti-6Al-4V with Machine Hammer Peening, Procedia Eng. 216 (2017) 8–17. <https://doi.org/10.1016/j.proeng.2018.02.083>.
- [31] F.W.C. Farias, J. da Cruz Payão Filho, V.H.P. Moraes e Oliveira, Prediction of the interpass temperature of a wire arc additive manufactured wall: FEM simulations and artificial neural network, Addit. Manuf. 48 (2021) 102387. <https://doi.org/10.1016/j.addma.2021.102387>.
- [32] E.R. Denlinger, J.C. Heigel, P. Michaleris, T.A. Palmer, Effect of inter-layer dwell time on distortion and residual stress in additive manufacturing of titanium and nickel alloys, J. Mater.

Process. Technol. 215 (2015) 123–131. <https://doi.org/10.1016/j.jmatprotec.2014.07.030>.

- [33] F. Montevercchi, G. Venturini, N. Grossi, A. Scippa, G. Campatelli, Idle time selection for wire-arc additive manufacturing: A finite element-based technique, Addit. Manuf. 21 (2018) 479–486. <https://doi.org/10.1016/j.addma.2018.01.007>.
- [34] B. Wu, Z. Pan, D. Ding, D. Cuiuri, H. Li, Z. Fei, The effects of forced interpass cooling on the material properties of wire arc additively manufactured Ti6Al4V alloy, J. Mater. Process. Technol. 258 (2018) 97–105. <https://doi.org/10.1016/j.jmatprotec.2018.03.024>.
- [35] F. Li, S. Chen, J. Shi, Y. Zhao, H. Tian, Thermoelectric Cooling-Aided Bead Geometry Regulation in Wire and Arc-Based Additive Manufacturing of Thin-Walled Structures, Appl. Sci. 8 (2018) 207. <https://doi.org/10.3390/app8020207>.
- [36] X. Bai, H. Zhang, G. Wang, Modeling of the moving induction heating used as secondary heat source in weld-based additive manufacturing, Int. J. Adv. Manuf. Technol. 77 (2015) 717–727. <https://doi.org/10.1007/s00170-014-6475-2>.
- [37] J. Xiong, Y. Lei, R. Li, Finite element analysis and experimental validation of thermal behavior for thin-walled parts in GMAW-based additive manufacturing with various substrate preheating temperatures, Appl. Therm. Eng. 126 (2017) 43–52. <https://doi.org/10.1016/j.applthermaleng.2017.07.168>.
- [38] E.A. Alberti, B.M.P. Bueno, A.S.C.M. D’Oliveira, Additive manufacturing using plasma transferred arc, Int. J. Adv. Manuf. Technol. 83 (2016) 1861–1871. <https://doi.org/10.1007/s00170-015-7697-7>.
- [39] Z. Li, C. Liu, T. Xu, L. Ji, D. Wang, J. Lu, S. Ma, H. Fan, Reducing arc heat input and obtaining equiaxed grains by hot-wire method during arc additive manufacturing titanium alloy, Mater. Sci. Eng. A. 742 (2019) 287–294. <https://doi.org/10.1016/j.msea.2018.11.022>.
- [40] X. Xu, J. Ding, S. Ganguly, C. Diao, S. Williams, Preliminary Investigation of Building Strategies of Maraging Steel Bulk Material Using Wire + Arc Additive Manufacture, J. Mater. Eng. Perform. (2018) 5–11. <https://doi.org/10.1007/s11665-018-3521-5>.
- [41] B. Cong, J. Ding, S. Williams, Effect of arc mode in cold metal transfer process on porosity of additively manufactured Al-6.3%Cu alloy, Int. J. Adv. Manuf. Technol. 76 (2015) 1593–1606. <https://doi.org/10.1007/s00170-014-6346-x>.
- [42] F. Chang, D. Gu, D. Dai, P. Yuan, Selective laser melting of in-situ Al₄SiC₄ + SiC hybrid reinforced Al matrix composites: Influence of starting SiC particle size, Surf. Coatings Technol. 272 (2015) 15–24. <https://doi.org/10.1016/j.surfcoat.2015.04.029>.
- [43] C. Wei, H. Gu, X. Zhang, Y. Chueh, L. Li, Hybrid ultrasonic and mini-motor vibration-induced irregularly shaped powder delivery for multiple materials additive manufacturing, Addit. Manuf. 33 (2020) 101138. <https://doi.org/10.1016/j.addma.2020.101138>.

- [44] M.J. Bermingham, D.H. StJohn, J. Krynen, S. Tedman-Jones, M.S. Dargusch, Promoting the columnar to equiaxed transition and grain refinement of titanium alloys during additive manufacturing, *Acta Mater.* 168 (2019) 261–274. <https://doi.org/10.1016/j.actamat.2019.02.020>.
- [45] M.J. Bermingham, S.D. McDonald, M.S. Dargusch, Effect of trace lanthanum hexaboride and boron additions on microstructure, tensile properties and anisotropy of Ti-6Al-4V produced by additive manufacturing, *Mater. Sci. Eng. A.* 719 (2018) 1–11. <https://doi.org/10.1016/j.msea.2018.02.012>.
- [46] F. Martina, J. Mehnen, S.W. Williams, P. Colegrove, F. Wang, Investigation of the benefits of plasma deposition for the additive layer manufacture of Ti-6Al-4V, *J. Mater. Process. Technol.* 212 (2012) 1377–1386. <https://doi.org/10.1016/j.jmatprot.2012.02.002>.
- [47] T.G. Santos, R.M. Miranda, P. Vilaça, J.P. Teixeira, J. dos Santos, Microstructural mapping of friction stir welded AA 7075-T6 and AlMgSc alloys using electrical conductivity, *Sci. Technol. Weld. Join.* 16 (2011) 630–635. <https://doi.org/10.1179/1362171811Y.0000000052>.
- [48] G.L. Sorger, J.P. Oliveira, P.L. Inácio, N. Enzinger, P. Vilaça, R.M. Miranda, T.G. Santos, Non-destructive microstructural analysis by electrical conductivity: Comparison with hardness measurements in different materials, *J. Mater. Sci. Technol.* 35 (2019) 360–368. <https://doi.org/10.1016/j.jmst.2018.09.047>.
- [49] A.P. Hammersley, S.O. Svensson, M. Hanfland, A.N. Fitch, D. Hausermann, Two-dimensional detector software: From real detector to idealised image or two-theta scan, *High Press. Res.* 14 (1996) 235–248. <https://doi.org/10.1080/08957959608201408>.
- [50] P. Crowther, C. Daniel, *xrdfit*: A Python package for fitting synchrotron X-ray diffraction spectra, *J. Open Source Softw.* 5 (2020) 2381. <https://doi.org/10.21105/joss.02381>.
- [51] J.D. Escobar, G.A. Faria, L. Wu, J.P. Oliveira, P.R. Mei, A.J. Ramirez, Austenite reversion kinetics and stability during tempering of a Ti-stabilized supermartensitic stainless steel: Correlative in situ synchrotron x-ray diffraction and dilatometry, *Acta Mater.* 138 (2017) 92–99. <https://doi.org/10.1016/j.actamat.2017.07.036>.
- [52] L. Lutterotti, R. Vasin, H.-R. Wenk, Rietveld texture analysis from synchrotron diffraction images. I. Calibration and basic analysis, *Powder Diffr.* 29 (2014) 76–84. <https://doi.org/10.1017/S0885715613001346>.
- [53] O. Arnold, J.C. Bilheux, J.M. Borreguero, A. Buts, S.I. Campbell, L. Chapon, M. Doucet, N. Draper, R. Ferraz Leal, M.A. Gigg, V.E. Lynch, A. Markvardsen, D.J. Mikkelsen, R.L. Mikkelsen, R. Miller, K. Palmen, P. Parker, G. Passos, T.G. Perring, P.F. Peterson, S. Ren, M.A. Reuter, A.T. Savici, J.W. Taylor, R.J. Taylor, R. Tolchenov, W. Zhou, J. Zikovsky, Mantid—Data analysis and visualization package for neutron scattering and μ SR experiments, *Nucl. Instruments Methods Phys. Res. Sect. A Accel. Spectrometers, Detect. Assoc. Equip.*

- 764 (2014) 156–166. <https://doi.org/10.1016/j.nima.2014.07.029>.
- [54] J. Blaber, B. Adair, A. Antoniou, Ncorr: Open-Source 2D Digital Image Correlation Matlab Software, *Exp. Mech.* 55 (2015) 1105–1122. <https://doi.org/10.1007/s11340-015-0009-1>.
- [55] J.-O. Andersson, T. Helander, L. Höglund, P. Shi, B. Sundman, Thermo-Calc & DICTRA, computational tools for materials science, *Calphad.* 26 (2002) 273–312. [https://doi.org/10.1016/S0364-5916\(02\)00037-8](https://doi.org/10.1016/S0364-5916(02)00037-8).
- [56] S.J. Zinkle, G.S. Was, Materials challenges in nuclear energy, *Acta Mater.* 61 (2013) 735–758. <https://doi.org/https://doi.org/10.1016/j.actamat.2012.11.004>.
- [57] S.K. Lee, S.-H. Yun, H.G. Joo, S.J. Noh, Deuterium transport and isotope effects in type 316L stainless steel at high temperatures for nuclear fusion and nuclear hydrogen technology applications, *Curr. Appl. Phys.* 14 (2014) 1385–1388. <https://doi.org/10.1016/j.cap.2014.08.006>.
- [58] M. Ziętala, T. Durejko, M. Polański, I. Kunce, T. Płociński, W. Zieliński, M. Łazińska, W. Stępniowski, T. Czujko, K.J. Kurzydłowski, Z. Bojar, The microstructure, mechanical properties and corrosion resistance of 316L stainless steel fabricated using laser engineered net shaping, *Mater. Sci. Eng. A.* 677 (2016) 1–10. <https://doi.org/10.1016/j.msea.2016.09.028>.
- [59] Y. Dai, X. Zheng, P. Ding, Review on sodium corrosion evolution of nuclear-grade 316 stainless steel for sodium-cooled fast reactor applications, *Nucl. Eng. Technol.* 53 (2021) 3474–3490. <https://doi.org/10.1016/j.net.2021.05.021>.
- [60] Q. He, F. Pan, D. Wang, H. Liu, F. Guo, Z. Wang, Y. Ma, Microstructure and properties of 316L stainless steel foils for pressure sensor of pressurized water reactor, *Nucl. Eng. Technol.* 53 (2021) 172–177. <https://doi.org/10.1016/j.net.2020.06.006>.
- [61] R.K. Desu, H. Nitin Krishnamurthy, A. Balu, A.K. Gupta, S.K. Singh, Mechanical properties of Austenitic Stainless Steel 304L and 316L at elevated temperatures, *J. Mater. Res. Technol.* 5 (2016) 13–20. <https://doi.org/https://doi.org/10.1016/j.jmrt.2015.04.001>.
- [62] H.P. Seifert, S. Ritter, H.J. Leber, Corrosion fatigue crack growth behaviour of austenitic stainless steels under light water reactor conditions, *Corros. Sci.* 55 (2012) 61–75. <https://doi.org/10.1016/j.corsci.2011.10.005>.
- [63] F.L. Xu, J.Z. Duan, C.G. Lin, B.R. Hou, Influence of Marine Aerobic Biofilms on Corrosion of 316L Stainless Steel, *J. Iron Steel Res. Int.* 22 (2015) 715–720. [https://doi.org/10.1016/S1006-706X\(15\)30062-5](https://doi.org/10.1016/S1006-706X(15)30062-5).
- [64] M.M. DEWIDAR, K.A. KHALIL, J.K. LIM, Processing and mechanical properties of porous 316L stainless steel for biomedical applications, *Trans. Nonferrous Met. Soc. China.* 17 (2007) 468–473. [https://doi.org/10.1016/S1003-6326\(07\)60117-4](https://doi.org/10.1016/S1003-6326(07)60117-4).
- [65] X. Lou, M.A. Othon, R.B. Rebak, Corrosion fatigue crack growth of laser additively-

manufactured 316L stainless steel in high temperature water, *Corros. Sci.* 127 (2017) 120–130. <https://doi.org/10.1016/j.corsci.2017.08.023>.

- [66] J.A. Brooks, F.J. Lambert, Effects of Phosphorus, Sulfur and Ferrite Content on Weld Cracking of Type 309 Stainless Steel., *Weld. J. (Miami, Fla.)*. 57 (1978).
- [67] A. Ben Rhouma, T. Amadou, H. Sidhom, C. Braham, Correlation between microstructure and intergranular corrosion behavior of low delta-ferrite content AISI 316L aged in the range 550–700 °C, *J. Alloys Compd.* 708 (2017) 871–886. <https://doi.org/10.1016/j.jallcom.2017.02.273>.
- [68] J.C. Lippold, W.F. Savage, Solidification of Austenitic Stainless Steel Weldments - 3. the Effect of Solidification Behavior on Hot Cracking Susceptibility., *Weld. J. (Miami, Fla.)*. 61 (1982) 388–396.
- [69] P.D. Jablonski, J.A. Hawk, Homogenizing Advanced Alloys: Thermodynamic and Kinetic Simulations Followed by Experimental Results, *J. Mater. Eng. Perform.* 26 (2017) 4–13. <https://doi.org/10.1007/s11665-016-2451-3>.
- [70] T.F. de Andrade, A.M. Kliauga, R.L. Plaut, A.F. Padilha, Precipitation of Laves phase in a 28%Cr–4%Ni–2%Mo–Nb superferritic stainless steel, *Mater. Charact.* 59 (2008) 503–507. <https://doi.org/10.1016/j.matchar.2007.03.006>.
- [71] A. Perron, C. Toffolon-Masclet, X. Ledoux, F. Buy, T. Guibert, S. Urvoy, S. Bosonnet, B. Marini, F. Cortial, G. Texier, C. Harder, V. Vignal, P. Petit, J. Farré, E. Suzon, Understanding sigma-phase precipitation in a stabilized austenitic stainless steel (316Nb) through complementary CALPHAD-based and experimental investigations, *Acta Mater.* 79 (2014) 16–29. <https://doi.org/10.1016/j.actamat.2014.06.066>.
- [72] M.J. Cieslak, A.M. Ritter, W.F. Savage, Chi-Phase Formation During Solidification and Cooling of Cf-8M Weld Metal., *Weld. J. (Miami, Fla.)*. 63 (1984).
- [73] A.D. Warren, I.J. Griffiths, P.E.J. Flewitt, Precipitation within localised chromium-enriched regions in a Type 316H austenitic stainless steel, *J. Mater. Sci.* 53 (2018) 6183–6197. <https://doi.org/10.1007/s10853-017-1748-4>.
- [74] D.M. Escriba, E. Materna-Morris, R.L. Plaut, A.F. Padilha, Chi-phase precipitation in a duplex stainless steel, *Mater. Charact.* 60 (2009) 1214–1219. <https://doi.org/10.1016/j.matchar.2009.04.013>.
- [75] X. Chen, J. Li, X. Cheng, B. He, H. Wang, Z. Huang, Microstructure and mechanical properties of the austenitic stainless steel 316L fabricated by gas metal arc additive manufacturing, *Mater. Sci. Eng. A.* 703 (2017) 567–577. <https://doi.org/10.1016/j.msea.2017.05.024>.
- [76] P. Long, D. Wen, J. Min, Z. Zheng, J. Li, Y. Liu, Microstructure evolution and mechanical properties of a wire-arc additive manufactured austenitic stainless steel: Effect of processing parameter, *Materials (Basel)*. 14 (2021). <https://doi.org/10.3390/ma14071681>.

- [77] D.M.E. Villanueva, F.C.P. Junior, R.L. Plaut, A.F. Padilha, Comparative study on sigma phase precipitation of three types of stainless steels: Austenitic, superferritic and duplex, Mater. Sci. Technol. 22 (2006) 1098–1104. <https://doi.org/10.1179/174328406X109230>.
- [78] C.-C. Hsieh, W. Wu, Overview of Intermetallic Sigma: Phase Precipitation in Stainless Steels, ISRN Metall. 2012 (2012) 1–16. <https://doi.org/10.5402/2012/732471>.
- [79] K. Chan, S. Tjong, Effect of Secondary Phase Precipitation on the Corrosion Behavior of Duplex Stainless Steels, Materials (Basel). 7 (2014) 5268–5304. <https://doi.org/10.3390/ma7075268>.
- [80] V.S. Raghunathan, V. Seetharaman, S. Venkadesan, P. Rodriguez, The influence of post weld heat treatments on the structure, composition and the amount of ferrite in type 316 stainless steel welds, Metall. Trans. A. 10 (1979) 1683–1689. <https://doi.org/10.1007/BF02811701>.
- [81] C.R. Arganis-Juárez, A. Vázquez, N.F. Garza-Montes-de-Oca, R. Colás, Sensitization of an austenitic stainless steel due to the occurrence of δ-ferrite, Corros. Rev. 37 (2019) 179–186. <https://doi.org/10.1515/correv-2018-0036>.
- [82] Q. Chao, S. Thomas, N. Birbilis, P. Cizek, P.D. Hodgson, D. Fabijanic, The effect of post-processing heat treatment on the microstructure, residual stress and mechanical properties of selective laser melted 316L stainless steel, Mater. Sci. Eng. A. 821 (2021) 141611. <https://doi.org/10.1016/j.msea.2021.141611>.
- [83] N. Chen, G. Ma, W. Zhu, A. Godfrey, Z. Shen, G. Wu, X. Huang, Enhancement of an additive-manufactured austenitic stainless steel by post-manufacture heat-treatment, Mater. Sci. Eng. A. 759 (2019) 65–69. <https://doi.org/10.1016/j.msea.2019.04.111>.
- [84] D. Kong, C. Dong, X. Ni, L. Zhang, J. Yao, C. Man, X. Cheng, K. Xiao, X. Li, Mechanical properties and corrosion behavior of selective laser melted 316L stainless steel after different heat treatment processes, J. Mater. Sci. Technol. 35 (2019) 1499–1507. <https://doi.org/10.1016/j.jmst.2019.03.003>.
- [85] V. Shankar, K. Bhanu Sankara Rao, S.. Mannan, Microstructure and mechanical properties of Inconel 625 superalloy, J. Nucl. Mater. 288 (2001) 222–232. [https://doi.org/10.1016/S0022-3115\(00\)00723-6](https://doi.org/10.1016/S0022-3115(00)00723-6).
- [86] J.N. DuPont, C. V. Robino, J.R. Michael, M.R. Nous, A.R. Marder, Solidification of Nb-bearing superalloys: Part I. Reaction sequences, Metall. Mater. Trans. A Phys. Metall. Mater. Sci. 29 (1998) 2785–2796. <https://doi.org/10.1007/s11661-998-0319-3>.
- [87] M. Sundararaman, P. Mukhopadhyay, S. Banerjee, Precipitation of the δ-Ni₃Nb phase in two nickel base superalloys, Metall. Trans. A. 19 (1988) 453–465. <https://doi.org/10.1007/BF02649259>.
- [88] E.A. Lass, M.R. Stoudt, M.E. Williams, M.B. Katz, L.E. Levine, T.Q. Phan, T.H. Gnaeupel-

- Herold, D.S. Ng, Formation of the Ni₃Nb δ-Phase in Stress-Relieved Inconel 625 Produced via Laser Powder-Bed Fusion Additive Manufacturing, *Metall. Mater. Trans. A Phys. Metall. Mater. Sci.* 48 (2017) 5547–5558. <https://doi.org/10.1007/s11661-017-4304-6>.
- [89] B. Hassan, J. Corney, Grain boundary precipitation in Inconel 718 and ATI 718Plus, *Mater. Sci. Technol.* 33 (2017) 1879–1889. <https://doi.org/10.1080/02670836.2017.1333222>.
- [90] M.J. Cieslak, The Solidification Behavior of an Alloy 625/718 Variant, in: *Superalloys 718, 625 Var. Deriv.*, TMS, 1991: pp. 71–80. https://doi.org/10.7449/1991/Superalloys_1991_71_80.
- [91] J.N. Dupont, Solidification of an alloy 625 Weld Overlay, *Metall. Mater. Trans. A Phys. Metall. Mater. Sci.* 27 (1996) 3612–3620. <https://doi.org/10.1007/BF02595452>.
- [92] S. Floreen, G.E. Fuchs, W.J. Yang, The Metallurgy of Alloy 625, in: *Superalloys 718, 625, 706 Var. Deriv.*, TMS, 1994: pp. 13–37. https://doi.org/10.7449/1994/Superalloys_1994_13_37.
- [93] M.R. Stoudt, E.A. Lass, D.S. Ng, M.E. Williams, F. Zhang, C.E. Campbell, G. Lindwall, L.E. Levine, The Influence of Annealing Temperature and Time on the Formation of δ-Phase in Additively-Manufactured Inconel 625, *Metall. Mater. Trans. A* 49 (2018) 3028–3037. <https://doi.org/10.1007/s11661-018-4643-y>.
- [94] F. Cortial, J.M. Corrieu, C. Vernot-Loier, Influence of heat treatments on microstructure, mechanical properties, and corrosion resistance of weld alloy 625, *Metall. Mater. Trans. A* 26 (1995) 1273–1286. <https://doi.org/10.1007/BF02670621>.
- [95] F. Xu, Y. Lv, Y. Liu, B. Xu, P. He, Effect of Heat Treatment on Microstructure and Mechanical Properties of Inconel 625 Alloy Fabricated by Pulsed Plasma Arc Deposition, *Phys. Procedia* 50 (2013) 48–54. <https://doi.org/10.1016/j.phpro.2013.11.010>.
- [96] E.G. Astafurova, M.Y. Panchenko, V.A. Moskvina, G.G. Maier, S. V. Astafurov, E. V. Melnikov, A.S. Fortuna, K.A. Reunova, V.E. Rubtsov, E.A. Kolubaev, Microstructure and grain growth inhomogeneity in austenitic steel produced by wire-feed electron beam melting: the effect of post-building solid-solution treatment, *J. Mater. Sci.* 55 (2020) 9211–9224. <https://doi.org/10.1007/s10853-020-04424-w>.
- [97] J.W. Elmer, S.M. Allen, T.W. Eagar, Microstructural development during solidification of stainless steel alloys, *Metall. Trans. A* 20 (1989) 2117–2131. <https://doi.org/10.1007/BF02650298>.
- [98] N. Suutala, T. Takalo, T. Moisio, Ferritic-austenitic solidification mode in austenitic stainless steel welds, *Metall. Trans. A* 11 (1980) 717–725. <https://doi.org/10.1007/BF02661201>.
- [99] J.W. Fu, Y.S. Yang, J.J. Guo, Formation of a blocky ferrite in Fe–Cr–Ni alloy during directional solidification, *J. Cryst. Growth.* 311 (2009) 3661–3666. <https://doi.org/10.1016/j.jcrysgro.2009.05.007>.
- [100] A.F. Padilha, P.R. Rios, Decomposition of Austenite in Austenitic Stainless Steels, *ISIJ Int.* 42

(2002) 325–327. <https://doi.org/10.2355/isijinternational.42.325>.

- [101] A.F. Padilha, D.M. Escriba, E. Materna-Morris, M. Rieth, M. Klimenkov, Precipitation in AISI 316L(N) during creep tests at 550 and 600°C up to 10 years, *J. Nucl. Mater.* 362 (2007) 132–138. <https://doi.org/10.1016/j.jnucmat.2006.12.027>.
- [102] T.. Chen, J.. Yang, Effects of solution treatment and continuous cooling on σ -phase precipitation in a 2205 duplex stainless steel, *Mater. Sci. Eng. A.* 311 (2001) 28–41. [https://doi.org/10.1016/S0921-5093\(01\)00911-X](https://doi.org/10.1016/S0921-5093(01)00911-X).
- [103] J.P. Oliveira, F.M.B. Fernandes, R.M. Miranda, N. Schell, J.L. Ocaña, Residual stress analysis in laser welded NiTi sheets using synchrotron X-ray diffraction, *Mater. Des.* 100 (2016) 180–187. <https://doi.org/10.1016/j.matdes.2016.03.137>.
- [104] B. Rivolta, R. Gerosa, F. Tavasci, The dilatometric technique for studying sigma phase precipitation kinetics in F55 steel grade, *J. Therm. Anal. Calorim.* 132 (2018) 869–877. <https://doi.org/10.1007/s10973-017-6940-x>.
- [105] S. Atamert, J.E. King, Sigma-phase formation and its prevention in duplex stainless steels, *J. Mater. Sci. Lett.* 12 (1993) 1144–1147. <https://doi.org/10.1007/BF00420548>.
- [106] A. Caballero, J. Ding, S. Ganguly, S. Williams, Wire + Arc Additive Manufacture of 17-4 PH stainless steel: Effect of different processing conditions on microstructure, hardness, and tensile strength, *J. Mater. Process. Technol.* 268 (2019) 54–62. <https://doi.org/10.1016/j.jmatprotec.2019.01.007>.
- [107] T.P.S. Gill, M. Vijayalakshmi, J.B. Gnanamoorthy, K.A. Padmanabhan, Transformation of Delta-Ferrite During the Postweld Heat Treatment of Type 316L Stainless Steel Weld Metal., *Weld. J. (Miami, Fla.)*. 65 (1986) 122–128.
- [108] A. Bénéteau, P. Weisbecker, G. Geandier, E. Aeby-Gautier, B. Appolaire, Austenitization and precipitate dissolution in high nitrogen steels: an in situ high temperature X-ray synchrotron diffraction analysis using the Rietveld method, *Mater. Sci. Eng. A.* 393 (2005) 63–70. <https://doi.org/10.1016/j.msea.2004.09.054>.
- [109] D. Manova, S. Mändl, H. Neumann, B. Rauschenbach, Analysis of in situ XRD measurements for low energy ion beam nitriding of austenitic stainless steel, *Surf. Coatings Technol.* 256 (2014) 64–72. <https://doi.org/10.1016/j.surfcoat.2014.03.047>.
- [110] S. Li, Q. Wei, Y. Shi, C.K. Chua, Z. Zhu, D. Zhang, Microstructure Characteristics of Inconel 625 Superalloy Manufactured by Selective Laser Melting, *J. Mater. Sci. Technol.* 31 (2015) 946–952. <https://doi.org/10.1016/j.jmst.2014.09.020>.
- [111] J. Hönnige, C.E. Seow, S. Ganguly, X. Xu, S. Cabeza, H. Coules, S. Williams, Study of residual stress and microstructural evolution in as-deposited and inter-pass rolled wire plus arc additively manufactured Inconel 718 alloy after ageing treatment, *Mater. Sci. Eng. A.* 801

(2021) 140368. <https://doi.org/10.1016/j.msea.2020.140368>.

- [112] X. Xing, X. Di, B. Wang, The effect of post-weld heat treatment temperature on the microstructure of Inconel 625 deposited metal, *J. Alloys Compd.* 593 (2014) 110–116. <https://doi.org/10.1016/j.jallcom.2013.12.224>.
- [113] G. Lindwall, C.E. Campbell, E.A. Lass, F. Zhang, M.R. Stoudt, A.J. Allen, L.E. Levine, Simulation of TTT Curves for Additively Manufactured Inconel 625, *Metall. Mater. Trans. A Phys. Metall. Mater. Sci.* 50 (2019) 457–467. <https://doi.org/10.1007/s11661-018-4959-7>.
- [114] T. Keller, G. Lindwall, S. Ghosh, L. Ma, B.M. Lane, F. Zhang, U.R. Kattner, E.A. Lass, J.C. Heigel, Y. Idell, M.E. Williams, A.J. Allen, J.E. Guyer, L.E. Levine, Application of finite element, phase-field, and CALPHAD-based methods to additive manufacturing of Ni-based superalloys, *Acta Mater.* 139 (2017) 244–253. <https://doi.org/10.1016/j.actamat.2017.05.003>.
- [115] T.A. Rodrigues, J.D. Escobar, J. Shen, V.R. Duarte, G.G. Ribamar, J.A. Avila, E. Maawad, N. Schell, T.G. Santos, J.P. Oliveira, Effect of heat treatments on 316 stainless steel parts fabricated by wire and arc additive manufacturing: Microstructure and synchrotron X-ray diffraction analysis, *Addit. Manuf.* 48 (2021) 102428. <https://doi.org/10.1016/j.addma.2021.102428>.
- [116] J.A. Spittle, Columnar to equiaxed grain transition in as solidified alloys, *Int. Mater. Rev.* 51 (2006) 247–269. <https://doi.org/10.1179/174328006X102493>.
- [117] M.J. Bermingham, D. Kent, H. Zhan, D.H. StJohn, M.S. Dargusch, Controlling the microstructure and properties of wire arc additive manufactured Ti–6Al–4V with trace boron additions, *Acta Mater.* 91 (2015) 289–303. <https://doi.org/10.1016/j.actamat.2015.03.035>.
- [118] P. Dirisu, S. Ganguly, A. Mehmanparast, F. Martina, S. Williams, Analysis of fracture toughness properties of wire + arc additive manufactured high strength low alloy structural steel components, *Mater. Sci. Eng. A.* 765 (2019) 138285. <https://doi.org/10.1016/j.msea.2019.138285>.
- [119] H. Bhadeshia, R. Honeycombe, *Steels: Microstructure and Properties*, 4th Ed., Butterworth-Heinemann, 2017.
- [120] S. Mereddy, M.J. Bermingham, D.H. StJohn, M.S. Dargusch, Grain refinement of wire arc additively manufactured titanium by the addition of silicon, *J. Alloys Compd.* 695 (2017) 2097–2103. <https://doi.org/10.1016/j.jallcom.2016.11.049>.
- [121] B. Song, S. Dong, P. Coddet, G. Zhou, S. Ouyang, H. Liao, C. Coddet, Microstructure and tensile behavior of hybrid nano-micro SiC reinforced iron matrix composites produced by selective laser melting, *J. Alloys Compd.* 579 (2013) 415–421. <https://doi.org/10.1016/j.jallcom.2013.06.087>.
- [122] G. Thawari, G. Sundararajan, S.. Joshi, Laser surface alloying of medium carbon steel with

SiC, *Thin Solid Films.* 423 (2003) 41–53. [https://doi.org/10.1016/S0040-6090\(02\)00974-4](https://doi.org/10.1016/S0040-6090(02)00974-4).

- [123] B. Basu, G.B. Raju, A.K. Suri, Processing and properties of monolithic TiB₂ based materials, *Int. Mater. Rev.* 51 (2006) 352–374. <https://doi.org/10.1179/174328006X102529>.
- [124] L. Xu, C. Cui, X. Sun, The effects of Co and Ti additions on microstructures and compressive strength of Udimet710, *Mater. Sci. Eng. A.* 528 (2011) 7851–7856. <https://doi.org/10.1016/j.msea.2011.07.019>.
- [125] B. Tang, Y. Tan, T. Xu, Z. Sun, X. Li, Effects of TiB₂ Particles Content on Microstructure, Mechanical Properties and Tribological Properties of Ni-Based Composite Coatings Reinforced with TiB₂ Particles by Laser Cladding, *Coatings.* 10 (2020) 813. <https://doi.org/10.3390/coatings10090813>.
- [126] B. Zhang, G. Bi, P. Wang, J. Bai, Y. Chew, M.S. Nai, Microstructure and mechanical properties of Inconel 625/nano-TiB₂ composite fabricated by LAAM, *Mater. Des.* 111 (2016) 70–79. <https://doi.org/10.1016/j.matdes.2016.08.078>.
- [127] S.S. Babu, The mechanism of acicular ferrite in weld deposits, *Curr. Opin. Solid State Mater. Sci.* 8 (2004) 267–278. <https://doi.org/10.1016/j.cossms.2004.10.001>.
- [128] A. Lambert-Perlade, A.F. Gourgues, J. Besson, T. Sturel, A. Pineau, Mechanisms and modeling of cleavage fracture in simulated heat-affected zone microstructures of a high-strength low alloy steel, *Metall. Mater. Trans. A Phys. Metall. Mater. Sci.* 35 (2004) 1039–1053. <https://doi.org/10.1007/s11661-004-1007-6>.
- [129] S. Zajac, V. Schwinn, K.H. Tacke, Characterisation and Quantification of Complex Bainitic Microstructures in High and Ultra-High Strength Linepipe Steels, *Mater. Sci. Forum.* 500–501 (2005) 387–394. <https://doi.org/10.4028/www.scientific.net/MSF.500-501.387>.
- [130] M.. Saleh, R. Priestner, Retained austenite in dual-phase silicon steels and its effect on mechanical properties, *J. Mater. Process. Technol.* 113 (2001) 587–593. [https://doi.org/10.1016/S0924-0136\(01\)00638-0](https://doi.org/10.1016/S0924-0136(01)00638-0).
- [131] E. Kozeschnik, H.K.D.H. Bhadeshia, Influence of silicon on cementite precipitation in steels, *Mater. Sci. Technol.* 24 (2008) 343–347. <https://doi.org/10.1179/174328408X275973>.
- [132] N. Jia, Z.H. Cong, X. Sun, S. Cheng, Z.H. Nie, Y. Ren, P.K. Liaw, Y.D. Wang, An in situ high-energy X-ray diffraction study of micromechanical behavior of multiple phases in advanced high-strength steels, *Acta Mater.* 57 (2009) 3965–3977. <https://doi.org/10.1016/j.actamat.2009.05.002>.
- [133] L.C.D. Fielding, N.G. Jones, J. Walsh, S. Van Boxel, M.S. Blackmur, P.D. Lee, P.J. Withers, H.J. Stone, H.K.D.H. Bhadeshia, Synchrotron analysis of toughness anomalies in nanostructured bainite, *Acta Mater.* 105 (2016) 52–58. <https://doi.org/10.1016/j.actamat.2015.11.029>.

- [134] D. Delagnes, P. Lamesle, M.H. Mathon, N. Mebarki, C. Levaillant, Influence of silicon content on the precipitation of secondary carbides and fatigue properties of a 5%Cr tempered martensitic steel, *Mater. Sci. Eng. A.* 394 (2005) 435–444. <https://doi.org/10.1016/j.msea.2004.11.050>.
- [135] W.J. Nam, H.C. Choi, Effect of Si on mechanical properties of low alloy steels, *Mater. Sci. Technol.* 15 (1999) 527–530. <https://doi.org/10.1179/026708399101506238>.
- [136] G. Miyamoto, J.C. Oh, K. Hono, T. Furuhashi, T. Maki, Effect of partitioning of Mn and Si on the growth kinetics of cementite in tempered Fe-0.6 mass% C martensite, *Acta Mater.* 55 (2007) 5027–5038. <https://doi.org/10.1016/j.actamat.2007.05.023>.
- [137] J. Yu, Carbide stability diagrams in 2.25Cr-1Mo steels, *Metall. Trans. A.* 20 (1989) 1561–1564. <https://doi.org/10.1007/BF02665512>.
- [138] B. Kim, C. Celada, D. San Martín, T. Sourmail, P.E.J. Rivera-Díaz-Del-Castillo, The effect of silicon on the nanoprecipitation of cementite, *Acta Mater.* 61 (2013) 6983–6992. <https://doi.org/10.1016/j.actamat.2013.08.012>.
- [139] F.G. Caballero, H.K.D.H. Bhadeshia, Very strong bainite, *Curr. Opin. Solid State Mater. Sci.* 8 (2004) 251–257. <https://doi.org/10.1016/j.cossms.2004.09.005>.
- [140] H. K. D. H. Bhadeshia, Bainite in steels: Transformations, Microstructure and Properties, 2nd ed., 2001.
- [141] E.O. Hall, The Deformation and Ageing of Mild Steel: III Discussion of Results, *Proc. Phys. Soc. Sect. B.* 64 (1951) 747–753. <https://doi.org/10.1088/0370-1301/64/9/303>.
- [142] N.J. Petch, The Cleavage Strength of Polycrystals, *J. Iron Steel Inst.* 174 (1953) 25–28.
- [143] R.M. Aikin, The mechanical properties of in-situ composites, *J. Miner.* 49 (1997) 35–39. <https://doi.org/10.1007/BF02914400>.
- [144] R.J. Arsenault, N. Shi, Dislocation generation due to differences between the coefficients of thermal expansion, *Mater. Sci. Eng.* 81 (1986) 175–187. [https://doi.org/10.1016/0025-5416\(86\)90261-2](https://doi.org/10.1016/0025-5416(86)90261-2).
- [145] T.G. Santos, P. Vilaa, R.M. Miranda, Electrical conductivity field analysis for evaluation of FSW joints in AA6013 and AA7075 alloys, *J. Mater. Process. Technol.* 211 (2011) 174–180. <https://doi.org/10.1016/j.jmatprotec.2010.08.030>.
- [146] J. Goldak, A. Chakrabarti, M. Bibby, A new finite element model for welding heat sources, *Metall. Trans. B.* 15 (1984) 299–305. <https://doi.org/10.1007/BF02667333>.
- [147] ASTM Standard E9-09, Standard Test Methods of Compression Testing of Metallic Materials at Room Temperature, (2012). <https://doi.org/10.1520/E0009-09>.
- [148] X. Wang, P.W. Liu, Y. Ji, Y. Liu, M.H. Horstemeyer, L. Chen, Investigation on Microsegregation

- of IN718 Alloy During Additive Manufacturing via Integrated Phase-Field and Finite-Element Modeling, *J. Mater. Eng. Perform.* 28 (2019) 657–665. <https://doi.org/10.1007/s11665-018-3620-3>.
- [149] B. Geddes, H. Leon, X. Huang, Superalloys, ASM International, 2010. <https://doi.org/10.31399/asm.tb.sap.9781627083133>.
- [150] J. Nakkki, J. Tuominen, P. Vuoristo, Effect of minor elements on solidification cracking and dilution of alloy 625 powders in laser cladding, *J. Laser Appl.* 29 (2017) 012014. <https://doi.org/10.2351/1.4973673>.
- [151] Y. Gao, Y. Ding, J. Chen, J. Xu, Y. Ma, X. Wang, Effect of twin boundaries on the microstructure and mechanical properties of Inconel 625 alloy, *Mater. Sci. Eng. A.* 767 (2019) 138361. <https://doi.org/10.1016/j.msea.2019.138361>.
- [152] D.H. StJohn, A. Prasad, M.A. Easton, M. Qian, The Contribution of Constitutional Supercooling to Nucleation and Grain Formation, *Metall. Mater. Trans. A.* 46 (2015) 4868–4885. <https://doi.org/10.1007/s11661-015-2960-y>.
- [153] H.P. Wang, C.H. Zheng, P.F. Zou, S.J. Yang, L. Hu, B. Wei, Density determination and simulation of Inconel 718 alloy at normal and metastable liquid states, *J. Mater. Sci. Technol.* 34 (2018) 436–439. <https://doi.org/10.1016/j.jmst.2017.10.014>.
- [154] B. Tang, Y. Tan, Z. Zhang, T. Xu, Z. Sun, X. Li, Effects of Process Parameters on Geometrical Characteristics, Microstructure and Tribological Properties of TiB₂ Reinforced Inconel 718 Alloy Composite Coatings by Laser Cladding, *Coatings*. 10 (2020) 76. <https://doi.org/10.3390/coatings10010076>.
- [155] W.-D. Cao, R. Kennedy, Role of Chemistry in 718-Type Alloys: Allvac 718plus Alloy Development, in: Superalloys 2004 (Tenth Int. Symp., TMS, 2004: pp. 91–99. https://doi.org/10.7449/2004/Superalloys_2004_91_99.
- [156] J.P. Collier, S.H. Wong, J.K. Tien, J.C. Phillips, The effect of varying Al, Ti, and Nb content on the phase stability of INCONEL 718, *Metall. Trans. A.* 19 (1988) 1657–1666. <https://doi.org/10.1007/BF02645133>.
- [157] S.-Y. Seo, S.-J. Lee, Effects of Ti and Nb on the Grain Refinement and Mechanical Properties of AISI 4145 Steel, *Trans. Indian Inst. Met.* 71 (2018) 3037–3043. <https://doi.org/10.1007/s12666-018-1405-x>.
- [158] A.N.M. Tanvir, M.R.U. Ahsan, G. Seo, J. duk Kim, C. Ji, B. Bates, Y. Lee, D.B. Kim, Heat treatment effects on Inconel 625 components fabricated by wire + arc additively manufacturing (WAAM)—part 2: mechanical properties, *Int. J. Adv. Manuf. Technol.* 110 (2020) 1709–1721. <https://doi.org/10.1007/s00170-020-05980-w>.
- [159] Y. Wang, X. Chen, Q. Shen, C. Su, Y. Zhang, S. Jayalakshmi, R.A. Singh, Effect of magnetic

Field on the microstructure and mechanical properties of inconel 625 superalloy fabricated by wire arc additive manufacturing, *J. Manuf. Process.* 64 (2021) 10–19. <https://doi.org/10.1016/j.jmapro.2021.01.008>.

- [160] Y.L. Hu, X. Lin, X.B. Yu, J.J. Xu, M. Lei, W.D. Huang, Effect of Ti addition on cracking and microhardness of Inconel 625 during the laser solid forming processing, *J. Alloys Compd.* 711 (2017) 267–277. <https://doi.org/10.1016/j.jallcom.2017.03.355>.
- [161] A.K. Jena, M.C. Chaturvedi, The role of alloying elements in the design of nickel-base superalloys, *J. Mater. Sci.* 19 (1984) 3121–3139. <https://doi.org/10.1007/BF00549796>.
- [162] L.C.M. Valle, L.S. Araújo, S.B. Gabriel, J. Dille, L.H. de Almeida, The Effect of δ Phase on the Mechanical Properties of an Inconel 718 Superalloy, *J. Mater. Eng. Perform.* 22 (2013) 1512–1518. <https://doi.org/10.1007/s11665-012-0433-7>.
- [163] A.N.M. Tanvir, M.R.U. Ahsan, C. Ji, W. Hawkins, B. Bates, D.B. Kim, Heat treatment effects on Inconel 625 components fabricated by wire + arc additive manufacturing (WAAM)—part 1: microstructural characterization, *Int. J. Adv. Manuf. Technol.* (2019). <https://doi.org/10.1007/s00170-019-03828-6>.
- [164] S.S. WANG, Fracture Mechanics for Delamination Problems in Composite Materials, in: *Stud. Appl. Mech.*, Elsevier Science Publishers B.V., 1984: pp. 369–383. <https://doi.org/10.1016/B978-0-444-42169-2.50029-2>.
- [165] C. Zhang, F. Chen, Z. Huang, M. Jia, G. Chen, Y. Ye, Y. Lin, W. Liu, B. Chen, Q. Shen, L. Zhang, E.J. Lavernia, Additive manufacturing of functionally graded materials: A review, *Mater. Sci. Eng. A.* 764 (2019) 138209. <https://doi.org/10.1016/j.msea.2019.138209>.
- [166] K. Pietrzak, D. Kaliński, M. Chmielewski, Interlayer of Al₂O₃–Cr functionally graded material for reduction of thermal stresses in alumina–heat resisting steel joints, *J. Eur. Ceram. Soc.* 27 (2007) 1281–1286. <https://doi.org/10.1016/j.jeurceramsoc.2006.04.102>.
- [167] B.E. Carroll, T.A. Palmer, A.M. Beese, Anisotropic tensile behavior of Ti–6Al–4V components fabricated with directed energy deposition additive manufacturing, *Acta Mater.* 87 (2015) 309–320. <https://doi.org/10.1016/j.actamat.2014.12.054>.
- [168] C. Tan, Y. Chew, G. Bi, D. Wang, W. Ma, Y. Yang, K. Zhou, Additive manufacturing of steel–copper functionally graded material with ultrahigh bonding strength, *J. Mater. Sci. Technol.* 72 (2021) 217–222. <https://doi.org/10.1016/j.jmst.2020.07.044>.
- [169] T.A. Mai, A.C. Spowage, Characterisation of dissimilar joints in laser welding of steel–kovar, copper–steel and copper–aluminium, *Mater. Sci. Eng. A.* 374 (2004) 224–233. <https://doi.org/10.1016/j.msea.2004.02.025>.
- [170] X. Sun, W. Hao, G. Geng, T. Ma, Y. Li, Solidification Microstructure Evolution of Undercooled Cu-15 wt.% Fe Alloy Melt, *Adv. Mater. Sci. Eng.* 2018 (2018).

<https://doi.org/10.1155/2018/6304518>.

- [171] S. Chen, J. Huang, J. Xia, H. Zhang, X. Zhao, Microstructural characteristics of a stainless steel/copper dissimilar joint made by laser welding, *Metall. Mater. Trans. A Phys. Metall. Mater. Sci.* 44 (2013) 3690–3696. <https://doi.org/10.1007/s11661-013-1693-z>.
- [172] S. Chen, J. Huang, J. Xia, X. Zhao, S. Lin, Influence of processing parameters on the characteristics of stainless steel/copper laser welding, *J. Mater. Process. Technol.* 222 (2015) 43–51. <https://doi.org/10.1016/j.jmatprotec.2015.03.003>.
- [173] M. Velu, S. Bhat, Metallurgical and mechanical examinations of steel-copper joints arc welded using bronze and nickel-base superalloy filler materials, *Mater. Des.* 47 (2013) 793–809. <https://doi.org/10.1016/j.matdes.2012.12.073>.
- [174] X. Zhang, C. Sun, T. Pan, A. Flood, Y. Zhang, L. Li, F. Liou, Additive manufacturing of copper – H13 tool steel bi-metallic structures via Ni-based multi-interlayer, *Addit. Manuf.* 36 (2020) 101474. <https://doi.org/10.1016/j.addma.2020.101474>.
- [175] U. Articek, M. Milfelner, I. Anzel, Synthesis of functionally graded material H13/Cu by LENS technology, *Adv. Prod. Eng. Manag.* 8 (2013) 169–176. <https://doi.org/10.14743/apem2013.3.164>.
- [176] X. Shu, G. Chen, J. Liu, B. Zhang, J. Feng, Microstructure evolution of copper/steel gradient deposition prepared using electron beam freeform fabrication, *Mater. Lett.* 213 (2018) 374–377. <https://doi.org/10.1016/j.matlet.2017.11.016>.
- [177] P. Varghese, E. Vetrivendan, M.K. Dash, S. Ningshen, M. Kamaraj, U. Kamachi Mudali, Weld overlay coating of Inconel 617 M on type 316 L stainless steel by cold metal transfer process, *Surf. Coatings Technol.* 357 (2019) 1004–1013. <https://doi.org/10.1016/j.surfcoat.2018.10.073>.
- [178] P.R.A. Bloemer, J.T. Pacheco, A. Cunha, M.T. Veiga, O.C. de M. Filho, V.H. Meura, M.F. Teixeira, Laser Cladding of Inconel 625 on AISI 316L: Microstructural and Mechanical Evaluation of Parameters Estimated by Empirical-Statistical Model, *J. Mater. Eng. Perform.* 31 (2022) 211–220. <https://doi.org/10.1007/s11665-021-06147-8>.
- [179] F.W.C. Farias, J. da C. Payão Filho, D.A. da Silva Júnior, R.N. de Moura, M.C.G. Rios, Microstructural characterization of Ni-based superalloy 625 clad welded on a 9% Ni steel pipe by plasma powder transferred arc, *Surf. Coatings Technol.* 374 (2019) 1024–1037. <https://doi.org/10.1016/j.surfcoat.2019.06.084>.
- [180] K. Shah, I. ul Haq, A. Khan, S.A. Shah, M. Khan, A.J. Pinkerton, Parametric study of development of Inconel-steel functionally graded materials by laser direct metal deposition, *Mater. Des.* 54 (2014) 531–538. <https://doi.org/10.1016/j.matdes.2013.08.079>.
- [181] S. Kou, Solidification and liquation cracking issues in welding, *JOM.* 55 (2003) 37–42. <https://doi.org/10.1007/s11837-003-0137-4>.

- [182] N. Chen, H.A. Khan, Z. Wan, J. Lippert, H. Sun, S.-L. Shang, Z.-K. Liu, J. Li, Microstructural characteristics and crack formation in additively manufactured bimetal material of 316L stainless steel and Inconel 625, *Addit. Manuf.* 32 (2020) 101037. <https://doi.org/10.1016/j.addma.2020.101037>.
- [183] B.E. Carroll, R.A. Otis, J.P. Borgonia, J.O. Suh, R.P. Dillon, A.A. Shapiro, D.C. Hofmann, Z.K. Liu, A.M. Beese, Functionally graded material of 304L stainless steel and inconel 625 fabricated by directed energy deposition: Characterization and thermodynamic modeling, *Acta Mater.* 108 (2016) 46–54. <https://doi.org/10.1016/j.actamat.2016.02.019>.
- [184] N. Kozamernik, D. Bračun, D. Klobčar, WAAM system with interpass temperature control and forced cooling for near-net-shape printing of small metal components, *Int. J. Adv. Manuf. Technol.* 110 (2020) 1955–1968. <https://doi.org/10.1007/s00170-020-05958-8>.
- [185] K. Wang, S.L. Shang, Y. Wang, A. Vivek, G. Daehn, Z.K. Liu, J. Li, Unveiling non-equilibrium metallurgical phases in dissimilar Al-Cu joints processed by vaporizing foil actuator welding, *Mater. Des.* 186 (2020) 108306. <https://doi.org/10.1016/j.matdes.2019.108306>.
- [186] Y. Yehorov, L.J. da Silva, A. Scotti, Exploring the use of switchback for mitigating homoepitaxial unidirectional grain growth and porosity in WAAM of aluminium alloys, *Int. J. Adv. Manuf. Technol.* 104 (2019) 1581–1592. <https://doi.org/10.1007/s00170-019-03959-w>.
- [187] L. Han, T. Han, G. Chen, B. Wang, J. Sun, Y. Wang, Influence of heat input on microstructure, hardness and pitting corrosion of weld metal in duplex stainless steel welded by keyhole-TIG, *Mater. Charact.* 175 (2021) 111052. <https://doi.org/10.1016/j.matchar.2021.111052>.
- [188] Y. Zhang, F. Cheng, S. Wu, The microstructure and mechanical properties of duplex stainless steel components fabricated via flux-cored wire arc-additive manufacturing, *J. Manuf. Process.* 69 (2021) 204–214. <https://doi.org/10.1016/j.jmapro.2021.07.045>.
- [189] J. Verma, R.V. Taiwade, Dissimilar welding behavior of 22% Cr series stainless steel with 316L and its corrosion resistance in modified aggressive environment, *J. Manuf. Process.* 24 (2016) 1–10. <https://doi.org/10.1016/j.jmapro.2016.07.001>.
- [190] B.T. Alexandrov, J.C. Lippold, J.W. Sowards, A.T. Hope, D.R. Saltzmann, Fusion boundary microstructure evolution associated with embrittlement of Ni-base alloy overlays applied to carbon steel, *Weld. World.* 57 (2013) 39–53. <https://doi.org/10.1007/s40194-012-0007-1>.
- [191] T. Soysal, S. Kou, D. Tat, T. Pasang, Macrosegregation in dissimilar-metal fusion welding, *Acta Mater.* 110 (2016) 149–160. <https://doi.org/10.1016/j.actamat.2016.03.004>.
- [192] M. Rozmus-Górnikowska, Ł. Cieniek, M. Blicharski, J. Kusiński, Microstructure and Microsegregation of an Inconel 625 Weld Overlay Produced on Steel Pipes by the Cold Metal Transfer Technique, *Arch. Metall. Mater.* 59 (2014) 1081–1084. <https://doi.org/10.2478/amm-2014-0185>.

- [193] M.A. Turchanin, P.G. Agraval, I. V. Nikolaenko, Thermodynamics of alloys and phase equilibria in the copper-iron system, *J. Phase Equilibria.* 24 (2003) 307–319. <https://doi.org/10.1361/105497103770330280>.
- [194] Y.Z. Chen, F. Liu, G.C. Yang, X.Q. Xu, Y.H. Zhou, Rapid solidification of bulk undercooled hypoperitectic Fe–Cu alloy, *J. Alloys Compd.* 427 (2007) L1–L5. <https://doi.org/10.1016/j.jallcom.2006.03.012>.
- [195] O. Zobac, A. Kroupa, A. Zemanova, K.W. Richter, Experimental Description of the Al-Cu Binary Phase Diagram, *Metall. Mater. Trans. A Phys. Metall. Mater. Sci.* 50 (2019) 3805–3815. <https://doi.org/10.1007/s11661-019-05286-x>.
- [196] A. Zafari, K. Xia, Laser Powder Bed Fusion of Ultrahigh Strength Fe-Cu Alloys Using Elemental Powders, *Addit. Manuf.* (2021) 102270. <https://doi.org/10.1016/j.addma.2021.102270>.
- [197] S. Liu, J. Jie, Z. Guo, G. Yin, T. Wang, T. Li, Solidification microstructure evolution and its corresponding mechanism of metastable immiscible Cu₈₀Fe₂₀ alloy with different cooling conditions, *J. Alloys Compd.* 742 (2018) 99–106. <https://doi.org/10.1016/j.jallcom.2018.01.306>.
- [198] L. Liao, S. Chumbley, Influence of Cooling Rate on the Ferrite Prediction Diagram of Duplex Stainless Steel Castings, *Metall. Mater. Trans. A* 50 (2019) 2435–2442. <https://doi.org/10.1007/s11661-019-05166-4>.
- [199] S. Curiotto, R. Greco, N.H. Pryds, E. Johnson, L. Battezzati, The liquid metastable miscibility gap in Cu-based systems, *Fluid Phase Equilib.* 256 (2007) 132–136. <https://doi.org/10.1016/j.fluid.2006.10.003>.
- [200] L. Zhu, S. Soto-medina, W. Cuadrado-castillo, R.G. Hennig, M. V Manuel, Materials & Design New experimental studies on the phase diagram of the Al-Cu-Fe quasicrystal-forming system, *Mater. Des.* 185 (2019) 108186. <https://doi.org/10.1016/j.matdes.2019.108186>.
- [201] C.C. Silva, V.H.C. de Albuquerque, E.M. Miná, E.P. Moura, J.M.R.S. Tavares, Mechanical Properties and Microstructural Characterization of Aged Nickel-based Alloy 625 Weld Metal, *Metall. Mater. Trans. A Phys. Metall. Mater. Sci.* 49 (2018) 1653–1673. <https://doi.org/10.1007/s11661-018-4526-2>.
- [202] S. Sui, H. Tan, J. Chen, C. Zhong, Z. Li, W. Fan, A. Gasser, W. Huang, The influence of Laves phases on the room temperature tensile properties of Inconel 718 fabricated by powder feeding laser additive manufacturing, *Acta Mater.* 164 (2019) 413–427. <https://doi.org/10.1016/j.actamat.2018.10.032>.
- [203] D. Wu, J. Shi, F. Niu, G. Ma, C. Zhou, B. Zhang, Direct additive manufacturing of melt growth Al₂O₃-ZrO₂ functionally graded ceramics by laser directed energy deposition, *J. Eur. Ceram. Soc.* 42 (2022) 2957–2973. <https://doi.org/10.1016/j.jeurceramsoc.2022.01.034>.
- [204] M. Landowski, A. Świerczyńska, G. Rogalski, D. Fydrych, Autogenous Fiber Laser Welding of

- 316L Austenitic and 2304 Lean Duplex Stainless Steels, Materials (Basel). 13 (2020) 2930. <https://doi.org/10.3390/ma13132930>.
- [205] D. Kotecki, T. Siewert, WRC-1992 constitution diagram for stainless steel weld metals: a modification of the WRC-1988 diagram, Weld. J. 71 (1992) 171–178.
- [206] S.-Q. Guo, X.-H. Li, Numerical simulation of solidification and liquation behavior during welding of low-expansion superalloys, Front. Mater. Sci. 5 (2011) 146–159. <https://doi.org/10.1007/s11706-011-0126-4>.
- [207] M.J. Cieslak, T.J. Headley, A.D. Romig, T. Kollie, A melting and solidification study of alloy 625, Metall. Trans. A. 19 (1988) 2319–2331. <https://doi.org/10.1007/BF02645056>.
- [208] S. Kou, A criterion for cracking during solidification, Acta Mater. 88 (2015) 366–374. <https://doi.org/10.1016/j.actamat.2015.01.034>.
- [209] J. Liu, S. Kou, Effect of diffusion on susceptibility to cracking during solidification, Acta Mater. 100 (2015) 359–368. <https://doi.org/10.1016/j.actamat.2015.08.064>.
- [210] T. Soysal, S. Kou, D. Tat, T. Pasang, Macrosegregation in dissimilar-metal fusion welding, Acta Mater. 110 (2016) 149–160. <https://doi.org/10.1016/j.actamat.2016.03.004>.
- [211] D.C. Hofmann, J. Kolodziejska, S. Roberts, R. Otis, R.P. Dillon, J.-O. Suh, Z.-K. Liu, J.-P. Borgonia, Compositonally graded metals: A new frontier of additive manufacturing, J. Mater. Res. 29 (2014) 1899–1910. <https://doi.org/10.1557/jmr.2014.208>.
- [212] T.A. Rodrigues, V. Duarte, J.A. Avila, T.G. Santos, R.M. Miranda, J.P. Oliveira, Wire and arc additive manufacturing of HSLA steel: Effect of thermal cycles on microstructure and mechanical properties, Addit. Manuf. 27 (2019) 440–450. <https://doi.org/10.1016/j.addma.2019.03.029>.
- [213] K. Chandra, N.N. Kumar, V. Kain, Effect of Retained δ-Ferrite Transforming to Sigma Phase on the Hardness and Corrosion Resistance of Stainless Steel 321, Trans. Indian Inst. Met. 75 (2022) 959–966. <https://doi.org/10.1007/s12666-022-02534-4>.
- [214] K.D. Ramkumar, J.L.N. Varma, G. Chaitanya, A. Choudhary, N. Arivazhagan, S. Narayanan, Effect of autogeneous GTA welding with and without flux addition on the microstructure and mechanical properties of AISI 904L joints, Mater. Sci. Eng. A. 636 (2015) 1–9. <https://doi.org/10.1016/j.msea.2015.03.072>.
- [215] S.H. Kim, H. Lee, S.M. Yeon, C. Aranas, K. Choi, J. Yoon, S.W. Yang, H. Lee, Selective compositional range exclusion via directed energy deposition to produce a defect-free Inconel 718/SS 316L functionally graded material, Addit. Manuf. 47 (2021) 102288. <https://doi.org/10.1016/j.addma.2021.102288>.
- [216] S.W. Yang, J. Yoon, H. Lee, D.S. Shim, Defect of functionally graded material of inconel 718 and STS 316L fabricated by directed energy deposition and its effect on mechanical properties,

J. Mater. Res. Technol. 17 (2022) 478–497. <https://doi.org/10.1016/j.jmrt.2022.01.029>.

- [217] J.S. Chen, Y. Lu, X.R. Li, Y.M. Zhang, Gas tungsten arc welding using an arcing wire, Weld. J. 91 (2012).
- [218] J. Wang, D. Wu, P. Liao, C.Y. Tian, M.Q. Li, J.C. Feng, Metal transfer and arc behaviour of novel consumable and non-consumable electrode indirect arc droplet welding, Sci. Technol. Weld. Join. 18 (2013) 261–270. <https://doi.org/10.1179/1362171812Y.0000000103>.
- [219] W. Liu, C. Jia, M. Guo, J. Gao, C. Wu, Compulsively constricted WAAM with arc plasma and droplets ejected from a narrow space, Addit. Manuf. 27 (2019) 109–117. <https://doi.org/10.1016/j.addma.2019.03.003>.
- [220] D. Ding, Z. Pan, D. Cuiuri, H. Li, Wire-feed additive manufacturing of metal components: technologies, developments and future interests, Int. J. Adv. Manuf. Technol. 81 (2015) 465–481. <https://doi.org/10.1007/s00170-015-7077-3>.
- [221] S.W. Thompson, D.J. Vin Col, G. Krauss, Continuous cooling transformations and microstructures in a low-carbon, high-strength low-alloy plate steel, Metall. Trans. A. 21 (1990) 1493–1507. <https://doi.org/10.1007/BF02672564>.
- [222] P. Kazanas, P. Deherkar, P. Almeida, H. Lockett, S. Williams, Fabrication of geometrical features using wire and arc additive manufacture, Proc. Inst. Mech. Eng. Part B J. Eng. Manuf. 226 (2012) 1042–1051. <https://doi.org/10.1177/0954405412437126>.
- [223] L. Yuan, Z. Pan, D. Ding, Z. Yu, S. van Duin, H. Li, W. Li, J. Norrish, Fabrication of metallic parts with overhanging structures using the robotic wire arc additive manufacturing, J. Manuf. Process. 63 (2021) 24–34. <https://doi.org/10.1016/j.jmapro.2020.03.018>.
- [224] H. Lockett, J. Ding, S. Williams, F. Martina, Design for Wire + Arc Additive Manufacture: design rules and build orientation selection, J. Eng. Des. 28 (2017) 568–598. <https://doi.org/10.1080/09544828.2017.1365826>.